PRODUCTION OF SINTERED NDFEB MAGNETS FROM SCRAP ALLOY POWDERS

by

ENRIQUE HERRAIZ LALANA

A thesis submitted to the University of Birmingham for the degree of DOCTOR OF PHILOSOPHY

School of Metallurgy and Materials
College of Engineering and Physical Sciences
University of Birmingham

November 2016

Abstract

Rare earth metals are at the highest supply risk of all metals used for clean-energy technologies in part due to supply restrictions from the main suppliers in China. Rare earth elements are essential to produce the highest energy product rare earth permanent magnets which are used in advanced green applications such as the generators in wind turbines and the motors in electric vehicles. This supply 'crisis' has been addressed by many authors by, for example, reducing or substituting the rare earths for less critical elements, or by finding new primary resources. The focus of this thesis, however, is on the recycling of rare earth magnets.

Previous work has shown that hydrogen is an effective process gas which can be used to break down the NdFeB magnets into a friable powder containing $Nd_2Fe_{14}BH_x$ and $NdH_{2.7}$. It has also been shown that it is possible to re-sinter this material into new magnets. However, the secondary material has higher oxygen content than the primary material, which reduces the quantity of Nd for liquid phase sintering.

The aim of this work was to maximise the magnetic performance, by investigating the (1) effect of particle size of the hydrogenated NdFeB powder, (2) addition of neodymium hydride to aid liquid phase sintering and hence magnetic performance; and (3) separation techniques to remove the oxidised Nd prior to liquid phase sintering. Uncoated end-of-life sintered NdFeB magnets from voice coil motors were exposed to hydrogen at room temperature to break them down into a friable hydrogenated NdFeB powder. The hydrogenated powder was then milled, sieved, aligned, pressed and sintered into recycled magnets. The resulting magnets were then tested on a permeameter (at room temperature, 75 °C and 150 °C) to measure the magnetic properties. Scanning electron microscopy was used to assess the microstructures of the final magnets. Mechanical properties such as Vickers hardness and fracture toughness were also studied.

When primary magnets made from cast alloys are hydrogen decrepitated, they are milled to decrease the particle size to single crystals. However, in a sintered magnet after hydrogen decrepitation it is unclear if the polycrystalline particles which are already aligned can rotate under an applied field, thus giving good magnetic performance. Therefore, different milling conditions and sieve sizes were tested to investigate this. The powder was then re-sintered as described above, resulting in magnets with an increase in density, remanence and maximum energy product at the expense of coercivity, with decreasing powder particle size. In all cases, the remanence and coercivity was substantially lower than for the starting magnet. The decrease in magnetic properties has previously been shown to be due to the fact that the grain boundary phase oxidises during primary production. Therefore it is necessary to blend some alloying elements into the hydrogenated powder to replace this oxidized phase.

In the second part of the study, neodymium hydride was blended systematically into the hydrogenated powder from 1-5 at%. This resulted in recovery of the coercivity of the recycled magnets with an associated decrease in remanence and maximum energy product. It was found that at 3 at% neodymium hydride, the coercivity of the recycled magnets was equal to that of the starting material; and that it was surpassed when larger quantities of neodymium hydride were added. The thermal stability of remanence and coercivity were also enhanced with such additions. The best magnetic properties were obtained at additions of 5 at% neodymium hydride, reaching a coercivity of 1400 kA m^{-1}, remanence of 975 mT, maximum energy product of 179 kJ m^{-3}; and thermal stability of coercivity and remanence better than in the starting material.

In the third part of the study, an investigation was carried out in order to remove the oxygen from the recycled magnets by separating the oxygen-rich grain boundary phase from the hydrogenated matrix phase. To do so, two different techniques were used, namely wet low-intensity magnetic separation and hydrocyclone separation. The separated powder was assessed by X-ray diffraction, X-ray fluorescence, inductively coupled plasma and scanning electron microscopy.

Hydrocyclone separation was shown to be a much more effective method than wet low-intensity magnetic separation in the separation of the oxygen-rich grain boundary phase particles. In addition, the hard magnetic phase particles were shown to be intact after exposure to water and air at 80 °C. This may open the door to a new family of water-based recycling processes for scrap NdFeB magnets, but further work is required.

The resultant powder was blended with neodymium tri-hydride (0, 5, 6 and 7 at%), aligned, pressed and sintered into recycled magnets. A high remanence of near 1 T was achieved, underlining that hard magnetic phase particles do not oxidise or corrode substantially during hydrocyclone separation and drying.

A Elena y a mi familia

Acknowledgements

I would like to thank Dr Allan Walton for his supervision, encouragement and advice along the project especially at the beginning, when I was lost and he came to point the direction to follow. Your help has been key to the development of this project and me as a researcher and as individual. Hope you finally learnt Herraiz is my first family name instead of a middle name. Thanks also to Professor Harris for sharing his knowledge and providing discussions of great interests, although you got wrong my name. No worries, Enriquo was only one letter away from my real name.

Special thanks to Dr Malik Degri for his advice and support when I started and I did not know much neither about magnets nor English. These months were of great help and I will always be grateful to you.

I also would like to thank Dr Richard Sheridan for his unconditional help and support at any time in every aspect of this project. I would not have been able to get to this of the project without your help. Once again, thank you very much.

Thanks also go to all members of Magnetic Materials Group for embracing me since the very beginning and make me feel part of this family. Thanks Vicky Mann, Olli Brooks, Matthew Farr, Alex Campbell, Muhammad Awais, Jonathan Meakin and Lydia Pickering for your help, discussions and support along these three years. Thanks to Andy Bradshaw for his technical advice, assistance and help during this three years and especially when building and fixing the sintering furnace. I would also like to thanks Wei Zhou for his support and feeding the entire group with such strange Chinese delicatessen. Thanks to Christian Jonsson for your help, discussions and general friendship.

I would like to thank all EREAN members: ESRs, ERs and supervisors. Special thanks to Iuliana Poenaru for her help on XRD, Rita Schulze for master lessons on GaBi and everyone that has contributed to reach this point in my career.

Gracias a la mujer de mi vida, Elena, por su cariño, amor, comprensión y apoyo incondicional durante estos ocho años en los que tantas cosas hemos vivido juntos. Sabes que sin ti todo esto no habría sido posible. Me faltan las palabras para describir lo mucho que te agradezco ser mi infinito y mi todo.

También le quiero agradecer a mis padres (y sus parejas) el apoyo y cariño durante todo este tiempo. No solo durante el doctorado, si no desde que hace 8 años empecé la Universidad. Todo vuestro esfuerzo y dedicación durante estos años han sido y serán impagables.

Gracias a mis 'parents in law' (suegros suena demasiado mal), por estar siempre ahí y, por supuesto, por haber traído al mundo a la persona más maravillosa del mundo, Elena. También quiero dar las gracias a mi abuela, mi cuñada, mis tíos y mis primos, tanto de sangre como políticos; aunque en realidad os siento a todos como sangre propia. No podía olvidarme de mi sobrino y mi hija, Friss y Terra, cuyos lametazos y anécdotas han sido un apoyo importante estos años.

En un momento así quiero recordar a aquellos que no están pero sin duda se alegrarían de este momento. Luis, Satur y Charly; siempre estáis presentes y nunca os olvidaremos.

Tampoco me quiero olvidar de mi alma mater, la Universidad Carlos III de Madrid, y en especial de Elena Gordo, por introducirme en el maravilloso universo de la investigación.

Enrique Herraiz Lalana

University of Birmingham

November 2016

Table of Contents

List of Abbreviations

$(BH)_{max}$ – Maximum Energy Product

μ – Permeability

μ_0 – Permeability of Free Space

Al-Ni-Fe – Aluminium Nickel Iron

B – Magnetic Induction

BH – Energy Product

$_bH_c$ – Inductive Coercivity

B_r – Remanence

BSE – Back-Scattered Electron

C – Curie Constant

c.g.s. – Centimetre-Gram-Second System of Units

CSV – Comma Separated Values

DEP – Diethylphthalate

dhcp – Double Hexagonal Close Packed

EC – European Commission

E_{ex} – Exchange Energy

EOL – End-of-Life

fcc – Face Centred Cubic

GBP – Grain Boundary Phase

GBDP – Grain Boundary Diffusion Process

H – Magnetic Field Applied

H_a – Anisotropy Field

HD – Hydrogen Decrepitation

HDDR – Hydrogenation Disproportionation Desorption and Recombination

HDDs – Hard Disk Drives

HPMS – Hydrogen Processing of Magnetic Scrap

HREEs – Heavy Rare Earth Elements

HV – Vickers Hardness

ICP – Inductively Coupled Plasma

ICP-OES – Inductively Coupled Plasma - Optical Emission Spectroscopy

$_iH_c$ – Intrinsic Coercivity

IL – Ionic Liquids

j – Magnetic Dipole Moment

J – Polarisation

J_{ex} – Exchange Integral

J_r – Remanence

K_1 – Anisotropy Constant

K_{IC} – Fracture Toughness

LPS – Liquid Phase Sintering

LREEs – Light Rare Earth Elements

m – Magnetic Moment

M – Magnetisation

MREE – Medium Rare Earth Elements

MF – Magnetic Fraction

M_s – Saturation Magnetisation

NdFeB – Neodymium Iron Boron

NMF – Non-Magnetic Fraction

OF – Overflow Suspension

R/P – Reserves over Production

REEs – Rare Earth Elements

REO – Rare Earth Oxide

RIP – Rubber Isostatic Pressing

S.I. – International System of Units

SiC – Silicon Carbide

Sm – Samarium

SmCo – Samarium Cobalt

Sr – Strontium

SX – Solvent Extraction

T – Temperature

Tb – Terbium

T_c – Curie Temperature

TiN – Titanium Nitride

UF – Underflow Suspension

US – United States

VCM – Voice Coil Motor

WEEE – Waste Electronics and Electrical Equipment

WLIMS – Wet Low Intensity Magnetic Separation

XRF – X-Ray Fluorescence

XRFS – X-Ray Fluorescence Spectroscopy

φ – Magnetic Flux

χ_m – Magnetic Susceptibility

Units

° – Degree

°C – Degrees Celsius

A – Ampere

A m^{-1} – Amperes per Metre

at% – Atomic Percentage

bar – Bar

erg – Erg

G – Gauss

G Oe –Gauss Oersted

J m^{-3} – Jules per Cubic Metre

K – Kelvin

kg – Kilogram

kgf – Kilogram Force

L – Litre

m – Metre

min – Minute

Mx – Maxwell

N – Newton

Oe – Oersted

ppm – Parts per Million

rpm – Revolutions per Minute

T – Tesla

t – Tonne

V – Volt

Wb – Webber

wt% – Weight Percentage

Prefix Multipliers

G – Giga: 10^{9}

M – Mega: 10^{6}

k – Kilo: 10^{3}

d – Deci: 10^{-1}

c – Centi: 10^{-2}

m – Milli: 10^{-3}

μ – Micro: 10^{-6}

n – Nano: 10^{-9}

Chapter 1. Introduction

1.1 Introduction to the Project

The rare earth elements (REEs) are made up of the 15 lanthanides plus scandium and yttrium. They are becoming progressively more important in the transition to a green, low-carbon economy due to their fundamental role in applications such as permanent magnets and catalysts [ERECON, 2015].

The most common rare-earth magnets, by both mass and value, are based upon neodymium, iron and boron (NdFeB) alloys with small amounts of alloying elements, which have the highest energy product of all permanent sintered magnets, ranging from 140 to 400 kJ m^{-3} [Gutfleisch et al, 2011]. NdFeB alloys can be manufactured either into resin bonded, hot-deformed or fully dense sintered magnets.

The European Commission (EC) has highlighted that the REEs are at greatest supply risk of all metals for clean technologies and, as a result, these materials are now at the top of the European Union critical materials list [European Commission, 2010]. In 2014, the EC split the REEs into three smaller groups, namely, light rare earth elements, heavy rare earth elements and scandium [European Commission, 2014]. This criticality is in part due to supply restrictions which have taken place, by the main supplier (China), over the last few years. It is expected that the demand for REEs will grow at between 6 and 9 % per year, reaching 20 and 50 % growth by 2017 and 2020 respectively [European Commission, 2014; Kingsnorth, 2014]. To alleviate the supply risk for REEs then multiple solutions will be required, including (1) substitution of critical REEs by less critical metals; (2) investing in sustainable primary mining from old or new REEs deposits; (3) recycling of REEs containing end-of-life (EOL) products such as hard disk drives (HDDs) and (4) using alternative technologies which do not contain REEs. It should be noted that these solutions are not mutually exclusive.

In reality, commercial recycling of REEs is still in its infancy (less than 1 % EOL recycling in 2011) despite significant research efforts [Meyer and Bras, 2011; Tanaka et al., 2013; Anderson et al., 2012].

This is mainly due to inefficient collection, technological difficulties and a lack of incentives [Graedel et al, 2011; Reck et al, 2012; ERECON, 2015, Binnemans, 2013a]. An upgrade in EOL recycling rates is a requirement but can only be achieved by developing efficient fully integrated recycling routes.

An important use of REEs is in permanent magnets, accounting for 38 % of the REE market by value and 21 % by volume [BGS, 2011]. As REE-based permanent magnets are the most powerful magnet, they yield better performance at smaller sizes, which has led to the miniaturisation of many applications such as speakers and HDDs amongst others.

HDDs have been identified as one of the most abundant and readily available forms of Waste Electronics and Electrical Equipment (WEEE) scrap containing NdFeB [Sprecher et al, 2014; Walton et al, 2015]. They are easy to identify in a mixed waste stream and have a rapid turnover at about 5 years. They contain between 2.5 and 20 g of NdFeB depending on the application [Walton et al, 2015; Sprecher et al, 2014]. In addition, around 550 million units are produced annually [Sprecher et al, 2014].

There are two NdFeB magnets in a HDD: a resin bonded magnet in the spindle motor which spins the disk and a sintered magnet in the voice coil motor (VCM) which controls the read head over the disk. The VCM magnets are nickel coated and glued into a soft magnetic assembly.

The main aim of this project is to maximise the magnetic properties of recycled sintered NdFeB magnets using EOL VCM magnets from HDDs as the starting material.

1.2 History of Magnetism

Magnetism and magnetic materials have been the focus of scientific investigation for over a millennium. The term magnet is derived from the town Magnesia ad Sypilum, modern Manisa, in the west of Turkey. Magnesia ad Sypilum was an ancient Greek city in Ionia, which was named after the Magnetes, an ancient Greek tribe of that region who discovered mysterious stones that could attract or repel each other; and named them lodestones. Those lodestones were essentially magnetite, Fe_3O_4,

and, although history indicates that ancient Egyptian, Greek, Asian and Central American civilisations were familiar with it, the first statement is by Thales of Miletus around 585 B.C. who said iron is attracted by lodestone because it has a soul. At the time, any kind of movement was considered as an indicator of life, or a soul, or a god. Thales attributed such movement to the materials itself, rather than to the intervention of some god. Apart from the evidences by the Greeks, it is believed that the Chinese used lodestone as a compass as early as 2500 B.C.

The first dissertation on the magnetic behaviour using a quasi-scientific style was written by Lucretius, around 50 B.C., entitled *On the Nature of Things*, *De Rerum Natura* in Latin, in which the principles of atomism were presented. Greek atomists believed everything was made up of atoms. Lucretius states that atoms emanating from the lodestone cleared the air and the consequent suction moved the iron piece closer. From then until approximately 1200 A.D. very little progress was made apart from the firm establishment of technology to manufacture compass needles, magnetised with lodestone, and its use in navigation and transport in China and Europe.

In the thirteenth century Petri Pergrinus, also known as Pierre de Maricourt, outlined the direction to which a needle would point at various positions around a lodestone. This fact helped him to conclude that magnets had two regions: north and south poles.

In 1600 the first printed scientific book based on experimental work and observation of magnetism was written by William Gilbert. In this treatise, entitled *On the Magnet and Magnetic Bodies, and on That Great Magnet the Earth*, *De Magnete, Magneticisque Corporibus, et de Magno Magnete Tellure* in Latin, Gilbert demonstrated that the Earth was a giant magnet, as shown in figure 1, and provided the north-south polar analogy between magnets and the Earth's poles. In addition, this work dispelled most of the magnetism effects attributed to magic and deities. Gilbert established magnetism as a scientific field and can be considered as the father of magnetism.

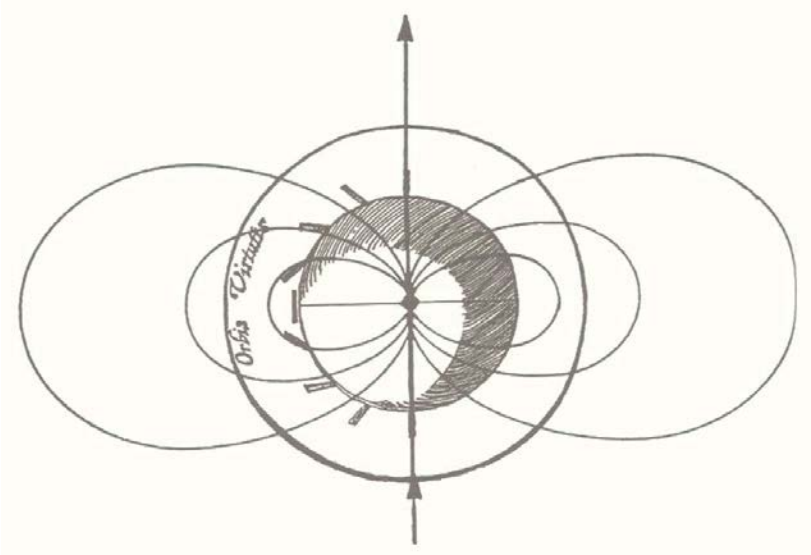

Figure 1. A dipole field pattern is superposed on Gilbert's picture of the Great Earth Magnet in which how magnets would naturally arrange about the surface is shown. Image from https://geologelizabeth.wordpress.com/2014/03/18/spotlight-on-science-magnetostratigraphy/, reproduced from Gilbert [1600]. Accessed 27/10/2016

At around 1750 John Michell proposed that the attractive, or repulsive, force between two magnets decreases when the square of the distance between the poles increases. This is known as the inverse square law. Charles-Augustin de Coulomb verified that experimentally and indicated that if a magnet were split in two, then two new poles would be created in each one.

In 1820 Hans Christian Oersted found accidentally the connection between magnetism and electricity. During a lecture Oersted noticed the deflection of the needle of a compass from the magnetic north when an electric current passed a wire near it. Later that year, Oersted announced the discovery of the magnetic effect of electric current. André Ampère confirmed this and, before 1820 finished, he developed and published an equation to explain experimentally the magnetic force between electric parallel currents.

Michael Faraday believed that since electricity could generate magnetism, the reverse could be true too. In 1831 Faraday announced the discovery of electromagnetic induction. In addition, he showed that the magnetic field lines converge to the point where the magnetic field is strong and spread out where the magnetic field is weak. It means that for a magnetic dipole the magnetic field lines

emanating from the south magnetic pole arch around its middle and converge again near the north magnetic pole.

During the 1850s and 1860s James Clerk Maxwell developed mathematical equations derived from mechanical models which described electricity and magnetism, the relationship between them and Faraday's lines of force. These equations were published in 1873 in a two-volume treatise entitled *A Treatise on Electricity and Magnetism* and defined classical electromagnetism.

In 1895, Pierre Curie was the first scientist who measured the magnetic susceptibility, which is the ratio of magnetisation to applied field, of different substances. He discovered that the magnetic susceptibility of paramagnetic materials is inversely proportional to temperature. Moreover, he found that there exists a critical temperature above which the magnetic properties disappear, which is nowadays known as Curie temperature.

In 1907 another French physicist, Pierre Weiss, developed his theory of magnetism which described magnetic interactions at microscopic and atomic scale. However, the current understanding of magnetism, which is based on the theory of motion and interactions of electrons in atoms, is due to the theoretical models developed by Ernest Ising and Werner Heisenberg.

1.3 History of Permanent Magnets

Magnetic materials are essential in the modern world as they played a vital role in the development of modern technology. Therefore, it is interesting to study the past and observe the development of such an important group of materials from an historical perspective.

1.3.1 Lodestone

The first known permanent magnet in history is lodestone, a variety of magnetite, Fe_3O_4, shown in figure 2, known to the Greeks. The intrinsic coercivity (described in section 2.5.2.2) of lodestones, typically 16 kA m^{-1}, is due to a fine intergrowth of γ-Fe_2O_3 (maghemite) by oxidation in the Fe_3O_4 material which impedes magnetic reversal [Geng, 2014; Livingston, 1996]. This fine microstructure

restricts the motion of the magnetic domain walls, hence impeding magnetic reversal, thereby increasing the overall coercivity of the samples.

Figure 2. Loadstone is a variety of magnetite, Fe_3O_4. Image from http://artsignsymbols.blogspot.co.uk/2013_09_01_archive.html Accessed 27/10/2016

Unlike magnetic theory, whose knowledge advanced progressively with time, the materials used to produce permanent magnets did not change over several centuries. In the 18th century, as a consequence of the high prices for lodestones new materials were investigated [Overshott, 1991].

1.3.2 Magnetic Steels

Servington Savery described briefly in 1730 the process by which he manufactured strong permanent magnets. It consisted of steel wire which Savery "seasoned very hard" and was afterwards magnetised by touching a lodestone [Savery, 1730]. His magnets were made up of 37 magnetised steel wires enclosed in a hexagonal bundle which was able to lift 12 times its own weight.

Gowin Knight, an English entrepreneur, gained fame by the strength of the magnets he manufactured, able to lift 28 times its own weight [Overshott, 1991]. However, he did not publish his methods whilst alive. After his death in the 1770's the manufacturing process was published and consisted of stirring a

slurry of iron fillings and linseed oil to obtain a suspension of finely divided iron oxide, which was moulded into shape and baked. The resulting block was magnetized.

Tungsten steel was introduced in the 1850s whereas chromium steel became popular at the end of the nineteenth century but it was not widely utilised until the First World War started and tungsten steel became unavailable. In 1897 Marie Curie studied magnetic steels and found that steels containing tungsten, chromium or molybdenum all had coercivities near 6 kA m^{-1} [Livingston, 1996]. In 1920 Japanese scientists found that by adding cobalt to chromium steels, the intrinsic coercivity increased to 20 kA m^{-1} and a maximum energy product (described in section 2.5.2.4) of 8 kJ m^{-3} [Overshott, 1991]. The cost of the raw materials, particularly cobalt, and the complicated heat treatment required, made cobalt magnetic steels very expensive, although they were the best available magnets at the time.

1.3.3 Al-Ni-Fe and Al-Ni-Co

In 1930, a new alloy of nickel, aluminium and iron (Al-Ni-Fe) was developed by Mishima in Japan with an intrinsic coercivity of 32 kA m^{-1} and a maximum energy product of 10 kJ m^{-3} [Mishima, 1931; Moosa, 2014]. After this discovery, a new generation of permanent magnets was developed based on Al-Ni-Fe with additions of copper, cobalt, niobium and titanium. These materials were given the family name of the AlNiCo magnets. The coercivity of Alnico alloys arises from the shape anisotropy of small ferromagnetic particles of approximately 20 nm in diameter.

These new alloys were cheaper than cobalt steels, presented higher magnetic properties and required fewer production operations than steel. Therefore, Alnico rapidly displaced small electromagnets in motors, transformers, and loudspeakers, lowering the cost and simplifying the construction. Consequently, for the next twenty years Alnicos were extensively researched throughout the world and many companies competed to maximize their properties.

AlNiCo magnets initially exhibited magnetic properties of approximately 0.75 T, 40 kA m^{-1} and 12.6 kJ m^{-3} of remanence (described in section 2.5.2.3), intrinsic coercivity and maximum energy product respectively. In 1938 it was found that a specific heat treatment under an applied field could

enhance the properties reaching values of 1.25 T, 44 kA m^{-1} and 36 kJ m^{-3} of remanence, intrinsic coercivity and maximum energy product respectively [Smithells, 1976]. However, even higher properties were achieved by producing a columnar grain structure and modifying the heat treatment conditions. These properties were 1.05 T, 128 kA m^{-1} and 72 kJ m^{-3} of remanence, intrinsic coercivity and maximum energy product respectively [McCaig, 1977].

1.3.4 Ceramic Magnets: Ferrites

During the 1950's, as a result of their work with soft ferrites, the Philips organisation discovered that hard magnetic ferrites could be produced. In general, these ferrites are based on $MFe_{12}O_{19}$ where M is barium or strontium [McCaig, 1977]. Typical properties are approximately of 0.39 T, 275 kA m^{-1} and 28.2 kJ m^{-3} of remanence, intrinsic coercivity and maximum energy product respectively [Ormerod, 1988]. The coercivity of the ferrite alloys is produced by the high magnetocrystalline anisotropy (described in section 2.5.1.4) of the hexagonal crystal of $MFe_{12}O_{19}$, which resulted in higher coercivities than in AlNiCo magnets. However, as it is a ferrimagnet, the remanence exhibited is lower.

The great advantage of ferrite over the AlNiCo magnets is that they have the lowest price per unit of energy product. Additionally, it is possible to produce flexible rubber magnets and plastic magnets by mixing ferrite powder with the rubber or plastic prior to its manufacture. These flexible ferrites have many applications such as fridge magnets, loudspeakers or magnetic recording tapes.

1.3.5 Rare Earth Permanent Magnets

Nd-Fe based rare earth magnets were first reported in 1935, even before ceramic magnets, exhibiting a coercivity of 340 kA m^{-1} [Drozzina et al, 1935]. However, these magnets were not developed until the 1960s, when a concerted research effort to identify new permanent magnets based on alloys of REEs was carried out.

1.3.5.1 $SmCo_5$ Alloy

In 1967, Strnat et al investigated phases of the type RCo_5, where R was one of the following rare earths: yttrium, cerium, praseodymium or samarium [Strnat et al, 1967]. This first generation of rare earth permanent magnets were produced by liquid phase sintering of magnetically aligned powders, being $SmCo_5$ the reference amongst them with values of remanence, intrinsic coercivity and maximum energy products of 1.04 T, 493 kA m^{-1} and 209 kJ m^{-3} respectively [Strnat, 1978]. Immediately after their discovery, samarium-cobalt (SmCo) magnets found a place in the space and military industries due to their large energy product compared with previous permanent magnets.

1.3.5.2 Sm_2Co_{17} Alloy

After the development of $SmCo_5$, a second generation of REEs-based magnets emerged in the early 1970's containing copper, cobalt and REEs, which led to the development of the high energy product alloy Sm_2Co_{17}-type magnets [Tawara et al, 1972]. These magnets evolved by the addition of iron to become $Sm_2(Co,Fe)_{17}$, which opened a door to the addition of more alloying elements such as niobium, vanadium or zirconium. Those helped to increase the magnetic properties of the material, thus giving values of remanence, intrinsic coercivity and maximum energy products of 1.12 T, 533 kA m^{-1} and 240 kJ m^{-3} respectively [Ormerod, 1989; Strnat, 1978]. However, nowadays the magnetic properties have increased reaching values of 1.133 T, 2613 kA m^{-1} and 242 kJ m^{-3} respectively [Sun et al, 2015].

1.3.5.3 Nd-Fe-B Alloy

Uncertainties in world cobalt supply in the 1970s led to huge fluctuations in the price of the raw material, therefore increasing the need for a new permanent magnet material to replace SmCo.

In 1983, a new material was discovered based upon a neodymium-iron-boron ternary alloy. This ternary alloy system was discovered simultaneously by General Motors in the United States (US) and Sumitomo Special Metals in Japan [Croat et al, 1984; Sagawa et al, 1984] using two totally different

processing routes. Magnets produced by Sumitomo were made by sintering aligned and compacted powder whereas magnets manufactured by General Motors were produced by mechanical compaction of melt spun ribbons, leading to values of maximum energy product of 290 and 114 kJ m^{-3} respectively. The intrinsic coercivity obtained from the NdFeB system was inferior to that found in SmCo type magnets, although it possessed a higher remanence. The temperature stability and corrosion resistance of NdFeB is also inferior to that of SmCo magnets.

1.3.6 Other Permanent Magnets

Alnicos, ferrites and rare earth-based magnets satisfy almost 100% of the market needs, but there are still a number of other permanent magnet materials that have been, or are, commercially available.

1.3.6.1 Cu-Ni-Fe and Cu-Ni-Co Alloys

The Cu-Ni-Fe and Cu-Ni-Co alloys were developed in the 1930s and were used due to their high ductility, thus easing the manufacturing process. They offered a remanence, intrinsic coercivity and maximum energy product of 0.55 T, 42 kA m^{-1} and 11 kJ m^{-3} respectively [McCaig, 1977]. Although this magnetic performance was higher than that exhibited by Al-Ni-Fe permanent magnets, it was surpassed when the Alnico alloys were developed.

1.3.6.2 Fe-Co-Mo Alloy

The Fe-Co-Mo alloy, commercially named Remalloy, Comol or Comalloy, was the first carbon free permanent magnet alloy. It was developed in 1931 by Western Electric scientists [Seljasater et al, 1932]. It offered a remanence, intrinsic coercivity and maximum energy product of 1.00 T, 28 kA m^{-1} and 10 kJ m^{-3} respectively [McCaig, 1977]. It was widely used as a bias magnet in telephone receivers from 1937 to 1980, when it was replaced [Bell Laboratories, 1983].

1.3.6.3 Fe-Co-V Alloy

The Fe-Co-V alloy was developed in 1938 and is commercially known as Vicalloy [Nesbitt et al, 1939; Nesbitt et al, 1940a; Nesbitt et al, 1940b]. It is characterised by a high mechanical strength and ductility; and showed values of 1.27 T, 33 kA m^{-1} and 27 kJ m^{-3} of remanence, intrinsic coercivity and maximum energy product respectively [Nesbitt, 1946].

1.3.6.4 Pt-Co Alloy

The equiatomic Pt-Co alloy was developed in the 1950's and was the most expensive permanent magnet in commercial production. With a remanence of 0.64 T, an intrinsic coercivity of 400 kA m^{-1} and a maximum energy product of 76 kJ m^{-3}, they were better than Alnico alloys and due to their corrosion resistance they were used in biomedical applications [McCaig, 1977]. However, with the discovery of superior rare earth-based permanent magnets they were inevitably superseded.

1.3.6.5 Cr-Co-Fe Alloy

The Cr-Co-Fe magnets, commercially known as Chromindur, were developed in the 1970's. This alloy offers a maximum energy product of just 78 kJ m^{-3}, comparable with those of Alnico magnets [Jin, 1979; Jin et al, 1980]. They are desired due to their ductility and high working temperature and are used in tachometers, micro relays and telephone receivers.

1.3.6.6 Sm-Fe-N Alloy

In the 1990s a new magnetic compound was discovered by Coey and Sun consisting of $Sm_2Fe_{17}N$ with an intrinsic coercivity of 880 kA m^{-1} and a maximum energy product about 228 kJ m^{-3} [Coey et al, 1990; Saito et al, 2005]. The development of this alloy is still ongoing and it is a promising new candidate for permanent magnet applications in spite of being unstable above 450 °C and hence only suitable for bonded magnets [Shaw et al, 2012].

The 20th century has witnessed an exponential improvement in the properties of permanent magnets. Each development has seen an improvement in the maximum energy product and the overall magnetic performance. The maximum energy product has risen from 2 kJ m^{-3} in 1900 to values over 450 kJ m^{-3} for the neodymium-iron-boron magnets as shown in figure 3.

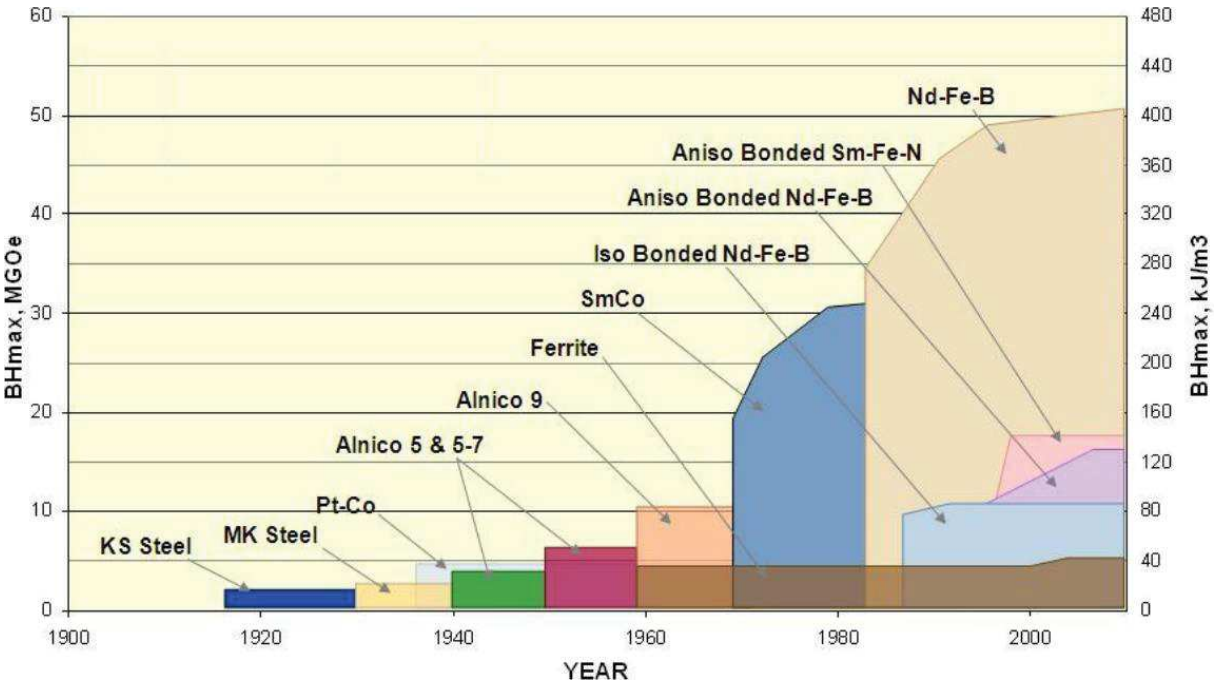

Figure 3. Graphic representation of the improvement of permanent magnet material in the 20th century in which red, green, blue, purple and grey correspond to Alnicos, ferrites, samarium-cobalt alloys, neodymium iron boron and Sm-Fe-N compound respectively [Shaw et al, 2012].

1.4 Rare Earths

1.4.1 Definition and classification

The REEs are a group of 17 metallic elements including the 15 lanthanides plus scandium and yttrium. The lanthanides include scandium (Sc, atomic number 21), yttrium (Y, 39), lanthanum (La, 57), cerium (Ce, 58), praseodymium (Pr, 59), neodymium (Nd, 60), promethium (Pm, 61), samarium (Sm, 62), europium (Eu, 63), gadolinium (Gd, 64), terbium (Tb, 65), dysprosium (Dy, 66), holmium (Ho, 67), erbium (Er, 68), thulium (Tm, 69), ytterbium (Yb, 70) and lutetium (Lu, 71). All lanthanides occur in nature except promethium, which is the only radioactive REE and, as it has no stable isotopes,

it only occurs in trace quantities [Castor et al, 2006]. Scandium and yttrium are also considered as REEs as they have very similar chemical and physical properties.

In general terms, with increasing atomic number, atoms attach one more electron which is added to the outer electron orbital and the atomic radius becomes larger. In the case of the lanthanides not only the outer shell is being filled with electrons but also the lower-lying 4f orbitals. This results in a similar outer electronic appearance for all lanthanides but also larger forces inside the atoms. As a consequence, the atomic radius decreases with increasing atomic number, a phenomenon known as the lanthanide contraction. Some REEs atoms have an atomic radius similar to rock-forming elements, which explains why REEs are often found in rocks that contain calcium, thorium, uranium, and strontium [Zepf, 2013].

The REEs are commonly divided into two groups. These are the group of elements with a low atomic weight referred to as the light rare earth elements (LREEs) and the group with a higher atomic weight referred to as the heavy rare earth elements (HREEs). Nonetheless, some authors such as Kingsnorth add a medium category of REEs, the medium rare earth elements (MREEs) [Kingsnorth, 2010]. The US Geological Survey (USGS) includes elements from lanthanum to gadolinium into the LREEs and from terbium to lutetium into the HREEs whereas under Kingsnorth nomenclature encompasses the elements from lanthanum to neodymium as LREEs, from promethium to gadolinium as MREEs and from terbium to lutetium plus scandium as HREEs [Kingsnorth, 2010; USGS, 2014].

1.4.2 Applications

The REEs are used in a wide variety of applications since they were first discovered, as can be observed in figure 4. They are used in the widest range of consumer products of any element group [Castor et al, 2006]. They are essential in electronic, optical, magnetic and catalytic applications.

Catalytic applications account for 19% share of the REE market by volume but just 5% of the market value [Kingsnorth, 2009]. REEs are essential in automotive catalytic converters, which transform primary pollutants in engine exhaust gases into non-toxic compounds.

An increasingly important use of REEs is in the permanent magnets sector, accounting for 38% of the REE market by value and 21% by volume [BGS, 2011]. As REE-based permanent magnets are more powerful than others types of magnets, they provide improved performance at smaller sizes. This has led to the miniaturisation of magnets in many applications such as in speakers and HDDs.

REEs are commonly used in phosphors with 32% of the REE market by volume but only 7% by value [Kingsnorth, 2009]. Phosphors are used in televisions as well as in screens and visual display devices. The red colour seen on the display comes from the use of europium and yttrium compounds, whereas green and blue colours come from terbium and cerium-based compounds respectively.

Glass and polishing industries also require REEs, accounting for 22% of REEs by volume and 6% by value [Kingsnorth, 2009]. Cerium is used as a decolourising agent in glass when added in tiny amounts, however, larger quantities turn it yellow and brown. Neodymium colours glass red, praseodymium green, erbium pink and holmium blue [Gupta et al, 2005].

REEs have major applications in metallurgical alloys such as mischmetal, which is widely use in the flint ignition device of many lighters and torches. However, REEs are also used as hydrogen storage materials and as alloying elements in steels and superalloys. The applications of REEs are summarised in figure 4.

La	• Nickel metal hydride batteries (Prius, forklifts) • Hydrogen storage alloys $LaNi_3$ • Alloying agent • Sputtering targets • Optical lenses • Host for phosphors • Petroleum fluid catalytic cracking (FCC) • Cathode material in solid oxide fuel cell	Dy	• Additive to $Nd_2Fe_{14}B$ permanent magnets to improve high-temperature performance, increase coercivity • Phosphors • Nuclear industry—radiation shielding
Ce	• Catalyst for automotive three-way-emission catalysts • Petroleum fluid catalytic cracking (FCC) • Glass additives • Decolorizer, opacifier • Ultraviolet light absorption • Polishing media for glass, lenses, semiconductors • Phosphors	Ho	• Research • Metal halide lamps • YIG (yttrium-iron-garnet) lasers • YAG and YLF solid-state lasers
Pr	• Additive to $Nd_2Fe_{14}B$ • Pr-stabilized ZrO_2 • Coloring agents • Glass blower's and welder's goggles (with Nd) • Telecommunication systems as dopant in fluoride fibers	Er	• Fiber optics—signal amplifiers • Lasers (mainly medical/surgical and dental use) • Coloring agent
Nd	• $Nd_2Fe_{14}B$ permanent magnets • Alloying agent for Mg alloys • Lasers • Metal halide lamps • Nd-stabilized ZrO_2 synthetic gems	Tm	• X-ray intensifying screens • Metal halide lamps • Research
Sm	• SmCo permanent magnets • Coloring agent • Phosphors • Nuclear industry—radiation shielding	Yb	• Optical lenses • Pressure sensors (metal) • Research
Eu	• Phosphors (red colors) • Nuclear industry—radiation shielding	Lu	• Research • Host for scintillator detectors and X-ray phosphors
Gd	• Host for phosphors • Magnetic resonance imaging contrast agents • Nuclear fuel rod addition, safety • X-ray intensifying screen • Laser YGG (yttrium-gadolinium-garnet)	Sc	• High-performance alloys • Lasers • Phosphors • Ceramics
Tb	• Phosphors (green) • X-ray intensifying screens • Terfenol-D $(Tb_xDy_y)Fe_2$ • Magneto-restrictive alloy	Y	• Host for phosphors • YAG laser host material • Y-stabilized ZrO_2 • YIG (yttrium-iron-garnet)—communications, radars, phase shifters • YBa_2CuO_2 high-temperature superconductor • Alloying agent

Figure 4. List of selected applications for the different rare earth elements [Zepf, 2015].

1.4.3 Occurrences

The term "rare earth" refers to the time of the discovery of REEs at around 1800. The use of the adjective "rare" since the fifteenth century was utilised as a synonym of extraordinary and astonishing [Reiners, 2001]. In contrast to its name, REEs are relatively plentiful in the Earth's crust as can be observed in figure 5.

Elements	Crustal Abundance (parts per million)
Nickel ($_{28}$Ni)	90
Zinc ($_{30}$Zn)	79
Copper ($_{29}$Cu)	68
Cerium ($_{58}$Ce)[a]	**60.0**
Lanthanum ($_{57}$La)	**30.0**
Cobalt ($_{27}$Co)	30
Neodymium ($_{60}$Nd)	**27.0**
Yttrium ($_{39}$Y)	**24.0**
Scandium ($_{21}$Sc)	**16.0**
Lead ($_{82}$Pb)	10
Praseodymium ($_{59}$Pr)	**6.7**
Thorium ($_{90}$Th)	6
Samarium ($_{62}$Sm)	**5.3**
Gadolinium ($_{64}$Gd)	**4.0**
Dysprosium ($_{66}$Dy)	**3.8**
Tin ($_{50}$Tn)	2.2
Erbium ($_{68}$Er)	**2.1**
Ytterbium ($_{70}$Yb)	**2.0**
Europium ($_{63}$Eu)	**1.3**
Holmium ($_{67}$Ho)	**0.8**
Terbium ($_{65}$Tb)	**0.7**
Lutetium ($_{71}$Lu)	**0.4**
Thulium ($_{69}$Tm)	**0.3**
Silver ($_{47}$Ag)	0.08
Gold ($_{79}$Au)	0.0031
Promethium ($_{61}$Pm)	10^{-18}

Figure 5. Table with the abundance of elements in the Earth's crust. REEs are presented in boldface type [EPA, 2012].

The relative abundance of REEs varies considerably and is related with the Oddo-Harkins effect by which the REEs with even atomic numbers have greater abundance than their odd numbered counterparts, as can be observed in figure 6 [Harkins, 1917; Oddo, 1914]. The chemically similar nature of the REEs in terms of ionic radius and oxidation states means they can substitute each other in crystal structures. This results in the occurrence of several REEs within a single mineral and entails a

challenge for further separation and extraction of pure single elements. Although REEs are abundant, they rarely occur in economic concentrations.

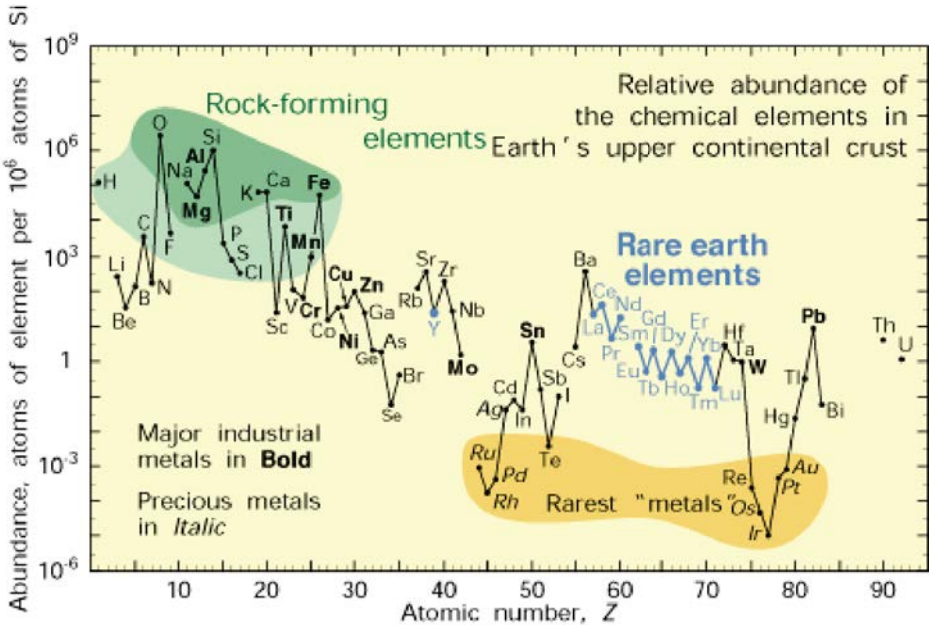

Figure 6. Abundance of the chemical elements in Earth's upper continental crust as a function of atomic number. REEs are presented in blue and the Oddo-Harkins effect can be observed [USGS, 2002].

1.4.4 Mining and Production

1.4.4.1 Rare earth element-bearing minerals

REEs do not occur in nature as metallic elements but within minerals in which they appear as either major or minor constituents. In order to form their own minerals, higher concentrations are required. Around 200 minerals are known to contain REEs being bastnaesite, monazite and xenotime the most common mineral from which REEs are extracted; and in which the total rare earth content is, respectively, 75%, 65% and 61% [BGS, 2011]. Although bearing minerals generally contain most of the REEs in varying concentrations, they tend to be biased to either LREEs or HREEs. Xenotime is richer in HREEs whereas bastnaesite and monazite are richer in LREEs.

1.4.4.2 Deposits

REEs mineral deposits occur in a range of sedimentary, metamorphic and igneous rocks. Sedimentary rocks are those formed from sediment which may in origin be organic or inorganic. Metamorphic rocks are those formed by temperature and pressure within the Earth's crust. Igneous rocks are those formed from molten rock and exhibit a crystalline texture. The four main type of REE deposits are carbonatites, alkaline igneous rocks, ion-adsorption clays and monazite-xenotime placers.

1.4.4.2.1 Carbonatite Associated Deposits

Carbonatites are igneous rocks with over 50% carbonate materials. They are also characterised by being enriched in LREEs and hosting the largest REEs deposits in the world such as Mountain Pass in the US and Bayan Obo in Inner Mongolia, China, where the latter is its highest exponent accounting 750 million tonnes (t) averaging 4.1% rare earth oxide (REO). These deposits have been the main source of LREE since they were first mined in the 1960s. There are more than 500 documented carbonatite occurrences across the world, with the main concentrations in eastern Canada, the East African Rift, northern Scandinavia, the Kola Peninsula and southern Brazil [Woolley et al, 2008].

1.4.4.2.2 Alkaline Igneous Rocks Associated Deposits

Alkaline igneous rocks comprise a group of uncommon igneous rock types deficient in silica. Several exploration projects are focused on large bodies of alkaline igneous rock with, some of them, finding REE concentrations between 0.3% and 2.6% REO [USGS, 2014]. The largest deposit of this kind is the Thor Lake in northwest Canada accounting 642 Mt of ore grading 1.96% REO. These deposits are highly desired as they are biased to larger concentrations of HREE. The main concentrations are in southern Greenland, the Kola Peninsula, eastern and northwest Canada and South Africa [BGS, 2011].

1.4.4.2.3 Ion-Adsorption Clay Deposits

Ion-adsorption clay deposits occur in southern China and are the primary source of HREEs in the world. These deposits usually have grades from 0.03% to 0.30% REO and account for between 3 and 12 kt [Grauch et al, 2008]. Despite their low concentration, they can be easily and economically mined as the ore is located between the surface and a depth of few meters.

1.4.4.2.4 Monazite-Xenotime Placer Deposits

Placer deposits are concentrations of heavy minerals transported and deposited with sand and gravel by rivers and coastal processes. Both monazite and xenotime can be recovered as a by-product during the extraction of titanium and zirconium from ilmenite and rutile. Monazite is recovered and processed as a source of both LREEs and thorium, which may be used as fuel material in thorium-based nuclear power plants. Xenotime is recovered as well but as a source of yttrium and HREEs. The most relevant concentrations are along the southern coast in India and in Australian coastline [BGS, 2011].

Monazite generally appears as a minor constituent of these placer deposits, usually less than 0.1 %. However, Australian deposits have demonstrated local concentrations of up to 1% and Indian ilmenite placer deposits can contain between 1 % and 2 % monazite [Möller, 1986].

1.4.4.3 Historical Development

REEs were initially produced in minor quantities from monazite-bearing placers, from pegmatites and carbonatites; the first geological source in which they were identified [Castor et al, 2006]. Brazil and India hosted the majority of such deposits until the 1940s, when Malaysia and Australia began mining production of REEs from placer deposits enriched in monazite. This first period of REE mining is known as the monazite-placer era [BGS, 2011; USGS, 2002].

Between 1960s and 1980s bastnaesite carbonatite deposits were exploited from the US mine in Mountain Pass, California, the main source of REEs [Naumov, 2008; USGS, 2002]. It was discovered

in 1949 and by 1965 it became the paramount source of REEs. Its development was accelerated by the use of europium in colour televisions. This second period is known as the Mountain Pass era.

During the 1980s China began to produce REEs mainly from the carbonatite-associated Bayan Obo deposit, in Inner Mongolia, but also from ion-adsorption clay deposits. Since 1984 production of REEs has increased dramatically overtaking the US and becoming the largest producer in the world in what is known as the Chinese era. These three eras are shown in figure 7.

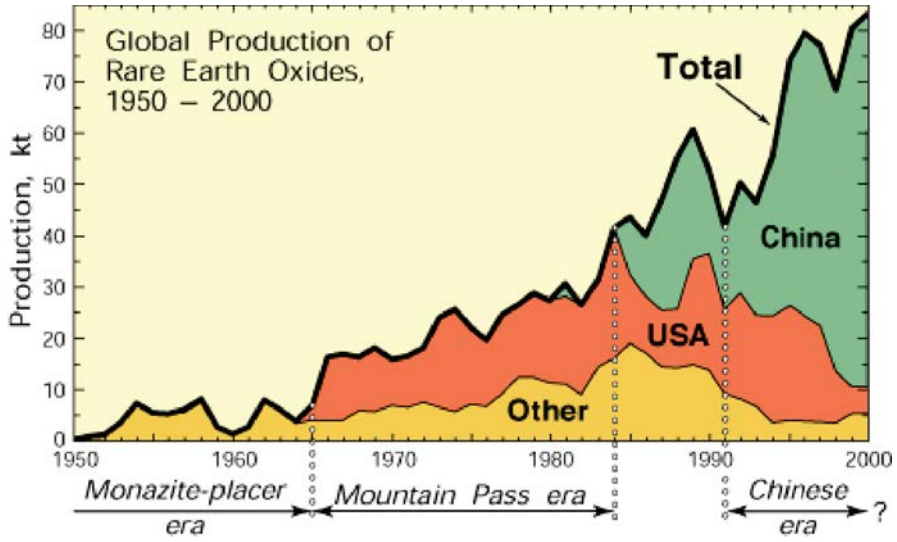

Figure 7. Global rare earth element production from 1950 through 2000 evidencing four different eras namely the monazite-placer era, starting in the late 1800s and ending abruptly in 1964; the Mountain Pass era, starting in 1965 and ending about 1984; a transitional period from about 1984 to 1991; and the Chinese era, beginning about 1991 [USGS, 2002].

1.4.4.4 Global Production

In the 1950s the worldwide production of REOs reached about 1 kt and this value doubled in 1960. In 1970 the production reached 16 kt, in 1980 this grew to 27 kt. In 1990 the production grew to 53 kt and to 90 kt in 2000. In 2006 the production peaked 137 kt and since 2009 it started to decline to 109 kt in 2013. However, it increased in 2014 reaching 123 kt [USGS, 2015a].

It must be mentioned that illegal mining is known to occur and will add to these numbers, reaching an estimated value of 40 kt [Xinhua, 2014]. At the final conference of the European Rare Earths

Competency Network, Kingsnorth revealed that 40 % of Chinese mining was likely to be due to illegal supplies of magnetic-related REEs [Moores, 2014].

Although annual global production is known, quantitative shares of the individual REEs are often hard to obtain. To obtain these figures it would be required to calculate it from known concentrations of single elements in the mined ores. If bastnaesite from Bayan Obo would be assumed as the global source of REEs, and taking into account its ore and mineral composition, it could be deduced that in 2014 when the global production was 110 kt, global production of neodymium would be of 18.7 kt.

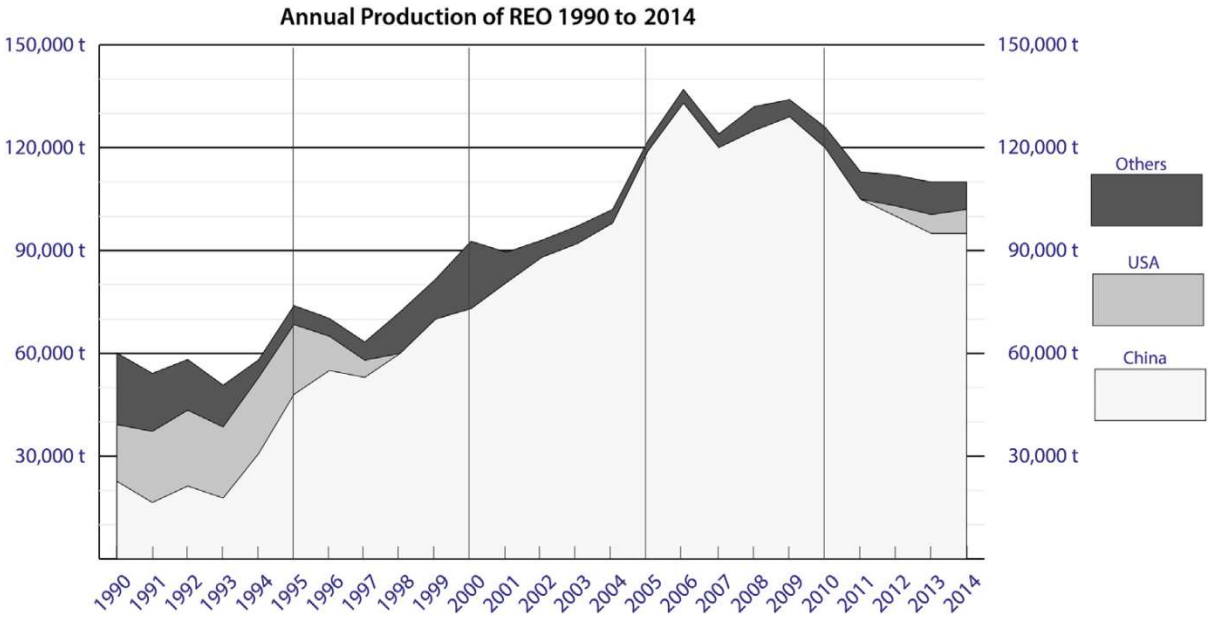

Figure 8. Rare earth element global production referring solely to the lanthanide elements, in the period between 1950 and 2014. [Zepf, 2015].

1.4.4.5 Reserves

Global reserves of REEs in 2014 are 130 Mt REO whereas in 2008 they were just 88 Mt [USGS, 2009; Zepf, 2015]. The gap between both figures is attributed both to the exploration work undertaken in the between 2009 and 2014; and to the influence the market price of the REEs has on the cut-off grade from which mining a deposit is economically feasible. Therefore, it is possible that these numbers could increase further as current exploration projects may find more deposits.

The ratio of global reserves over production (R/P) is an indicator of the adequacy of mineral supplies. It can range from over a millennium such as aluminium to a few centuries as in the case of lithium or platinum or even to several decades as for indium or cadmium [USGS, 2015b]. Based on the values of production and reserves in 2014, REEs show a R/P value of almost 1200 years, which is at the range of aluminium. However, this parameter is only of theoretical value.

1.4.4.6 Major Mines

Nowadays, the main REE mining activity is located in China and Australia although a number of projects have already been developed.

The largest Chinese rare earth mine, which is also the largest mine worldwide, is located in Bayan Obo, Inner Mongolia; 150 km north of Baotou, where the separation and refinement take place. HREEs are mainly mined in the southeast provinces and in Sichuan. In the US, the Mountain Pass mine was re-opened in 2012. However, in the 2014 annual report, Molycorp reported low production in addition to risks and problems [Molycorp, 2015a]. In 2015, because of the continuous descent of REEs prices since 2011, Molycorp filed voluntary petition for relief under Chapter 11 of the US Bankruptcy Code, ending production and entering into bankruptcy [Molycorp, 2015b]. In 2014, Lynas opened the Mount Weld mine in southwestern Australia, producing 4 kt REOs that year, far away from the 22 kt REOs predicted in 2010 [Lynas, 2010; Lynas, 2015].

In 2011, 381 known REE projects were ongoing worldwide at different stages and 53 of those are in advanced states of progress [Hatch, 2015]. Among them, those projects which have caught the largest interest of investors are located in Greenland, Canada, the US, and Australia.

1.4.4.7 Environmental Concerns

There are many environmental problems linked with REEs production. These usually result from insufficient environmental regulations and controls in the areas where REEs are mined and processed.

One of the main concerns is related to the radioactivity of some ores. For example, xenotime in Malaysian placer deposits contains up to 1.24% uranium and 0.75% thorium [Meor Yusoff, 1994].

Regarding radioactive elements, a major advantage of the ion adsorption clay deposits in southern China is their low content in elements such as uranium and thorium [Kanazawa et al, 2006]. However, the environmental issues associated with these deposits are related to the miners' lack of adherence to the environmental regulation. The concerns regarding the long-term effects of injecting strong reagents into the ground to dissolve REEs led to the closure or suspension of some mines in the past as the acids were then washed into rivers and poison soils; although improved environmental practices enabled many mines to resume production [Roskill, 2007].

Both REEs mining and separation pose significant hazards because of the intensive use of chemicals. In 2009, a report indicated that the chemicals used in Baotou for the refining process were responsible of water pollution, occupational poisoning of local residents and destruction of farmland [Hilsum, 2009]. The US Environmental Protection Agency confirmed in 2012 the negative environmental impact in China and the US of all REE mining activities [EPA, 2012].

1.4.5 Criticality

The criticality of the REEs was firstly addressed by the USGS in a Fact Sheet published in 2002 referring to REEs as "critical resources for high technology" [USGS, 2002]. The National Research Council published in 2008 a study in which the criticality matrix was introducing showing the supply risk and the economic importance as main indicators [NRC, 2008]. In 2009, a detailed study on raw materials for emerging technologies was conducted ranking neodymium as the second most critical element [Angerer et al, 2009]. The EC in 2010 published a report highlighting REEs as critical with the highest supply risk and medium economic importance [European Commission, 2010]. In 2011, a report attributed dysprosium and neodymium an overall high risk rating based on the market and political factors [JRC, 2011]. In 2014, the EC split REEs into HREEs and LREEs, where the HREEs had a high supply risk, LREEs had a medium supply risk and both were highlighted with medium

economic importance [European Commission, 2014]. In 2014, the United Nations Conference on Trade and Development produced a report on REEs discussing global high dependence on China and their importance for defence applications [UNCTAD, 2014]. Since 2010, many more studies were published with a similar assessment underlining the criticality of REEs.

1.4.6 Politics, Policies and Price

After the closure in 2000 of the US mine in Mountain Pass, Chinese monopoly in REEs production was reaffirmed. At the same time, the first export quotas were introduced by China, although they were never fully applied. In 2006 and 2008, production and processing quotas were respectively imposed. In 2010, export taxes were introduced and the export quota for 2010 was reduced by 37% compared to 2009 values, which led to a global critical perspective of REEs supply.

Halfway through 2011, REEs soared to unprecedented prices, as can be observed in Figure 9, mainly due to export restrictions and the crackdown of some Chinese mines by Beijing [Hook, 2011]. China argued that they had to solve severe environmental problems that occurred during REE mining and processing. In 2012, the US, Japan and Europe brought a case to the World Trade Organisation against that argument and against the Chinese export restrictions [WTO, 2015]. As a consequence of this dispute settlement China withdrew the export quota in the beginning of 2015 and abolished the export taxes on May 2015. Instead, a new resource tax system was implemented. Prices have come back down, which resulted with Molycorp entering into bankruptcy and Great Western selling Less Common Metals to Indian Ocean Rare Metals.

To break Chinese dominance over production, a large number of exploration projects started worldwide; 381 by 2011; as well as research projects focused on substitution and recycling of the REEs [Hatch, 2015].

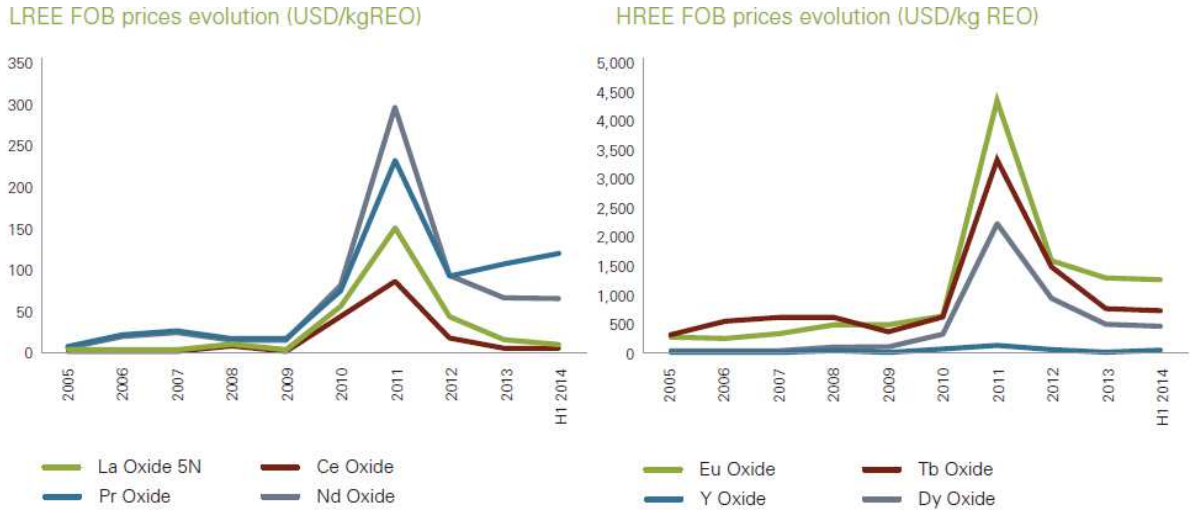

Figure 9. Historical development of REO prices of LREEs (left) and HREEs (right) between 2005 and 2014 [ERECON, 2015]

1.5 General Aim

It is clear from this chapter that it is necessary to find solutions to alleviate the supply risk for REEs. In this project, recycling of EOL VCM magnets is investigated by hydrogen processing and re-sintering directly from the scrap alloy.

The main aim of this work is to produce recycled sintered NdFeB magnets with the highest possible magnetic properties compared with the starting material.

Chapter 2. Principles of magnetism

2.1 The Origin of Magnetism

A magnetic field is created whenever there is an electrical charge in motion. For example, a wire with a current passing through it generates a magnetic field of concentric circles where the field decreases as the distance from the wire increases. A charged particle moving through a magnetic field will experience a force which will affect its course. The magnitude and direction of the magnetic force depends on the velocity of the particle and on the magnitude and direction of the magnetic field.

At an atomic level, magnetism occurs from two types of motions of the electrons. These are the motion of the electrons around the nucleus, comparable to the movement of planets in the Solar System; and the spin of electrons around its axis, similar to the rotation of the Earth on its own axis. Both motions can be observed in figure 10. Each electron is subjected to the magnetic moments caused by the orbital and the spin motions independently, causing each electron to behave as a magnet.

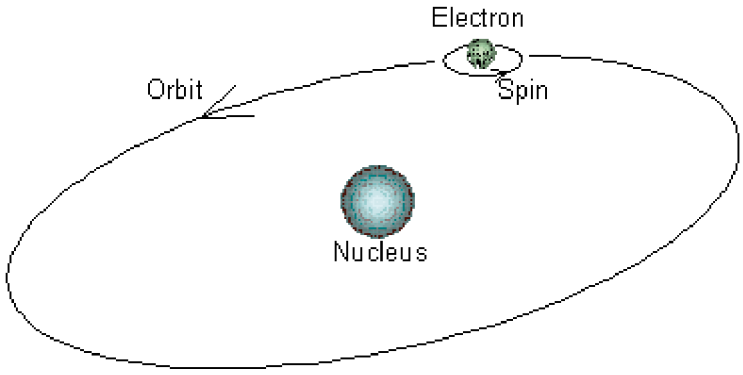

Figure 10. The orbit of a spinning electron about the nucleus of an atom. Image from http://www.gitam.edu/eresource/Engg_Phys/semester_2/magnetic/intro.htm Accessed 27/10/2015

In a wide range of elements, the magnetic moment of the electrons cancels out because they contain a paired number of electrons, with spins anti-parallel. These opposite spins effectively cancel each other out, resulting in zero spin momentum and hence no magnetic moment. Therefore, completely filled electron shells do not contribute to the magnetic moment as the total amount of electrons is even and

the net magnetic moment is zero. Despite this, a number of elements have incomplete electron shells with unpaired electrons. The atoms of such elements have magnetic moments that are not cancelled and therefore exhibit magnetisation.

If we consider a region where a magnetic induction, B_0, exists, where the region is filled with a magnetic substance, the total field in that region will be given by:

$$B = B_0 + B_m \qquad \text{Equation 1}$$

Where B_m is the induction produced by the magnetic substance, whose contribution is:

$$B_m = \mu_0 M \qquad \text{Equation 2}$$

Where the constant μ_0 is the permeability of free space, which is the value of magnetic permeability in vacuum. By substituting the relation of B_m in equation 2 into equation 1, it becomes:

$$B = B_0 + \mu_0 M \qquad \text{Equation 3}$$

The total magnetic induction, B, in a substance depends on two contributions. These are the external applied field, H, and the magnetisation, M, of the material. The magnetisation is the response of a material when a field is applied to it. The relation can be expressed by:

$$B = \mu_0 (H + M) \qquad \text{Equation 4}$$

The relationship between the magnetisation and the applied field is related to the magnetic susceptibility, χ_m, by the expression:

$$M = \chi_m H \qquad \text{Equation 5}$$

Magnetic susceptibility is a dimensionless intrinsic property that relates the magnetisation of a material in response to an applied magnetic field. Therefore, magnetic materials can be classified as diamagnetic, paramagnetic, ferromagnetic, antiferromagnetic and ferrimagnetic on the basis of their magnetic susceptibility value.

2.2 Magnetic Behaviour

The magnetic behaviour of materials when under the influence of a magnetic field may be different and can be categorised into five types: ferromagnetism, paramagnetism, diamagnetism, antiferromagnetism and ferrimagnetism. Figure 11 shows the periodic table of elements and the magnetic behaviour associated with each element at room temperature. It should be added that Gd and Dy exhibit a ferromagnetic behaviour below 290 K and 85 K respectively [Darnell et al, 1964; Vorobev et al, 1989]. It should be noted that ferrimagnetism is only exhibited in ferrites and in some garnets; and, as these are compounds, they do not appear in this table.

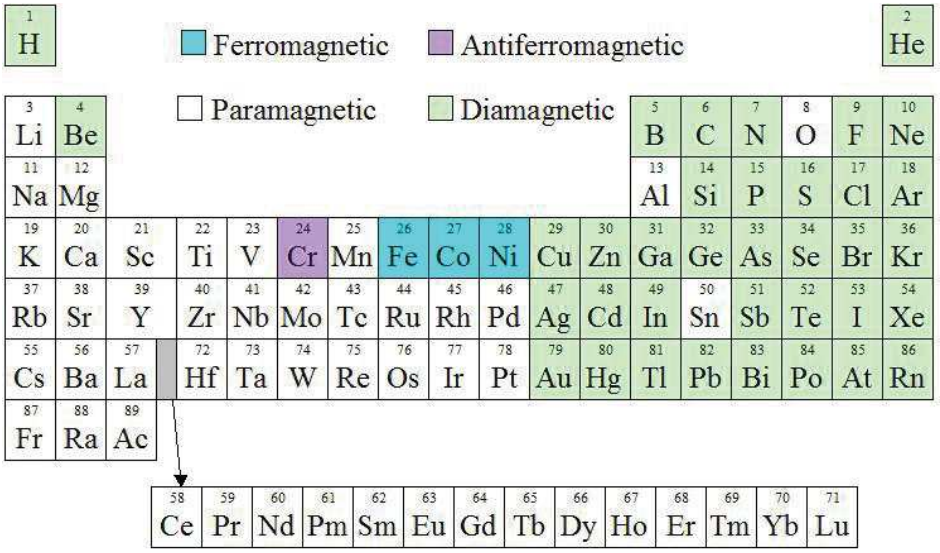

Figure 11. Periodic table of elements showing the magnetic behaviour of each element at room temperature. http://www.birmingham.ac.uk/Documents/college-eps/metallurgy/research/Magnetic-Materials-Background/Magnetic-Materials-Background-4-Classification-of-Magnetic-Materials.pdf Accessed 27/10/2016

2.2.1 Diamagnetism

Diamagnetism is the magnetic behaviour that opposes any applied magnetic field. This magnetic behaviour is present in all materials, although it is extremely weak and its effects can be masked by other behaviours. Diamagnetic elements have all the orbital shells filled and there are no unpaired electrons which results in zero net magnetic moment. Therefore, in the absence of an applied field this magnetic behaviour will not occur.

When an external applied field is applied to a diamagnetic material, the electrons experience an additional force which increases the orbital speed of the electrons whose magnetic moment is antiparallel to the applied field and decreases the speed of the electrons whose magnetic moment is parallel to the applied field. Consequently, the magnetic moments no longer cancel each other out and a net magnetic dipole moment is induced in the direction opposite to the applied field, which increases proportionally to the applied field. This effect is very small in nature when compared to ferromagnetic behaviour.

The magnetic susceptibility of diamagnetic materials is negative and temperature independent and of the order of 10^{-5}.

2.2.2 Paramagnetism

The distinguishing feature of paramagnetic materials is the presence of atoms or ions with permanent magnetic dipole moments. This occurs when there are electrons with unpaired spins. When no external field is applied the dipoles interact with each other weakly and are randomly oriented due to thermal agitation. Nonetheless, when a field is applied the magnetic dipole moments align in the same direction as the field and overcome the influence of temperature. This conduct is explained by the fact that the outermost electrons are less tightly bound to the atom than the inner ones causing diamagnetism and, as a consequence, able to change their direction freely. The magnetic susceptibility of paramagnetic materials is positive, of the order 10^{-3} – 10^{-5} and is inversely proportional to the temperature as shown by Curie's law [Curie, 1895]:

$$\chi_m = \frac{C}{T} \qquad \text{Equation 6}$$

Where C is the Curie constant of the material and T is the temperature expressed in Kelvin.

2.2.3. Ferromagnetism

As with paramagnetism, ferromagnetic materials have partially filled electronic shells containing unpaired electrons that form magnetic dipole moment. But as opposed to paramagnets, in ferromagnets the magnetic dipole moments align parallel to each other in the absence of an external applied field due to a strong coupling between neighbouring moments. This spontaneous alignment relies on the ability of the material to minimise the overall energy state of the atom.

At room temperature, thermal agitation is not sufficiently high to disrupt this orientation of magnetic moments but at some critical value of temperature specific to each material, it can lose its alignment. The temperature at which it occurs is known as the Curie temperature, T_c, and at this point the thermal energy is high enough to disrupt the alignment of magnetic moments in the material. Surpassing the Curie temperature leads to zero magnetisation and the material becomes paramagnetic. However, the recovery of the alignment of the magnetic moments is possible if the material is placed under the influence of an external field at a temperature below the Curie temperature.

At absolute zero the magnetic dipole moments align perfectly and the magnetic field reaches saturation magnetisation. The saturation magnetisation is the maximum induced magnetic moment that can be obtained in a magnetic field. Figure 12 shows the decrease in magnetisation with increasing temperature until reaching the Curie temperature.

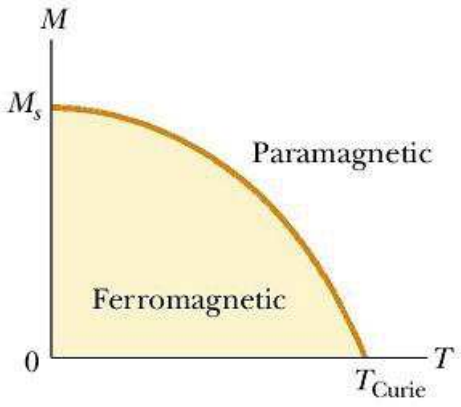

Figure 12. Variation of magnetisation versus absolute temperature for a ferromagnetic substance. http://www.kshitij-iitjee.com/Classification-of-magnetic-substances Accessed 27/10/2016

The modern theory of ferromagnetism, due to Heisenberg and Weiss, is an extension of that put forward by Ewing; which supposes ferromagnetic materials are made up of a large number of magnetic domains (see section 2.3), which can be smaller than the grains or crystals of the material itself [Ewing, 1900; Heisenberg, 1928, Weiss, 1906]. To explain the strong magnetic properties in ferromagnets, Weiss proposed a molecular field theory, Mean Field Theory. He assumed that there is a field proportional to the magnetisation, which tends to keep the magnetic moments of neighbouring atoms parallel. The theory of this field can be derived using quantum mechanics.

The interatomic spacings between atoms are such, that the orbits of the electrons responsible for the magnetic moments of the individual atoms can interpenetrate one another. This interaction, which gives rise to the molecular field, is described in terms of an exchange integral, denoted J_{ex}. From quantum mechanical considerations it can be shown that the interaction exchange energy E_{ex} between two atoms having spins S_i and S_j is given by:

$$E_{ex} = -2\,J_{ex}\,S_i\,S_j\,\cos\phi_{ij} \qquad \text{Equation 7}$$

Where S_i and S_j are vectors that represent the spin values and ϕ_{ij} is the angle between the magnetic moments of the two spins. It is possible to calculate the exchange integral J_{ex} as a function of the ratio of the interatomic spacing r_a to the unfilled shell radius r_{3d}. This is shown by the Bethe-Slater curve in figure 13.

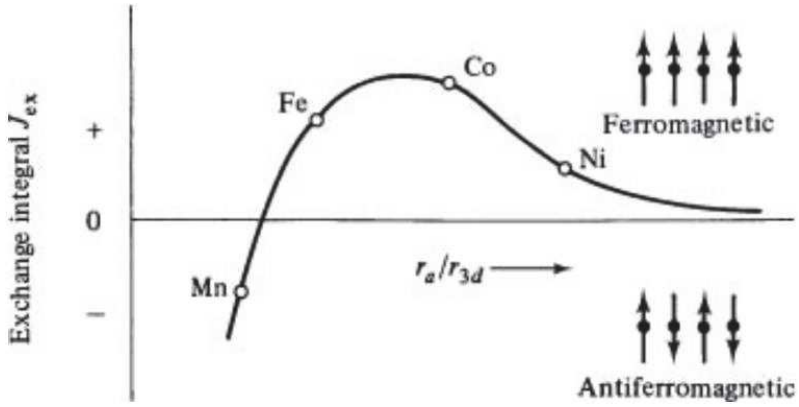

Figure 13. The Bethe-Slater curve shows the exchange integral as a function of the ratio of r_a to r_{3d}. [Cullity et al, 2009]

When the ratio of r_a to r_{3d} is large, the exchange integral is positive, the material is ferromagnetic as the interaction exchange energy is minimised and the spins of neighbours align parallel. The state of ferromagnetism corresponds to minimum energy. When J_{ex} is negative, the interaction energy is only minimum when the angles ϕ_{ij} is 180°, so the spins S_i and S_j are antiparallel, resulting in an antiferromagnetic behaviour.

The magnetic susceptibility of ferromagnetic materials is positive, of the order $10^1 - 10^4$ and is described by the Curie-Weiss law [Weiss, 1906]:

$$\chi_m = \frac{C}{T - T_c} \qquad \text{Equation 8}$$

2.2.4 Antiferromagnetism

Antiferromagnetism arises through a similar mechanism to ferromagnetism, in that there is a strong coupling between neighbouring magnetic dipole moments. In this case there is a negative interaction and the ordering is antiparallel, resulting in zero net magnetic moment. Like ferromagnetism, antiferromagnetic materials suffer an order-disorder transition above a critical temperature, called the Néel temperature. This temperature is analogous to Curie temperature.

The magnetic susceptibility of antiferromagnets is positive and of the order $10^{-5} - 10^{-3}$.

2.2.5 Ferrimagnetism

Ferrimagnetism is similar to antiferromagnetism in that the magnetic dipole moments are ordered in an antiparallel sense. However, the sum of the moments in one direction is larger than in the opposed direction leading to net magnetic moment. Like ferromagnets, ferrimagnets retain their magnetisation when the external applied field is removed and, in addition, they become paramagnetic above the Curie temperature.

The magnetic susceptibility of ferrimagnets is positive and of the order $10^1 - 10^4$.

2.2.6 Summary of Magnetic Behaviours

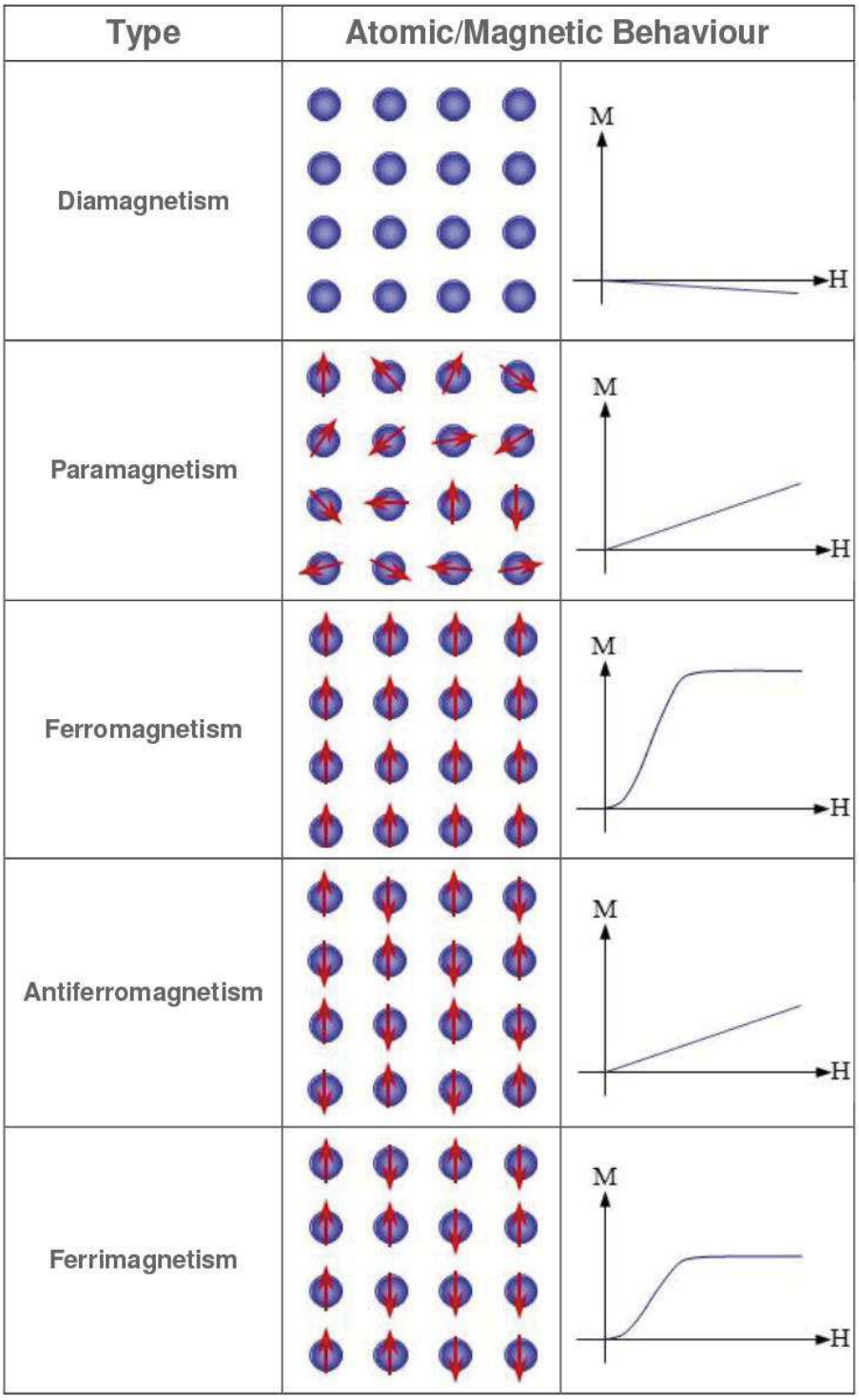

Figure 14. A summary of the magnetic behaviours of magnetic dipole moments and the relationship between magnetisation (M) and applied field (H). Adapted from http://www.birmingham.ac.uk/Documents/college-eps/metallurgy/research/Magnetic-Materials-Background/Magnetic-Materials-Background-4-Classification-of-Magnetic-Materials.pdf Accessed 29/01/2016

2.3 Magnetic Domains

A magnetic domain is a region in which the material has uniform magnetisation. Within a domain, the magnetic moments are aligned in the same direction so it behaves like a magnet. The concept of domains was originally proposed by Weiss in 1906 to explain how a material with spontaneous magnetisation can exist in a demagnetised state.

When a material is uniformly magnetised, then there are surface charges at the ends of the material due to magnetisation that cause self-demagnetising fields. The energy associated with these fields is called magnetostatic energy. The creation of domains reduces self-demagnetising fields by reducing the general energy state of the system as shown in figure 15. Therefore, the existence of domains is a consequence of energy minimisation.

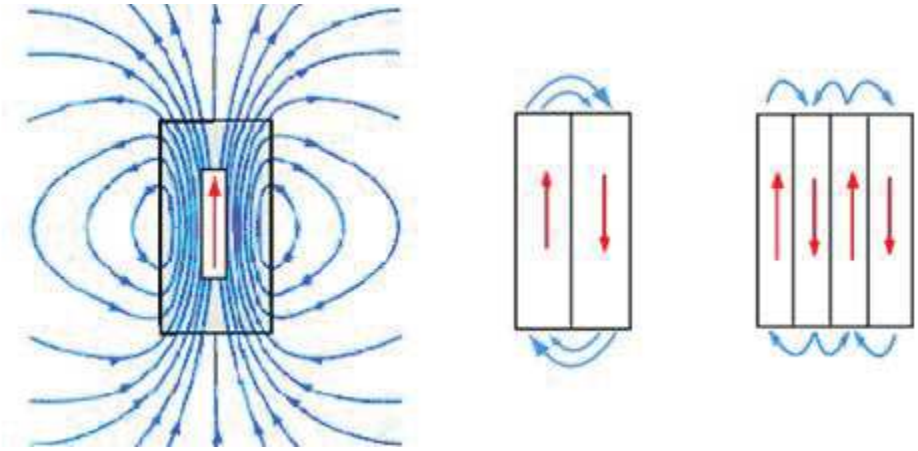

Figure 15. Reduction of the magnetostatic energy by the creation of addition domains. Image from https://earthref.org/MagIC/books/Tauxe/Essentials/WebBook3ch4.html Accessed 27/10/2016

A uniformly magnetised specimen with one single domain has a high magnetostatic energy associated with it. Breaking up the magnetisation into regions where spins are aligned in the same direction reduces the magnetostatic energy and, providing that the decrease in magnetostatic energy is larger than the energy needed to form domain walls, multi-domain particles arise. Although the magnetostatic energy decreases as the number of domains increases, the material will not continue to separate into more and more domains because the introduction of a domain wall has an energy

associated with it which is proportional to its area and raises the overall energy of the system. Consequently, there will be a point where the energy required to create another domain is equal to the energy required to create a domain wall.

A minimum energy of the system can be achieved with a specific number of domains. This number depends on the size and shape of the specimen, which affect the magnetostatic energy, and the intrinsic properties of the material, which affect the magnetostatic energy and the domain wall energy.

The boundaries between the domains are regions where the directions of the spins of the constituent electrons change. This transition layer is called Bloch wall, named after the physicist Felix Bloch and has energy associated with it. Figure 16 shows a Bloch wall between two neighbouring domains with opposite directions of magnetisation.

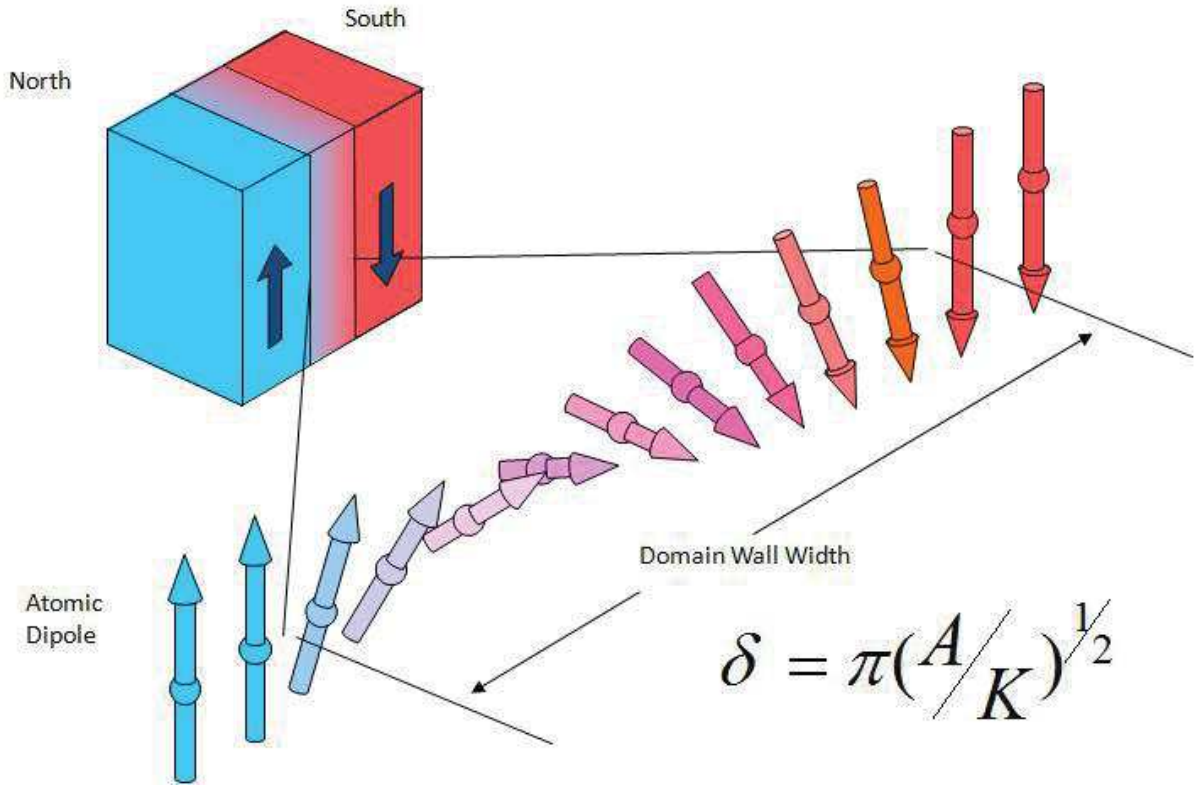

Figure 16. Schematic diagram to show the change of magnetisation direction through a domain wall. Where δ is the domain wall width, A is the exchange constant, K is the anisotropy constant. Image reproduced from http://www.gitam.edu/eresource/Engg_Phys/semester_2/magnetic/domain.htm Accessed 27/10/2016

The angular displacement of the magnetic dipole moments across the wall is usually 180° and, as it can be seen in figure 16, the orientation of the electron spins changes gradually through the wall rather than in one discontinuous jump. The width of the wall is the result of the exchange energy trying to minimise the angle between neighbouring spins by making the wall as wide as possible, and the magnetocrystalline anisotropy energy (see section 2.5.1.4) trying to minimise the number of non-easy axis spins by making the wall as thin as possible. The combination of these two competing energies provides a finite thickness to the wall.

Bloch walls are not rigid meaning that one domain can increase in volume in the expense of another under an applied field as shown in figure 17.

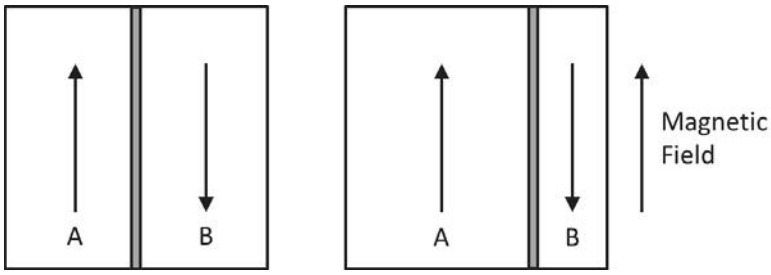

Figure 17. Motion of the Bloch wall when an external field is applied.

When plane polarised light illuminates the surface of a magnetic specimen the reflected light is elliptically polarised. With the assistance of polarising filters, the changes in polarisation due to the interaction with the magnetic material generate a magnetic domain contrast as observed in figure 18.

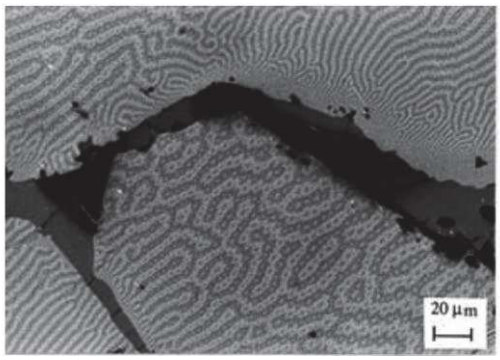

Figure 18. Kerr effect image of homogenised $Nd_{16}Fe_{76}B_8$ showing domain patterns. Reproduced from http://www.birmingham.ac.uk/Documents/college-eps/metallurgy/research/Magnetic-Materials-Background/Magnetic-Materials-Background-8-Domain-Observation.pdf Accessed 14/11/2016

2.4 Units of Magnetism

There are currently two systems of magnetic units widely used in magnetism. These are the Gaussian or c.g.s. unit system and the MKS unit system, adopted as the S.I. system. The S.I. system of units was adopted at the 11th General Congress on Weights and Measures in Paris in October 1960 and subsequently accepted for magnetic measurements by the International Union for Pure and Applied Physics.

In most areas of science and engineering, S.I. units have now been completely adopted. Nonetheless, the older c.g.s. system is still in widespread use. In this thesis S.I. units are used for presentation of results and its discussion. A table of units and conversion factor between the systems is given in table 1.

Table 1. Table of units and conversion between c.g.s. and S.I. unit systems.

Quantity	Symbol	S.I. Units	c.g.s. Units	Conversion c.g.s. to S.I.
Energy Product	BH	kJ m^{-3}	MG Oe	$10^2\ 4^{-1}\ \pi^{-1}$
Magnetic Dipole Moment	j	Wb m	emu, erg G^{-1}	$4\ \pi\ 10^{-10}$
Magnetic Field	H	A m^{-1}	Oe	$10^3\ 4^{-1}\ \pi^{-1}$
Magnetic Flux	ϕ	Wb	Mx, G cm^2	10^{-8}
Magnetic Induction	B	T, Wb m^{-2}	G	10^{-4}
Magnetic Moment	m	A m^2	emu, erg G^{-1}	10^{-3}
Magnetisation	M	A m^{-1}	emu cm^{-3}	10^3
Permeability	μ_0	Wb A^{-1} m^{-1}	Dimensionless	$4\ \pi\ 10^{-7}$
Polarisation	J	T, Wb m^{-2}	emu cm^{-3}	$4\ \pi\ 10^{-4}$

2.5 Magnetic Properties

In magnetism, there is a fundamental distinction between intrinsic and extrinsic properties. Intrinsic properties are realised on atomic and crystal levels and do not change regardless the amount of substance or its shape. By contrast, extrinsic properties are affected by the processing route used and the microstructure shown by the final product.

2.5.1 Intrinsic Properties

The intrinsic properties refer to the material itself and hence to the atomic origin of magnetism and involve quantum phenomena. The most relevant intrinsic properties in magnetism are introduced in this section.

2.5.1.1 Saturation Magnetisation

The saturation magnetisation, M_s, of a magnetic material is the maximum amount of field that it can apply on its environment. This property is largely dependent on the alignment of the magnetic moments, the crystal structure and the presence of elements with zero net magnetic moment within the system.

2.5.1.2 Curie Temperature

As explained in section 2.2.3, the Curie temperature is the point at which the thermal energy is high enough to disrupt the alignment of magnetic moments in the material. Exceeding the Curie temperature lead the material to become paramagnetic.

2.5.1.3 Anisotropy

Anisotropy is a property of matter which is directionally dependant and is opposed to isotropy, which implies identical properties in all directions.

2.5.1.4 Magnetocrystalline Anisotropy

Quantum-mechanical interactions between electrons tend to align the spontaneous magnetization along particular preferred directions in a crystal. This effect is known as magnetocrystalline anisotropy. Certain materials will be more easily magnetised in one direction than another because of the ordering along preferred axes and differing strengths of interactions along the axes. The magnetisation curves for single crystals of iron and cobalt along several crystallographic directions are

shown in in figure 19. For iron, which has a cubic lattice, and for cobalt, which has a hexagonal crystal lattice, the magnetic moments align preferentially along the <100> and <0001> axes respectively.

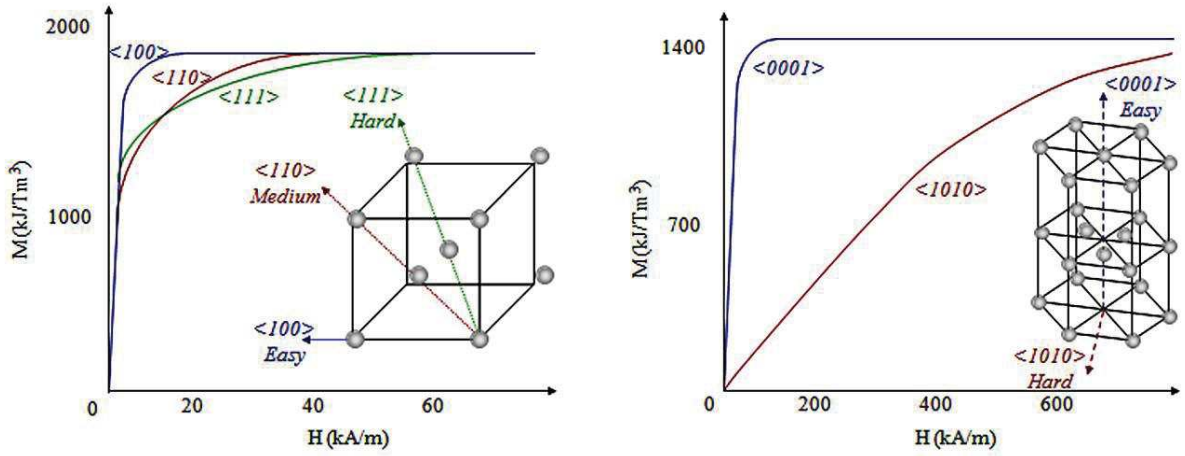

Figure 19. Magnetisation curves for single crystals of iron (left) [Adapted from Honda et al, 1926] and cobalt (right) [Adapted from Kaya, 1928].

In figure 19 it can be observed that a smaller applied field is required to magnetise along the easy directions and that a higher field must be applied to magnetise along the hard axes. The spontaneous magnetisation goes along one of the easy directions when no external field is applied.

The magnetic materials that show uniaxial anisotropy are very hard to demagnetise as they require large amounts of energy to rotate the direction of magnetisation. However, some magnets may have more than one easy direction and they are, therefore, easier to demagnetise.

A measure of the magnetocrystalline anisotropy in the easy direction of magnetisation is the anisotropy field, H_a, which is required to align the magnetic moments of a material perpendicular to its spontaneous axis or plane of magnetisation. The anisotropy is caused by a coupling of the electron orbitals to the lattice. In the easy axes this coupling is such that these orbitals are in the state of lowest energy. The field required to reverse all the spins in a single saturated crystal is the anisotropy field, and is given by:

$$H_a = \frac{2\,K_1}{M_s} \qquad \text{Equation 9}$$

Where K_1 is an anisotropy constant which represents the work done in rotating the direction of magnetisation from the easy direction to that perpendicular to this direction.

2.5.1.5 Shape Anisotropy

Shape anisotropy appears when a magnetic particle of a substance is not perfectly spherical. It causes a difference of magnetic properties in each direction depending on the morphology of the particle, hence creating one or more easy axes. It is easier to magnetise along the long axis than the short axis due to the influence of the internal demagnetising field.

2.5.2 Extrinsic Properties

Extrinsic properties arise from the shape, size and microstructure of the final product and these are influenced by the processing route to manufacture the final magnet. The most relevant extrinsic magnetic properties are derived from the hysteresis loop.

2.5.2.1 Hysteresis Loops

The magnetisation demonstrated by a hard ferromagnetic material or permanent magnet varies, when anisotropic, depending on the magnetic field applied to it and the direction in which the magnetic field is applied. The red line describes the relationship between the applied field, H, and the magnetisation in terms of polarisation, J, whereas the blue line shows the induction, B, in response to an applied field, H, as observed in figure 20.

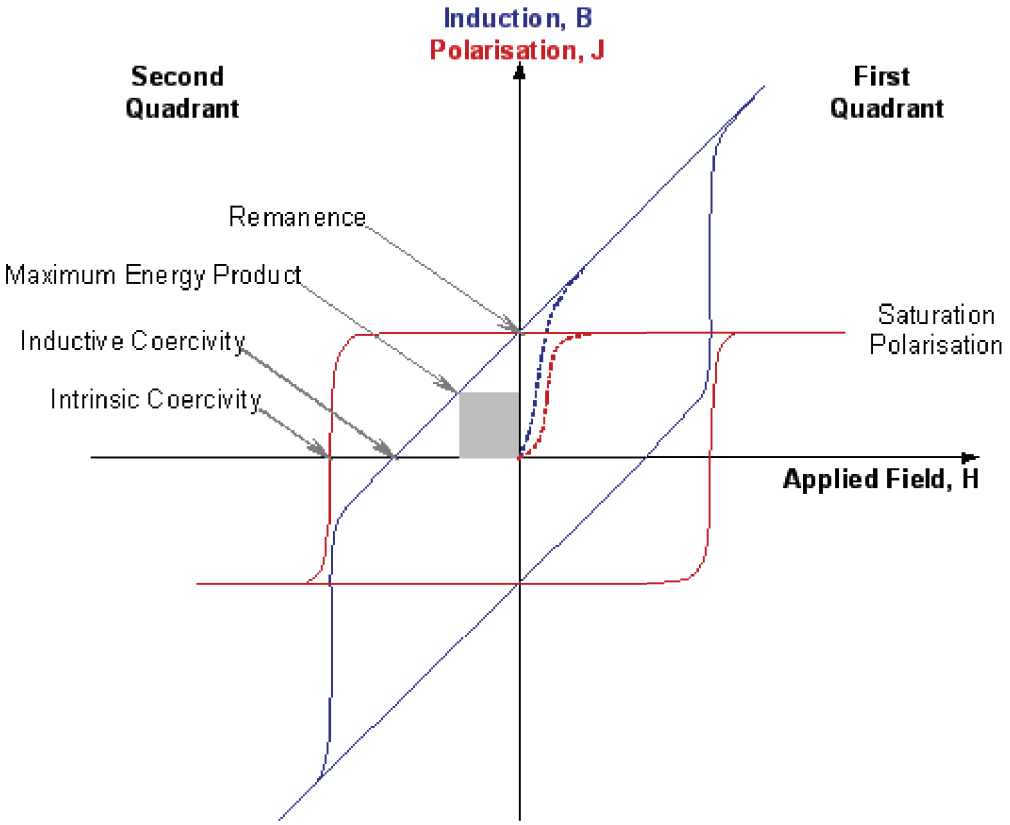

Figure 20. Typical hysteresis loop for a hard ferromagnetic material. Image from http://www.gitam.edu/eresource/Engg_Phys/semester_2/magnetic/hyst.htm Accessed 27/10/2016

The remanence and coercivity can be calculated from both hysteresis curves. Nonetheless, the most commonly used loop is the polarisation hysteresis loop.

In the hysteresis loop the origin is the point at which the material is in a demagnetised state with the magnetic domains are randomly oriented, hence exhibiting zero net magnetisation; and in absence of an external applied field. Then a magnetic field is applied to the magnet until saturation magnetisation, denoted by M_s, is complete in both induction and polarisation, aligning all the domains in the direction of the applied field. When the applied field is reduced to zero, the hysteresis loop crosses the y-axis. The point in which the hysteresis loop and the axis intercept is the remanence, denoted by B_r or J_r.

The direction of magnetisation is then reversed to the opposite direction. During this process the magnetic domains rotate because of the applied field. At a certain value of applied field, the domains orient randomly to the point to where zero magnetisation occurs and the hysteresis loop intercepts the

x-axis. The interception point between the x-axis and the polarisation hysteresis loop is known as intrinsic coercivity, denoted by $_iH_c$, while the point in which the x-axis and the induction hysteresis loop intercepts is known as inductive coercivity, referred to as $_bH_c$. This quadrant, the second quadrant, is acknowledged as the demagnetisation quadrant. It is the part of the loop where the coercivity, remanence and maximum energy product are derived from.

The applied magnetic field is continually augmented until the magnetisation is saturated in the reverse direction where all the domains will be aligned in the direction of the applied field. This process is then repeated to complete the hysteresis loop and the applied field is reduced to zero.

The magnetisation stage, shown in figure 20 as dashed lines, depends on the material and the direction of applied field, easy or hard. As previously shown in 2.5.1, applying a magnetic field in the easy direction aligns the moments at a low field to reach saturation magnetisation while applying it in the hard direction requires higher values of applied field to align the magnetic moments in the direction parallel to the applied field.

The motion of domain walls can explain qualitatively the shape of the magnetisation stage of the hysteresis loop, as shown in figure 21.

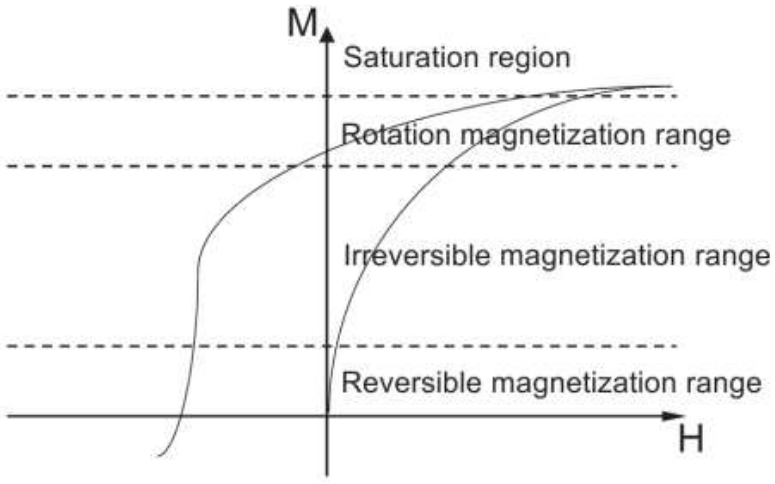

Figure 21. Magnetisation process of the hysteresis loop explained in terms of magnetic domain boundary changes [Yuan, 2005].

The magnetisation stage corresponds to the change in the domain structures when a magnetic field is applied. During this process both the reversible and the irreversible changes occur together. Four different ranges can be distinguished according to the change in the direction of the domain magnetisation and in the intensity of spontaneous magnetisation:

Reversible magnetisation range. Starting from the demagnetised state, this is the first range in which the motion of the domain walls is reversible. If the field is decreased the magnetisation follows the same curve.

Irreversible magnetisation range. In this region, the displacement of the walls is irreversible and is accompanied by the magnetothermal effect, resulting in the dissipation of some energy from the magnetic field as heat. If the field is decreased the magnetisation does not follow the same curve.

Rotation magnetisation region. A region in which the domain boundaries stop moving and the magnetic moments of the domain rotate to align with the applied field direction.

Saturation region. In this region the saturation magnetisation inside the domains is achieved.

The reason for the irreversible domain boundary displacement is that no material is free from lattice defects and in particular the strain fields cause by such defects. Dislocations, precipitates, inclusions and grain boundaries have an associated local stress field which creates microstrains within the material. These strain fields have the effect of impeding the domain walls to displace further.

Like the magnetisation stage, the shape of the hysteresis loop and specifically the shape of the demagnetisation quadrant depend also on the material the magnet is made of and the direction of the applied field. A square loop in the easy direction is the desired shape because of its predictability. A magnet with a square shape will produce the same magnetisation until a certain field is applied, whereas a rounded or curved loop will change in magnetisation at different fields. In the hard direction the demagnetisation loop exhibits a shallow sloped line as different domains and moments will require different applied field to rotate the moments. Therefore, there is no squareness to the loop.

2.5.2.2 Coercivity

The intrinsic coercivity, ${}_iH_c$, represents the ability of the magnet to resist demagnetisation, which means the amount of demagnetising field needed to reduce the polarisation to zero. It must not be confused with the inductive coercivity, ${}_bH_c$, and also referred as extrinsic coercivity, which is a measure of the demagnetising field needed to reduce the magnetic induction to zero.

The intrinsic coercivity can be measured by analysing the value of the hysteresis loop when crossing the x-axis from the second quadrant to the third quadrant.

2.5.2.3 Remanence

The remanence of a magnet is denoted by Br or Jr as noted before. The remanence is a measure of the maximum residual magnetisation obtained in a magnet in absence of any applied field after being magnetised. It can be calculated by reading the intercept from the hysteresis loop and the border between the first and the demagnetization quadrants.

2.5.2.4 Maximum Energy Product

The maximum energy product is denoted by $(BH)_{max}$. It is a measure of the maximum amount of energy that can be supplied by a magnet of a finite size to an external magnetic circuit. The maximum possible energy product a magnet can give is calculated by:

$$(BH)_{max} = \frac{J_r^2}{4\,\mu_0} \qquad \text{Equation 10}$$

It is a figure of merit used to compare magnets. The higher the maximum the energy product, the more usable work a magnet can offer and the better the magnet is. This can be measured by calculating the largest square possible in the demagnetisation quadrant of the induction hysteresis loop.

2.5.2.5 Squareness Factor

The squareness factor is a measure that indicates how square the hysteresis loop is. It is a dimensionless value between 0 and 1, which is defined by the ratio of the reverse field required to reduce the polarisation by 10% from the remanence to the intrinsic coercivity. Thence, a squareness factor of one matches a perfectly squared loop.

There are other methods which allow the quantification of the squareness of the hysteresis loop, such as the ratio between of the remanence to the saturation magnetisation.

2.6 Coercivity Mechanisms

A ferromagnet can reverse its direction of magnetisation either continuously or discontinuously. The former occurs through coherent or incoherent rotation processes; whereas the latter happens through domain processes. The coercivity will be determined by the easiest of these processes.

The coercivity mechanism of a magnet depends on its type and composition. The three main mechanisms are nucleation, pinning and single domain. Each of them has different effects on the maximum potential value of coercivity for the magnet. However, a magnet does not need to show one mechanism that controls the coercivity but a combination of them, as they are not mutually exclusive. Sometimes, it is possible to identify the principal coercivity mechanism from its initial magnetisation curve as the magnetic domains react differently in order to align in the direction of the applied field. The initial magnetisation curves for nucleation controlled and pinning controlled coercivity mechanisms are shown in figure 22.

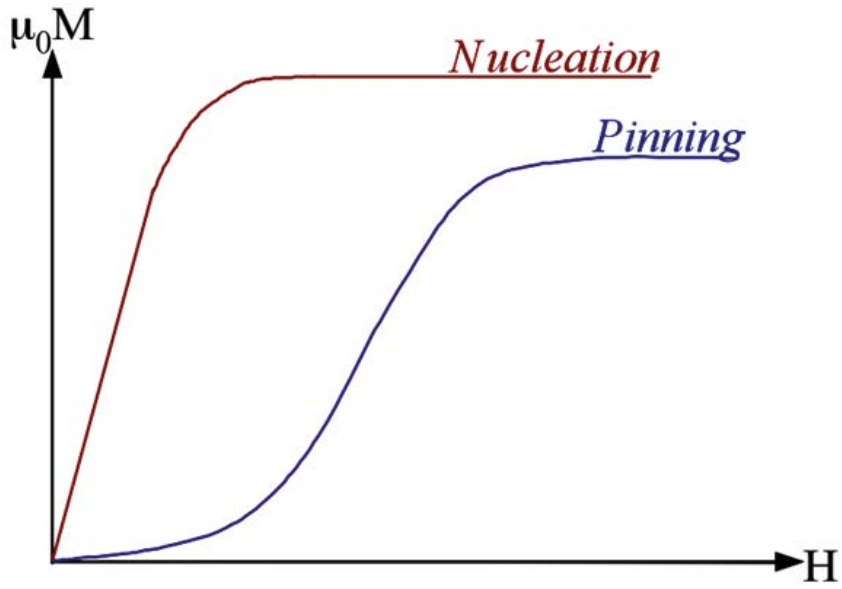

Figure 22. Initial magnetisation curves for pinning and nucleation type magnets [Walton Undergraduate Lecture (2013)].

2.6.1 Nucleation

The nucleation of reverse domains commonly occurs at physical defects in the lattice or surface irregularities, where the crystal anisotropy is locally lowered hence causing antiparallel domains and finally decreasing the overall magnetisation. These reverse domains can appear spontaneously or under the influence of an external applied field. The inhibition of the reverse domains is necessary in permanent magnets as they could, afterwards, grow and expand through the whole grain.

Magnets which are controlled by a nucleation mechanism prevent reverse domains by having a small density of defects, which is achieved by separating the main magnetic phase into smaller regions surrounded by a smooth non-ferromagnetic phase. This reduces the number of reverse domain nucleation sites and it results in the isolation of the domains and hence the reverse domains do not spread throughout the material.

In figure 22 it can be observed that the initial magnetisation of nucleation type materials exhibit a rapid rise at low applied fields as preferentially aligned domains grow and merge at the expense of reverse magnetised domains. This continues until the expansion of the aligned domains is impeded,

where the magnetisation of the magnet increases slowly as the reverse domains are forced to change their direction of magnetisation with increasing applied field. This coercivity mechanism applies to neodymium iron boron-type magnets.

2.6.2 Pinning

The pinning of domain walls can be achieved by defects, precipitates or grain boundaries interacting with the domain walls, reducing the domain wall energy and, if a non-magnetic precipitate is present within the grains, the domain wall will have a decreased area and lower energy. As the domain walls have reduced energy there will be a barrier to their movement from these pinning sites requiring additional energy to overcome the pinning barrier. The coercivity is controlled by the field required to overcome the pinning barriers, which is known as pinning field. This results in a very slow initial magnetisation curve as it requires a high field to reach the pinning field and overcome the pinning barriers.

A schematic diagram of the processes involved in magnetisation reversal is shown in figure 23.

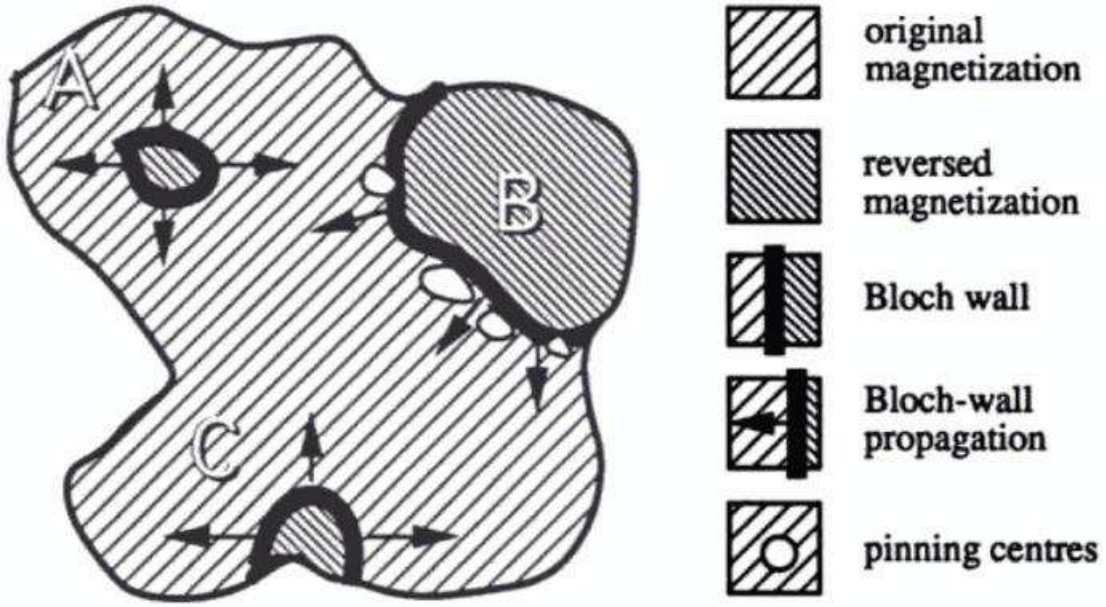

Figure 23. Processes involved in magnetisation reversal in the second quadrant of the hysteresis loop. A is a reverse domain which nucleates in the bulk at a defect or from a spontaneous thermal fluctuation. B is a reverse domain which has grown to a point where the wall is trapped by pinning centres. C is a reverse domain which nucleates at a rough surface [Coey, 1996].

2.6.3 Single Domain Particle

There is a balance between the reduction of energy by dividing the domains into smaller ones and the increase in energy associated with the introduction of domain walls. As the size of the particle decreases, there is a critical size below which the decrease in magnetostatic energy is lower than the increase in energy caused by the introduction of the domain wall. Those particles below that size are known as single domain particles. In the single domain particle mechanism, the domains resist the demagnetising field from flipping or rotating the domains. As a consequence, the initial magnetisation curve is very slow as high field is required to flip and rotate all the domains. Materials utilising the single domain coercivity mechanism tend to have high coercivities.

Chapter 3. Literature Review I: NdFeB Alloys

3.1 Introduction

In the 1970's the highest energy permanent magnet material was based upon SmCo. However uncertainties in the supply of cobalt on the world market in the late 1970s led to massive fluctuations of its price, which prompted wide-scale research and development to find new magnetic materials with little or no cobalt.

At the 29th Magnetism and Magnetic Materials Conference held in Pittsburgh in 1983, Sagawa et al [1984] announced that Sumitomo Special Metals Company (Japan), had succeeded in making a fully dense sintered permanent magnet of composition $Nd_{15}Fe_{77}B_8$ (at%) with a $(BH)_{max}$ of 290 kJ m^{-3}, by using a powder metallurgy route similar to that employed for SmCo magnets. At the same conference, it was reported that independent research involving Hadjipanayis et al [1984], Koon et al [1984] and principally Croat et al [1984] at General Motors (US), had developed isotropic permanent magnets from melt-quenched Nd-Fe-B alloys.

3.2 Neodymium Iron Boron Alloys

3.2.1 Phases in the Neodymium Iron Boron System

The first information provided on the ternary Nd-Fe-B phase diagram was due to Chaban et al in 1979, reporting an isothermal section at 600 °C, showing that there were three stable ternary phases in the system as shown in figure 24. These were the $Nd_2Fe_{14}B$ (ϕ), the $Nd_{1+\varepsilon}Fe_4B_4$ (η) and the $Nd_5Fe_2B_6$ (ρ) phases, although at the time the reported compositions were not correct.

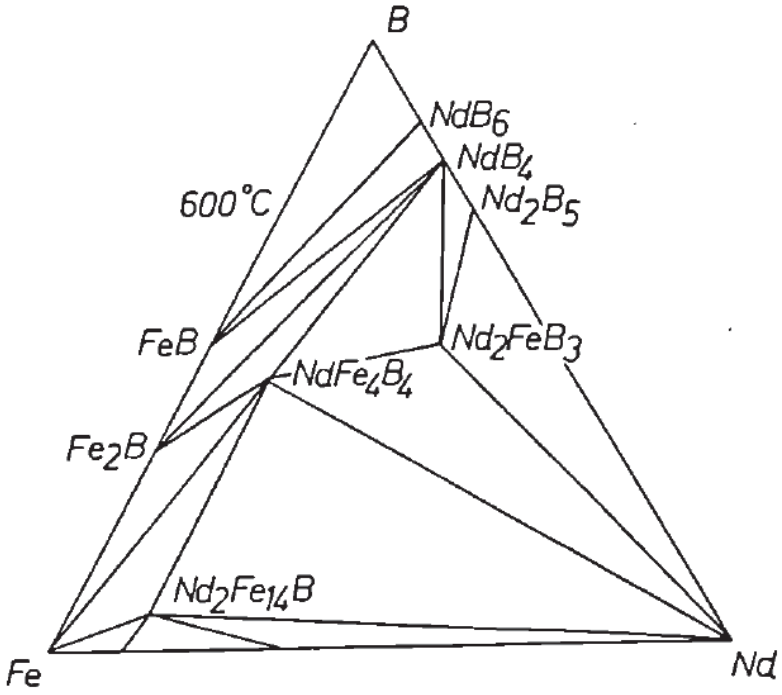

Figure 24. The Nd-Fe-B phase diagram [Commission of the European Communities, 1985; Chaban et al, 1979].

Since then, numerous studies have reported phase relations in the ternary Nd-Fe-B system [Matsuura et al, 1985; Schneider et al, 1986; Hiraga et al, 1985; Grieb et al., 1992; Knoch et al, 1994; Hallemans et al, 1995]. Most of them focused on the area around the Fe-rich corner and around the commercially available composition known as Neomax $Nd_{15}Fe_{77}B_8$. These studies showed that Neomax comprised three main phases namely $Nd_2Fe_{14}B$ (ϕ), $Nd_{1+\varepsilon}Fe_4B_4$ (η) and a grain boundary eutectic region that is composed principally of Nd-rich material.

Neomax composition is of special commercial interest at the expense of the stoichiometric composition $Nd_{12}Fe_{82}B_6$ because the former avoids the peritectic reaction that takes place at 1180 °C, whereas the latter does not, as shown in figure 25. If the peritectic reaction does not go to completion, then soft magnetic α-Fe may remain in the final microstructure, which has a detrimental effect on the milling behaviour of the powders and on the magnetic performance of the magnet. Avoiding the formation of α-Fe can be achieved by having a high boron content or by cooling quickly so Fe does not have time to form or by increasing the overall Nd content.

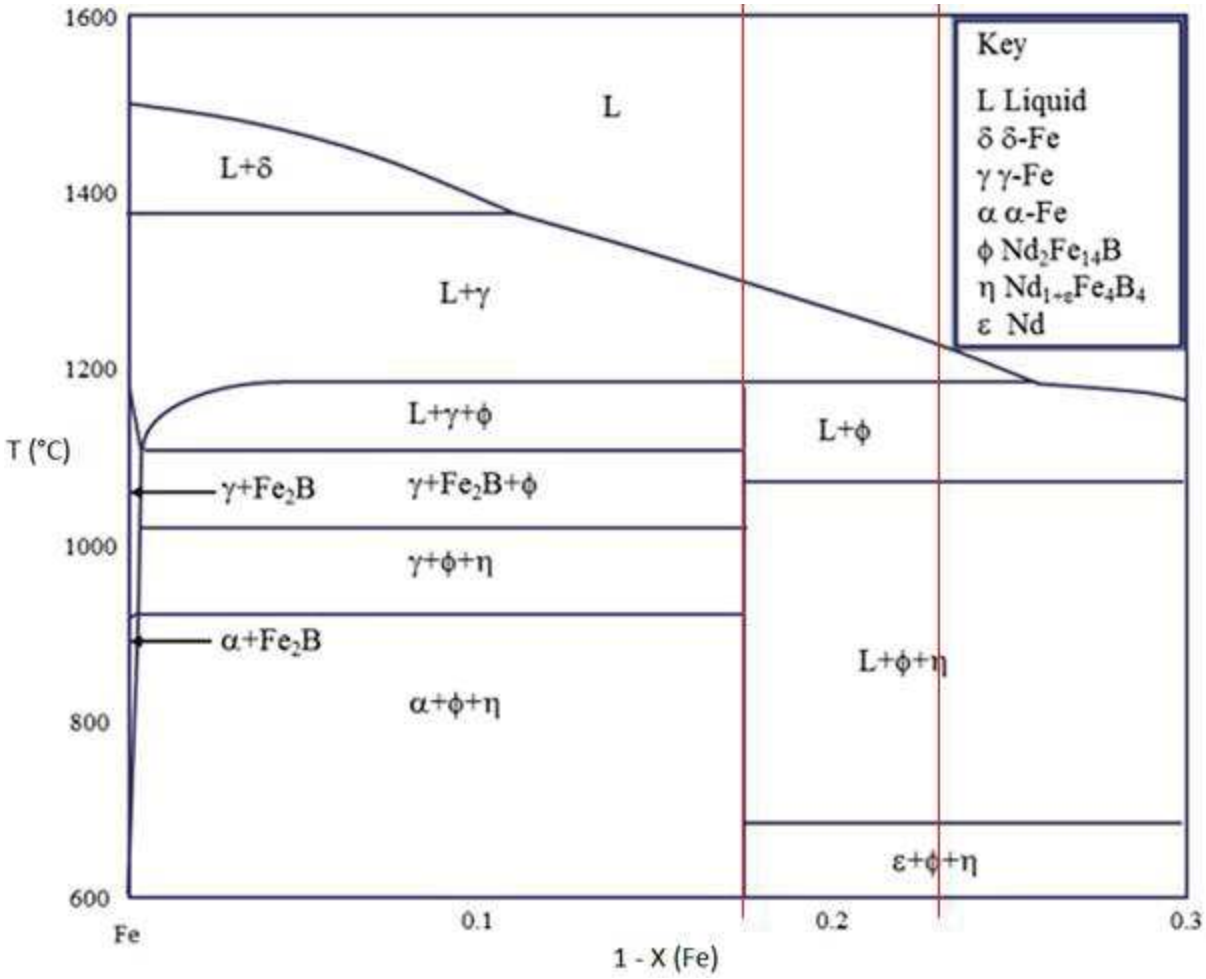

Figure 25. The Fe - $Nd_2Fe_{14}B$ isopleth for Nd / B = 2. The left red line corresponds to stoichiometric $Nd_{12}Fe_{82}B_6$ whereas the right line corresponds to the Neomax $Nd_{15}Fe_{77}B_9$ [Hallemans et al, 1995].

Besides the $Nd_2Fe_{14}B$, the $Nd_{1+\varepsilon}Fe_4B_4$ and the Nd-rich phase, there are six other stable or metastable Nd-Fe-B ternary compounds namely the $Nd_5Fe_2B_6$ (ρ), $Nd_2Fe_{23}B$, $NdFe_{12}B_6$, $Nd_2Fe_{17}B$, ε and A'1 phases [Buschow et al, 1986; Iwamura et al, 1989; Linetsky, 1992].

3.2.2 The $Nd_2Fe_{14}B$ Phase

The $Nd_2Fe_{14}B$ phase is the main matrix phase in Nd-Fe-B alloys and is the responsible for the high saturation magnetisation. The first detailed determination of the structure was performed by Herbst et al in 1984 using neutron diffraction in polycrystalline samples. The $Nd_2Fe_{14}B$ phase has a tetragonal structure and belongs to the space group $P4_2/mnm$ with a unit cell containing 68 atoms and lattice

parameters a = 0.880 nm and c = 1.221 nm. Figure 26 shows a schematic of the crystal structure of the $Nd_2Fe_{14}B$ phase.

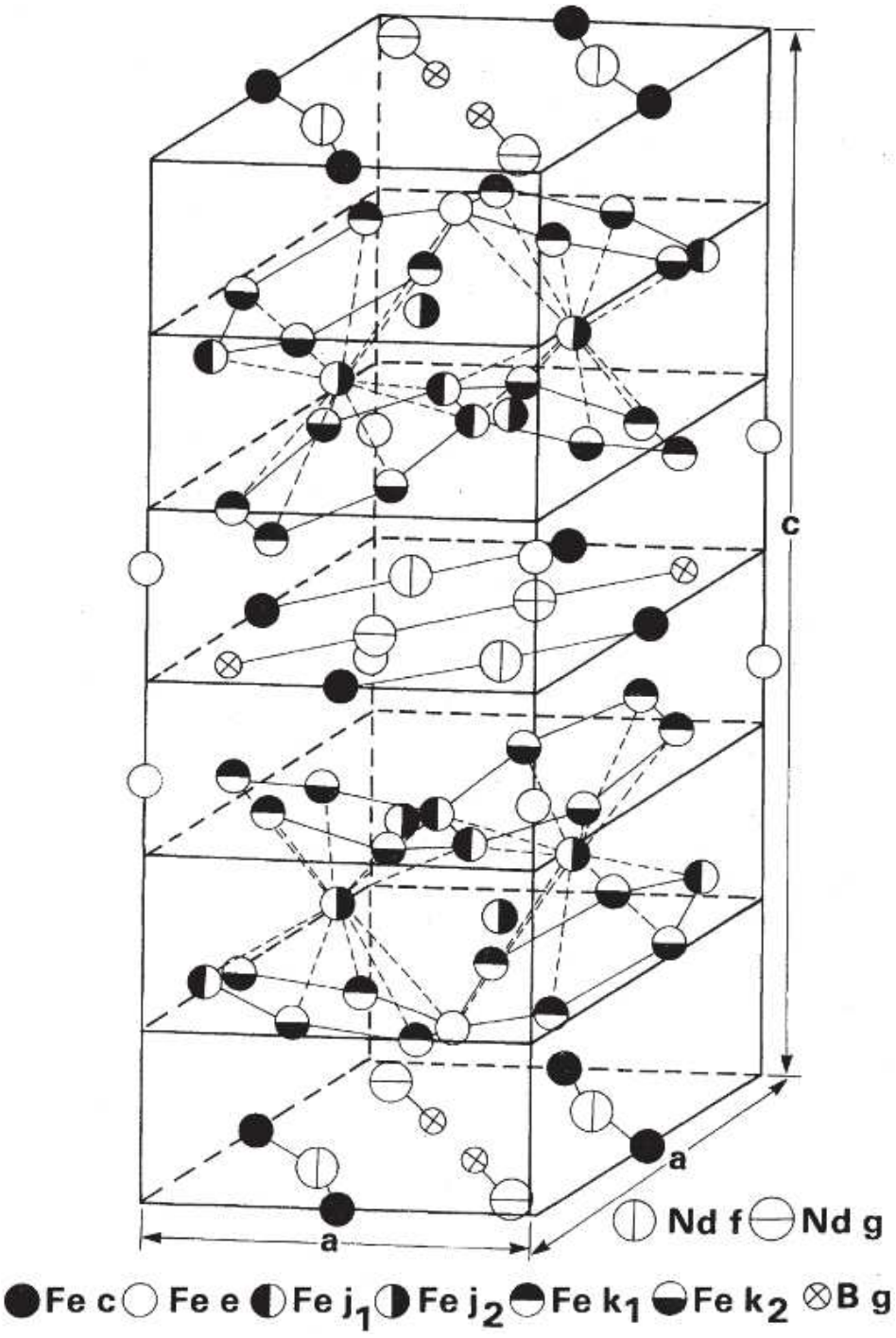

Figure 26. Crystal structure of $Nd_2Fe_{14}B$. The Fe, Nd and B sites are denoted according to the Wycoff notation. [Herbst et al, 1984]

In parallel, Givord et al [1984a] and Shoemaker et al [1984] investigated the crystal structure of the $Nd_2Fe_{14}B$ phase obtaining identical results confirming those of Herbst et al [1984]. However, there were slight disagreements on the location of individual atoms due to the densely packed structure.

Basic magnetic properties have been widely reported in both polycrystalline [Sinnema et al, 1984l; Yamamoto et al, 1984] and single crystalline [Givord et al., 1984b; Hirosawa et al, 1984; Koon et al, 1985] samples, although the studies on the latter are more accurate and detailed.

One of the fundamental features of the $Nd_2Fe_{14}B$ compound is that it exhibits a conical spin reorientation at about 135 K [Givord et al, 1984b; Hirosawa et al, 1985; Huang et al, 1985]. Research on temperature dependence of both the magnetocrystalline anisotropy and saturation magnetisation have shown that at room temperature the easy axis of the magnetisation is along the c-axis of the crystal structure. However, below approximately 135 K the magnetisation begins to tilt away, reaching tilting angles of about 30° at 4.2 K. This spin reorientation has a detrimental effect on the magnetic properties of the $Nd_2Fe_{14}B$ phase at that given range of temperatures [Heisz et al, 1987]. Therefore, they are not suitable at those temperatures. However the $Pr_2Fe_{14}B$, exhibits no spin reorientation [Sagawa et al, 1984b; Yamamoto et al, 1984] and Pr is added to NdFeB in low temperature applications [Pourarian et al, 1990].

3.2.3 The $Nd_{1+\varepsilon}Fe_4B_4$ Phase

The $Nd_{1+\varepsilon}Fe_4B_4$ phase was firstly reported in 1979 by Chaban et al, and is shown in the centre of the diagram phase in figure 24. Crystallographic investigations determined that the structure of the phase consisted of two closely interpenetrating sublattices of tetragonal symmetry [Givord et al, 1985; Braun et al, 1982; Bezinge et al, 1985]. The value of ε is determined by the ratio of the translation periods or the two periods along the c-axis, where $\varepsilon = C_{Fe}/C_R - 1$. For neodymium, ε is approximately 1. This parameter was found to decrease as R varies from Tm to La, which was attributed to the contraction of the atomic radius along the rare earth series [Niarchos et al, 1986].

The $Nd_{1+\varepsilon}Fe_4B_4$ phase is paramagnetic at room temperature and becomes ferromagnetic at temperatures below 25 K [Niarchos et al, 1986]. In addition, this phase presents a low T_c [Wang et al, 2005a]. The presence of this phase in NdFeB magnets does not improve the overall magnetic performance and may have the detrimental effect of nucleating reverse domains [Durst et al, 1987].

3.2.4 The Nd-Rich Phase

The neodymium-rich phase has been found to play an essential role in both sintering and coercivity mechanisms of the material [Fidler, 1987; Hiraga et al, 1985]. Davies et al [2001] showed that the Nd-rich phase plays a vital role in the densification behaviour of green compacts. They also showed that increasing the effective Nd content resulted in greater densification at lower temperatures.

The Nd-rich phase has also been demonstrated to be key in the improvement of magnetic properties of NdFeB magnets. This is reported to be due to improved magnetic separation between the $Nd_2Fe_{14}B$ phase grains as the Nd-rich phase is paramagnetic. Woodcock et al [2012] also reported an improvement in magnetic properties as a consequence of the reduction or removal of defects at the $Nd_2Fe_{14}B$ phase grain surfaces. Therefore, as the ratio of Nd-rich to matrix increases, the $_iH_c$ increases; whereas if that ratio decreases, the B_r increases.

The neodymium-rich phase is still not fully understood due to its complex structure. There are conflicting reports on the morphology and the structure and studies by various authors having identified this phase as a body centred cubic structure [Hiraga et al, 1985], a double hexagonal close packed (dhcp) structure [Fidler, 1987] or a face centred cubic (fcc) structure [Ramesh et al, 1987]. Hiraga et al [1985] established that this phase could be present in an amorphous state, which was later confirmed by Holc et al [1990].

The Nd-rich phase is mainly composed of neodymium, but also comprises iron, a small amount of boron [Fidler, 1987] and oxygen [Shinba et al, 2005; Wang et al, 2005b]. An investigation by Tang et al [1988a, 1988b] showed the presence of thin Nd-rich layers at grain boundaries, grain junctions and within the matrix phase with a fcc structure and a composition about $Nd_{75}Fe_{25}$ at%, which were in

agreement with those obtained by Ramesh et al [1987]. A second Nd-rich phase was identified with a dhcp structure and a composition about $Nd_{95}Fe_5$ at% [Tang et al, 1988a; Tang et al, 1988b]. This second Nd-rich phase was finely distributed between the $Nd_2Fe_{14}B$ grains.

It was later concluded that the crystal structure of the Nd-rich phase depends on the oxygen content showing a dhcp structure when the oxygen is below 9 at%, a fcc structure when it is between 11 and 43 at%, and a hcp structure when it is above 55 at% [Mo et al, 2008]. These results are in agreement with those by Shinba et al [2005]. Therefore, the Nd-rich phase can contain multiple oxides such as NdO, Nd_2O_3 and NdO_2 [Woodcock, 2012].

3.2.5 Coercivity Mechanism

The high coercivity of NdFeB magnets originates from magnetocrystalline anisotropy in the $Nd_2Fe_{14}B$ phase. If there was no anisotropy to prevent the magnetic polarisation rotation into the direction of the applied field, there would be no coercivity. If magnetisation reversal involved only uniform coherent rotation of the magnetic moments, the coercive force would be then equal to the anisotropy field.

In all magnets characterised by a large magnetocrystalline anisotropy, the coercivity is always lower than the anisotropy field [Hirosawa et al, 1990] and is known as the Brown's paradox [Brown, 1945; Brown, 1959]. Then, the coercive force would be given by:

$$H_a = \frac{2\,K_1}{M_s} - N\,M_s \qquad \text{Equation 11}$$

Where N is the demagnetising factor. It can be seen that the coercivity given by this equation is equivalent to the anisotropy field given in equation 9 plus the detrimental effectual of a demagnetising factor which is proportional to the spontaneous magnetisation. However, this equation does not include the effects of temperature and composition on coercivity, which have been studied [Kronmuller et al, 1988] and can be described by [Durst et al, 1987]:

$$H_a = \alpha(T)\,\frac{2\,K_1}{M_s} - N\,M_s \qquad \text{Equation 12}$$

Where α is an experimental temperature dependant parameter. It implies that real magnets are never homogeneous. The observed values of coercivity in NdFeB magnets only account for approximately 40 % of the theoretical value given by equation 11, which arises from the nucleation and growth of reverse domains and the motion of domain walls, to which the temperature contribution in equation 12 should be added.

The initial magnetisation curve of sintered NdFeB magnets increases rapidly up to saturation magnetisation, which is an indicator that nucleation is the coercivity mechanism that controls the magnet [Sagawa et al, 1984a]. This confirms that the size of the grains is greater than the single domain size and indicates that free domain wall motion occurs with no pinning. This has been confirmed by high-resolution transmission microscopy, showing that the $Nd_2Fe_{14}B$ phase has no precipitates of secondary phases or lattice defects [Fidler et al, 1985; Hiraga et al, 1985].

3.2.6 Microstructure of Sintered NdFeB Magnets

The microstructure of sintered NdFeB magnets is mainly characterised by the phases and their distribution, the porosity, the grain size and the degree of alignment of the $Nd_2Fe_{14}B$ phase grains. These microstructural parameters depend on alloy composition and processing techniques used to manufacture the magnets. Therefore, the improvement in the magnetic properties of sintered NdFeB magnets lies in a clear understanding of the microstructure.

In a commercial sintered NdFeB magnet three principal phases appear. The ferromagnetic $Nd_2Fe_{14}B$ phase constitutes about 82 to 85 % of the total volume of the magnet and is responsible of the magnetic properties of the material [Corfield, 2003]. The Nd-rich phase occupies approximately 10 % of the volume and is responsible of good densification, through LPS, and of separating neighbouring $Nd_2Fe_{14}B$ grain by acting as a magnetic isolation layer. The third phase is the $Nd_{1+\varepsilon}Fe_4B_4$ phase, which

does not contribute to the overall magnetic performance as it is non-ferromagnetic at room temperature. The microstructure of a typical sintered NdFeB magnet is shown in figure 27.

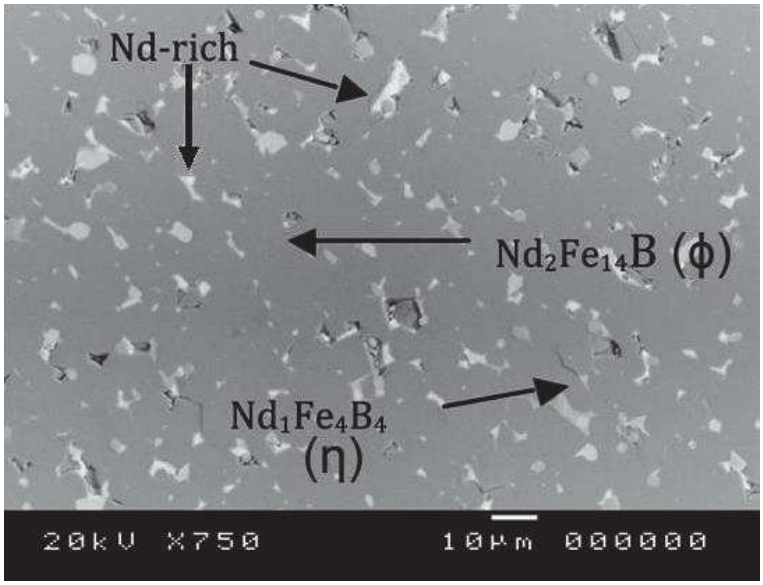

Figure 27. Back scattered scanning electron microscopy micrograph of a typical microstructure of sintered NdFeB [Zakotnik et al, 2008].

The occurrence of non-ferromagnetic phases in the microstructure leads to a reduction in the B_r but also in ${}_iH_c$ as its presence leads to stray field effects [Durst et al, 1987] which contribute to the effective demagnetisation of surrounding $Nd_2Fe_{14}B$ phase grains. Pastushenkov et al [1987] observed magnetic domains and found that magnetisation reversal starts in the $Nd_2Fe_{14}B$ phase grains near non-ferromagnetic inclusions. Although pores and Nd_2O_3 are also non-ferromagnetic inclusions, they were found not to contribute to such decrease as their volume fraction is small [Kronmuller, 1962].

The ideal microstructure would comprise only two phases. These would be $Nd_2Fe_{14}B$ rounded grains of approximately 3 to 7 μm in diameter perfectly isolated by the Nd-rich phase free of any non-magnetic inclusions [Kaneko et al, 1994]. This can be achieved by avoiding the formation of the $Nd_{1+\varepsilon}Fe_4B_4$ phase, which is possible by using a $Nd_{18.5}Fe_{75}B_{6.5}$ composition resulting, however, in a magnet with an excess of Nd-rich and a decrease in B_r [Knoch et al, 1994]. The typical grain sizes are at about 10 μm.

The $_iH_c$ is dependant on the grain size [Ramesh et al, 1988, Nothnagel et al, 1991, Liu et al, 1990].It has been reported that the $_iH_c$ decreases as the grain size increases. An increase in the grain size leads to an increase in the probability of having a defect on the $Nd_2Fe_{14}B$ grain surface which could act as a site for nucleation of reverse domains. A small grain has less surface and, hence, is less likely to have sites were reverse domains could nucleate.

Alignment also plays a significant role in the overall magnetic performance of sintered NdFeB magnets. Cui et al [2013] reported B_r to gradually increase with the increase of alignment magnetic field, whereas the $_iH_c$ decreases, which is similar to previous results by Gao et al [1998] and Kawai et al [1990] but contrary to those by Givord [1988] regarding $_iH_c$ values. Therefore, the effect of alignment on $_iH_c$ is still controversial.

3.3 Processing of NdFeB Permanent Magnets

3.3.1 Introduction

Rare earth iron boron alloys can be processed into fully dense permanent magnets utilising different routes, most relevant of which are shown in figure 28. As the magnetic properties of magnets are highly dependent on the processing conditions, each step can critically affect the quality and the performance of the final magnet.

The two main processing routes (A and B) for the production of magnets include techniques related to the conventional powder metallurgy route, where small particles of a few microns in size are oriented and sintered as shown in figure 28. A considerable advantage of powder metallurgy is that it is a near net shape technique, meaning the final shape is very close to the initial shape, hence decreasing or suppressing the machining stage. However, NdFeB powders are very reactive and oxidise easily and have to be produced in a controlled inert atmosphere. The production routes C and D include the production of magnets from cast NdFeB which avoids the handling of powder, hence minimising the oxygen contamination during the process.

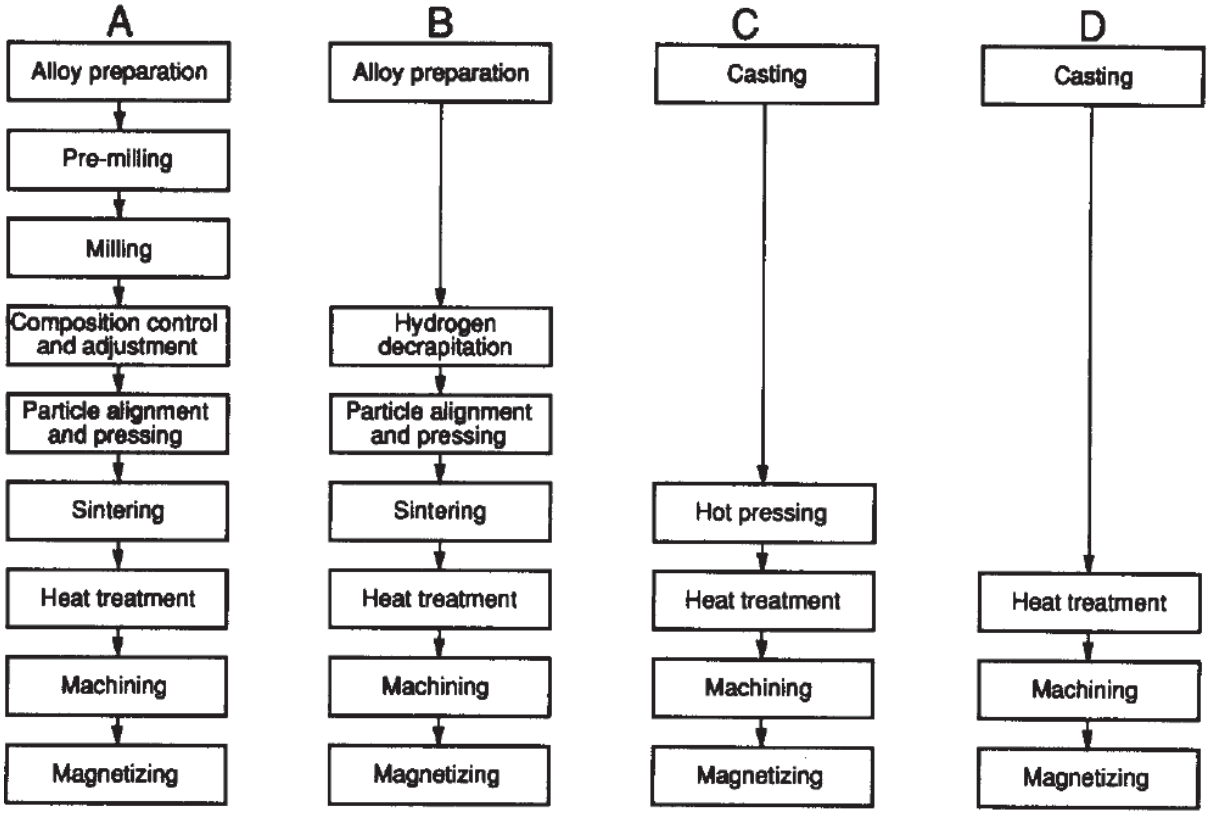

Figure 28. Survey of manufacturing routes in the production of high anisotropy rare earth permanent magnets [Buschow, 1989].

Processing routes suitable for bonded magnets are not shown in figure 28. These include the production of powder or flakes by melt spinning which are, afterwards, blended with polymer to make injection-moulded bonded magnets. A comprehensive review of this processing route can be found in Coey [1996] and Hadjipanayis [2003]

Most commercial NdFeB magnets are produced via the conventional HD powder metallurgy route shown in route B. The following sections will discuss the production of sintered NdFeB magnets using this route.

3.3.2 Alloy Production

3.3.2.1 Conventional Casting Techniques

The two principal conventional casting methods in the production of rare earth iron boron alloys are induction-melting and co-reduction of oxides. However, co-reduction is not used as the resultant alloys have high oxygen contents.

The induction-melting method uses the metallic components in pure form, which are melted together under argon and then poured and cast into thin moulds. The oxygen content using this technique is below 200 ppm [Corfield, 2003].

Conventional casting techniques make it difficult to suppress the formation of α-Fe dendrites [Bernardi et al, 1998] when the alloy composition approaches the stoichiometric $Nd_2Fe_{14}B$ ($Nd_{12}Fe_{82}B_6$ wt%). This is because the $Nd_2Fe_{14}B$ phase forms from a peritectic reaction after the formation of primary Fe crystals during solidification as discussed in section 3.2.1. In order to eliminate these α-Fe dendrites, standard homogenisation heat treatment at temperatures around 1000 °C for several hours or cyclical homogenisation at higher temperatures for shorter time periods are required to remove free iron [Ahmad, 1994; Clarke, 1997; Zhang et al, 1995]. However, this tends to cause the formation of large Nd-rich regions, which are very sensitive to oxidation, hence, deteriorating the uniformity of the microstructure [Hirose et al, 1998].

3.3.2.2 Strip Casting

The strip casting process entails pouring the molten alloy, through a series of ceramic tundishes, onto a water-cooled copper wheel, which cools the material at 10^4 K s^{-1} rates, enabling the continuous formation of few millimetres thickness flake-shape ingots. Fast cooling suppresses the formation of α-Fe dendrites, eliminating the need of homogenisation heat treatments [Bernardi et al, 1998]. Figure 29 shows a comparison between the typical microstructure of a strip cast alloy and a conventional cast ingot for a near stoichiometric alloy.

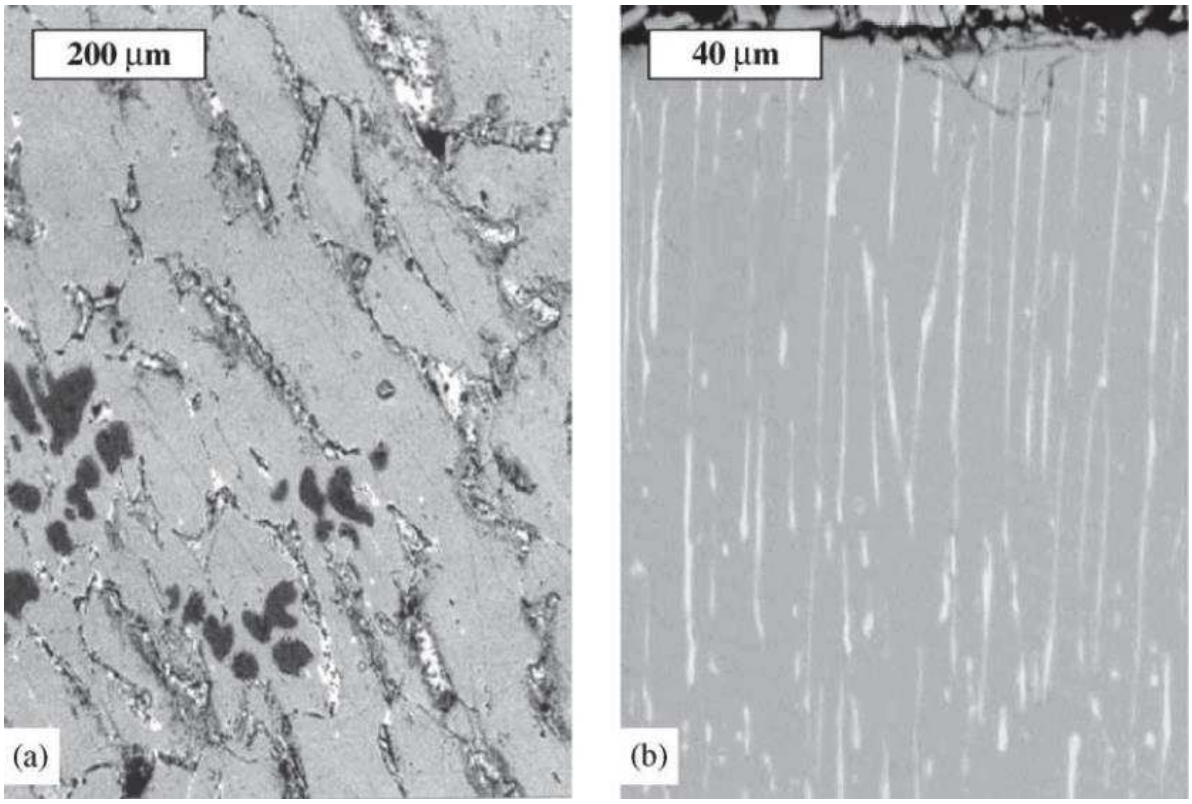

Figure 29. Back-scattered electron micrographs of an NdFeB alloy prepared by (a) conventional book moulding casting and (b) strip casting [Pei et al, 2002].

The magnets obtained after sintering process using conventional cast and strip casting materials were compared by Pei et al [2002]. It was found that improved ${}_iH_c$, B_r and $(BH)_{max}$ was achieved with the strip cast material compared to the conventional cast NdFeB. In addition, the microstructure of magnets from strip cast starting materials had a more homogeneous microstructure.

3.3.3 Hydrogen Decrepitation Process

The cast alloy, usually in ingot form, must be first broken down to a size suitable for milling. In the conventional route utilised by Sagawa et al [1984a], similar to that employed for $SmCo_5$ alloys [Benz et al, 1970], the cast material is broken down mechanically using a jaw crusher. A novel process developed at the University of Birmingham involving the use of hydrogen to break up the cast alloy overcame the difficulties encountered with mechanical breaking [Harris et al, 1985].

3.3.3.1 Hydrogen Absorption in Rare Earth Alloys

Many intermetallic materials containing REEs absorb large quantities of hydrogen [Wallace et al, 1980], hence changing its properties [Pourarian et al, 1982a; Pourarian et al, 1982b]. The use of hydrogen in the processing of rare earth magnets was first proposed by Harris et al [1979], involving the use of $SmCo_5$ magnets. Larsen et al [1980] investigated the kinetics of the hydrogen absorption and desorption processes in $SmCo_5$ alloys, finding that the hydrogen absorbed can be removed immediately by reducing the hydrogen over-pressure.

The hydrogen decrepitation (HD) process was later extended to $Sm_2(Co,Fe,Cu,Zr)_{17}$ alloys [Kianvassh et al, 1984; Kianvash et al, 1985]. It was found that the absorption and desorption properties of these alloys were different from those of $SmCo_5$. A temperature of 200 °C at a pressure of 20 bar was required for successful HD of a $Sm(Co_{0.65}Fe_{0.23}Cu_{0.10}Zr_{0.02})_{7.1}$ alloy [Kwon et al, 1991].

3.3.3.2 Hydrogen Absorption in Neodymium Iron Boron Alloys

When NdFeB alloy Neomax was announced by Sagawa et al [1984a] a number of investigations on the hydrogen absorption behaviour of the material were performed [Harris et al, 1985; Wiessinger et al, 1987; Oesterreicher et al, 1985]. These studies showed that upon exposure to hydrogen, the bulk material broke into friable powder at room temperature.

The HD process, shown schematically in figure 30, initially utilised high hydrogen pressure until McGuiness et al [1986] showed that the process is effective using a hydrogen pressure of just 1 bar. The hydrogen absorption consists of two stages. First hydrogen is preferentially absorbed at the grain boundary phase (GBP) by the Nd-rich forming neodymium hydride of composition $NdH_{2.7}$ [Moosa et al, 1988]. The absorption of hydrogen into the Nd-rich phase causes a volume expansion in the intergranular regions leading to intergranular cracking. The heat generated by this reaction causes hydrogen absorption into the $Nd_2Fe_{14}B$ phase matrix forming a hydride [McGuiness et al, 1996; Williams et al, 1991; Book et al, 1995] of composition $Nd_2Fe_{14}BH_{2.7}$ [Oesterreich et al, 1985], which

results in transgranular cracking. The hydrogen absorption is exothermic and is accompanied by a 5 % volume expansion [Harris et al, 1985]. The resulting powder needs to be handled in an inert protective atmosphere due to its high reactivity with oxygen.

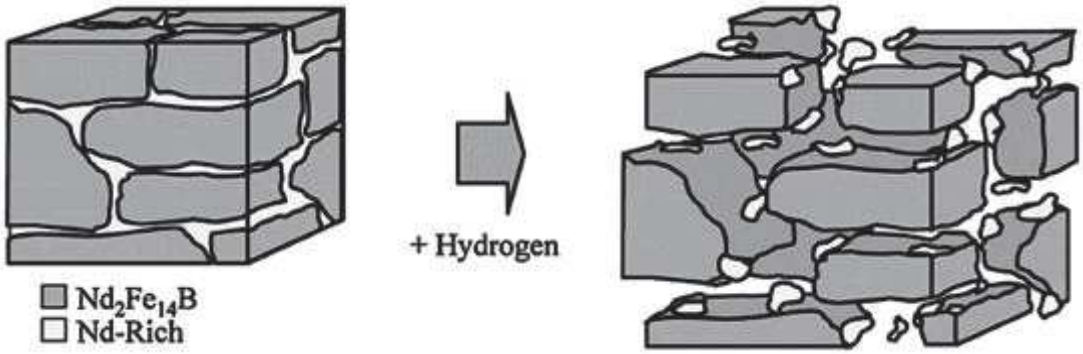

Figure 30. Schematic of the hydrogen decrepitation process [Williams, 1994].

The presence of the Nd-rich phase was found to be crucial when hydrogenating an NdFeB alloy at room temperature. Cadogan et al [1986] found that the stoichiometric $Nd_2Fe_{14}B$ phase did not absorb hydrogen at room temperature, even at elevated pressures. It was necessary to heat the material up to 220 °C before hydrogen absorption occurred. McGuiness et al [1989a] showed an $Nd_{11.8}Fe_{82.3}B_{5.9}$ alloy quite close to the stoichiometric $Nd_2Fe_{14}B$ inactive at room temperature when exposed to hydrogen, hence confirming previous results.

McGuiness et al [1990a] studied the influence of the initial microstructure of the alloys, using a cast and a homogenised $Nd_{16}Fe_{76}B_8$ alloy, on the HD behaviour, showing that the morphology of the hydrogenated powder was dependent on the initial state of the alloy. This study showed that when the alloy contained significant amounts of α-Fe, a flake like morphology shown in figure 31(a) is obtained. The flakes are produced by hydrogen diffusion into the alloy to a certain depth, after which strain due to the differential volume expansion results only in intergranular fracture. On the other hand, if the alloy is free of α-Fe, the hydrogenated powder is produced by transgranular and intergranular fracture due to the more brittle nature of the alloy as shown in figure 31(b).

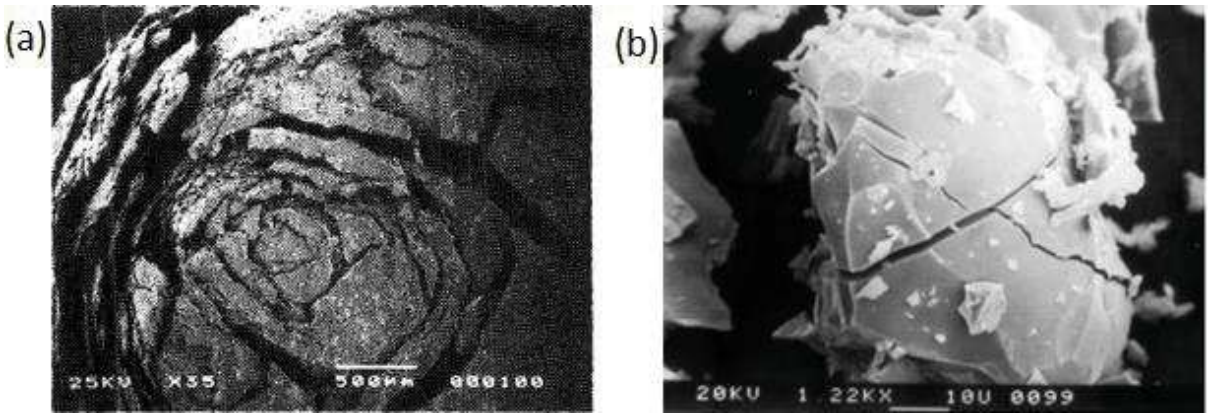

Figure 31. Morphology of the hydrogenated material obtained from (a) $Nd_2Fe_{14}B$ cast material and (b) $Nd_2Fe_{14}B$ alloy free of α-Fe [McGuiness et al, 1990a].

3.3.3.3 Hydrogen Absorption in Neodymium Iron Boron Sintered Magnets

McGuiness et al [1994] investigated the decrepitation behaviour of sintered NdFeB magnets with composition $Nd_{16}Fe_{76}B_8$ in both isotropic (unaligned) and anisotropic (aligned) states. It was found that the activation time was longer for the anisotropic magnets compared to the isotropic magnets. This study also found that the decrepitation behaviour varied significantly depending on the anisotropic or isotropic nature of the magnets. The isotropic magnets were attacked by hydrogen at all points on their surface whereas the anisotropic samples were found to decrepitate exclusively from the ends of the rods.

The resulting powder after the HD process was found to have a reduced ${}_iH_c$ when compared with the starting NdFeB magnets [Harris et al, 1991]. That powder therefore needs to undergo further processing such as sintering or Hydrogenation Disproportionation Desorption and Recombination (HDDR) to regain its magnetic properties, although it is still capable of c-axis alignment. Wiesinger et al [1987] suggested that the $(BH)_{max}$ is significantly reduced by the presence of hydrogen in the material and so a heat treatment is required to remove it and regain the magnetic properties. Rupp et al [1988] proposed to mill, align and sinter under vacuum the hydrogenated powders to completely desorb the hydrogen from the material.

3.3.3.4 Hydrogen Desorption in Hydrogenated Neodymium Iron Boron Alloys

The hydrogenated NdFeB material contains neodymium hydride in the form of neodymium trihydride of composition $NdH_{2.7}$, which is unstable in air and reacts forming neodymium hydroxide. By heating the hydrogenated material above 250 °C it is possible to desorb a portion of the hydrogen hence obtaining neodymium dihydride of composition NdH_2, which is more stable than the trihydride form [Verdier et al, 1994].

The desorption behaviour of hydrogen from neodymium trihydride was studied by Yartys et al [1997] and is shown in figure 32. When heated, the neodymium trihydride desorbs hydrogen in two stages. Firstly, the neodymium trihydride decomposed to neodymium dihydride at 220 °C to 380 °C and was completed at 450 °C. Secondly, the neodymium dihydride to neodymium reaction started at 550 °C and finished at 800 °C.

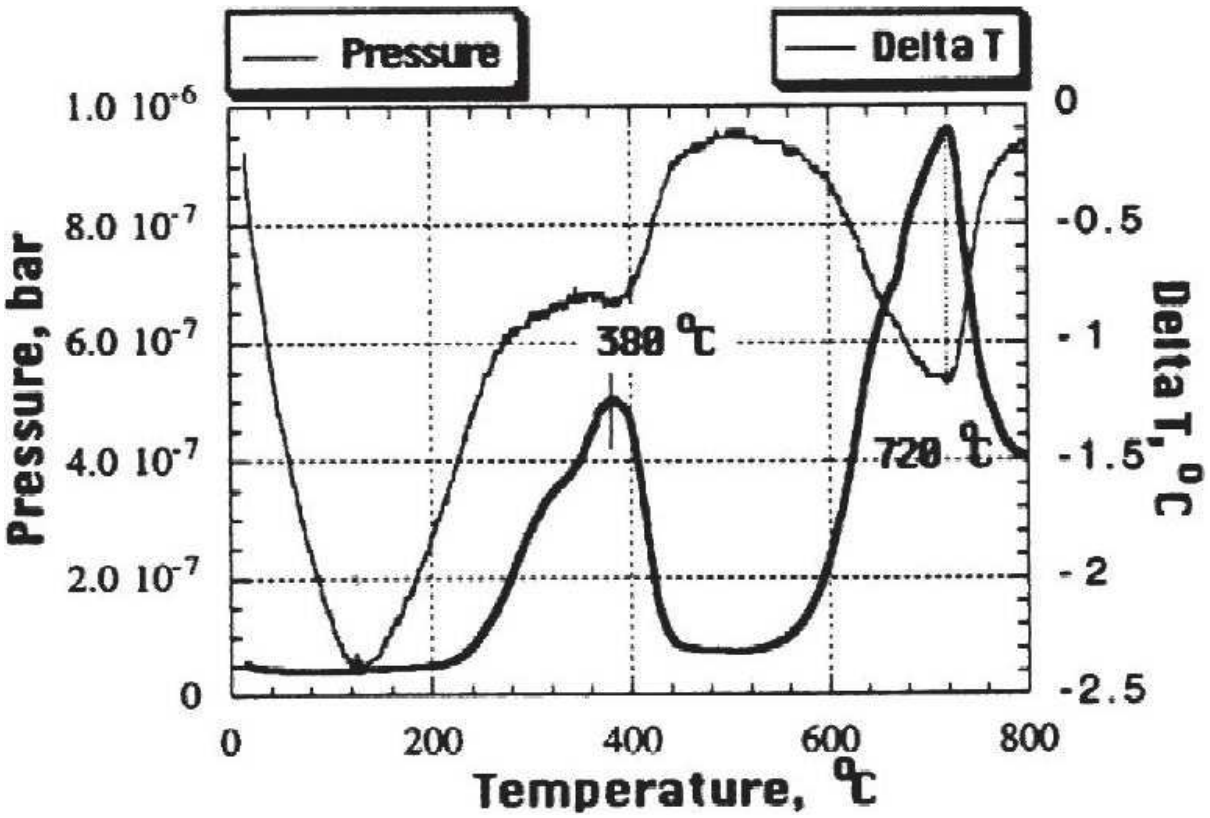

Figure 32. Desorption trace of $NdH_{2.7}$ [Yartys et al, 1997].

Harris et al [1987] investigated the desorption behaviour of $Nd_{16}Fe_{76}B_8$ and $Nd_2Fe_{14}B$ samples. It was found that $Nd_2Fe_{14}B$ showed an initial peak that started at 50 °C, finished at about 300 °C and peaked at 150 °C and it was suggested that the initial peak was due to the loss of hydrogen from the $Nd_2Fe_{14}B$ phase.

Further work by Williams et al [1991] found that desorption of hydrogen from the $Nd_2Fe_{14}B$ phase consisted on a sharp peak centred on 150 °C followed by a broad shoulder which indicated a peak centred on approximately 250 °C, as shown in figure 33. As the studied sample was a single phase alloy, this dual stage process was attributed to the desorption of hydrogen from different sites within the $Nd_2Fe_{14}B$ phase and to microstructural effects.

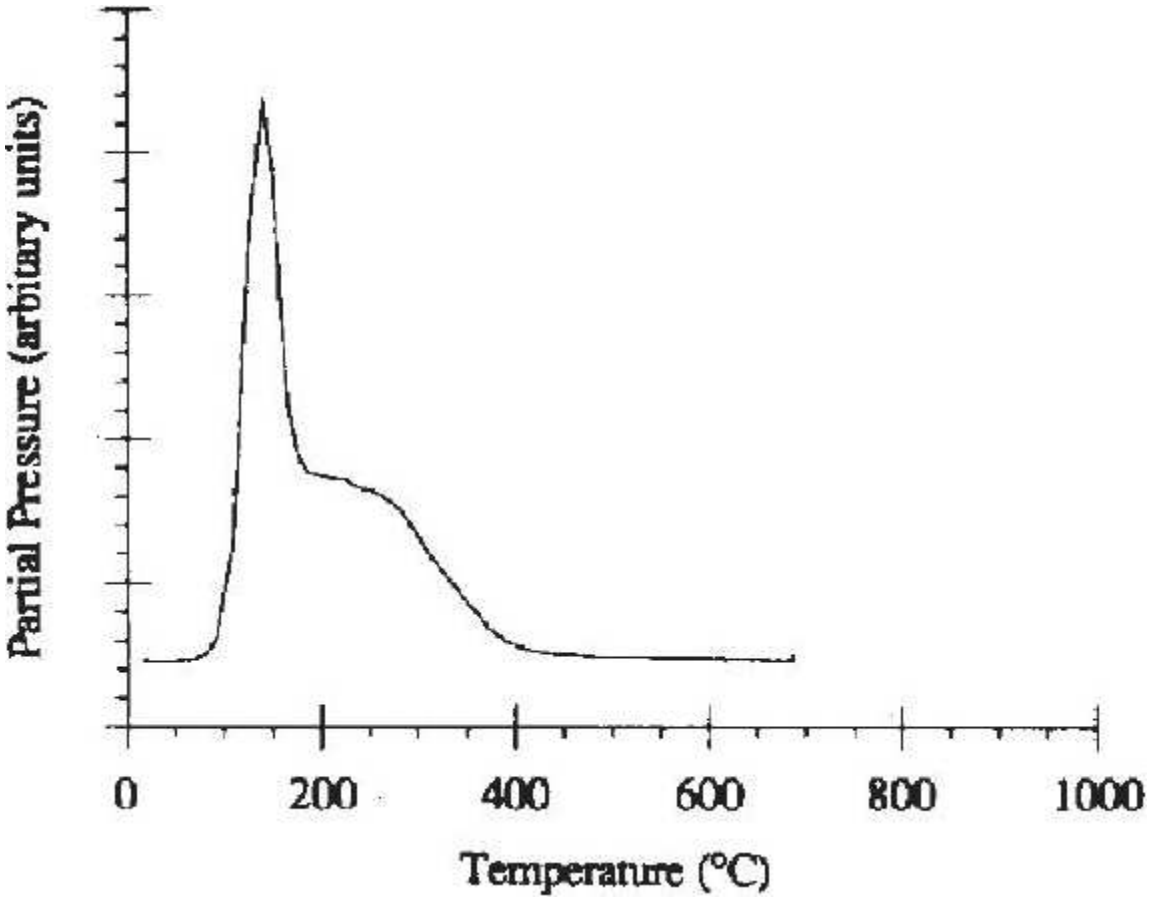

Figure 33. Desorption trace of $Nd_2Fe_{14}B$ phase [Williams et al, 1991].

The desorption behaviour of NdFeB magnets is a combination of the desorption of both the Nd-rich phase and the $Nd_2Fe_{14}B$ phase. A desorption trace of an $Nd_{15.5}Fe_{77.5}B_7$ alloy after HD is shown in

figure 34. The initial peak is centred at 125 °C and shows a shoulder at around 200 °C which correspond, respectively, to the desorption of hydrogen from the $Nd_2Fe_{14}B$ phase, and the decomposition of neodymium trihydride into neodymium dihydride [Williams et al, 1990; Williams et al, 1991]. The final peak is centred at approximately 600 °C and is associated with the complete desorption of hydrogen from neodymium dihydride to from neodymium. The temperature of this final peak was demonstrated to be lower than that of 720 °C observed by Yartys et al [1997] and lower than that of 650 °C observed by Harris et al [1987].

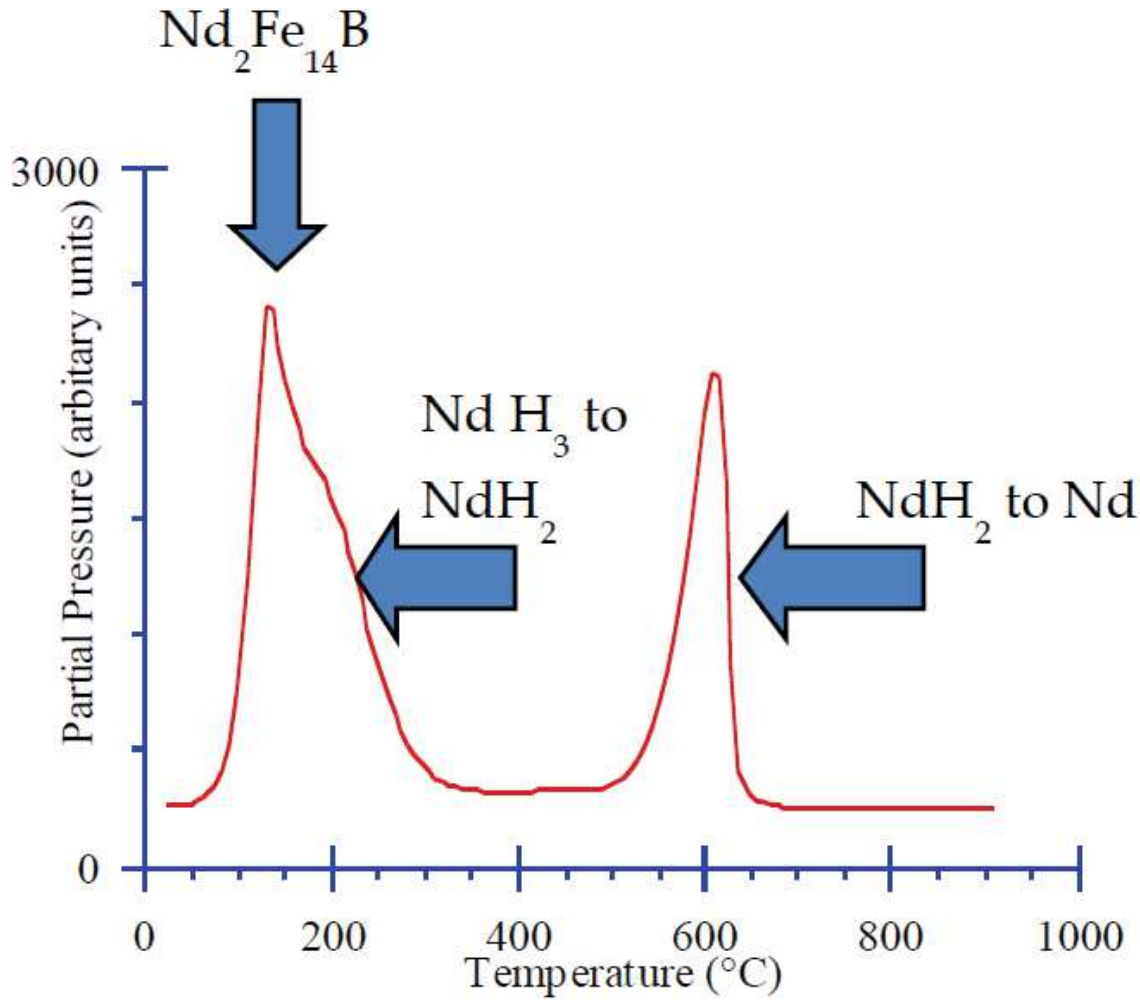

Figure 34. Desorption trace of an $Nd_{15.5}Fe_{77.5}B_7$ alloy [Williams et al, 1991].

3.3.4 Fine Milling

The main objective of fine milling the HD alloys is to produce a narrow particle size distribution. The two more common milling techniques are mechanical milling and jet milling.

3.3.4.1 Mechanical Milling

Mechanical milling is performed utilising hardened steel balls in an organic liquid media which is used to aid dispersal of the material to ensure good particle size distribution, and to act as a coolant and to limit oxidation. Due to the introduction by the organic liquid of carbon, oxygen and water and, also, further corrosion of the milling parts, this technique is widely employed in small scale laboratory research and not in the usual commercial route, where jet milling is more common.

Mottram et al [2001a] reported milling of cast HD NdFeB in cyclohexane for 20 hours leading to an average particle size of 3-7 μm. Nothnagel et al [1991] reported mean particle sizes of 1.5 μm and 2.5 μm depending on the size of the milling ball utilised. They also found that decreasing the mean grain size by increasing the milling time lead to an increase of $_iH_c$, but the $_iH_c$ decreased dramatically at a critical value of mean grain size. That study concluded that the increase in oxygen associated with the decrease in mean particle size resulted in the wipe out of the Nd-rich phase which had a negative effect on the liquid phase sintering (LPS). Therefore, the critical oxygen content increased with the rare earth content of the alloy.

3.3.4.2 Jet Milling

In the jet milling process the NdFeB powder is subjected to high pressures gas jets, between 5 and 10 bar, resulting in a fine powder by colliding the particles at each other. This milling technique presents a sharper particle size distribution and lower oxygen content when compared to mechanically milled powder [Corfield, 2003].

Namkung et al [2011] investigated the effect of the particle size distribution on the magnetic properties and microstructure of sintered magnets and stated that the B_r and $(BH)_{max}$ improved when

removing the fine particles and that $_iH_c$ increased when removing the coarse particles. It was found that as the mean particle size decrease, the $_iH_c$ increased and at a mean particle size of 3.35 μm there was a decrease in $_iH_c$. They suggested an increase in the oxygen content as a consequence of the reduction in average particle size and, subsequently, the oxidation of the Nd-rich phase and a decrease in $_iH_c$.

Uestuener et al [2006] reported mean particle sizes of 1.9, 2.2, 2.6, 3.0 and 3.5 μm and reported that $_iH_c$ increased when decreasing the particle size. They suggested that smaller grains may achieve higher coercivities. The average grain size in the sintered magnets decreased quasi linearly with the average particle size of the respective starting powders.

Li et al [2009] investigated the reduction of $_iH_c$ associated with the reduction in particle and grain size and they concluded that the degradation of the $_iH_c$ below a critical grain size could be attributed to the oxidation of the dhcp-Nd-rich phase to NdO_x phase and to the lack of dhcp-Nd-rich phase at the triple junctions.

3.3.5 Alignment and Pressing

For the purpose of achieving good magnetic properties, the easy axis of all the powder particles must be aligned in the direction of the final magnetisation. This is done by magnetically aligning the powder in an applied field which is followed by a pressing stage to keep the orientation in the pressed compacts. These pressed compacts, which are also known as green compacts [EPMA, 2008], have typically a density of around 60 % of the theoretical density of the alloy.

There are three main pressing and aligning techniques: (1) axial pressing, in which the compact is pressed in the presence of a magnetic field parallel to the pressing axis; (2) transverse pressing, in which the compact is pressed in the presence of a magnetic field perpendicular to the pressing axis; (3) isostatic pressing, in which the magnetic field is applied to the compact and is then isostatically pressed. The degree of alignment of isostatic pressed compacts is higher than that of axial or transverse pressed compacts, hence leading to higher magnetic properties.

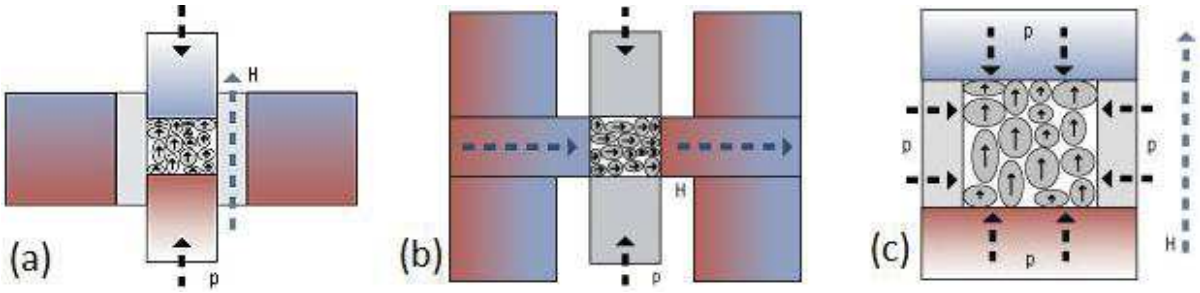

Figure 35. Schematic of (a) axial pressing, (b) transverse pressing and (c) isostatic pressing; where the pressure is denoted as p and dashed in black; and the applied field is denoted as H and dashed in blue. Images from http://www.vacuumschmelze.com/en/research-innovation/process-technology/permanent-magnets-systems/magnetic-field-pressing-technology.html Accessed 27/10/2016

A cross between the uniaxial and isostatic pressing is the so called rubber isostatic pressing (RIP) method developed by Sagawa and co-workers [Sagawa et al, 1994; Sagawa et al, 1995; Sagawa et al, 1993] and a comprehensive review of this technique can be found in Sagawa et al [2000]. In this technique the magnet powder is packed in a rubber mould prior to magnetic alignment using a strong pulsed field. The powder is then pressed isostatically prior to sintering

3.3.6 Sintering and Heat Treatment

Sintering is a heat treatment applied to a powder compact by which particles are fused together to form a solid, dense material at a temperature below the melting point of the major constituent. Sintering occurs by solid state diffusion which implies transportation of mass in a number of different ways, as is shown in figure 36 [Blackford et al, 2012].

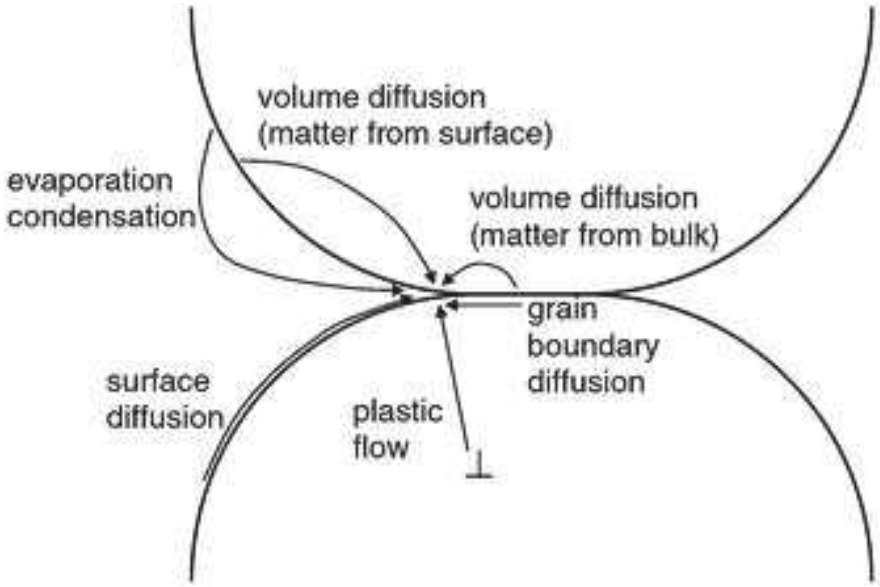

Figure 36. Schematic of transport mechanisms in solid state diffusion between two particles in contact [Blackford et al, 2012].

The sintering of NdFeB permanent magnets is carried out in an inert gas atmosphere or under vacuum and a constant and well-defined sintering temperature is necessary in order to ensure good final density of the magnet. A final density above 95 % of the theoretical should be achieved to minimise porosity, which could lead to oxidation and ageing during use [Ormerod, 1985]. The sintering process and the final density are enhanced by the presence of a liquid phase.

3.3.6.1 Liquid Phase Sintering

Sintering of NdFeB magnets is determined primarily by the liquid phase type of sintering mechanism, which involves the presence of a low melting rare earth rich eutectic. At approximately 655 °C the grain boundary eutectic phase melts and this liquid acts as a sintering aid and enables LPS [Sagawa et al, 1984a]. Therefore, densification can occur without significant grain growth.

The driving force for densification during the sintering of NdFeB magnets is the capillary pressure and the surface tension, although both grain boundary diffusion and volume diffusion also play a relevant role during densification. When surfaces energies are dominant, liquid-phase densification occurs in

stages as shown in figure 37 [German, 1996; German et al, 2009; Lü et al, 2001; Thümmler et al, 1993].

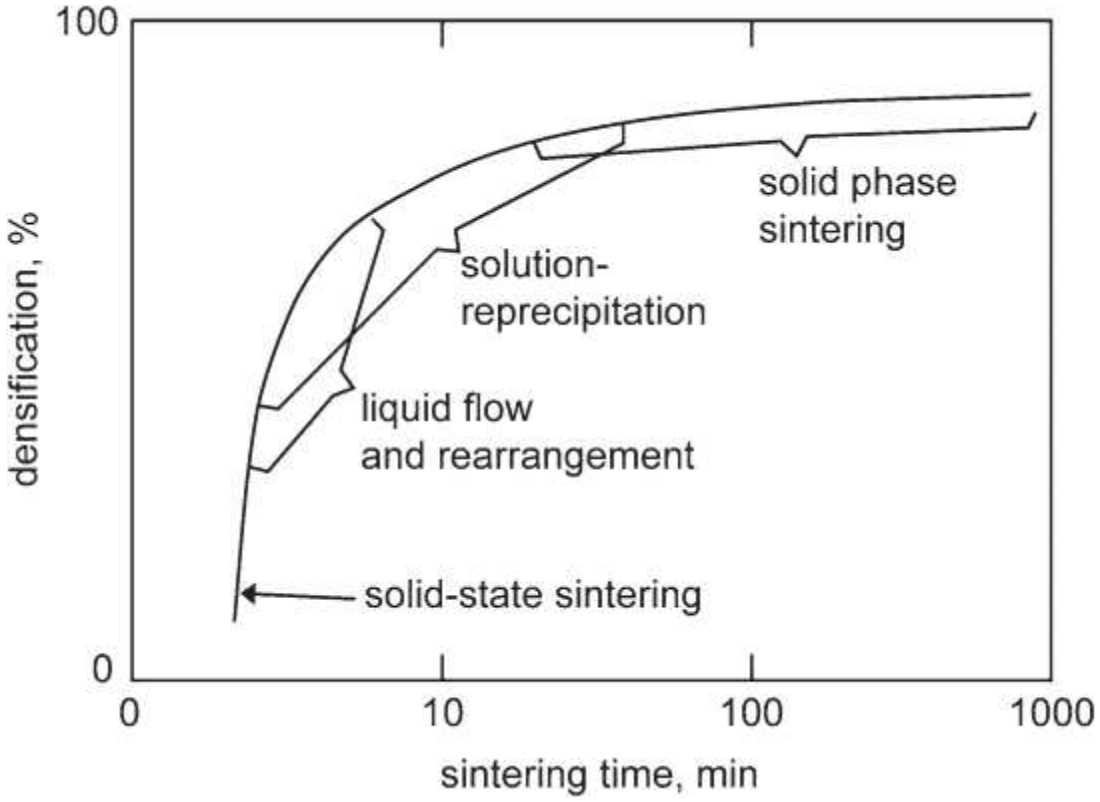

Figure 37. Schematic of the liquid phase sintering stages [German et al, 2009]

These stages occur sequentially during heating with certain overlap after the liquid forms. The first stage is rearrangement, in which, as the liquid melts, it wets the surface of the particles and the capillary action forces the liquid to enter inside the pores and cause grains to rearrange into a more favourable packing arrangement.

The degree of wetting, also known as wettability, is characterised by the contact angle, θ, which is the included angle in the liquid as shown in figure 38. When a liquid forms, the microstructure consists of solid, liquid and vapour phases. The contact angle represents a balance of the three involved interfacial energies; and the lower the value, the better the wettability. A low contact angle increases the capillary force and the amount of rearrangement, whereas with a large contact angle no rearrangement is possible and the liquid causes separation of the particles.

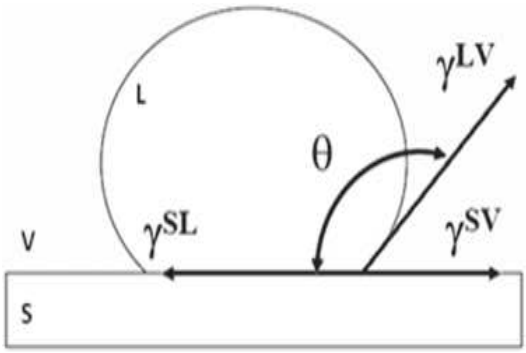

Figure 38. Schematic of the solid-liquid-vapour- equilibrium where θ is the contact angle, and γ_{SL}, γ_{LV}, and γ_{SV} are, respectively, the interfacial energies at between the solid-liquid, liquid-vapour and solid-vapour interfaces [Vicente et al, 2012].

The volume fraction of liquid is also important in the rearrangement stage. With a high volume fraction of liquid, it is possible to achieve complete densification by rearrangement.

The second stage is solution-reprecipitation where solution refers to solid dissolution into the liquid in areas where capillary pressures are high and reprecipitation refers to solid leaving the liquid by precipitation on existing grains. Solution-reprecipitation contributes to grain coarsening and also to densification via grain shape accommodation which in addition helps to eliminate porosity.

Densification occurs, as shown in figure 39 by the elimination of smaller grains and their preferential reprecipitation on the larger grains, which allows the release of liquid into any remaining pores. A wetting liquid induces particle contact due to an attractive capillary force. The coalescence of small grains with contacting large grains also contributes to grain coarsening and shape accommodation.

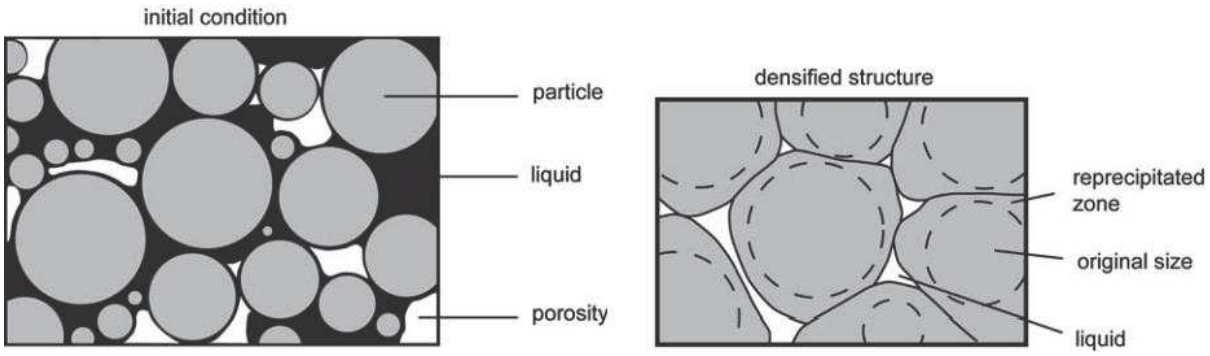

Figure 39. Schematic of the solution-reprecipitation densification where both grain growth and grain shape accommodation act to release liquid to fill residual pores [German et al, 2009].

The third and last stage is solid phase sintering and corresponds to a microstructure of connected solid grains with liquid occupying the space in between. In this rigid system grain growth continues and there is liquid movement from efficiently packed regions into pores to increase densification.

3.3.6.2 Sintering of NdFeB Magnets

A number of authors have investigated the progressive development of the microstructure for $Nd_{16}Fe_{16}B_8$ hydrogenated material during the sintering process [Mottram et al, 2000a; Davies et al, 2001; Nasseri-Pouryazdi et al, 1993].

No significant changes in the microstructure were observed when sintering at temperatures below 600 °C although on heating to this temperature the density increased from 4.0 to 4.2 g cm^{-3} [Nasseri-Pouryazdi et al, 1993]. This increase in density was explained as being possible due to desorption of hydrogen accompanied by a rearrangement of the particles to a denser configuration. This was later confirmed by dilatometer and microstructural studies, where a slight densification was observed between 200 °C and 300 °C [Mottram et al, 2000a; Davies et al, 2001]. Densification was shown to begin at 655 °C as the grain boundary melts, and finishes at around 1060 °C, as revealed by dilatometry for sintering of $Nd_{16}Fe_{16}B_8$ [Mottram et al, 2000a].

Microstructural studies showed the influence of sintering temperature on the densification of $Nd_{16}Fe_{76}B_8$ magnets as shown in figure 40 [Davies et al, 2001]. In the temperature range from 700 °C to 800 °C an increase in particle contact, due to solid state sintering mechanisms, can be observed, resulting in rearrangement of the particle. At 900 °C connectivity between the particles increased as a consequence of the decrease in porosity. This change was attributed to a change in the sintering mechanism, where increased wetting of the matrix phase grains by Nd-rich liquid phase results in the coalescence of rearranged grains and, then, the solution-reprecipitation mechanism become dominant. In the range from 1000 to 1100 °C an increase in density occurs from 90% to 98% of the theoretical full density. It was also reported that increasing the effective Nd content to 15 at% resulted in a densification above 98% of the theoretical full density at lower temperatures, 1060 °C.

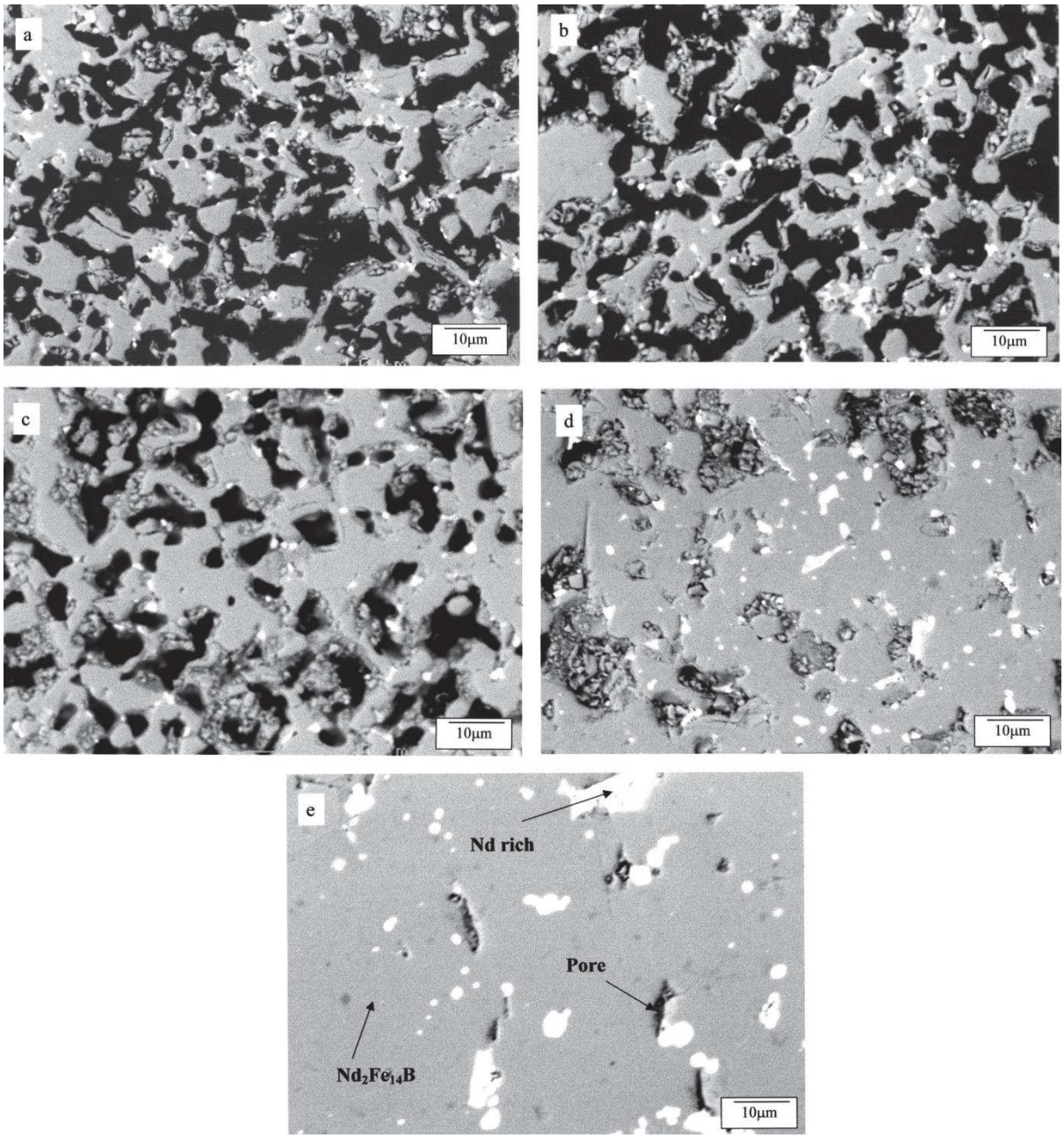

Figure 40. Back scattered images of $Nd_{16}Fe_{76}B_8$ sintered magnets at: (a) 700 °C, (b) 800 °C, (c) 900 °C, (d) 1000 °C and (e) 1100 °C at 1300 magnifications [Davies et al, 2001].

Good magnetic properties have been reached in $Nd_{15}Fe_{77}B_8$ magnets sintered at 1080 °C for 1 hour following a HD/attritor milling route [McGuiness, 1986]. The results were comparable to those obtained by Sagawa et al [1984a] who used the same sintering profile and the conventional powder metallurgy route.

For comparison, magnets were produced using jet milling on HD powder and sintered over a range of temperatures between 960 °C and 1080 °C [McGuiness et al, 1988; McGuiness et al, 1989b]. Sintering between 980 and 1040 °C resulted in excellent coercivities as well as excessive grain growth, which has a detrimental effect in coercivity.

Direct comparisons were made between magnets produced from jet milled hydrogenated material with those from jet milled conventional powder [Liu et al, 1990; Kim et al, 1996]. These studies showed that optimum magnetic properties were achieved in the hydrogenated material when sintered between 900 and 1000 °C for 1.5 hours.

Liu et al [1990] also reported that magnets made from the hydrogenated powder with a small percentage of oxygen, of approximately 0.94 wt%, introduced during processing exhibited good $_iH_c$ and a fine microstructure when sintered at 1060 °C. This is in comparison to an oxygen content of approximately 0.4 wt% reported by McGuiness et al [1986].

Hu et al [2014] reported that the magnetic properties of sintered NdFeB magnets have no difference with increasing sintering temperature from 1047 to 1071 °C of jet milled HD powder.

Cyclic sintering processes have been recently investigated for up to 2 cycles, in which $Nd_{13}Dy_2Fe_{79}B_6$ samples were heated and cooled from 950 to 1050 °C in an attempt to modify the microstructure of the Nd-rich GBP [Kim et al, 2012a; Kim et al, 2012b]. Cyclic sintering caused the formation of a Nd-rich phase at the triple points containing Nd_2O_3, which resulted in an increase in $_iH_c$. A second phase consisting of amorphous Nd-rich phase formed at the GBP that also contributed to the increased $_iH_c$.

Kim et al [2013] produced $Nd_{13}Dy_2Fe_{79}B_6$ magnets sintered at temperatures between 950 and 970 °C for 20 h in a process called low temperature sintering by which the grain growth of the $Nd_2Fe_{14}B$ phase is suppressed. This inhibition of grain growth resulted in improved magnetic properties.

3.3.6.3 Grain Growth

Grain growth results from the decrease in free energy, which is due to the reduction in GBP area and takes place by diffusion when the temperature is high enough and the time of heat treatment is long enough. It occurs during LPS by microstructural coarsening in conjunction with coalescence. Grains with a size smaller than average shrink, while larger than average grow. The rate of grain growth for a particular grain depends on the relative difference of size with its neighbours.

The presence of a Nd-rich liquid phase at the sintering temperature has a great influence on the grain growth process by advancing the diffusional mass transport [Wecker et al, 1994]. The effect of different rare earth contents has been shown to have a marked effect on the sensitivity to the formation of abnormal large grains, which have a detrimental effect on ${}_iH_c$. Reducing the total rare earth content and therefore the Nd-rich constituents has been shown to reduce abnormal grain growth during isothermal sintering with time [Rodewald et al, 1997; Liu et al, 2001]. Differences in the Nd-rich constituents were also believed to affect the grain growth process, although not the grain growth mechanism. Impurities, such as oxygen or oxides formed, could effectively hinder the mobility of the grain boundaries during sintering [Corfield et al, 2008].

A reduction in the total rare earth content influences the critical sintering temperature, above which abnormal grain growth is observed [Vial et al, 1998; Sasaki et al, 2000]. Higher sintering temperatures are required to achieve full densification in low rare earth alloys, as compared to high rare earth compositions [Mottram et al, 1998b; Mottram et al, 2000a]. In general terms, an increase in grain size is observed with increasing temperature [McGuiness et al, 1989b].

Lie et al [1990] suggested that increased oxygen content in the hydrogenated powder forms a finely dispersed Nd oxide layer at the GBP, which may impede grain growth at high sintering temperatures. Kim et al [1996] also reported that an unspecified, small amount of oxygen is beneficial in preventing abnormal grain growth. This is attributed to the fact that as the Nd-rich phase oxidises it solidifies,

thus inhibiting the rapid material transport that occurs during LPS by limiting the extent of the solution-reprecipitation process.

3.3.6.4 Cooling Rates

The cooling rate from the sintering temperature has been found to be an important parameter in determining the as-sintered ${}_iH_c$ of NdFeB magnets and has been studied in detail [Ramesh et al, 1988b; Ramesh et al, 1988a; Ramesh, 1990]. These studies observed that the ${}_iH_c$ and the $(BH)_{max}$ varied inversely with the cooling rate.

Further research showed that the reduction in ${}_iH_c$ was reversible by a post sinter anneal at 650 °C for 1 h followed by rapid cooling [Hsu et al, 1987; Yang et al, 1993]. The changes in ${}_iH_c$ were shown to be independent of initial cooling and heat treatment profiles, as shown in figure 41 exhibiting the reversible nature of ${}_iH_c$. Work by McGuiness et al [1989c] showed that the ${}_iH_c$ decreases linearly with increasing cooling rate and that annealing at 630 °C for 1 hour restore the ${}_iH_c$, independently of the initial cooling rate.

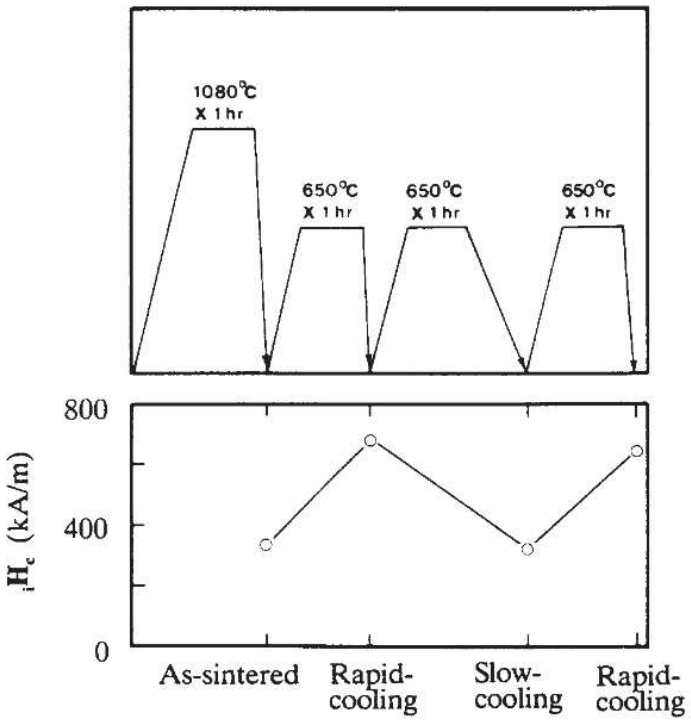

Figure 41. Variation of coercivity with cyclic heat treatment [Yang et al, 1993]

3.3.6.5 Post Sintering Heat Treatments

Post-sintering heat treatment can increase the ${}_iH_c$ of sintered NdFeB magnets because of the recovery of defects at the GBP and the formation of more continuous layers of the Nd-rich intergranular phase [Kaneko et al, 2006].

Annealing the material at temperatures from 600 to 650 °C for 1 hour under an atmosphere of either vacuum or helium resulted in a reaction between the Nd-rich GBP and the excess iron, thus increasing the amount of the $Nd_2Fe_{14}B$ phase and, as a consequence, the magnetic properties [Holc, 1990]. The B_r and the density were found to increase when annealed at 620 °C in vacuum.

It has been found that annealing NdFeB magnets at 600 °C for 1 h led to an increase in ${}_iH_c$ from 716 to 939 kA m^{-1} which was attributed to the formation of a continuous, thin layer of amorphous Nd-rich around the matrix phase grains [Li et al, 2009].

Hu et al [2014] annealed sintered magnets at different temperatures from 480 to 560 °C and found the ${}_iH_c$ to increase, reached a maximum of 2057 kA m^{-1} at 540 °C and then slightly decreased with increasing annealing temperature.

3.3.7 Alloying Elements

In spite of the exceptional magnetic properties of NdFeB magnets, its use has been limited in certain applications since it has a low T_c, poor corrosion resistance and low thermal stability of coercivity. However, these problems can be reduced or supressed by the addition of alloying elements.

The alloying elements can be distinguished in three different groups [Fidler et al, 1995]. The first group comprises elements that substitute into the matrix phase, replacing either the REE or the transition metal element. The second contains elements that improve the wettability and hence influence LPS forming intergranular phases. The third comprises elements that form precipitates either in the matrix phase or in the GBP.

3.3.7.1 Aluminium

The addition of aluminium has been shown to be highly beneficial to ${}_iH_c$ at the expense of both B_r and $(BH)_{max}$ [Liu et al, 2013]. Aluminium is prone to substitute the boron of $Nd_2Fe_{14}B$ phase and forms the Nd_2Fe_{14}(B, Al) phase, although some Al element diffuses into the Nd-rich phase [Legras et al, 1995; Liu et al, 2013]. Aluminium decreases the T_c by 8 K at%$^{-1}$ Al added [Rodewald, 1987].

The improvement in ${}_iH_c$ is a result of grain boundary modification [Fidler et al, 1990]. Knoch et al [1990; 1989] reported that aluminium increases the wettability, resulting in a more even distribution of the Nd-rich material, which gives rise to better magnetic decoupling of the grains, smoother boundaries and hence higher coercivities.

The addition of Al creates extra quantities of grain boundary material thus diluting the matrix phase with a proportional decrease in B_r [Mizogouchi et al, 1986; Knoch et al, 1989]. An additional phase of $Nd(Fe, Al)_2$ has been identified at the grain boundaries [Fidler, 1990], with a reported composition of $Nd_{36}Fe_{58}Al_6$ [Knoch et al, 1990].

3.3.7.2 Cobalt

Cobalt is added to NdFeB magnets to increase the T_c [Matsuura et al, 1985b] and substitutes Fe in the matrix phase [Szymura et al, 1991]. This increase happens at the expense of ${}_iH_c$ which decreases when the amount of Co added increases [Arai et al, 1985]. It has been found that Co was also present in the grain boundary [Fidler, 1985]. The majority of the Co containing GBP are soft magnetic and detrimental to ${}_iH_c$. The addition of cobalt has also been found to increase the corrosion resistance [Nakamura et al, 1989].

3.3.7.3 Copper

The addition of copper has been widely investigated and it has been found that the amount of copper added entering the matrix phase, if any, is of no significance to the intrinsic properties [Mottram et al, 2001a; Kianvash et al, 1991]. Copper is concentrated in the GBP, modifying significantly the

composition and distribution of the phases present. The GBP was identified as $NdCu_2$, NdCu and $Nd_6Fe_{13}Cu$ [Knoch et al, 1992a]. It was found to increase the corrosion resistance [Nozieres et al, 1992] as well as ${}_iH_c$ without any detrimental effect on the B_r [Ragg et al, 1997].

3.3.7.4 Dysprosium

The addition of dysprosium, substituting neodymium in the matrix phase, leads to an increase in ${}_iH_c$ due to the magnetocrystalline anisotropy of $Dy_2Fe_{14}B$ is higher than that of $Nd_2Fe_{14}B$ [Sagawa et al, 1984b]. The increase in ${}_iH_c$ is at the rate of approximately 640 kA m^{-1} per at% of dysprosium added in a $(Nd_{1-x}Dy_x)_{15}Fe_{77}B_8$ magnet [Sagawa et al, 1985]. Dysprosium has been found to inhibit grain growth during sintering, preventing the formation of large grains which are afterwards detrimental to ${}_iH_c$ [Ma et al, 1991]. However, dysprosium has been found to decrease the magnetisation saturation and the $(BH)_{max}$.

To overcome these problems, the so-called grain boundary diffusion process (GBDP) was proposed by Park et al [2000], where the Dy is first deposited on to the magnet'´s surface and then diffused into the magnet during a post-sintering annealing treatment. The idea is to concentrate the Dy in the vicinity of the grain boundaries where nucleation and propagation of magnetization reversal is initiated [Gutfleisch et al, 2011, Woodcock et al, 2012b, Dempsey et al, 2013]. As a result, a significantly reduced amount of Dy is required, which in turn allows the fabrication of high ${}_iH_c$ magnets with a minimized loss of saturation magnetization.

3.3.7.5 Gallium

Gallium has been found to increase the ${}_iH_c$ and the thermal stability of the resultant NdFeB magnet at the expense of a small loss in B_r [Tokunaga et al, 1987]. Ga additions have been identified as a beneficial addition to hot deformed magnet compositions [Leonowicz et al, 1994]. When 0.5 at% of Ga is added, an increase in both ${}_iH_c$ and B_r has been reported as it appears to substitute REEs in the matrix phase as well as forming phases in the grain boundary [Brown et al, 2004; Grieb et al, 1991].

3.3.7.6 Niobium

The addition of small amounts of niobium has been found to be beneficial to the $_iH_c$ and loop shape of NdFeB magnets [Xiao et al, 1987; Rodewald et al, 1989]. In addition, latter studies showed that B_r and $(BH)_{max}$ were also increased when niobium was added to NdFeB magnets processed by hot pressing [Jun et al, 2012]. Niobium has been also found to improve the corrosion resistance of NdFeB magnets when added in conjunction with copper, achieving fairly good magnetic properties [Zhang et al, 2014].

3.3.7.7 Terbium

Small additions of the HREE element terbium are shown to increase the $_iH_c$ at the expense of B_r and $(BH)_{max}$ [Pan et al, 2010; Lukin et al, 2013]. The increase in $_iH_c$ has been attributed to an increase in the anisotropy of non-perfect grains [Pan et al, 2010]. Terbium is found within the matrix phase substituting other REEs [Lukin et al, 2013]. As it has the second highest T_c [Thoburn et al, 1958] within the rare earth series, only exceeded my gadolinium, Tb is added to NdFeB magnets in order to increase this parameter and, hence, its potential applications.

3.3.8 Powder Blending

Since the appearance of NdFeB magnets processed using the powder metallurgy route, a wide range of elements have been added to standard compositions in an attempt to modify, amongst others, the magnetic properties. Most techniques involve melting all the elemental components into an alloy of the desired composition and start to work it onwards.

However, mixing standard compositions with added elements can be done at a different stage of the process. Therefore, a number of authors have used powder blending techniques instead of melting mixing techniques. Some studies have powder blended stoichiometric $Nd_2Fe_{14}B$ powders with HD powders compositionally equivalent to the liquid phase during sintering [Otsuki et al, 1990; Hong et al, 1995], whereas others have powder blended stoichiometric $Nd_2Fe_{14}B$ powders with HD powders rich in Nd content [Alander et al, 1994]. In addition, some authors have produced magnets by blending

near stoichiometric $Nd_2Fe_{14}B$ powders with a wide range of low melting point elements [Fernengel et al, 1995; Velicescu, 1998].

A range of master alloys have been blended with elemental Al, Co and Cu [Mottram et al, 2001a; Mottram et al, 2000a; Mottram et al, 2000b; Mottram et al, 2000c] as well as with Nd and Dy, in hydride form, powders [Mottram et al, 1998b; Mottram et al, 1999; Mottram et al, 2000a; Davies et al, 2001]. These studies showed that an exact adjustment of the final magnet composition is achievable with powder blending as well as the modification of the GBP and the magnetic properties.

3.3.9 Oxidation and Corrosion

NdFeB magnets are very susceptible to corrosion and oxidation. The reaction of NdFeB-type materials at temperature and in humid air have been shown to be significantly different. In humid air the reaction occurs mainly in the Nd-rich GBP due to galvanic corrosion between the phases present in the NdFeB system. Higher and drier temperatures in the range from 335 °C to 500 °C result in the formation of a dark grey surface layer and reaction zone.

3.3.9.1 Oxidation

The oxidation behaviour of NdFeB magnets is determined by a number of factors including composition, temperature, surface finish and material form either bulk or powder.

Edgley et al [1997] investigated the oxidation behaviour of $Nd_{16.4}Fe_{75.7}B_{7.9}$ commercial sintered magnets by exposing them to either a pure oxygen atmosphere at up to 500 °C or to air at from 350 °C to 600 °C. Figure 42 shows the different oxide products formed depending on the temperature at which the material oxidised. It was found that the $Nd_2Fe_{14}B$ phase dissociates into a mosaic of α-Fe nanocrystals with small precipitates of Nd oxides and undetermined compounds of boron. It was also found that the Nd-rich GBP oxidises to form Nd_2O_3 and that there is no observable change in the composition of the boron rich $Nd_{1+\varepsilon}Fe_4B_4$ phase. The products of the reaction, which were shown to be Fe_2O_3, NdO and Nd_2O_3, form an adherent grey layer which grows transgranularly into the magnet.

$T < 500°C$

$Nd_2Fe_{14}B \rightarrow \alpha\text{-}Fe + Nd_2O_3 \rightarrow Fe_2O_3 + Nd_2O_3$

$Nd\text{-rich } (NdO_x) \rightarrow c\text{-}Nd_2O_3 \rightarrow c\text{-}Nd_2O_3$

$Nd_{1.1}Fe_4B_4 \rightarrow Nd_{1.1}Fe_4B_4 \rightarrow Nd_{1.1}Fe_4B_4$

$T > 500°C$

$Nd_2Fe_{14}B \rightarrow \alpha\text{-}Fe + Nd_2O_3 \rightarrow Fe_2O_3 + FeNdO_3$

$Nd\text{-rich } (NdO_x) \rightarrow NdO_x \rightarrow c\text{-}Nd_2O_3$

$Nd_{1.1}Fe_4B_4 \rightarrow Nd_{1.1}Fe_4B_4 \rightarrow ?$

Figure 42. Chemical reactions observed in the oxidation of NdFeB above and below 500 °C of a $Nd_{16.4}Fe_{75.7}B_{7.9}$ alloy [Edgley, 1997]

Li et al [2003] investigated the high temperature oxidation of NdFeB magnets in the range of 335 – 500 °C. Their work showed that oxidation resulted in the formation of external scales of Fe_2O_3 and Fe_3O_4, with the principal degradation being the formation of an internal oxidation zone, in accordance with previous results by Edgley et al [1997]. This zone was shown to increase parabolically with time and comprises an α-Fe matrix containing a dispersion of NdO particles.

When NdFeB alloys are in powder form, oxidation is observed at an accelerated rate compared to solid materials due to the larger surface area that is exposed to air and that oxygen can react with [Higgins et al, 1987; Skulj et al,2006].

Lien et al [1995] showed that the milling stage causes a dramatic increase in the oxygen content as can be observed in figure 43. Namkung et al [2011] reported the oxygen content to increase by up to 4400 ppm as a result of jet milling.

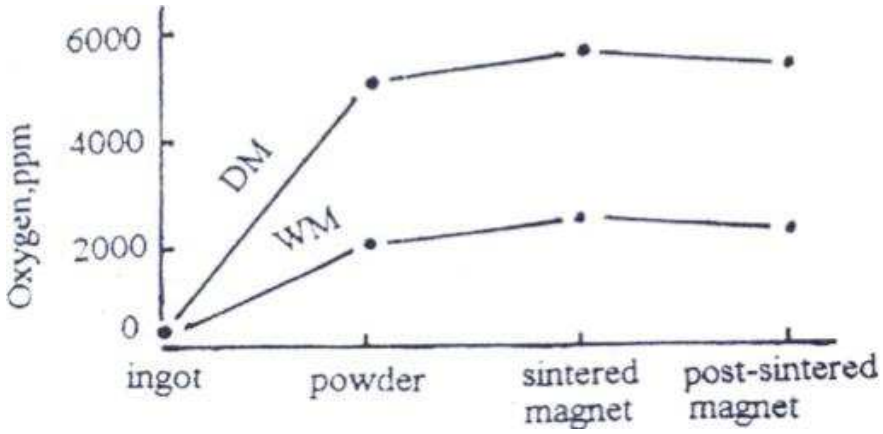

Figure 43. Oxygen content during various stages in the processing of a sintered NdFeB permanent magnet; where DM denotes dry milling under argon and WM refers to wet milling with toluene [Lian et al, 1995].

3.3.9.2 Corrosion

The corrosion mechanism for NdFeB magnets is shown in figure 44 and follows these equations [Katter et al, 2001]:

$$2\,Nd + 3\,H_2O \rightarrow NdH_3 + Nd(OH)_3 \qquad \text{Equation 13}$$

$$NdH_3 + 3\,H_2O \rightarrow 3\,H_2 + Nd(OH)_3 \qquad \text{Equation 14}$$

$$Nd + \frac{3}{2}\,H_2 \rightarrow NdH_3 \qquad \text{Equation 15}$$

Equations 13 and 14 illustrate the reaction between the GBP and water. The products of these reactions are neodymium hydroxide and hydrogen, with the latter reacting according to equation 15 with the Nd-rich phase to form neodymium hydride. Neodymium hydride is not stable under these conditions and decomposes again into neodymium hydroxide and hydrogen according to equation 14 and the whole sequence starts again. The effect of this conversion of the Nd-rich phase into neodymium hydroxide causes a strong volume increase in the GBP what results in cracks along it and the matrix grains may be pulled-out.

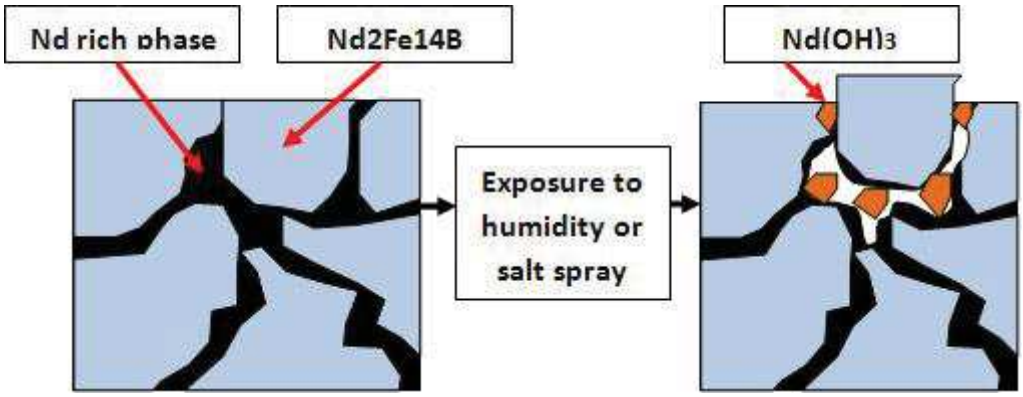

Figure 44. Corrosion mechanism for NdFeB permanent magnets. Image from http://www.emcoatingsuk.co.uk/1000-hour-salt-spray-resistance-of-rare-earth-magnets/ Accessed 27/10/2016

Hydrogen has been found to accelerate the corrosion of HD powders in humid media [Chun-lin et al, 2004]. The hydrogen in the HD powder bonds with water, hence facilitating the electrochemical corrosion which is accelerated by the defects caused by hydrogen in the surface of HD powder.

The corrosion of NdFeB can be limited or prevented by a combination of techniques whose target is to modify the grain boundaries to enhance the corrosion resistance of the magnets. Previous works [Madaah Hosseini et al, 2006; Bala et al, 1997; Yu et al, 2004; Ni et al, 2014a; Isotahdon et al, 2012; Hu et al, 2013] showed that the additions of alloying elements, such as Al, Co, Cu, Ni, Nb and Sn amongst others, to the basic composition can improve the corrosion resistance. But this method is possibly accompanied by a reduction in magnetic performance due to the magnetic dilution effect that originates from the dissolution of alloying elements in the matrix phase. Hence the grain boundary optimization to control alloying-element distributions is required, which can be achieved by post-sinter annealing at 420 °C, 520 °C and 620 °C [Ni et al, 2014b]; this results in greatly improved corrosion resistance.

Corrosion can also be limited by the addition of a barrier coating. Some of these coatings are Au, Ag, Ni, Ni-Cr, Ni-Cu, Ni-Cu-Ni, Ni-TiN and Zn; where each coating has its own advantages and disadvantages [Man et al, 1996].

Chapter 4. Literature Review II: Recycling of NdFeB

4.1 Recycling of NdFeB Permanent Magnets

4.1.1 Introduction to the Recycling of Rare Earth Elements

Recycling and the recovery of REEs can mitigate some of the supply risks described in Chapter 1 and minimise some of the environmental impacts of mining and processing activities of REEs. Jones et al [2011] distinguished, as shown in figure 45, between (1) direct recycling of pre-consumer manufacturing REE scrap and residues [Binnemans et al, 2013b]; (2) urban mining of post-consumer EOL products [Schüler et al., 2011; Hitachi, 2013]; and (3) landfill mining of urban and industrial waste residues containing REEs [Jones et al., 2012].

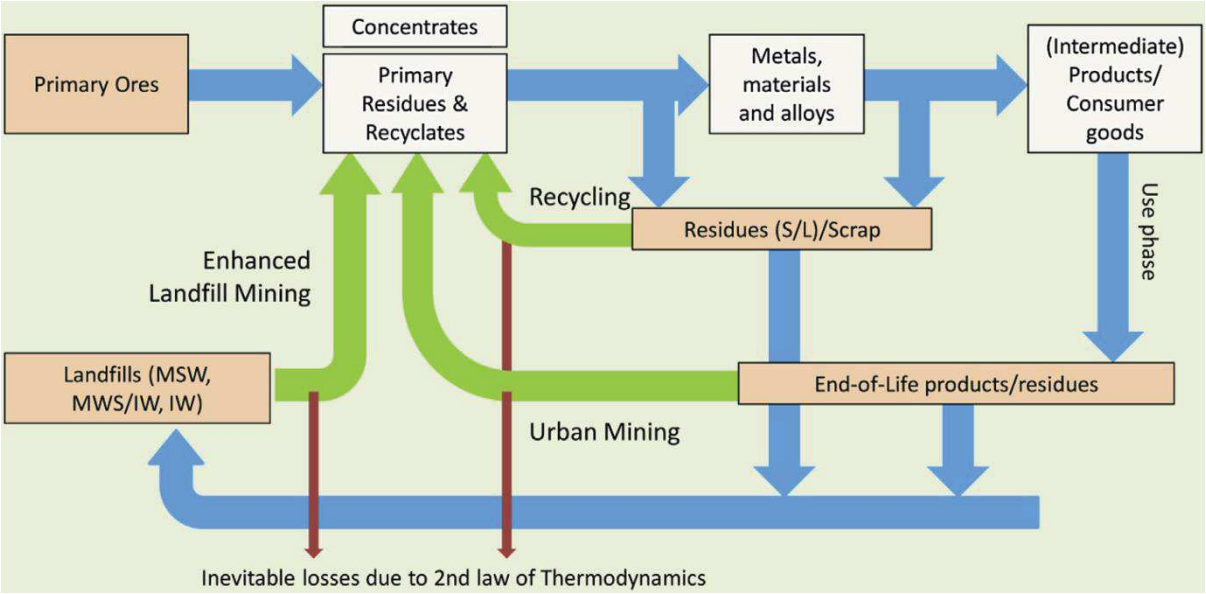

Figure 45. Flowsheet of REEs recycling [Binnemans et al, 2013a].

In reality, commercial recycling of REEs is still in its infancy, less than 1% of the REEs were being recycled in 2011, despite significant research effort [Meyer and Bras, 2011; Tanaka et al., 2013; Anderson et al., 2012]. This is mainly due to inefficient collection, technological difficulties and, a lack of incentives [Graedel et al., 2011; Reck et al, 2012; ERECON, 2015]. An improvement in EOL recycling rates is a necessity but can only be achieved by developing integrated recycling routes.

Recycling of REEs is important to guarantee a supply of these critical raw materials. In addition, recycling is important because of the so-called "balance problem" [Falconnet, 1985]. The demand and supply of the individual REEs have to be equal at any time; otherwise there will be shortages or excesses. The REEs occur in different ratios, reflecting the natural unequal abundance of the elements. The balance problem evidences that recycling is becoming an issue even for countries with consolidated primary REEs mining such as China [Xu and Peng, 2009].

4.1.2 Direct Re-Use of NdFeB Magnets

The first, and most obvious, approach to recycling NdFeB magnets is direct re-use of the EOL magnets in their present size and shape. However, this option is only possible for magnets which are large and easy to access as those used in wind turbines and some electric motors and generators. The magnets used in such applications are expected to be in service for long periods, meaning that they have a slow turnover, and are not available in great quantities in scrap at the moment. As a consequence of such a long lifespan of the magnets in these applications, it is possible that once they are no longer in operation newer magnets will be economically more worthwhile due to an enhancement in the overall performance compared to the EOL magnet. In addition, current NdFeB permanent magnets used in the as-mentioned applications are frequently difficult to extract. An effort to develop strategies based on Design-for-Reuse to be implemented in the manufacture of NdFeB permanent magnets is required.

4.1.3 Electronic Waste

HDDs have been identified as one of the most abundant and readily available forms of WEEE scrap containing NdFeB [Sprecher et al., 2014a; Walton et al., 2015]. However, NdFeB magnets can also be found in loudspeakers and mobile phones amongst others. In HDDs, they are easy to identify and have a rapid turnover at about 5 years. Each 2½ inch HDD, mainly in laptops, contains 2.5 g of NdFeB whereas each 3½ inch HDD, mainly in desktop PCs, contains between 10 and 20 g [Walton et al.,

2015; Sprecher et al., 2014a]. In addition, around 550 million units are produced annually and this amount is expected to keep stable in the near future [Sprecher et al., 2014a].

There are two magnets in a HDD: a resin bonded magnet in the spindle motor which spins the disk and a sintered magnet in the voice coil motor (VCM) which controls the read head over the disk. The VCM magnets are nickel coated and glued into a soft magnetic assembly, as shown in figure 46.

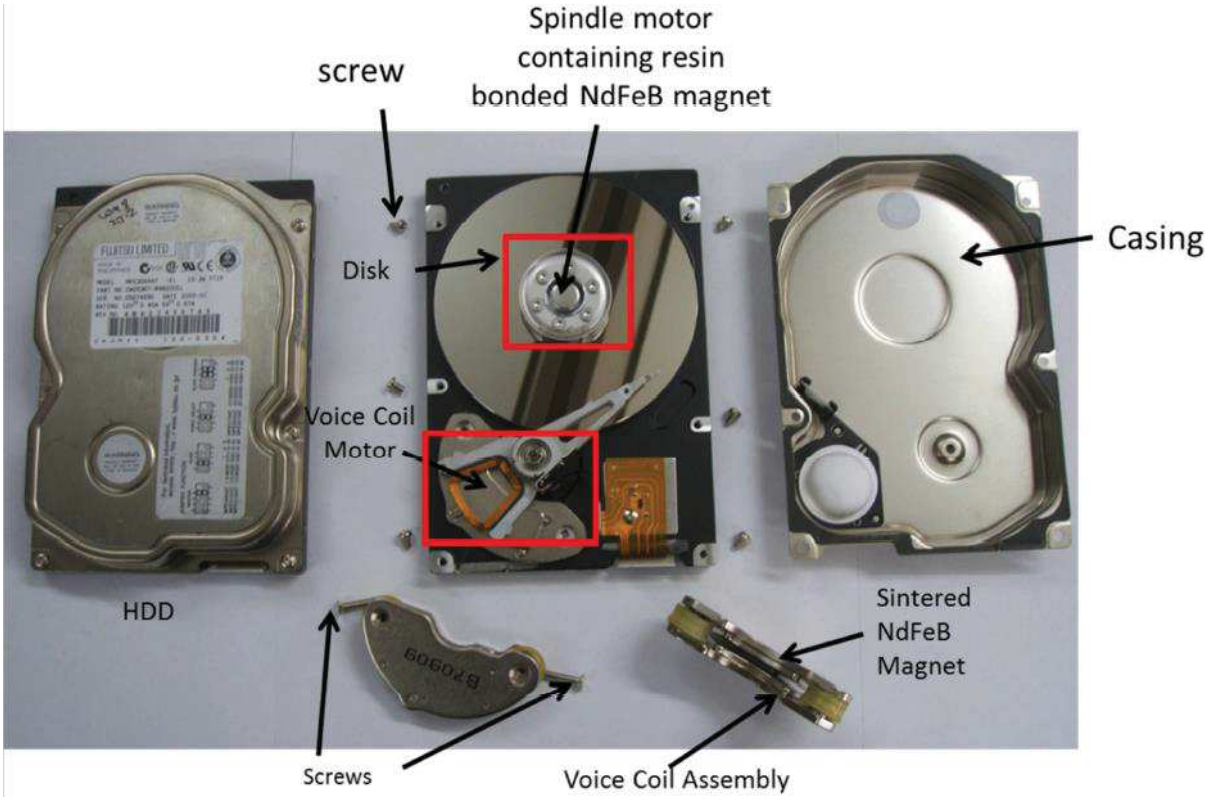

Figure 46. Manually disassembled HDD containing a resin bonded NdFeB magnet and two sintered NdFeB magnets [Walton et al, 2015]

Most scrap HDDs are presently shredded to destroy the data present on the disk. Resulting from the fact that NdFeB permanent magnets are brittle, they break up into pieces which are still magnetic. Such pieces then stick to the other ferrous waste making separation a difficult operation. There are several challenges when attempting to recycle EOL NdFeB magnets, including the identification and collection of devices, the identification of NdFeB magnets within the scrap and the separation of the identified magnets from the waste.

Nevertheless, large scale industrial plants for the recovery of REEs from WEEE are scarce [Vander Hoogerstraete, 2014]. Hitachi developed a process able to dismantle and recover NdFeB magnets on HDDs and compressors of air conditioners [Hitachi, 2010; Hitachi, 2013]. The recovery machine for HDDs consists of a drum unit which spins and shakes the HDDs to loosen the casing screws. Then, the magnetic components are extracted separately from the machine and the NdFeB containing desired parts can be picked up by hand.

Santoku Corporation has also begun a recycling line in order to chemically extract and separate individually valuable elements from NdFeB magnet [Kamiyoshi et al, 2012, Kaneko et al, 2007]. The magnets are first crushed and grinded into particles smaller than 75 μm. This powder is oxidised at high temperature prior selective leaching and individual separation by solvent extraction (SX).

4.1.4 Hydrometallurgy

The traditional route used for recovery of REEs from permanent magnets is via hydrometallurgy of pre-consumer production scrap in sintered permanent magnets production [Ellis et al, 1994; Bounds, 1994]. The process begins with the dissolution of the rare earth scrap using HNO_3, H_2SO_4 or HCI in aqueous solution. The insoluble fraction is removed by filtration and a complete separation of all elements can be accomplished by using SX or ion exchange technology which are both currently used in producing the REOs from natural ores. The REEs are then precipitated from solution as double sulphates, oxalates or fluorides. The leaching solution must contain only rare earth elements and so, unwanted elements, such as nickel and copper from the coating of the magnets, are present in these precipitates, further separation is required [Binnemans et al, 2013a]. The main disadvantages of this process are firstly its need of great amounts of chemicals to occur and secondly that for the recycling of NdFeB magnets, they have to be converted into oxides, chlorides or fluorides; before being reduced back to the metal form.

To separate REEs from NdFeB magnet scrap, the US Bureau of Mines developed a technique which involves dissolution of the scrap magnet in H_2SO_4 prior to precipitation using NH_4OH [Lyman et al,

1992; Ellis et al, 1994]. This creates a strong acidic solution to which NaOH or KOH is added to form a neodymium alkali or ammonium salt sulphate; which can be converted to NdF_3 by leaching in HF acid solution and then calciothermically reduced to the metallic state. In this process, iron remains in the solutions and is removed after treatment of the solution.

An alternative approach of recycling NdFeB magnets is the production of a Nd-Fe master alloy that can be further used to produce new magnets. In this process, the NdFeB scrap magnet is dissolved in HNO_3 and HF is added to form a neodymium-iron fluoride double salt; which is then dried and calciothermically reduced to the metallic state [Ellis et al, 1994].

Ionic liquids (ILs) offer a large potential for increasing the efficiency of SX processes, which includes the extraction of REEs [Riaño et al, 2015; Binnemans, 2007]. ILs are solvents, which consist entirely of ions and have unique properties such as an intrinsic electric conductivity and a very low vapour pressure. In spite of most extraction tests have been conducted at a very small laboratory scale, large scale IL extraction processing has been demonstrated to be feasible [Wellens et al, 2012].

4.1.5 Pyrometallurgy

Pyrometallurgy processes have emerged as an alternative to the hydrometallurgical recycling routes for REEs. Four pyrometallurgical routes to treat REE alloys are currently used, namely (1) direct melting, in which REE alloys are remelted; (2) liquid metal extraction, in which the REEs are separated from the transition metals in the metallic state; (3) electroslag refining and (4) glass slag method; being these two latest processes the most suitable routes to recycle scrap NdFeB magnets.

4.1.5.1 Electroslag Refining

Electroslag refining is a viable processing for the recovery of scrap if the material to be recycled is in relatively large clean pieces [Ellis et al, 1994]. In this process, scrap material is melted either by addition to a molten bath or as a consumable electrode [Schmidt et al, 1992]. The process involves the contact between the NdFeB scrap alloy and a suitable flux, which is a prefused $CaCl_2$ or CaF_2

compound, whose aim is to remove impurities such as, O, H, N, Li, Na, Al and Si to produce a contaminant-free rare earth fluoride salt. This process cannot be used to separate REEs, so it produces an alloy which is dependent on the input feed. The main drawback of these techniques is that they are not effective on swarf scrap because of high contamination and fine particulate nature.

In the case of consumable electrode, the scrap is melted from the electrode and the molten material passes through a slag layer and into a shallow molten pool where it is quickly directionally solidified thanks to a water cooled crucible, as seen in figure 47. As the molten material passes through the slag layer, the impurities become entrained on it, hence removing them definitely.

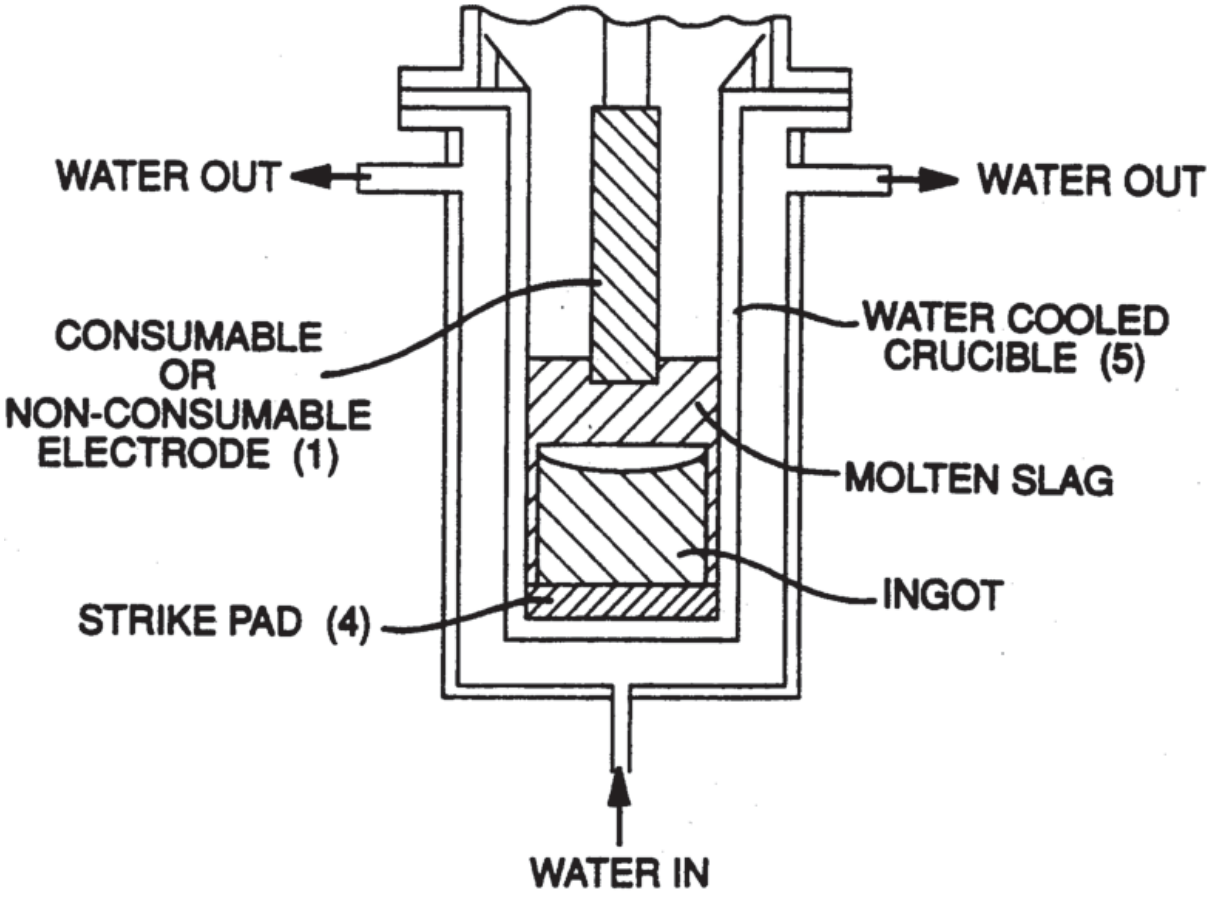

Figure 47. Schematic consumable/non-consumable electrode type electroslag refining apparatus during the melting operation [Schmidt et al, 1992].

In the case of adding the NdFeB scrap material to a molten bath, the process is similar, in which a slag is used, although the material has to be held molten for enough time to allow impurities to react with

the slag. After some time, the metal is poured from the crucible in to a water cooled mould, where the scrap solidifies directionally.

4.1.5.2 Liquid Metal Extraction

The liquid metal extraction process was developed to overcome the difficulties of both and electroslag refining and hydrometallurgical processing, so it would be able to handle a variety of scrap feed material to produce a low contaminated material avoiding the final reduction step from an inorganic compound to a metal [Ellis et al, 1994]. The liquid metal extraction process lies in the selective dissolution of the rare earth alloy by a liquid alloy in which the rare earths and transition metals allocate themselves between two immiscible liquid metal phases.

The Ames Laboratory has developed a process to recycle the REEs from NdFeB alloys [Xu et al., 2000; Xu, 1999]. Each type of rare earth scrap will require a different liquid alloy system to separate the REEs from the transition metals depending on the miscibility of each element with the alloy system. Neodymium can be recycled using molten magnesium over crushed NdFeB particles or by immersing the crushed NdFeB in liquid magnesium. After separation, neodymium can be extracted from magnesium via vacuum distillation of magnesium.

This process has not been commercialised yet because it cannot be applied to fully or partially oxidised NdFeB scrap and because the process is moderately slow as it takes between 24 hours and 72 hours. However, Japanese researchers have further advanced the magnesium extraction method to a continuous extraction process which is a great step further [Takeda et al., 2006; Okabe et al., 2003a, 2003b].

Silver can also be used instead of magnesium for the extraction of Nd from NdFeB scrap magnets [Takeda et al., 2004]. Silver can dissolve neodymium but not iron. Furthermore, neodymium can be separated from silver by oxidation as Nd_2O_3 is not soluble in silver. Although being more expensive than magnesium, silver can be easily recycled and re-used, hence being an interesting industrial choice.

4.1.5.3 Glass Slag Method

In the glass slag method, the scrap magnet is placed in contact with a molten agent that selectively dissolves the REEs from the alloy and tends to supercool to a glass. Saito et al [2003] successfully extracted neodymium from NdFeB alloys. It was achieved by the reaction of the NdFeB alloy with molten boron trioxide, leaving α-Fe and ferroboron behind with a neodymium content of less than 0.01 wt%. Neodymium can be regained from the boron trioxide glass slag by dissolving the glass slag in sulfuric acid followed by selective precipitation of neodymium as a double sulphate salt or a hydroxide [Saito et al, 2006]. The main drawback of this process is the large amount of inorganic waste generated [Satio et al, 2003].

4.1.5.4 Direct Melting

NdFeB magnets can also be recycled by direct melting the scrap alloy in a furnace into a new alloy. However, this technique is problematic as a consequence of the oxygen and carbon presence in the scrap. The oxygen will result in slag formation and carbon will decrease the magnetic performance of the alloy. To remove carbon, the scrap needs to be decarburised by heating so the carbon forms carbon dioxide, whereas for the removal of oxygen the scrap needs to be deoxidised by heating in hydrogen followed by calciothermic reduction [Asabe et al, 2001; Saguchi et al., 2002; Saguchi et al, 2006; Suzuki et al., 2001; Saguchi et al, 2014]. The final content of oxygen and carbon in the reduced metal can be below 0.1 wt% and 0.001 wt% respectively [Saguchi et al, 2006; Saguchi et al, 2014].

NdFeB magnets can also be recycled using melt spinning, in which the melted metal is rapidly cooled by pouring it on a water cooled rotating wheel producing thin ribbons which can be later re-used in NdFeB magnet production [Itoh et al., 2004a, 2004b].

4.1.6 Hydrogen Processing

The first description for the use of the HD process for re-processing of sintered NdFeB was initially proposed by Rivoirard et al [2000]. They used hydrogen to break down a demagnetised uncoated

magnet into powder which was later heated under vacuum to desorb the hydrogen and finally annealed to recover the magnetic properties. The resultant powder was anisotropic and, therefore, usable in the production of resin bonded magnets.

Walton et al. [2012, 2015] showed that by processing VCM assemblies or sections of HDDs in hydrogen it is possible to break the magnets down into friable, demagnetised, hydrogenated NdFeB powder in the Hydrogen Processing of Magnet Scrap (HPMS) process. In doing so, the HD powder can be recovered without the need to shred or disassemble the HDDs as previously reported [Harris et al, 2012; Walton et al, 2011; Walton et al, 2012]. After hydrogen processing, the HDDs are rotated in a porous drum for the purpose of liberating the HD NdFeB powder. The collected powder consists of HD NdFeB particles with some small plastic pieces from the HDDs and nickel flakes that were peeled away from the surface of the magnets. By mechanically processing the separated powder using mills and sieves it is possible to reduce the nickel content down to 400 ppm using a 90 μm sieve. At this nickel content, it should be possible to reprocess the magnets in alloy form into a new material avoiding its adverse effect on the re-sintering process.

The recovered HD powder can be re-processed in a number of ways, as presented schematically in figure 48, to finally produce NdFeB magnets, including:

- Refining the HD powder to chemically extract the REEs (Nd, Dy and Pr) for further use in cast alloys.
- Melting and re-casting the powder to form new alloy ingots.
- Milling, aligning, pressing and re-sintering the powder into new magnets.
- Degassing the powder and mixing it with resin prior to pressing into bonded magnets.
- Degassing and melt spinning the powder into ribbons which are then mixed with resin and pressed into bonded magnets.
- HDDR processing of the powder prior to mixing it with resin and pressing into bonded magnets.

This work focuses on the re-sintering route into new NdFeB magnets using the recovered HD powder.

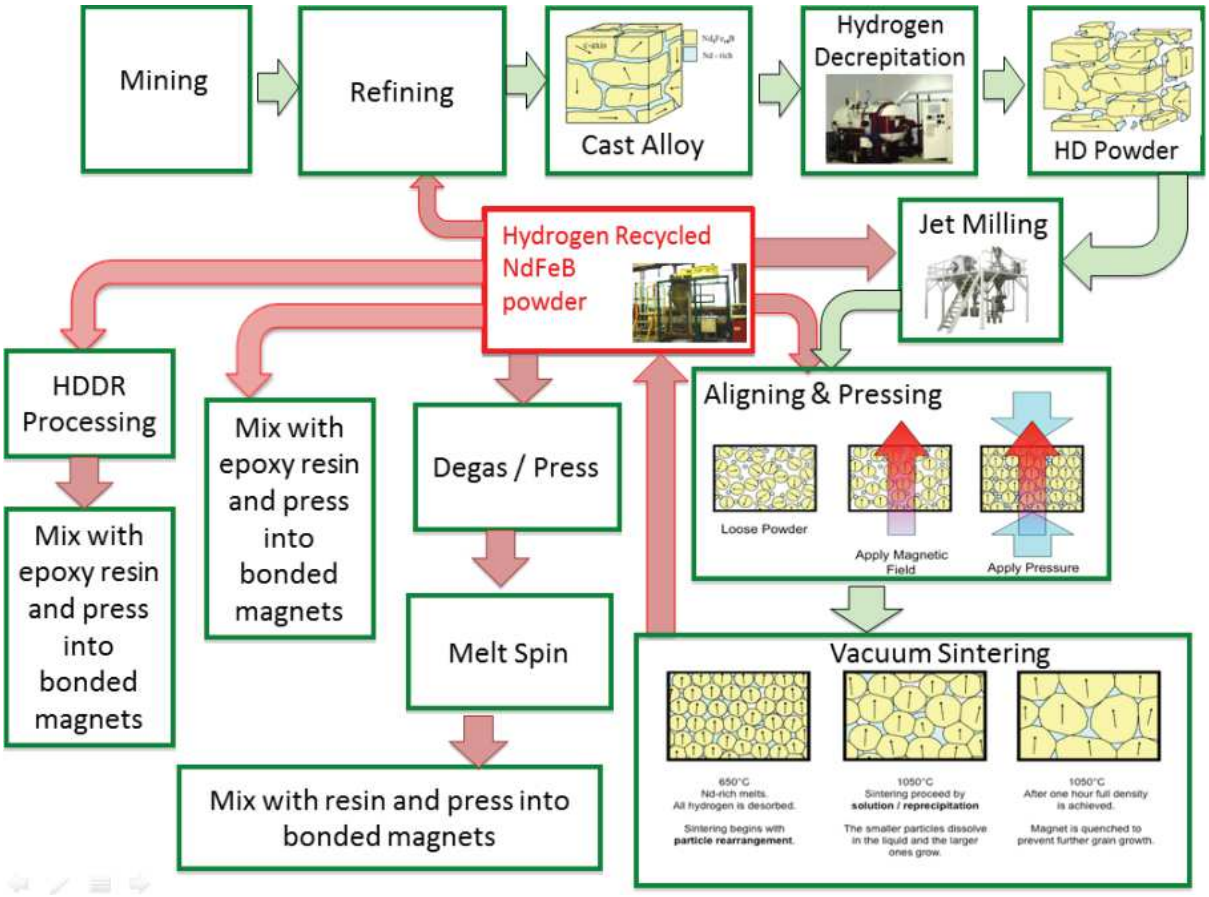

Figure 48. Multiple recycling routes for the hydrogen recycled NdFeB powder [Walton et al, 2012].

4.1.7 Re-Sintering

Previous work has shown that hydrogen can be used to process scrap NdFeB sintered magnets and to re-process this powder into 'new' or recycled magnets by re-sintering [Zakotnik et al, 2006; Zakotnik et al, 2008; Zakotnik et al, 2009; Walton et al, 2015; Li et al, 2015; Liu et al, 2015].

The route proposed by Rivoirard et al [2000] for recycling NdFeB magnets using the hydrogen decrepitation process was further investigated by Zakotnik et al [2006, 2008]. They produced 'new' or recycled fully dense sintered magnets from clean, uncoated blocks of scrap sintered $Nd_{13.98}Pr_{0.06}Dy_{0.63}Fe_{77.81}Nb_{0.36}Al_{0.69}B_{6.44}$. The HD process was found to decrease significantly the magnetic properties, hence requiring vacuum desorption to enhance the magnetic performance when

producing resin bonded magnets. The HD powder was roller ball milled for 0, 0.5, 1 and 20 h, before aligning, pressing and vacuum sintering at 1030, 1080 and 1130 °C for 1 hour. The remanence and maximum energy product were found to increase with increasing milling time and sintering temperature whereas the intrinsic coercivity exhibited a maximum when sintered at 1080 °C. The demagnetisation loop of the starting material and the best recycled magnet are shown in figure 49, where the recycled magnet exhibited a decrease in the maximum energy product, remanence and intrinsic coercivity of 15 %, 10 % and 20 %, respectively, as a result of adverse effects of oxidation.

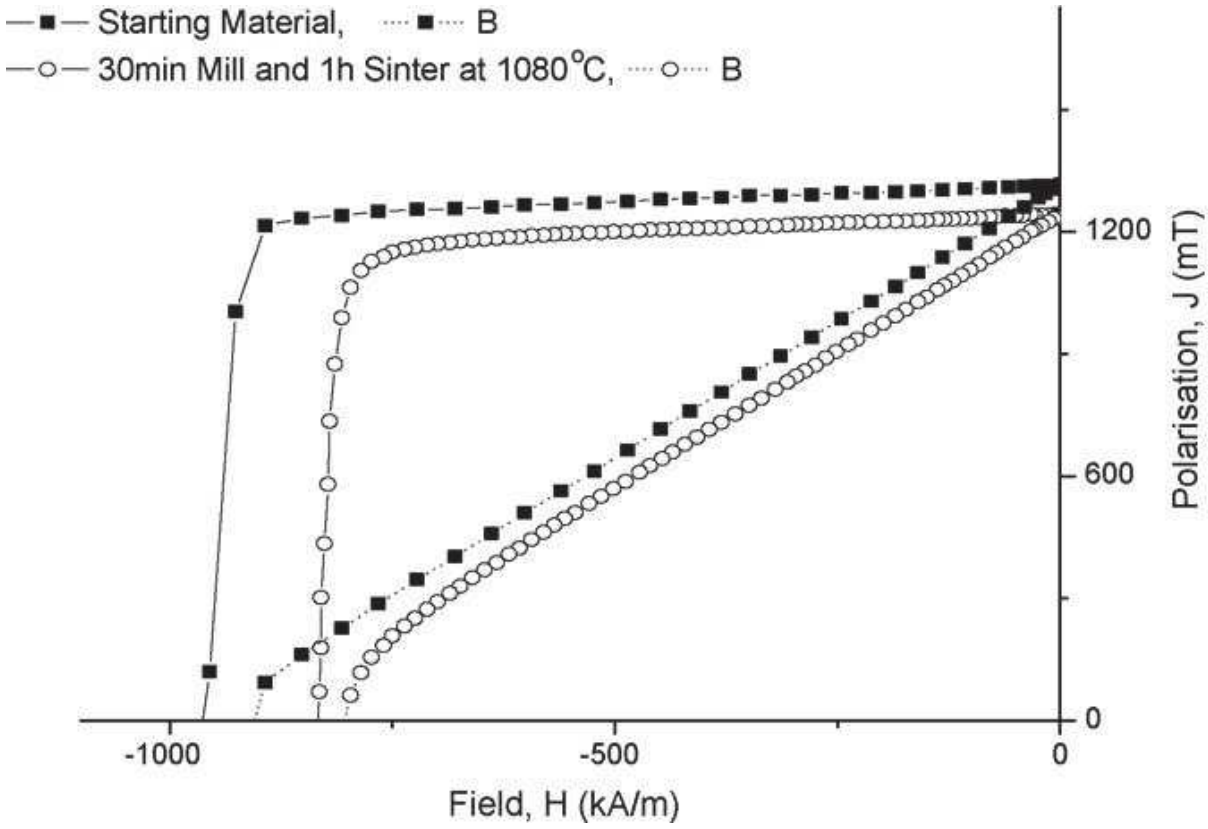

Figure 49. Demagnetisation curves for the starting sintered magnet and its best recycled magnet [Zakotnik et al, 2006].

The best recycled magnet was produced by roller milling the HD powder for 0.5 h, followed by aligning, isostatic pressing and vacuum sintering at 1080 °C for 1 h. The microstructures of both the starting material and the recycled material at optimum conditions are shown in figure 50. The recycled

magnet exhibited an increased grain size compared with that of the initial magnet and evidence of porosity, which is consistent with the decrease in the magnetic properties.

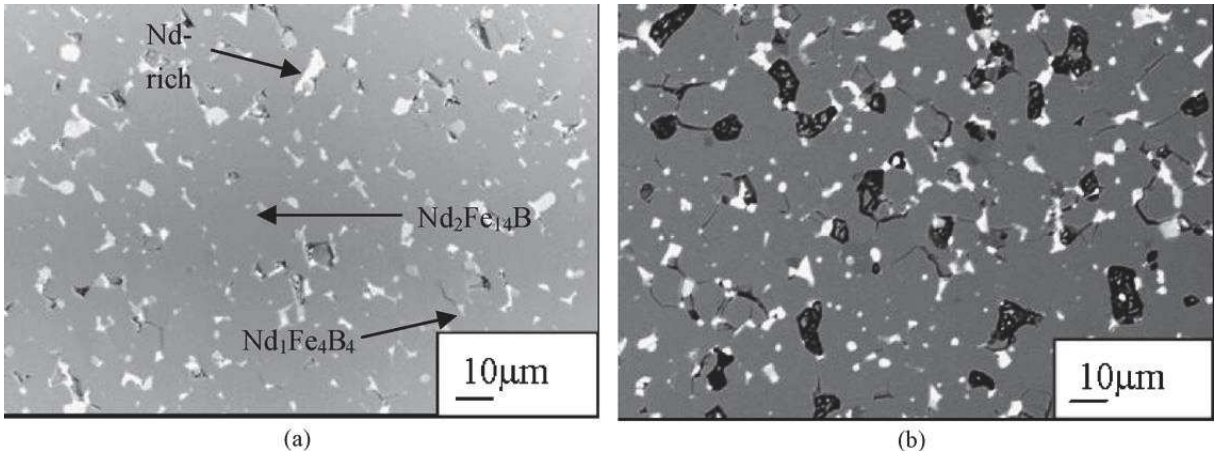

Figure 50. Back-scattered electron images showing (a) the starting material and (b) the recycled magnet produced by HD, followed by 0.5 h roller ball milling, aligning, pressing and sintering at 1080 °C for 1 h [Zakotnik et al, 2008].

Further studies by Zakotnik et al [2009] determined the effect of multiple re-sintering cycles on VCM magnets from HDDs of initial composition $Nd_{13.78}Dy_{0.66}B_{6.30}Al_{0.76}Fe_{75.51}C_{0.32}O_{1.84}$. After each cycle the magnet was broken down in hydrogen and reprocessed again using the same conditions, namely, HD at 1 bar and roller ball milling for 0.5 h, before aligning, pressing and vacuum sintering at 1080 °C for 1 h. It was found that recycling resulted in a marked reduction in the loop squareness as well as in intrinsic coercivity and remanence as can be seen in figure 51(a). This was accompanied by a fall in density indicating incomplete sintering. During the sintering process for the primary production of NdFeB magnets, the Nd-rich GBP melts resulting in LPS. When sintered material is used as the feedstock then the GBP has a higher oxygen content and therefore it does not all melt during re-sintering, resulting in a lower density magnet and a reduction in magnetic performance.

To overcome this problem previous work showed that the addition of neodymium in hydride form by powder blending effectively increased the magnetic properties of the sintered magnet [Mottram et al, 1999]. Metal hydrides have several advantages over the use of pure metals: (1) expansion of the lattice during hydrogenation assists in the breaking up of the bulk into smaller particles; (2) hydrides are

brittle and readily milled; (3) rare earth hydride powders are more stable than corresponding metal form, reducing oxygen uptake during processing; (4) high reactivity after hydrogen removal aid alloying; and (5) hydrogen presence can enhance solid state diffusion.

The neodymium was hydrided at 8 bar at room temperature before ball milled for 40 h; whereas the $Nd_{13}Fe_{80.5}B_{6.5}$ alloy was decrepitated at 10 bar before ball milled for 20 h. Both were blended, aligned, pressed and sintered at 1070 °C for 1 h. It was found that by blending the alloy with neodymium hydride full density was achieved at lower temperatures (1070 °C) compared with the unblended sintered magnets (1130 °C). The intrinsic coercivity of the magnets blended with neodymium hydride was higher than that exhibited by the unblended sintered magnets, which was attributed to improved magnetic isolation of the $Nd_2Fe_{14}B$ grains as a result of the increased proportion of Nd-rich phase. The remanence, however, was lower than that observed in unblended magnets with very similar composition produced by conventional processing.

Zakotnik et al [2009] investigated the effect of blending 1 at% of neodymium hydride after every cycle after the first cycle of re-sintering, i.e. after the first, second and third cycle of re-sintering. In this study, the $NdH_{2.7}$ additions were not added systematically to optimise its use. The beneficial effect of blending on the recovery of intrinsic coercivity after the first cycle was effectively demonstrated as can be observed in figure 51(b). This was suggested to occur by the increase in Nd-rich phase, resulting in an improved magnetic isolation of the grains. The density exhibited very little change over all four cycles, thus indicating complete sintering after each step. The blended magnets showed lower overall grain growth, although the addition of more neodymium in hydride form was expected to encourage grain growth as it melts during LPS. This was attributed to a suitable blend of Nd-rich phase and Nd_2O_3 at the grain boundaries, hence inhibiting the grain growth.

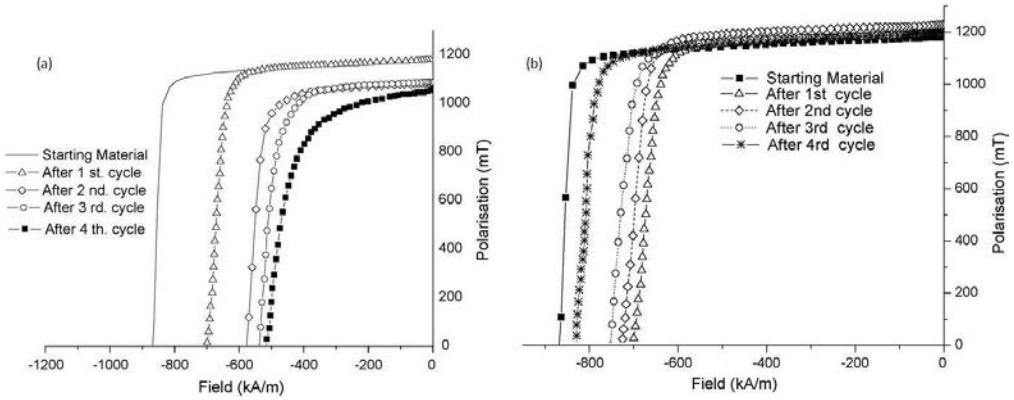

Figure 51. Demagnetisation loops of the magnets cyclically re-sintered (a) neodymium hydride additions and (b) with neodymium hydride additions [Zakotnik et al, 2009].

Zakotnik et al [2015] reported a commercial scale process in which scrap NdFeB magnets from a range of different EOL application were blended with REEs-rich master alloys. The coating of the NdFeB scrap magnets was removed mechanically and the surfaces were chemically cleaned. The REEs-rich alloys were either NdPr or $(Nd_{0.22}Dy_{0.78})(Co_{0.84}Cu_{0.12}Fe_{0.04})_{0.84}$ blended at 1 at% or at 0.5, 2 and 3 at%, respectively. The blended batches were HD at 80 °C and 0.9 bar before jet milling, aligning and pressing, followed by sintering at 1080 °C for 1 h and a post sintering heat treatment at 650 °C for 1 h. The intrinsic coercivity increased above 25% compared with the starting material in every case, reaching 844 kA m^{-1} when a 3 at% $(Nd_{0.22}Dy_{0.78})(Co_{0.84}Cu_{0.12}Fe_{0.04})_{0.84}$ was blended. This increase was at the expense of remanence, although reached a maximum of 1.42 T when a 0.5 at% $(Nd_{0.22}Dy_{0.78})(Co_{0.84}Cu_{0.12}Fe_{0.04})_{0.84}$ was blended.

Kawasaki et al [2003] recycled scrap NdFeB powder from jet milling by blending it with binary $Nd_{80}Fe_{20}$ alloy in different scrap to binary powder ratios, including 100/0, 98/2, 95/5, 90/10; which was aligned, pressed and sintered at 1050 °C, 1100 ° and 1150 °C for 1 and 2 h. It was found that sintering at 1150 °C for 1 h led to better density and magnetic properties than lower sintering temperatures or longer sintering times. With increasing the binary powder content, the intrinsic coercivity increased, which was attributed to the Nd-rich surrounded sufficiently the $Nd_2Fe_{14}B$ phase grains; whereas the remanence increased to reach a maximum and then decreased. The saturation magnetisation decreased due to the magnetic dilution effect with increasing binary powder content.

The best magnet was produced at a scrap powder to binary powder ratio of 90/10 and reached a remanence, intrinsic coercivity and maximum energy product of 1.14 T, 1600 kA m^{-1}, 246 kJ m^{-3}, respectively.

Li et al [2014] reported blending of waste sintered NdFeB magnets with a $(Nd_{20}Dy_{80})_{76}Co_{20}Cu_3Fe_1$ REE-rich alloy, after HD at 150 °C and 1 bar, and ball milling. The blending occurred at different quantities from 0 to 3 wt%, followed by alignment, pressing, sintering at 1130 °C for 1 h and two subsequent post-sintering heat treatments at 900 °C for 3 h and at 515 °C for 2 h. The remanence was found to increase, reaching a maximum at 2 wt% addition followed by a decrease, which was attributed to the Dy-rich content of the addition thus forming $(Dy,Nd)_2Fe_{14}B$, whose saturation magnetisation is lower than in $Nd_2Fe_{14}B$ leading to a decrease in remanence. The intrinsic coercivity rose linearly for all recycled magnets and the magnet recycled with 3 wt% reached higher intrinsic coercivity than that of the starting scrap magnet. The magnet recycled with 2 wt% addition showed a recovery of 97.5%, 92.4%, and 93.1% of remanence, intrinsic coercivity, and maximum energy product of original magnets, respectively.

Li et al [2015] recycled large batches of up to 500 kg of NdFeB scrap magnets by blending it with 24 wt% $Nd_3PrFe_{14}B$ ribbons before HD at 260 °C at 1 bar. The mixture was degassed at 550 °C for 8 h before jet milling, aligning, pressing, sintering at 1043 °C – 1060 °C for 3 h and post-sintering heat treatments at 900 °C for 3 h and at 480 °C for 2h. It was found that, with increasing the sintering temperature, the magnetic properties increased, reaching a maximum at 1058 °C and then decreased. The best magnetic properties of the recycled magnets where obtained when sintering at 1058 °C reaching a remanence, intrinsic coercivity and maximum energy product value of 1.238 T, 1980 kA m^{-1} and 290 kJ m^{-3}.

Liu et al [2015] recycled waste NdFeB sintered magnets by blending dysprosium hydride nanoparticles. The scrap magnets were HD at 150 °C and 1 bar, degassed at 600 °C for 10 h and then blended with 0 to 2 wt% dysprosium hydride nanoparticles, which were prepared by inert gas

condensing method. The blended powders were then aligned, pressed, sintered at 1130 °C for 1 h followed by a post-sintering heat treatment. The blended recycled magnets showed a continuous decrease in remanence and maximum energy product and an increase in intrinsic coercivity with increasing dysprosium hydride content. The best recycled magnets were produced blending 1 wt% dysprosium hydride nanoparticles reaching a recovery in intrinsic coercivity, remanence and maximum energy product of 101.7%, 95.4%, and 88.58%, respectively.

Farr [2013] showed the oxygen average content during various recycling stages, as can be observed in figure 52 including the starting VCM magnets, the HD powder, the burr milled powder and the final re-sintered magnet at 1070 °C for 1 hour.

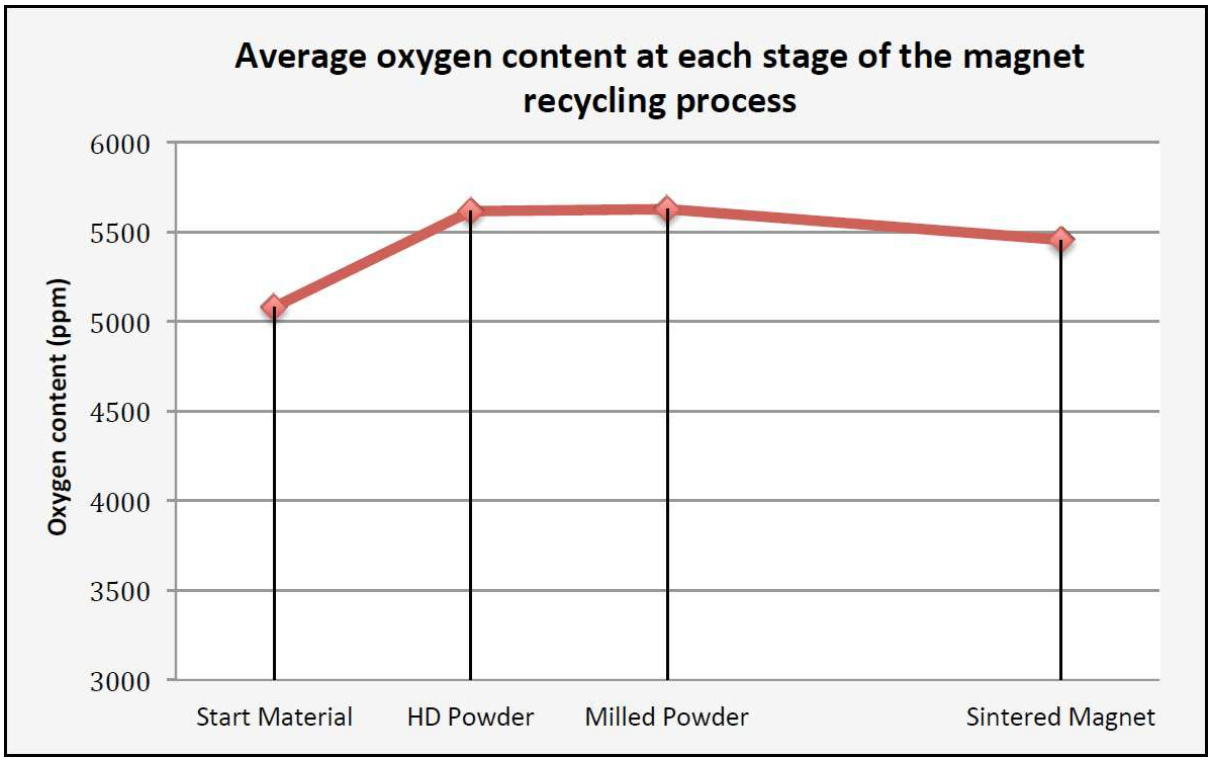

Figure 52. Oxygen content during various stages in the recycling of a sintered NdFeB permanent magnet [Farr, 2013].

The oxygen content increased after HD the VCM magnets, however it remained stable after burr milling and even decreased slightly after aligning, pressing and re-sintering into a new magnet. The stabilization after HD was suggested to be due to most of the Nd-rich phase was already oxidised,

hence being unable to increase the oxygen uptake in further operations. The overall increase in oxygen content for the whole recycling process was shown to be 535 ppm, which is much smaller than the oxygen pick up expected for primary production from a cast NdFeB alloy, typically between 2000 ppm and 5000 ppm [Lian et al, 1995; Namkung et al, 2011].

Sprecher et al [2014b] performed a life cycle assessment (LCA) of the production of primary NdFeB magnets and the production of recycled magnets, using the same route as used in this thesis, to compare them regarding energy consumption and some environmental indicators such as human toxicity and acidification potential. The recycling route includes manual recovery of NdFeB magnets from HDDs, HD, milling, aligning, pressing and sintering. They found that this hydrogen recycling process consumes 88 % less energy compared to the primary production process and scores 98 % lower on human toxicity than the primary production process, because recycling does not include the most polluting processing steps associated with primary production. In addition, compared to the primary production process, recycling scores better as shown in figure 53 as a consequence of the lower energy usage.

name	primary NdFeB magnet, baseline	recycled NdFeB magnet via hand picking	unit
eutrophication potential	1.9-E01	7.7-E03	kg NOx-Eq
acidification potential	0.44	0.027	kg SO_2-Eq
photochemical oxidation (summer smog)	1.7-E02	1.1-E03	kg ethylene-Eq
climate change	27	3.3	kg CO_2-Eq
ionizing radiation	5.1×10^{-08}	2.0×10^{-08}	DALYs
freshwater aquatic ecotoxicity	14	5.3	kg 1,4-DCB-Eq
stratospheric ozone depletion	2.6×10^{-06}	9.3×10^{-08}	kg CFC-11-Eq
human toxicity	150	3.6	kg 1,4-DCB-Eq

Figure 53. Life Cycle Assessment (LCA) results for NdFeB production [Sprecher et al, 2014b].

4.2 Review of Project Aims

The main aim of this research is to increase current available knowledge on the re-processing of sintered NdFeB from EOL scrap sources. This aim can be broken down as follows:

- Study the effect of decreasing the particle size of the hydrogenated NdFeB powder on the magnetic and physical properties of the final magnet and relate this to the microstructure.
- Investigate the systematic addition of neodymium hydride to hydrogenated recycled NdFeB powder on the magnetic properties and microstructure of the final magnet to alleviate the adverse effect of oxidation.
- Investigate separation techniques (wet low-intensity magnetic separation (WLIMS) and hydrocyclone separation) to remove the oxidised grain boundary phase from NdFeB sintered magnets.
- Investigate the use of the NdFeB powder with removed oxygen as a feedstock to prepare recycled sintered magnets.

Ultimately, the main aim of this project is to maximise the magnetic performance of recycled NdFeB magnet by investigating the effect of the manufacturing route and the influence of adding alloying elements.

4.3 Separation Techniques

The main separation processes are listed in figure 54 according to its class and driving force.

Classes of separation processes	Driving force of separation process	Separation processes
Mechanical separations	Gravity Centrifugal force Pressure	Sorting (s – s) Dense-media separation (s – l) Flotation (s – l – g) Sedimentation (s – l) Filtration (s – l) Pressing (s – l) Centrifugation (s – l) Hydrocyclone separation (s – l) Classification Sieving (s – s) Air classification (s – g) Hydraulic classification (s – l)
Membrane separation	Pressure Electrical field Concentration gradient	Ultrafiltration (s – l) Reverse osmosis (hyperfiltration) (s – l) Dialysis (s – l) Electrodialysis (s – l) Electrophoresis (s – l) Permeation (l – l, g – g) Gas diffusion (g – g)
Electrical separation	Electrical field	Electro osmosis (s – l) Electrical dust removal (s – g)
Magnetic separation	Magnetic field	Magnetic separation (s – s, s – l)
Thermal separation	Concentration gradient Temperature gradient	Distillation (l – l) partial condensation (g – g) Absorption (g – g), (A) Adsorption (g – g, s – l), (A) Chromatography (g – g, l – l) Extraction (s – s, l – l), (A) Sublimation (g – g) Crystallization (s – l, l – l) Drying (s – l) Thermal diffusion (g – g, l – l)

Abbreviations: s solid, l liquid, g gas, (A) thermal separation process with auxilliary component.

Figure 54. Summary of separation processes [Sattler et al, 1995].

The separation of substances in a hydrocyclones relies upon the effect of centrifugal forces. Hydrocyclones have many industrial applications such as classification of particles and solid-solid separation. The particle size is the key parameter on the separation of the feed into two streams.

The use of a magnetic field intends the removal of ferromagnetic particles from a feed. In mineral processing, magnetic separation has been widely used in the separation of ferromagnetic particles from liquid suspension. The magnetic behaviour of the particles is the main parameter on this type of separation.

4.3.1 Hydrocyclone Separation

4.3.1.1 Introduction

Hydrocyclones have been in use in industry since the 1940s, although the first patent on this technique appeared in the 19th century [Bretney, 1891]. Because of a simple design, low cost, easy operation, and low maintenance, hydrocyclones have assumed an important role in the separation of solids and liquids. Although hydrocyclones are widely used at present, such as in closed circuit grinding [Casali et al, 1998], desliming [Yalamanchili et al, 1995], liquid clarification [Puprasert et al, 2004], degritting [Murray, 1980], and thickening operations [Yang et al, 2004], the phenomena leading to separation are not fully understood yet.

4.3.1.2 Working Principle

Figure 55 shows a cross-section of a hydrocyclone of conventional design. It comprises a cylindrical stationary section connected to a conical part. The suspension of particles in a liquid is introduced tangentially through the inlet opening in the upper part of the cylindrical section and, as a result, a strong swirling motion is developed in the cyclone. The suspension is then further accelerated in the conical part as a consequence of its geometry. As a consequence of this acceleration; a low-pressure vortex appears in the centre of the hydrocyclone. The fine fraction of particles may migrate into this inner vortex, and exit the hydrocyclone with the overflow stream by an upward swirling flow. The

coarse fraction of particles is removed through the apex of the hydrocyclone by the high-pressure downward swirling flow.

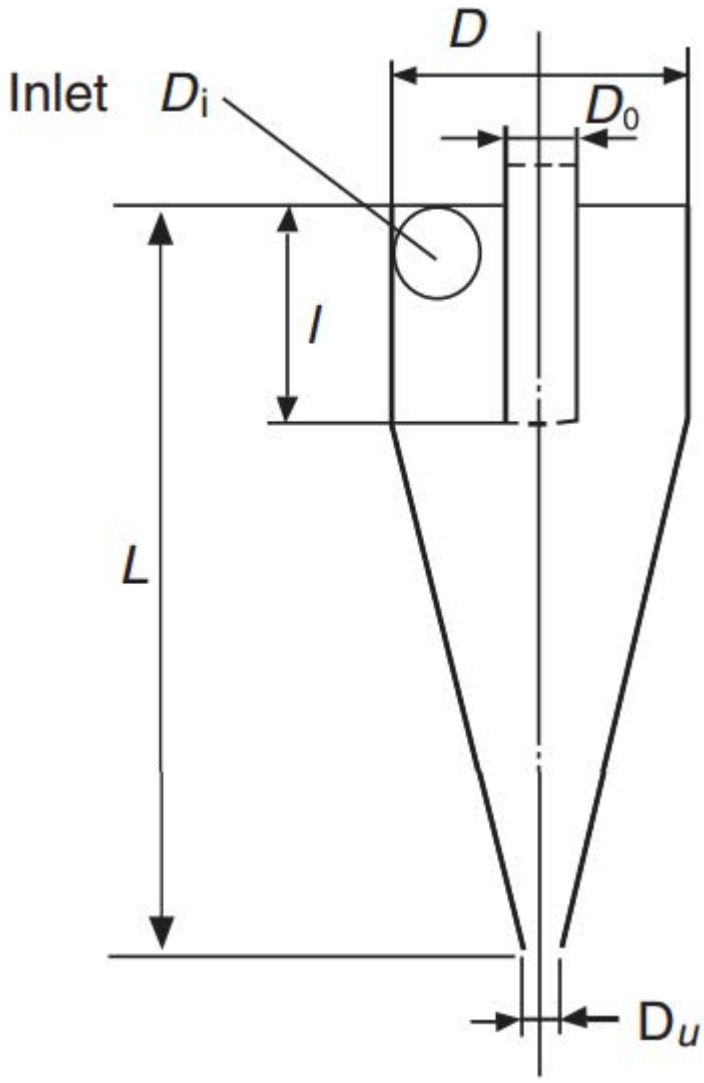

Figure 55. Schematic diagram of a typical hydrocyclone [Svarovsky, 2000].

4.3.1.3 Flow Pattern

As with all separation principles which entail particle dynamics, deep knowledge of the flow pattern in the hydrocyclone is fundamental for optimum design and evaluation of the particle trajectories, as well as for further prediction of the separation efficiency. The flow pattern in a hydrocyclone has circular symmetry, except the region in and around the tangential inlet opening.

Kelsall [1953] performed a classic series of experiments measuring axial and tangential fluid velocity profiles in a hydrocyclone; whereas the radial velocity was calculated by continuity. The velocity profiles are shown in figure 56.

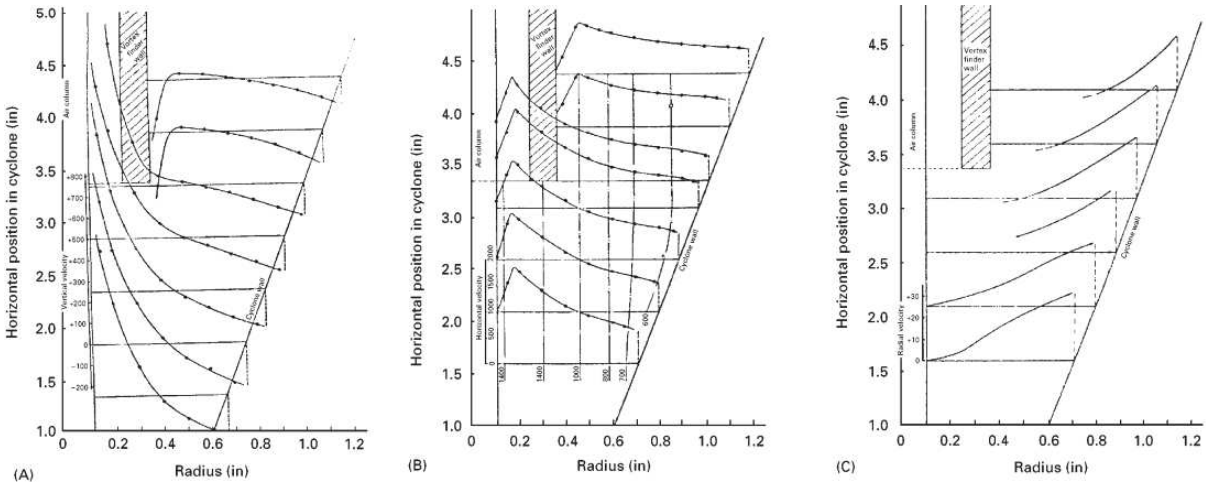

Figure 56. (a) Axial, (b) tangential and (c) radial velocity profiles in a hydrocyclone [Cilliers, 2000].

The axial velocity is negative (downward) near the cone's walls and positive (upward) near the air core, increasing towards the apex. This results in a locus of zero vertical velocity between the two vortices, which roughly follows the profile of the cyclone. Toroidal rotation in the inlet flow and interaction between the vortices result in multiple flow reversals.

The tangential velocity increases toward the axis, reaching a maximum near the air core, thereafter decreasing in a forced vortex region. It is the tangential velocity component that generates the centrifugal force, which separates the coarser particles from the finer ones. The radial velocity, which is two orders of magnitude smaller than the axial or tangential velocities, is directed toward the centre of the cyclone and increases toward the apex.

4.3.1.4 Motion of Particles

When the solid particles enter into the cylindrical section, they can be dispersed radially inwards because of the turbulent flow in the feed sections. Nevertheless, there is very little information about

the behaviour of the liquid in the cylindrical section. Therefore, it is usually treated as a preliminary area while the main separation is thought to occur in the conical section.

The velocity of both the flow and a particle at any point within the cyclone can be separated into three components: namely the tangential velocity; the radial or centrifugal velocity; and the vertical or axial velocity; whereas the forces exerted on a particle are the drag force and the centrifugal force, as shown in figure 57.

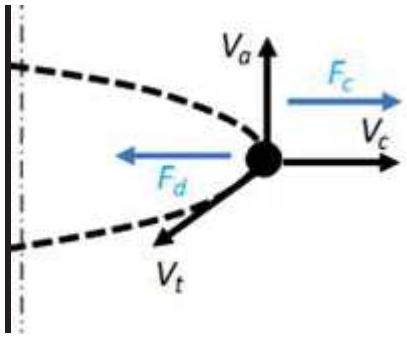

Figure 57. Force and velocity balance in a particle inside a hydrocyclone. Where F_c is the centrifugal force, F_d is the drag force, V_t is the tangential velocity, V_a is the axial velocity and V_c is the centrifugal velocity [Bagdi et al, 2012].

Any particle within the flow is basically subjected to two forces: one from the external and internal fields of acceleration (gravity and centrifugal forces); and the other from the drag exerted on the particle by the flow. The effect of the gravity is neglected in hydrocyclones, so only centrifugal and drag forces are taken into account. The movement of a particle in both the tangential and vertical or axial directions is unopposed by any forces, so that its velocity components in those directions can be taken to be equal to the corresponding flow velocity.

Since the centrifugal force acts in the radial direction, it prevents the particle following the inward radial flow and the particle is subjected to centrifugal elutriation. If the centrifugal force acting on a particle exceeds the drag, the particle moves radially outwards and, if the drag is greater, the particle is carried inwards.

Since the drag force and the centrifugal force are determined by the values of radial velocity and tangential velocity respectively for a given particle, the relative values of these velocities at all positions within the separation zone are decisive for the overall performance of the cyclone.

4.3.1.5 Theories of Separation

The objective of developing a theory of the separation in hydrocyclones is to create a model that describes the process so accurately that no test work is required.

A large quantity of work has been published on modelling the flow and the separation process which occurs in a hydrocyclone. The different approaches to the problem can be classified into either fundamental and empirical, or numerical, according to Aldrich [2015]. The most important fundamental and empirical models are the equilibrium orbit theory [Driessen 1951; Bradley et al, 1959], the crowding theory [White, 1991], the residence time theory [Rietema, 1961; Dwari et al, 2004], the turbulent two-phase flow theory [Neesse et al, 2004a] and the empirical model theory [Shepherd et al, 1939; Nageswararo et al, 2004; Kraipech et al, 2006]; whereas the most used numerical models are thanks to Chen et al [2000], Brennan [2006] and Delgadillo et al [2007].

4.3.1.6 Cut Size

The efficiency of a hydrocyclone is often presented in terms of the equiprobable size, x_{50} [Rushton et al, 2000]. At particle size equal to x_{50}, the separation efficiency is equal to 50%. This means that the particle has a 50% chance of entering the overflow or the underflow from the cyclone. Most of the particles in the feed that are smaller than x_{50} will follow the overflow, while most of the particles coarser than x_{50} will leave the cyclone through the underflow. This equiprobable size is also known as the cut size of the cyclone.

4.3.1.7 Design

4.3.1.7.1 Cone Angle

There are two basic design configurations for the conventional hydrocyclone with a single tangential inlet duct, whose main difference is the included angle of the cone [Svarovsky, 2000]. The difference in design is presented in figure 58. The long cone with a narrow-angle design, provides a thicker underflow concentration, whereas the design with the long cylinder gives a sharper cut, which means that less material is misplaced [Rushton et al, 2000]. The narrow-angle design has angles up to about 25°, while the wide-angle design vary from 25° to 180° [Svarovsky, 2000].

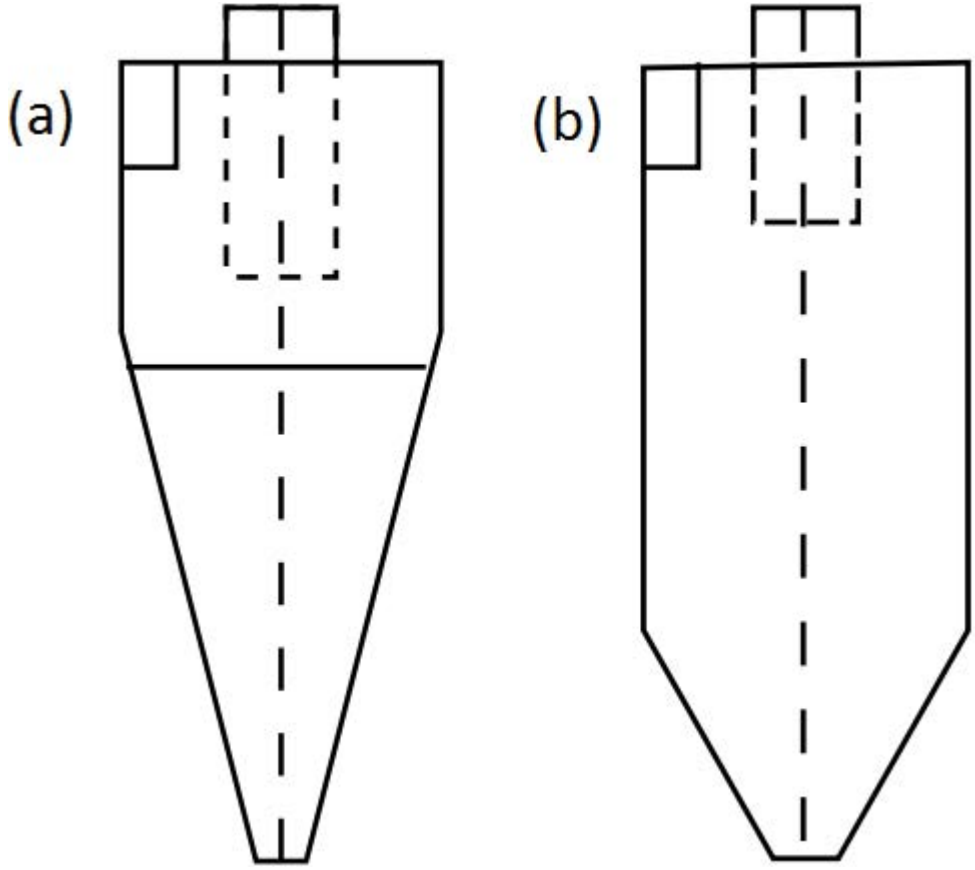

Figure 58. (a) Narrow-angle and (b) wide-angle configurations of a conventional hydrocyclone [Marthinussen, 2011].

The length of the cylindrical section in a hydrocyclone is usually equal to the hydrocyclone diameter [Olson et al, 2012]. The longer cylindrical section provides a longer residence time at the expense of a lower tangential velocity.

4.3.1.7.2 Inlet

The separation starts where the liquid carrying the solid particles first experience rotation. Therefore, the inlet of the hydrocyclone must be carefully designed. The shape of the inlet can be either rectangular or circular and its cross section can also vary [Svarovsky, 2000]. Different inlet configurations are shown in figure 59.

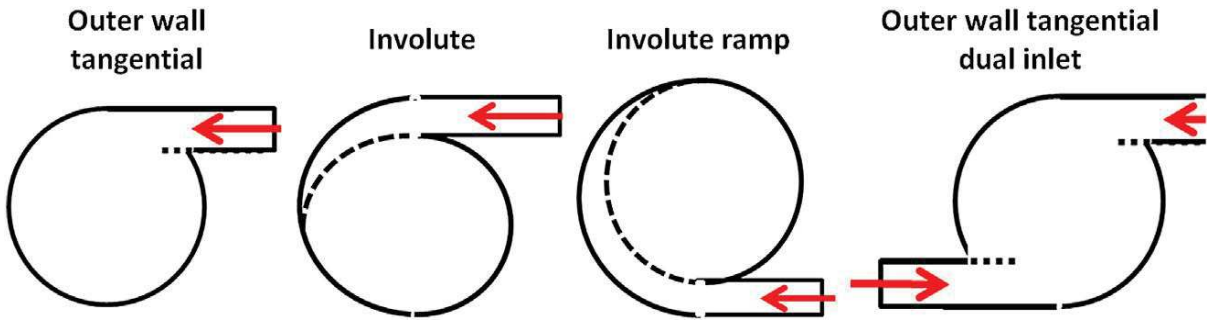

Figure 59. Feed inlet configuration in hydrocyclones [Aldrich, 2015].

Nenu et al [2009] compared one-inlet with two inlet cyclones and concluded that the underflow particle collection efficiency of the two-inlet cyclone was better than that of the one-inlet cyclone with the same total flow rate, due to enhancement of the tangential velocity profile of the particles in the former.

4.3.1.7.3 Materials of Construction

The materials used on the construction of hydrocyclones vary depending on the application; however, most designs include a metal housing with replaceable liners. The most common liner material is natural gum rubber because of its low cost and high wear resistance. Nonetheless, they are not always suitable. In aggressive chemical environments, elastomers as neoprene perform better; whereas in presence of abrasive slurries, ceramic materials as silicon carbide are preferred [Aldrich, 2015].

4.3.1.8 Classification of Solids According to Size

Hydrocyclones can be used not only in separation but also in the classification of solids regarding its particle size. As the grade efficiency of a cyclone increases with particle size, it can be used to split the feed solids into fine and coarse fractions.

In this particular application, hydrocyclones are most frequently used either to remove coarse particles from the product as a refining operation, or to remove fine particle from the product as a washing operation. In other applications, although not that frequent, the feed material is split into two useful products.

The main goal in classification operations is to be able to set the cut size to a predetermined value and to decrease the amount of material misplaced. When classifying at cut sizes up to 50 μm, narrow-angle hydrocyclones are used whereas for cut sizes up to 250 μm, wide-angle hydrocyclones are employed.

4.3.1.9 Multiple Cyclones in Series

Series connections of separators are a common path to improve the overall performance of the process. Due to their low capital and operational costs, hydrocyclones are frequently used in a multiple series arrangement, which may vary from one application to another.

In solid-solid classification, hydrocyclone separation misplaces a noteworthy amount of material in one pass. Therefore, in order to minimize the amount of misplaced material, the classification may have to be done in two or more stages. If the cut size of all involved hydrocyclones is the same, then the process will cut at the same particle size. Typically, the amount of misplaced material can be reduced a third with every subsequent hydrocyclone [Svarovsky, 2000].

4.3.2 Wet Low Intensity Magnetic Separation

4.3.2.1 Introduction

Magnetic separation has been a widely employed technique in the field of mineral processing for the concentration of magnetic materials and the removal of magnetic impurities, under either dry or wet conditions.

The first efforts to implement the use of permanent magnets to the processing of magnetite ores go back to the 17th century, as summarized by Derkach et al [1947]. The first patent on ore separation using a magnet date to 1792 [Fullerton, 1792] and in 1854 a magnetic separator with magnet polarities alternating along the direction of the material movement was proposed [Derkach et al, 1947]. In 1855, Nonteponi was first time using electromagnets in magnetic separation and in 1870 the first continuous separator, with a belt surrounding an electromagnet, was suggested [Bikbov et al, 2004]. At the beginning of the 20th century, significant development happened with the design of the first wet magnetic separator. With the arrival of rare earth permanent magnets to magnetic separation technology in the 1980s, the use of electromagnet-based equipment was mostly replaced [Chen et al, 2015].

With the aim of eliminating the forces due to molecular and electrostatic cohesion that hinders separation, several methods were proposed, such as the superposition of steady magnetic fields and high-frequency magnetic fields [Bikbov, 2004].

4.3.2.2 Classification of Magnetic Separators

Magnetic separators can be classified attending to a number of characteristics or factors [Svoboda, 2004]. However, two classifications are usually enough to define properly the process. The first classification is based on the media carrying the particles; being either wet or dry. The second is based on the magnetic field; including low-intensity magnetic separators (LIMS); high-intensity magnetic separators (HIMS); and high-gradient magnetic separators (HGMS).

4.3.2.3 Working Principle

The separation is achieved by passing a mixture or slurry, in the case of wet media, containing both magnetic and non-magnetic particles through an inhomogeneous magnetic field. It leads to the selective separation of magnetic particles.

All materials exhibit certain magnetic behaviour in the presence of an external magnetic field as explained in detail in section 2.2; where magnetic susceptibility was introduced as a dimensionless intrinsic property that indicates the magnetisation of a material in response to an applied magnetic field. Although all materials possess a certain magnetic susceptibility, only a small number of elements and minerals are sensitive to magnetic fields and, therefore, likely to be separated using magnetic processing. Only ferromagnetic type materials can be effectively separated this way.

In general terms, magnetic separation becomes increasingly inefficient as particle sizes of the feed particles are reduced. This results in low recoveries and unacceptable grades [Dobbins et al, 2009].

Static charge build-up between the feed particles surfaces, especially the fine particles, can be detrimental in terms of separation efficiency. When feed travels along the separating apparatus, particles rub together creating a static charge known as triboelectric charge that can cause the fine non-magnetic particles to adhere to the magnetic particles surface, hence inhibiting efficient separation [Dobbins et al, 2009]. Although the use of ionizers has been proved to disrupt this phenomenon, it does not eliminate it completely [Dobbins et al, 2010].

4.3.2.4 Motion of Particles

In the magnetic separation of magnetic particles, the dominant force that differentiates magnetic particles from non-magnetic particles is the magnetic force F_m, as shown in figure 60, which is highly dependent on the magnetic induction and the field gradient.

In a magnetic separator, the competing forces, F_c, are also acting in the particle, as observed in figure 60. This force comprises mainly gravity and hydrodynamic drag when performing the separation in a wet media [Xiong et al, 1998].

Magnetic particles will be separated from non-magnetic or less magnetic particles only if the magnetic force, F_m, upon the particles is greater than the sum of competing forces, F_c.

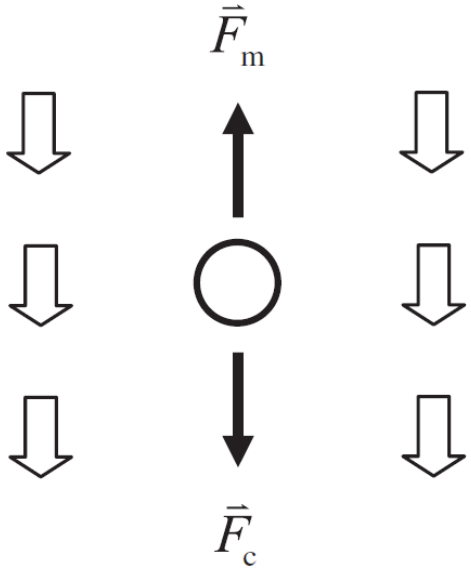

Figure 60. Schematic diagram of a magnetic separation process [Chen et al, 2015].

4.3.2.5 Low-Intensity Magnetic Separators

There are several types of low-intensity magnetic separators (LIMS) in operation in the field of mineral processing including, magnetic pulley, drum magnetic separator, column magnetic separator and screen magnetic separator. LIMS are basically limited to the concentration of strongly magnetic materials such as magnetite and to the removal of iron and ferromagnetic impurities.

Dry low-intensity magnetic separators (DLIMS) are usually used to remove tramp iron, to concentrate coarse strongly magnetic iron ores, and to recover iron values from blast furnace and steel mill slag. Removal of strongly magnetic impurities from a variety of materials is also accomplished with DLIMS. Tramp iron magnetic separators are used to protect handling and processing equipment such

as crushers and pulverisers. This type of separator is preferred for coarse, above 1 mm, particle concentration.

WLIMS separators are used to recover ferromagnetic solids from a slurry feed. The major areas for their use are in recovery in dense medium separation plants and in beneficiation of magnetite ore. They are by far the most widely used type of magnetic separation. In spite of its capital, operating and maintenance costs, WLIMS separators are preferred due to their ability to make sharp separations and handle a variety of feeds. This type of separation is preferred for the concentration of fine particles, below 1 mm.

Chapter 5. Materials and Experimental Techniques

5.1 Introduction

The present chapter details the starting materials and experimental techniques used to process and manufacture the powders and magnets in this study. In addition, the characterisation techniques utilised to assess the materials obtained are hereby presented and explained.

5.2 Production of Re-Sintered Magnets

5.2.1 Starting Materials

5.2.1.1 Voice Coil Motor Sintered Magnets

The starting material was in the form of nickel coated arc segments obtained from scrap VCM magnets from the former Philips factory, based in Southport UK. The composition is shown in table 2 and was determined by inductively coupled plasma mass spectrometry (ICP-MS) on an Optima 5300V ICP machine, accurate to ±0.01 at%. The oxygen content was obtained using a LECO analyser, accurate to 1 ppm. The ICP and LECO analysis were performed by Less Common Metals Ltd.

Table 2. ICP data for the VCMs. Values shown are expressed in at%, from Al to Pr, and in ppm from C to Zr.

Elements present in at%								
Al	B	Co	Cu	Dy	Fe	Ga	Nd	Pr
0.75	6.04	1.44	0.10	0.531	77.89	0.05	11.61	1.59
Elements present in ppm								
C	Mg	Mn	Ni	O	S	Si	Zr	
1779	<20	474	325	5080	<10	398	<20	

5.2.1.2 Neodymium

Neodymium, with purity above 99.9% in ingot shape and submerged in mineral oil, was supplied by Alfa Aesar and Sigma-Aldrich Corporation.

5.2.2 Hydrogen Decrepitation

5.2.2.1 Voice Coil Motor Sintered Magnets

The nickel coating layer was removed from the surface of the VCMs by scoring and peeling using a scalpel. The magnets were then fractured to produce a fresh surface which helps to initiate the HD reaction.

100 g of the fractured magnets was weighed and placed into a clean stainless steel hydrogenation vessel, which was then sealed. The vessel was later introduced in a large, hollowed cast iron block to act as a heat sink during the process and attached to the hydrogen rig shown in figure 61. All the HD runs were performed at room temperature.

The vessel was then evacuated using a rotary vacuum pump to ~10^{-2} mbar as measured by a Pirani gauge. Hydrogen was then manually introduced into the decrepitation chamber at a pressure of 4 bar. When the pressure inside the chamber started to decrease due of the initiation of the HD reaction, more hydrogen was introduced to maintain the pressure at 4 bar. After pressure stabilisation, meaning the end of the HD reaction, the vessel was evacuated, sealed and removed from the hydrogen rig to transfer it into a glove box under an argon atmosphere with oxygen content below 50 ppm. The HD powder was then unloaded and stored in the glove box.

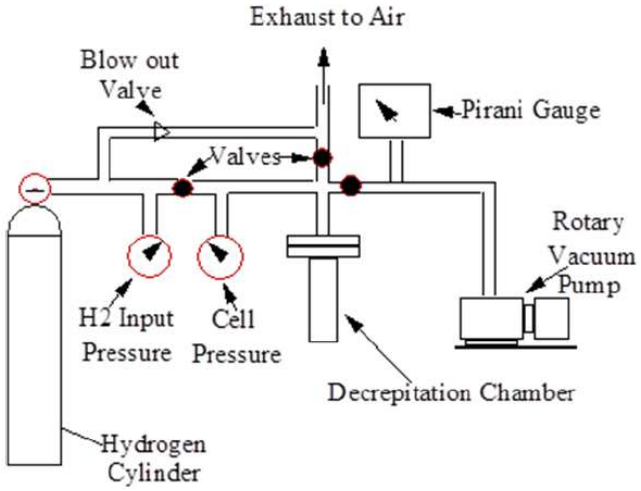

Figure 61. Schematic hydrogen decrepitation rig [Corfield, 2003].

5.2.2.2 Neodymium

Neodymium ingots were extracted from its package and the mineral oil was removed by wiping in air to avoid mineral oil spillage inside the glove box. However, a thin oxide layer was created in the surface of the ingots. Straight after cleaning the ingots were transferred into an argon filled glove box where the oxide layer was removed by hand grinding using 120 silicon carbide (SiC) paper.

Approximately 35 g of neodymium was weighed out and placed inside a clean stainless steel hydrogenation vessel inside the glove box. The vessel was sealed and transferred out the glove box and attached to the hydrogen decrepitation rig. The neodymium was then HD at 4 bar and at room temperature proceeding alike in the case of fractured VCM magnets. The vessel was then sealed and transferred to the glove box where the neodymium tri-hydride was unloaded and stored.

5.2.3 Milling

Two different milling techniques has been utilised in this study, namely burr milling, used for HD VCM magnet powder; and ball milling, employed for hydrided neodymium.

5.2.3.1 Burr Milling

The hydrided VCM magnets were milled under argon inside the glove box using an electric coffee grinder, shown in figure 62.a, which uses a form of burr milling. This technique uses two revolving abrasive surfaces, shown in figure 62.b, to break up the material with one of them fixed and the other able to rotate. The fine powder particles fell through the gap between the two revolving abrasive surfaces whereas the coarser particles became trapped between the surfaces and fractured; and then fell through the gap to a collection container.

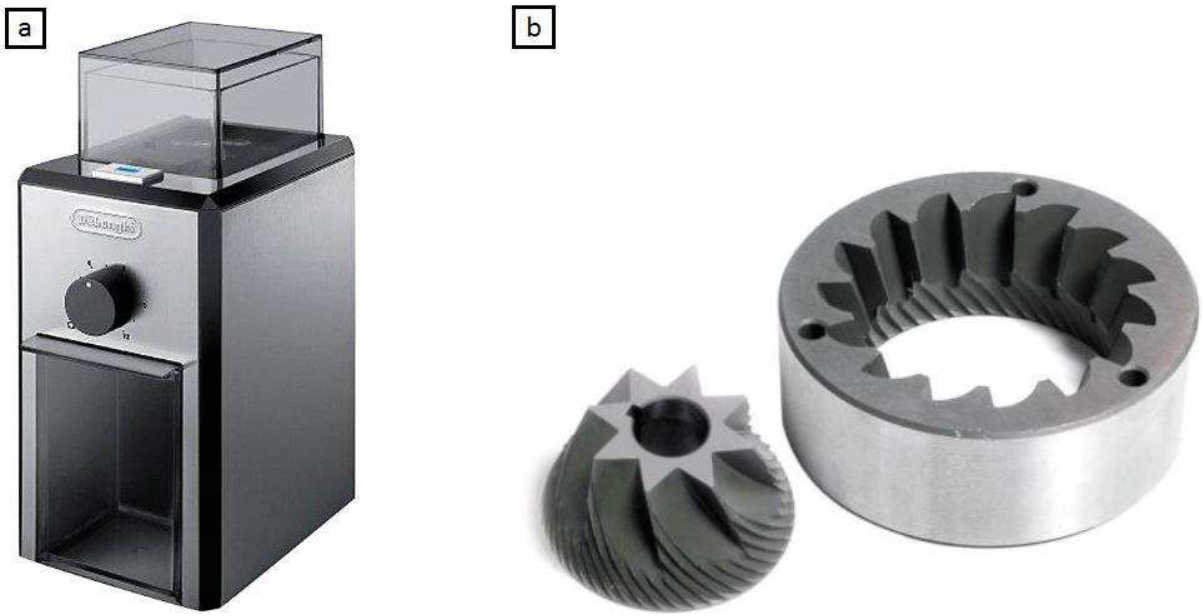

Figure 62.a. Electric coffee grinder utilised in this study to burr mill the HD VCM magnet powder. Image from http://www.delonghi.com/WebImage/Global/Products/Images/Coffee-Makers/Grinders/Kg79/1249859273_240x180.png Accessed 27/10/2016. b. Parts with abrasive surfaces responsible of the comminution of the material. Image from http://ferlibs.com/conical-burr-grinder/handsome-mazzer-robur-single-phase-mm-conical-espresso-grinder-burrs-burr-coffee-maz/ Accessed 02/03/2017.

A fraction of the HD VCM magnets was not subjected to burr milling in order to study the effect of this step in the magnetic performance of the final recycled re-sintered recycled magnet.

5.2.3.2 Ball Milling

The neodymium hydride was placed into a milling pot, in the glove box, which contained tungsten carbide milling balls at a ratio of approximately 8 to 1. Therefore, for every gram of neodymium hydride, there were approximately 8 grams of tungsten carbide, weighing each individual ball 2.25 g. The milling pot was then filled three quarters with high purity cyclohexane and then sealed tightly.

The milling pot, shown in figure 63(a), was then transferred outside the glovebox and placed in a roller mill where the neodymium hydride was milled for a total of 20 hours at 100 rpm. After milling, the powder was transferred back inside the glove box where the top cover of the milling pot was substituted by one with a valve for subsequent drying as shown in figure 63(b).

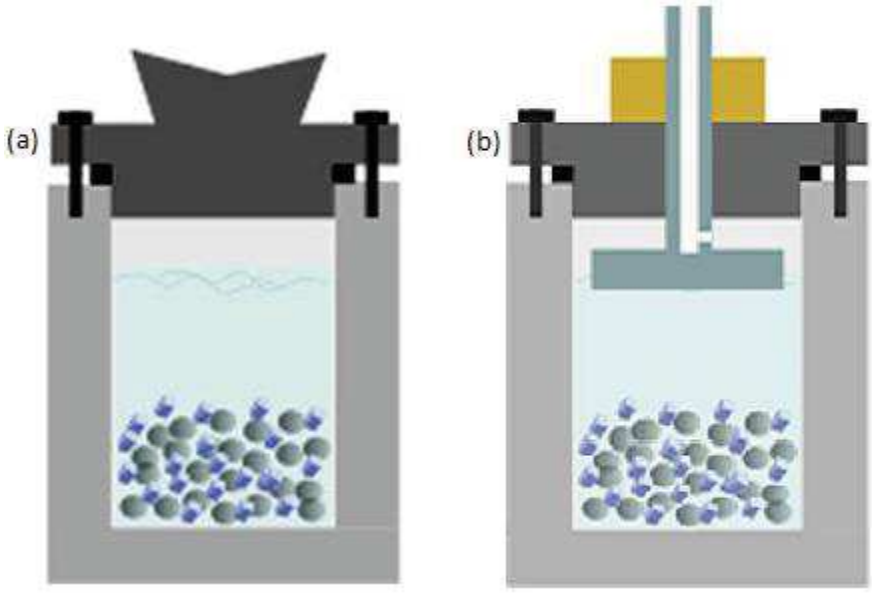

Figure 63. Milling pot with (a) the lid used for roller milling and (b) the lid with a valve used for evaporating the cyclohexane after milling [Degri, 2014].

The milling pot was sealed tightly and the valve was slightly open prior to transfer into the evacuation chamber of the glove box. There, the milling pot was left for 1 hour under vacuum to allow cyclohexane to fully evaporate off. The dried powder was then collected, under argon, from the milling pot and passed through a sieve of 150 μm mesh to separate the powder from the milling balls. After separation, the powder was stored under argon in the glove box.

5.2.4 Sieving

5.2.4.1 VCM Magnet Powder

The powder from hydrogen decrepitated VCM magnets, which was either burr milled or non-milled, was then sieved under argon through either a 90 μm or a 45 μm mesh size sieve. The sieves used were 21 mm in diameter and manufactured by Retsch. The different powders obtained were bagged and stored in individual containers under argon in the glove box. Most nickel was removed by scoring and peeling; nevertheless, a tiny amount was stuck to the surface. It was then removed during sieving as the nickel flakes were not able to go through the sieve mesh and were extracted and disposed reaching a nickel-free powder.

5.2.4.2 Neodymium Powder

The resulting ball milled HD neodymium was sieved under argon through a 45 µm mesh size sieve to separate the coarser particles. The particles under 45 µm were later used for blending them with recycled VCM magnet powder whereas the particles above 45 µm were kept under argon in the glove box for further ball milling.

5.2.4.3 Blending

When alloying additions were added, the weights of the alloying additions as well as the weights of the recycled VCM magnets powder were calculated to obtain in total 15.0 (±0.01) g of powder. After weighing, both types of powders were passed, simultaneously under argon, through a 90 µm mesh sieve. This process was repeated up to five times to ensure the homogeneity of the resultant mixed powder.

5.2.5 Aligning

15.00 (±0.01) g of powder was weighed and loaded under argon into an isostatic bag, as shown in figure 64, which was then tapped to settle the powder prior closure with a rubber bung and sealing with tape. The isostatic bags are cylindrical tubes made of neoprene with an outer diameter of 15 mm. The sealed isostatic bag was then transferred out of the glove box and placed in a capacitor discharge pulse magnetiser, which is able to produce a field of up to 9 T through a coil. The isostatic bag was placed inside the coil and was pulse magnetised at a pulse field of 9 T three times using a MAGNETECH 8000 J.

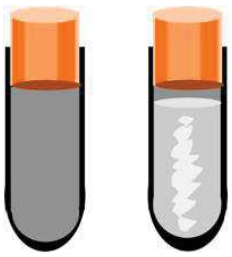

Figure 64. Neoprene isostatic bag (left) empty and (right) loaded with powder [Degri, 2014].

5.2.6 Pressing

After alignment, the sealed bag was placed into a water-filled isostatic press where pressure is applied equally from every direction. The powder was then pressed, in a Clarke Strong Arm 10 ton, at 620 kg cm^{-2}, approximately 60 MPa, holding the pressure for one minute and then releasing it progressively. After pressing, the sealed bag was extracted from the isostatic press and the water from the surface was removed prior to transfer to the glove box.

5.2.7 Sintering

The pressed sample, also referred to as a green compact, was unloaded under argon from the neoprene isostatic bag and was placed in a stainless steel foil tube. The foil with the sample inside was later introduced, also under argon, inside a sintering furnace tube, which was attached to a butterfly valve, hence, isolating the green compact inside the sintering furnace tube in an argon atmosphere.

The sintering furnace tube was then transferred from the glove box and attached to a vacuum sintering furnace. Afterwards, the tube was evacuated successively with a rotary and a diffusion pump achieving a vacuum level in the order, respectively, of 10^{-3} to 10^{-5} mbar, measured by a penning gauge.

The green compacts were then heated up at a rate of 7 °C min^{-1} to 1060 °C and held for 1 h and were subsequently furnace cooled under vacuum. The temperature profile used during the sintering process is shown in figure 65.

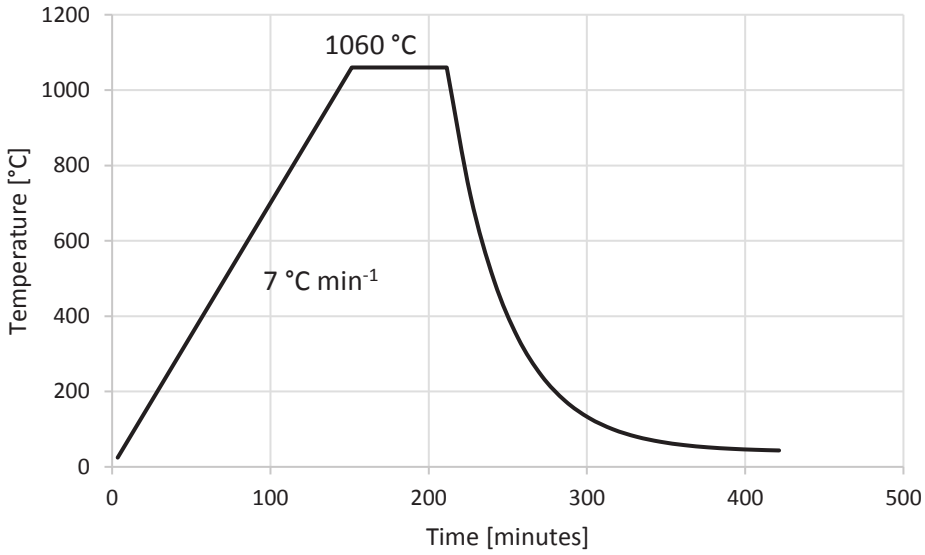

Figure 65. Temperature profile of sintering process used in this study.

The sintered magnet was extracted from the sintering furnace tube in air. It was then bagged and stored inside the glove box under argon prior to further characterisation.

Heat treatments are used in order to increase the intrinsic coercivity value of the magnet, as discussed in section 3.3.6.5. Nevertheless, all magnets prepared during this work were not heat treated or annealed as a consequence of the time constraint of the present PhD Thesis.

5.3 Separation Techniques

Two different separation techniques were employed in an attempt to separate the $Nd_2Fe_{14}B$ phase from the Nd-rich GBP. These are hydrocyclone separation, based on the differences in particle size; and wet low intensity magnetic separation, based on the differences in magnetic behaviour.

5.3.1 Hydrocyclone Separation

5.3.1.1 Starting Material

The starting material utilised in hydrocyclone separation was HD powder from VCM magnets either in a non-milled or burr milled state. 900 g of each of these two different starting materials were subjected to hydrocyclone separation.

5.3.1.2 Separation Process

The hydrocyclone separation system used in this study, shown in figure 66, is a homemade non-commercial piece of equipment that consists of a porcelain tub, a pump, a set of pipes and the cyclone separator. In addition, there are two valves to regulate the flow circulating in each pipe as well as a pressure reader.

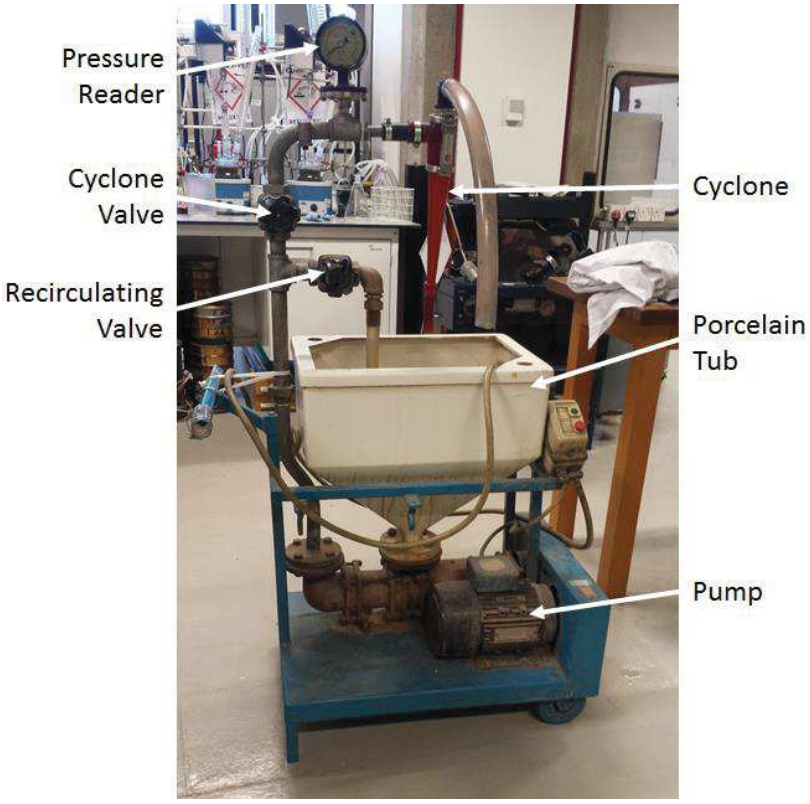

Figure 66. Hydrocyclone separation system used in this study.

The porcelain tub was filled with 10 L of water and then the powder was poured in, generating a dark sludge. At the beginning, the cyclone valve was closed and the recirculating valve was opened, so when the system was switched on, the pump started moving the liquid in a closed loop to enhance mixing. Then, the cyclone valve was progressively opened, so the slurry could reach the cyclone. At the cyclone two streams were generated, namely the underflow stream (UF), also referred as concentrated suspension, where most of the powder will end; and the overflow suspension (OF), also referred as diluted suspension. Both fractions were collected in independent containers.

The main part of the separation system is the cyclone. A diagram showing the main cyclone dimensions is shown in figure 67, and the corresponding dimensions are listed in table 3.

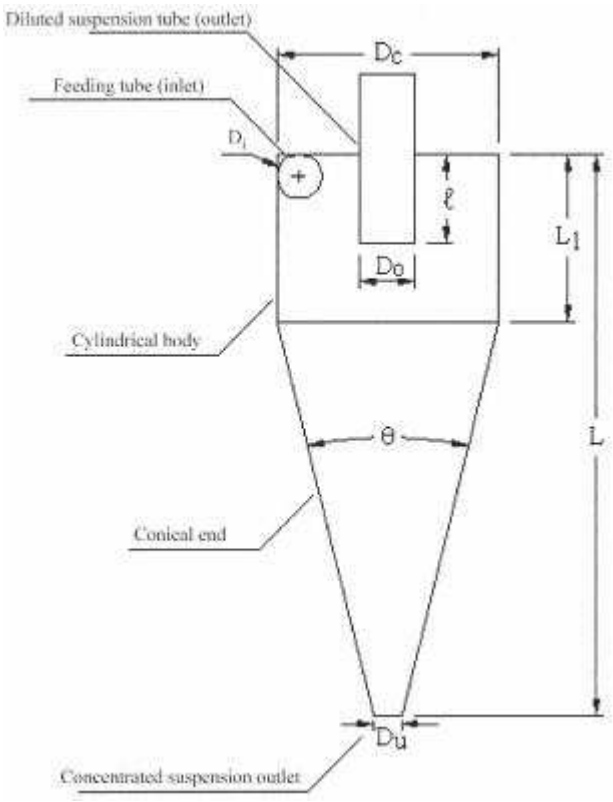

Figure 67. Diagram showing the main hydrocyclone dimensions [Soccol et al, 2004].

Table 3. Main dimensions of the cyclone used in this study.

Dimension	Symbol	Magnitude
Cyclone Diameter	D_c	50 mm
Feeding Tube Diameter	D_i	32 mm
Overflow Tube Diameter	D_o	32 mm
Underflow Tube Diameter	D_u	10 mm
Cyclone Length	L	252 mm
Cylindrical Part Length	L_1	82 mm
Overflow Tube Re-entrance	ℓ	32 mm
Cone Angle	θ	6.7 °

As the aim was to obtain the UF consisting predominantly of $Nd_2Fe_{14}B$ particles free of oxidised GBP; a total of three hydrocyclone separation experiments were performed on each sample. After the first separation, the OF was collected whereas the UF was the input for the next separation. Figure 68 shows, for a better understanding of this process, the cyclic arrangement of separation.

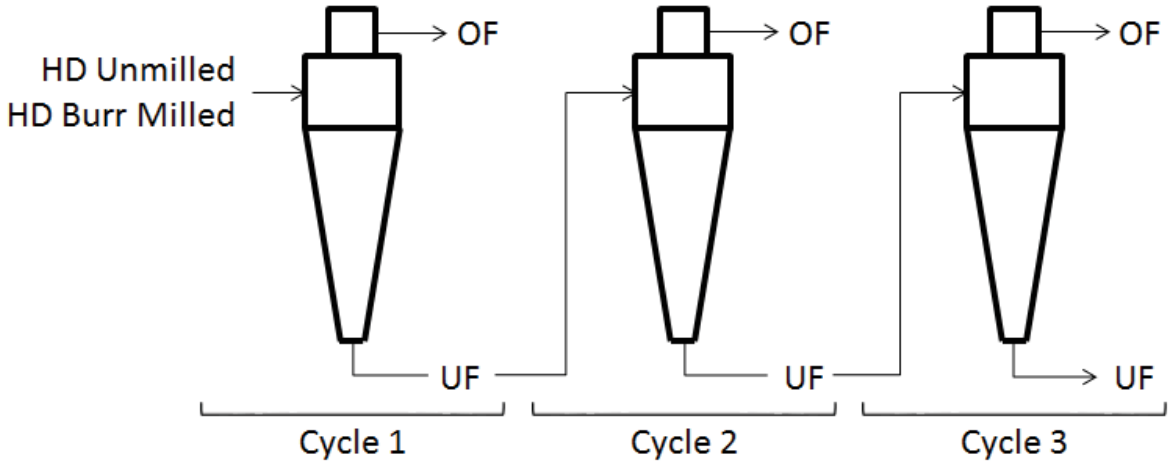

Figure 68. Schematic of the three cyclic hydrocyclone separations.

The first hydrocyclone cycle started with 900 g of HD-processed NdFeB powder either burr milled or non-milled. The entire OF suspension and a fraction of the UF suspension were kept for further characterisation, after each hydrocyclone cycle. The second and third hydrocyclone cycles started, respectively, with 800 g and 700 g.

5.3.1.3 Filtration

After separation, both fractions required filtration in order to remove the water and recover the powder. The filtration system, shown in figure 69, consists on a filtering glass flask connected to a vacuum pump, and a porcelain Büchner funnel on top of the flask in which a paper filter was placed.

The slurry from separation, consisting of water and powder, was then poured on the paper filter, at the bed of the Büchner funnel. The vacuum forced water to go through both the paper and the funnel and was then collected in the filtration flask; whereas the powder particles were retained in the paper filter. The mesh size of the paper filter was smaller than the particle size of the powder to avoid any loss of material. Although most of the water had been completely removed, the powder was still wet, hence, requiring a drying stage.

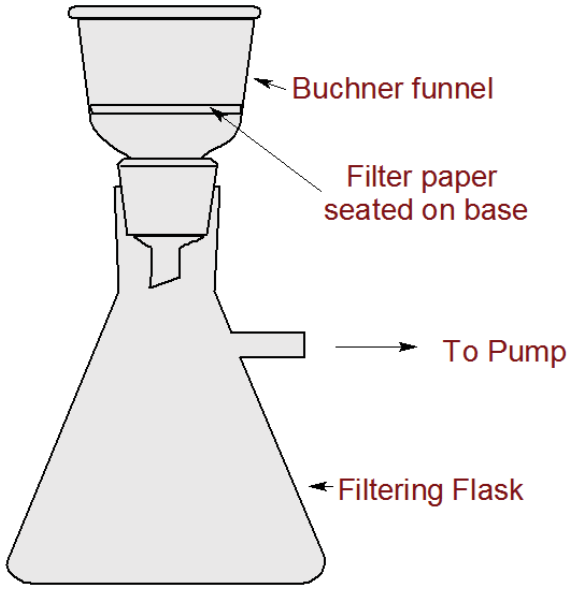

Figure 69. Schematic of the filtration system. Image from http://camblab.info/wp/wp-content/uploads/2015/02/vacuum-filtration.gif Accessed 27/10/2016

5.3.1.4 Drying

The paper filters with powder on top were placed in metal trays that were then introduced into an oven in air at 80 °C for a period between 2 hours and 4 hours until the powder was fully dried. Drying was performed in air as no advantage was found in doing so in a protective atmosphere as the material was already submerged in water and the phases had already changed. When the powder was dried, it was collected and stored.

5.3.2 Wet Low Intensity Magnetic Separation

5.3.2.1 Starting Material

The starting material utilised in WLIMS was HD-processed NdFeB powder from VCM magnets either non-milled or burr milled. Two separations were performed using this system. 250 g of each of these two different starting materials were subjected to WLIMS.

5.3.2.2 Separation Process

The WLIMS system used in this study, shown in figure 70, consists of a metal slope with two magnets underneath. These two magnets are magnetised in perpendicular to the slope. The principle was to separate the hard magnetic matrix phase particles, attracted to the magnets, from the non-magnetic GBP particles, which would go down the slope.

Figure 70. Wet low intensity magnetic separation system.

The powder was poured in a water containing beaker which was stirred to enhance mixing. This suspension was then progressively dropped on the left side of the slope. At the time the slurry was being poured, a squeeze bottle was used to add a source of water that could slightly move the particles attracted to the magnet and, hence, allow the non-magnetic particle to pass down the slope. The non-magnetic particles were collected at the end of the slope during this process. To collect the magnetic particles it was necessary to turn the slope of the WLIMS as in the right image in figure 70. After collection, the powder required filtration and drying as described in sections 5.3.1.3 and 5.3.1.4.

5.4 Characterisation Techniques

5.4.1 Sample Preparation

The as-sintered magnets were sliced in two halves using a low speed diamond saw thus obtaining two discs (of approximately 10 mm diameter and 9 mm height) from every sintered magnet. The samples were then ground using a grinding wheel and SiC paper to ensure sample uniformity for subsequent characterisation and analysis.

5.4.2 Density Measurement

Density measurements were carried out using a standard liquid displacement method using diethylphthalate (DEP) as liquid media. The density of the magnets was calculated according to the MPIF 42 [MPIF, 1986] and ASTM B 962 [ASTM B 962, 2008], using the following equation.

$$\rho_{magnet} = \frac{w_{air}}{\left(\frac{w_{air\ with\ lacquer} - w_{fluid\ with\ lacquer}}{\rho_{fluid}}\right) - \left(\frac{w_{air\ with\ lacquer} - w_{air}}{\rho_{lacquer}}\right)} \qquad \text{Equation 16}$$

Where ρ_{magnet} is the density of the sample, ρ_{fluid} is the density of the DEP in, $\rho_{lacquer}$ is the density of the lacquer, w_{air} is the weight of the sample in air, $w_{air\ with\ lacquer}$ is the weight of the lacquered sample in air, $w_{fluid\ with\ lacquer}$ is the weight of the lacquered sample in the fluid. All weights are in g and densities are in g cm^{-3}.

A Mettler Toledo AX205 balance, with an accuracy of 0.00001 g, was used to weigh the samples in air, whereas an Ohaus Galaxy 160, with an accuracy of 0.0001 g, was used to weight the lacquered samples submerged in the DEP. The lacquer and the DEP have a nominal density of 1.2 g cm^{-3} at 24 °C and 1.1298 g cm^{-3} at 8 °C respectively. The density measurement using this technique is accurate to ±0.05 g cm^{-3}.

Only the density of sintered magnets were measured, due to measuring the density of green compacts may have required a different density-determination technique as helium picnometry and it was not possible to get access to such equipment.

5.4.3 Magnetic Measurements

The magnetic properties of the samples prepared in this study were assessed with a permeameter, shown in figure 71, consisting of an electromagnet with two moveable pole pieces. The pulse magnetised sample is placed in the centre of a set of measuring coils between the two pole pieces. The arrangement

of the coils is such that it is able to measure both the applied field and resultant magnetic induction in the sample.

The pole tips of the electromagnet are then lowered to be in contact with the samples, hence, forming a closed loop. The magnet forms part of a closed loop of magnetic field so self-demagnetising fields are not found, negating any effects of sample geometry providing the surfaces are parallel and the cross section remains uniform.

The electromagnet is water cooled to keep the electromagnet at a constant temperature during measurements. All samples in this work were tested at room temperature (20-24 °C) and, some of them, were also tested at 75 and 150 °C. To do so, the permeameter includes a system, that comprises heating poles, a thermocouple and a control unit; able to increase and control the temperature in the surrounding of the sample.

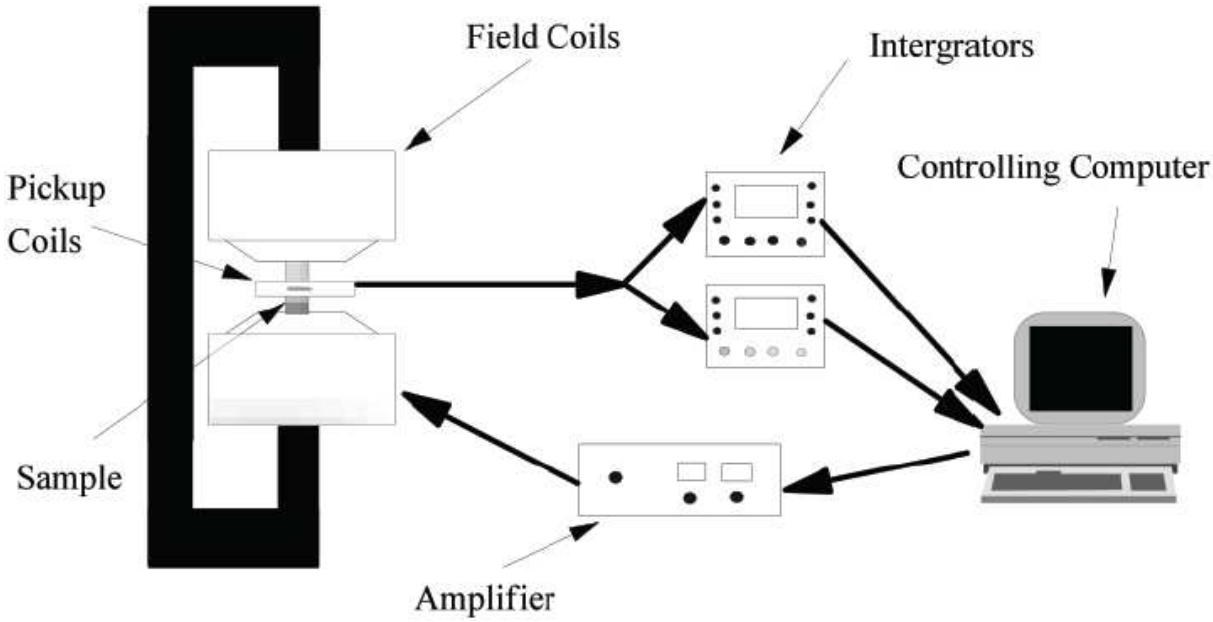

Figure 71. Schematic of a permeameter system [Walton, 2001].

When a magnetic field is applied and increased, the measuring coils measure the rate of change of magnetic flux by measuring the induced voltage with time. This change in voltage, from Faraday's law of electromagnetic induction, is proportional to the change in flux density. Therefore, as the cross section

and the area of the coils are known, the flux density can be measured. Further integration of the voltage leads to the total magnetic induction and also the magnetisation of the sample.

The applied field was first increased to saturation magnetisation before lowering to zero. The direction of the field was then reversed and increased to apply a demagnetising field up to saturation magnetisation. The field was then reduced to zero, the direction of applied field reversed again and increased to saturation magnetisation to complete the hysteresis loop. The field was then lowered back to zero.

The cross section of the sintered samples was obtained by measuring the diameter of the disc at 8 different points around the sample and averaging the values. It should be noted that as samples are not perfectly cylindrical extra care needs to be taken at this step. The samples were pulse magnetised with a field of 9 T prior to measurement in a Permagraph von Dr Steingroever. The experimental errors in the determination of the measurements have been determined as B_r ±5 mT, ${}_iH_c$ ±5 kA m^{-1} and $(BH)_{max}$ ±5 kJ m^{-3}.

5.4.4 Thermal Stability

The stability of remanence (α) and coercivity (β) with temperature is known as thermal stability and measures the percentage change of the magnetic performance per single degree change in temperature for a range of temperatures. It is given by the following equations [Kim et al, 2012a]:

$$\alpha = \frac{B_r(T) - B_r(T_0)}{B_r(T_0)\,(T - T_0)} \qquad \text{Equation 17}$$

Where α is the thermal stability of remanence in % $°C^{-1}$, T is the upper temperature chosen in °C, T_0 is the lower temperature chosen in °C, $B_r(T)$ is the remanence at the upper temperature expressed in T, $B_r(T_0)$ is the remanence at the lower temperature in T.

$$\beta = \frac{{}_iH_c(T) - {}_iH_c(T_0)}{{}_iH_c(T_0)\,(T - T_0)} \qquad \text{Equation 18}$$

Where β is the thermal stability of coercivity in % °C^{-1}, $_iH_c$ (T) is the coercivity at the upper temperature in T, $_iH_c$ (T_0) is the coercivity at the lower temperature in T.

Therefore, using intrinsic coercivity and remanence values obtained at different temperature tests using the permeameter, described in the previous section, it is possible to further calculate the stability of remanence and coercivity at temperature

5.4.5 Inductively Coupled Plasma – Optical Emission Spectrometry

Optical emission spectrometry (OES) equipment uses an inductively coupled plasma (ICP) as the excitation source. The ICP source consists of three concentric quartz tubes surrounded by a radio frequency (RF) coil. The sample is mixed with argon and are carried to the plasma through the central tube of the torch. When a spark is added the plasma formation initiates. The argon ions and free electrons are further agitated by the RF field, causing the plasma to reach temperatures above 8000 °C.

The sample is introduced in liquid form. Therefore solid samples are required to be dissolved in a solution prior to elemental analysis. The sample-containing liquid is converted to an aerosol and is sprayed into the plasma. In a very short lapse of time and distance, the particles within the aerosol are dried, atomized, ionized, excited and relaxed.

The light emitted from the plasma is split into discrete component wavelengths using a diffraction grating. Each element has its unique set of wavelengths. The amount of light at a given wavelength is detected and quantified; and it is proportional to the concentration of the corresponding element in the solution. Once this concentration is known, the mass fraction of such element can be calculated.

In this study different powder samples were analysed in an ICP-OES Varian 720-ES. For each sample analysed, 1 g of powder was dissolved in 10 mL dilution composed by 2 mL of H_2O, 4 mL of HNO_3 and 4 mL of HCl. This was further diluted with extra 40 mL of H_2O. The experimental errors in the determination of the measurements have been determined as ±0.01 wt%.

5.4.6 X-Ray Fluorescence Spectroscopy

When a primary X-ray source strikes a sample, the X-ray can be either absorbed by the atom or scattered through the material. When an X-ray is absorbed by the atom, all of its energy is transferred to an electron closer to the nucleus. This effect is known as photoelectric effect and, during this this process, if the X-ray has energy enough, electrons are ejected from inner shells, creating vacancies. These vacancies entail instability in the atom's condition. In order to return the atom to a stable condition, the electrons move from the outer to the inner shells. In this transition electrons emit a characteristic X-ray.

The energy of the X-rays is the difference between the two binding energies of the corresponding shells and each element has a unique set of energy levels. Therefore, the elemental composition of the sample can be measured non-destructively. The process of emissions of characteristic X-rays is called X-ray fluorescence (XRF). Analysis in which X-ray fluorescence is involved is known as X-ray fluorescence spectroscopy.

The characteristic X-rays are identified as K, L, M or N in order to indicate in which shell they were originated and as alpha (α), beta (β) or gamma (γ) to denote how close the shells of the transference of electrons were. For example, a Kα X-ray is produced from a transition of an electron from the L to the K shell, and a Kβ X-ray is produced from a transition of an electron from the M to a K shell, as demonstrated in figure 72. Due to there are multiple orbits of different binding energy electrons within the shells, a further designation is made as α1, α2 or β1, β2, and so on. This denotes transitions of electrons into the same shell from the different starting orbits.

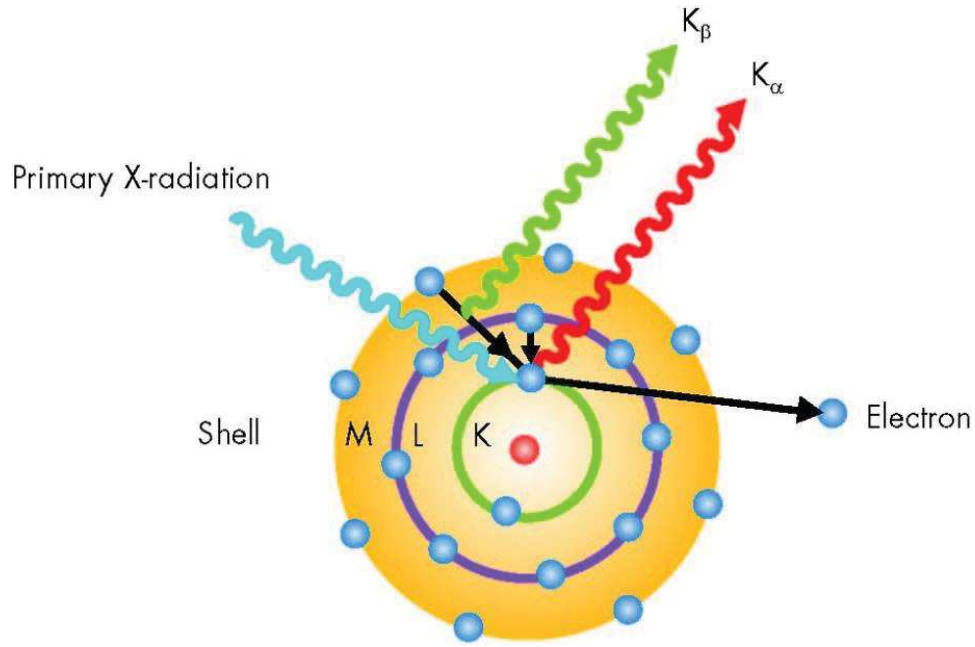

Figure 72. The principle of the XRF spectroscopy. Image from http://xrf-spectroscopy.com/ Accessed 27/10/2016.

Disassembled plastic cups, with an outer diameter of 35 mm, and Mylar film, of 6 µm thickness were assembled together into sample cups where 5 g of the powder was added. This cup was later placed in the centre of a 37.5 mm window metal cup prior to introduction into the XRF equipment. XRFS was performed in a Philips XRF PW2400 at which X-rays were produced at 40 kV and 60 mA. The technique is accurate to ±0.01 wt%.

5.4.7 X-Ray Diffraction

X-ray diffraction (XRD) is a non-destructive technique in which a sample is irradiated with x-rays of a fixed wavelength and the intensity of the reflected radiation is recorded by a detector mounted in a goniometer.

X-rays are generated by heating a filament in order to produce electrons which, by applying a voltage, are accelerated towards a target. When electrons have energy enough to displace inner shell electrons of the target material, characteristic X-rays are generated. Foils or crystal monochromators are required to filter the wavelength and produce monochromatic X-rays.

The interaction of the incident rays with the sample produces constructive interference and, hence, a diffracted ray when conditions satisfy Bragg's Law, given in equation 19.

$$n\,\lambda = 2\,d\,\sin\theta \qquad \text{Equation 19}$$

Where n is the order of reflection, λ is the wavelength of the incident X-rays, d is the interplanar spacing and θ is the angle of incidence.

Bragg's Law relates the wavelength of electromagnetic radiation to the diffraction angle and the lattice spacing in a crystalline sample. In order to cover all possible diffraction directions the crystalline sample is scanned through a range of 2θ angles. When the x-rays are detected and processed, then, they are counted. Conversion of the diffraction peaks to d-spacings allows identification of the compounds present in the sample due to each material has a set of unique d-spacings. This is reached by comparing the obtained d-spacings with standard reference patterns.

XRD was carried out in a PANalytical EMPYREAN using cobalt and $K_{\alpha 1}$ on 5 g powder samples. Data acquisition, peak identification and quantitative analysis were performed by Iuliana Poenaru at Fraunhofer Institut. The technique is accurate to ±0.01 wt% in qualitative and to ±0.1 wt% in quantitative analysis.

5.4.8 Thermal Desorption

To investigate desorption of hydrogen from different powder samples, a home-built data logger designed by Degri [20104] was utilised. The data logger system, shown in figure 73, consists of a Pirani gauge, a 945 Controller from Kurt J. Lesker Ltd and a thermocouple. These components are connected to an Arduino microcontroller which recorded all the data as an excel file to a Secure Digital card.

The 945 gauge controller has an analogue output whose voltage varies depending on the pressure on the system monitored by the Pirani gauge. A type K thermocouple was placed inside the vacuum tube and was located as close as possible to the green compact or powder. The microcontroller logged the

analogue signal from the pressure gauge controller, the cumulative time and the temperature from the thermocouple amplifier.

The microcontroller's analogue to digital conversion (ADC) is 10 bit and the range of voltages measured was from 0 V to 5 V. This means that for a 10bit ADC, the analogue voltage is split into 1024 discrete units, which leads to a resolution of 0.005 V. Therefore, the pressure is recorded in arbitrary units and can be converted into pressure [Degri, 2014].

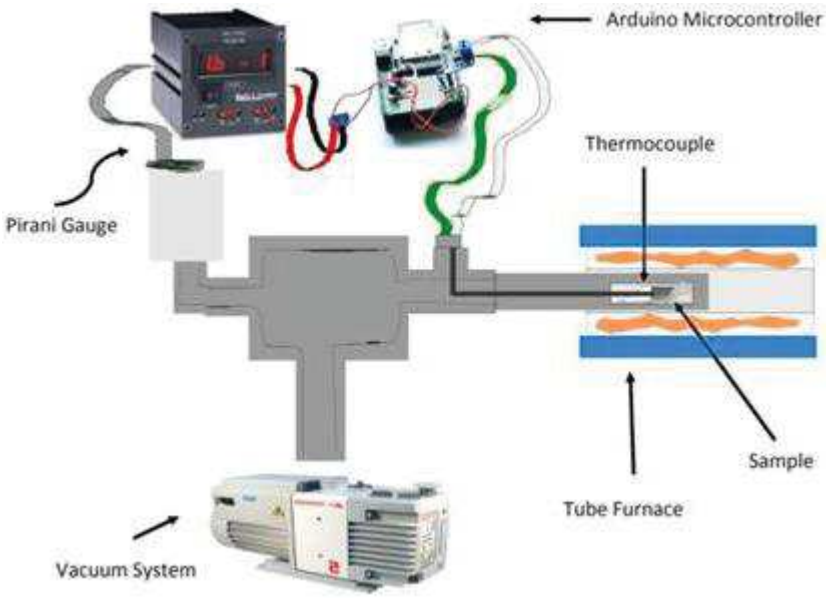

Figure 73. The data logging system [Degri, 2014].

5 g powder samples were inertly loaded into the furnace tube which was then evacuated to about 9.5 10^{-2} mbar. The sample was then heated up at 5 °C m^{-1} to 1000 °C after which the sample was furnace cooled until room temperature was reached.

5.4.9 Mechanical Properties

5.4.9.1 Vickers Hardness

Hardness is the ability of a material to resist plastic deformation by the indentation of a harder body, the indenter, with a determined shape and size, which does not suffer any deformation from the force applied.

Vickers hardness (HV) value is based on the evaluation of the small indentation formed in the surface of samples being evaluated. A Vickers indenter, shown in figure 74, is a highly polished, pointed, square-based pyramidal diamond with angles facing 136°. The indenter is pressed into the test sample surface by applying force, which is accurately controlled.

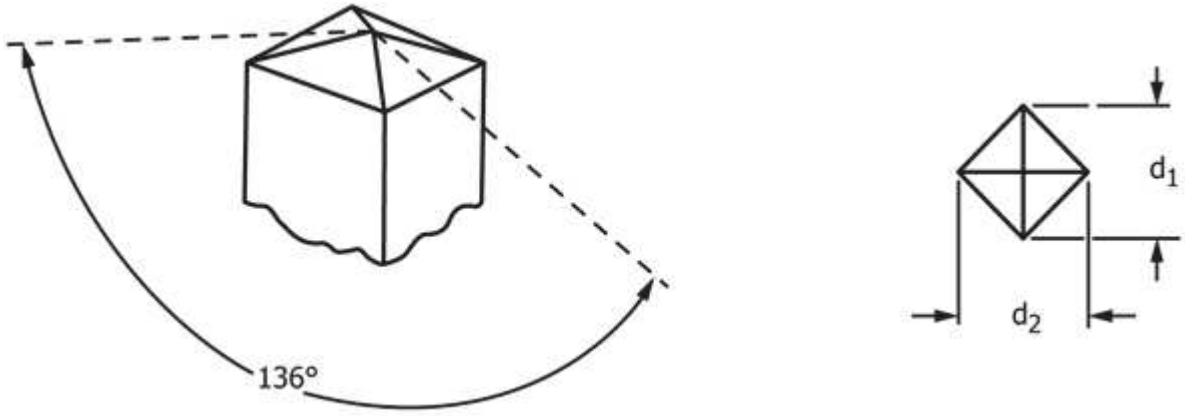

Figure 74. The Vickers indenter is a highly polished, pointed, square-based pyramidal diamond with face angles of 136°, which is pressed into the test specimen surface leaving on it an indentation characterized by two diagonals denoted by d_1 and d_2 [ASTM E 384].

HV measurements were performed using a 5030 SKV Vickers Hardness Testing Machine by Indentec. The Vickers hardness of the magnets was measured and calculated according to the ASTM E 384 [ASTM E 384, 2012], using the following equation:

$$HV = \frac{P}{A} \qquad \text{Equation 20}$$

Where P is the force selected for the indentation and A is the pyramidal contact area of the indenter and the sample. By deducing the pyramidal contact area, equation 20 can be simplified to:

$$HV = 1.8544 \frac{P}{d^2} \qquad \text{Equation 21}$$

Where the force is expressed in kilograms force (kgf) and the diagonal in mm. Theoretically both diagonals would have the same length; however, experimentally this rarely occur, giving:

$$d = \frac{d_1 + d_2}{2} \qquad \text{Equation 22}$$

The selected force in this work was 30 kgf (294.3 N); and was held for 7 seconds to indent the sample surface. The diagonals were measured with a light microscope, attached to the hardness test equipment, after force removal. The results of Vickers hardness presented in this work are the average of a total of 10 measurements per sample, with a minimum distance between them of three times the diameter of the first indentation made.

Results from Vickers hardness, according to ASTM E 92 are expressed as 000 HV 30/7, or simply, 000 HV 30, where 000 is the result from test rounded to the next three significant digits number [ASTM E 92, 2013]. The experimental errors in the determination of the measurements have been determined as ±5 HV 30/7.

5.4.9.2 Fracture Toughness

When testing the hardness of a sample, cracks are generated in or near the corners of the indentation. Because the cracks did not always initiate in the corners of the indentations and did not always form a straight line, the crack lengths were measured as shown in figure 75.

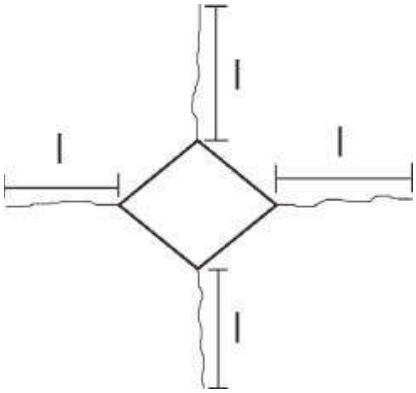

Figure 75. Schematic diagram of the cracks and the measurement of its length, denoted as l [Hu et al, 2012].

The fracture toughness (K_{IC}), expressed in $MN^{-3/2}$, was calculated by applying the following equation [Hu et al, 2012; Roebuck, 1992; Schubert et al, 1998]:

$$K_{IC} = A\sqrt{HV}\sqrt{\frac{P}{\Sigma l}} \qquad \text{Equation 23}$$

Where A is a constant whose value is 0.0028, HV is the Vickers hardness, P is the load applied during the Vickers hardness test expressed in N and Σl is the sum of crack lengths in mm.

The results of fracture toughness presented in this work are the average of the 10 calculated values derived from Vickers hardness test. The experimental errors in the determination of the measurements have been determined as ±0.01 $MN^{-3/2}$.

5.5 Microstructural Examinations

5.5.1 Microscopy Sample Preparation

Magnets in the shape of small discs were cut in two halves, both of which were and mounted in Bakelite in order to expose two different surfaces. These are parallel to the c-axis and perpendicular to the c-axis, as shown in figure 76.

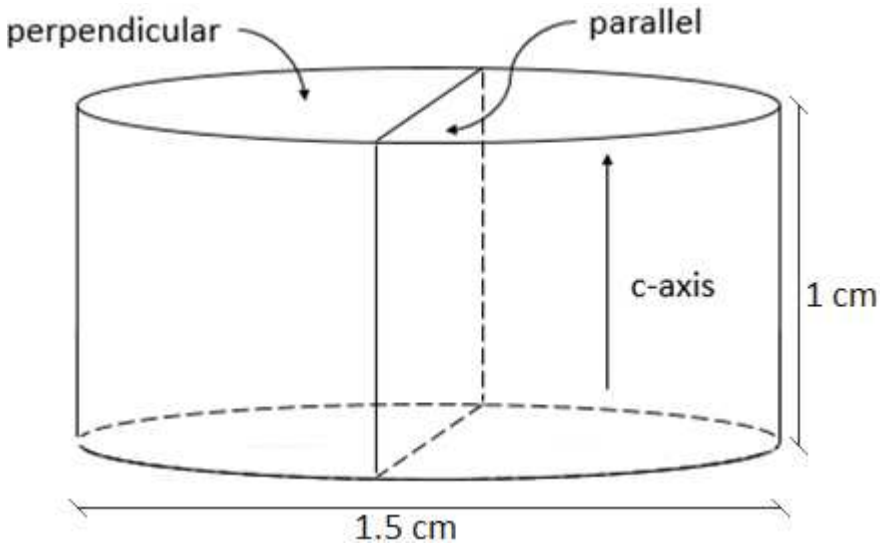

Figure 76. Schematic of parallel and perpendicular surfaces to the c-axis.

The samples were then ground flat using successive P120, P400, P800 and P1200 grit SiC papers. The samples were then polished in an automatic polishing machine using successive 1 and 1/4 μm diamond

impregnated polishing cloths. After every polishing stage the samples were washed in industrial methylated spirit to ensure clean surfaces and to avoid any detrimental surface abrasions from contaminates during polishing.

5.5.2 Optical Microscopy

Prepared magnet samples were examined using a Leitz Laborlux 12HL optical microscope, which is capable of magnifications up to 100x.

Some samples were etched using a 5% citric acid solution as it is very effective in revealing the grain boundaries of NdFeB magnets, as previously reported [Degri, 2014]. The etchants preferentially attack the grain boundaries, causing the GBP to scatter light so that they appear darker when viewed with an optical microscope.

In addition, the Leitz microscope contains a polariser which allows the observation of magnetics domains using Kerr-effect microscopy.

The Kerr-effect is the rotation of polarisation of a light beam when it is reflected from the surface of a demagnetised sample. The Kerr-effect can be observed depending on the direction of magnetisation with respect to the plane of incidence and the reflecting surface plane. The incident light is first polarised, which after reflection from the magnetic sample passes through an analyser and then into the microscope.

For a sample with oppositely magnetised domains, the plane of polarisation of the reflected beams is rotated in opposite sense. The analyser is rotated until it cuts out one of the reflected beams, which is then extinguished and the domain appears dark whereas the other beam goes through and the domain remains bright. Therefore, grains with the c-axis perpendicular to the imaging plane exhibit a ‘cog’ wheel or maze pattern, whereas grains with the c-axis parallel to the imaging plane show typical striped shaped domains.

5.5.3 Scanning Electron Microscopy

A JOEL 6060 scanning electron microscope (SEM) was used mainly for obtaining back-scattered electron (BSE) micrographs of magnets. A BSE image is obtained using a detector which picks up high energy electrons which have been reflected from the surface due to interaction with the atoms. Atoms with a large atomic number are more likely to interact with primary electrons and they will appear brighter than elements with a low atomic number. Therefore, BSE images are useful for the observation of the different phases present within the microstructure of re-sintered magnets.

5.6 Summary

Figure 77 summarises the schematic diagram of the production of all samples in this study. Characterisation of the manufactured products took place before and after magnetic separation and hydrocyclone separation; as well as after sintering.

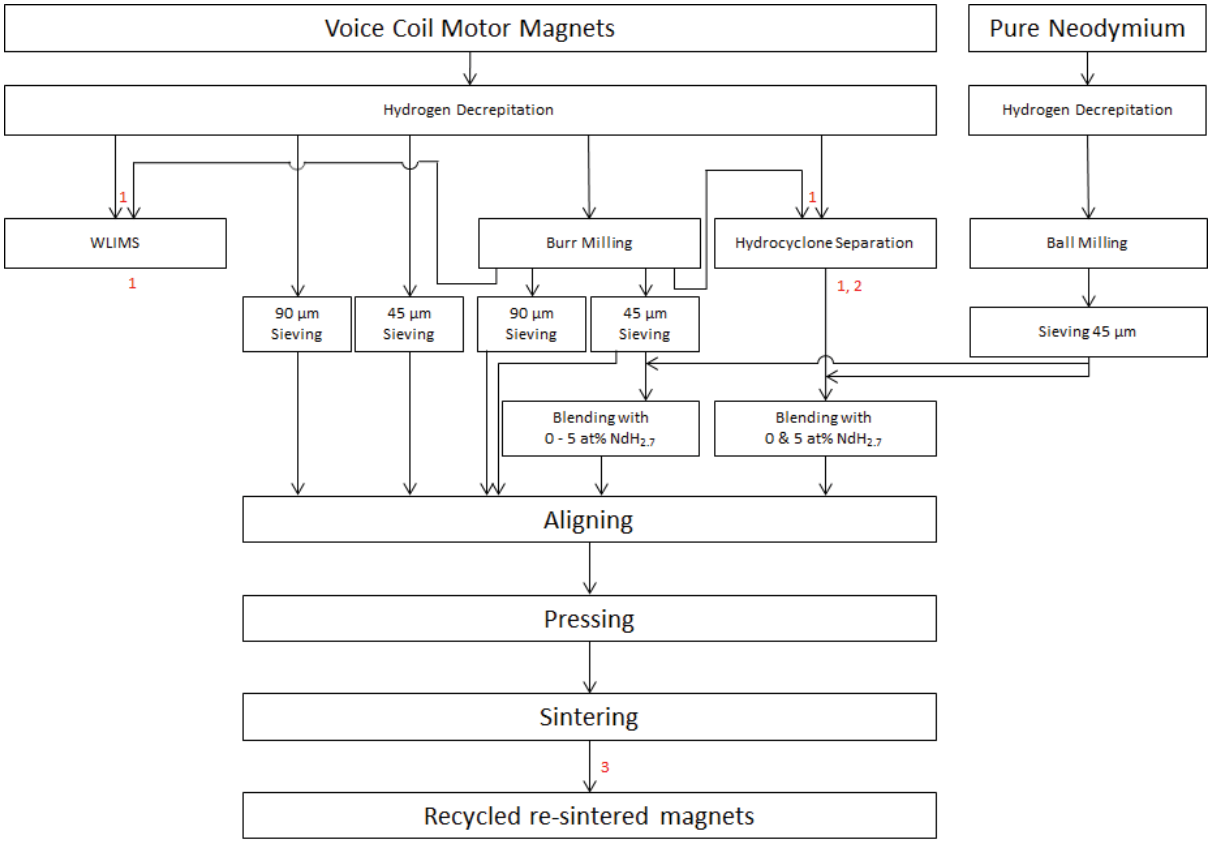

Figure 77. Schematic of the production of every sample. The characterisation stages are pinpointed in red where 1 represents XRD, XRF and ICP; 2 represents thermal desorption and 3 represents density measurements and mechanical and magnetic properties.

Chapter 6. Particle Size Effect: Results and Discussion

6.1 Introduction

At present, when the HPMS process is used to separate NdFeB magnets from electronics, then sieving to 90 μm is sufficient to remove all the nickel impurities [Walton et al., 2015]. To reduce the particle size of the material closer to near single crystal particles (around 10 μm) then further milling and sieving would be required which increases the time, energy consumption and therefore cost of this step.

At 90 μm, the HD powder will contain multiple $Nd_2Fe_{14}B$ grains, which may still be aligned from the starting sintered magnet. It may be possible to align these 90 μm particles, with all the grains pointing in the c-axis direction during pulse magnetisation prior to re-sintering into a new magnet. If good alignment can be achieved in the final magnet then it may not be necessary to sieve the material down to near single crystal particles.

When primary NdFeB magnets made from cast alloys are hydrogenated, they are further milled to decrease the particle size to near single crystal particles. However, in a sintered magnet after hydrogen decrepitation it is unclear if the polycrystalline particles which are already aligned can rotate under an applied field, thus giving good magnetic performance. Therefore, it is necessary to investigate the effect of decreasing the particle size of the HD powder, produced from EOL VCM magnets, on the subsequent magnetic performance of re-sintered magnets in order to determine whether further milling and sieving steps are required to obtain desirable magnetic properties in the final re-sintered magnet.

A total of four different configurations have been investigated, as shown in table 4, to study the properties of the recycled re-sintered magnets. These configurations are: non-milled <45 μm, non-milled <90 μm, burr milled <45 μm and burr milled <90 μm HD powders. Recycled re-sintered magnets, from HD powders with the same milling or sieving state, were studied to determine whether further milling and sieving steps were required in the HPMS process.

Table 4. List of the samples produced to study the influence of decreasing the particle

Starting Material	Burr Milling	Sieving
Hydrogen Decrepitated EOL VCM Magnets	No	45 µm
	Yes	45 µm
	No	90 µm
	Yes	90 µm

As already mentioned in section 5.2.7, all manufactured magnets were not heat treated. The resultant re-sintered magnets were analysed for magnetic properties and microstructural comparisons.

6.2 Results and discussion

In the present section, the results of the recycled magnets re-sintered from hydrogenated NdFeB powder from a range of different particle sizes are shown and discussed.

6.2.1 Density

The density and relative density of the samples studied are shown in table 5. The relative density is the percentage ratio between the experimental and the theoretical densities of the magnet, which, in the case of EOL VCM magnets, is 7.562 g cm^{-3}. This corresponds to the theoretical density using the composition shown in Table 2 in section 5.2.1.1.

Table 5. Density and relative density results of the EOL VCM magnet and the recycled re-sintered magnets from a range of different particle sizes.

Sample	Density [g cm^{-3}]	Relative density [%]
Starting material	7.59	99.98
Non-milled <90 µm	7.09	93.81
Burr milled <90 µm	7.33	96.90
Non-milled <45 µm	7.37	97.45
Burr milled <45 µm	7.46	98.59

Sieving to 90 µm has been demonstrated to be sufficient to remove all the nickel impurities when the HPMS process is used to separate NdFeB magnets from electronics as discussed in section 4.1.6 [Walton et al., 2015]. Nevertheless, to decrease the particle size of the powder to near single crystal particles, which is around 10 µm, then further milling and sieving would be required. To do so, sieving

to 45 μm has been used as sieves below this mesh size are not appropriate as they may be costly and particles will electrostatically stick beyond this point.

Results observed in table 5 show that the recycling process led to a reduction in density and, subsequently, in relative density, when compared with the EOL VCM magnet. An increase in the oxygen content of the hydrogenated powder could have caused partial oxidation of the highly reactive Nd-rich grain boundary phase (GBP). The source of this oxygen is the end-of-life magnet itself as shown by Farr [2013] in figure 52. Therefore, it came from primary production, specifically from the milling stage, as shown by Lien et al [1995] in figure 43. This oxidation results in less liquid phase during sintering because neodymium oxide has a higher melting point than the sintering temperature. This leads to incomplete sintering and to an increase in the porosity of the resultant magnet as there is insufficient redistribution of the liquid phase to fill all the present pores. This is in good agreement with previous studies in which density decreased when re-sintering EOL VCM magnets [Degri, 2013; Zakotnik et al, 2008; 2009].

It was found that recycled re-sintered magnets from burr milled HD powder led to a higher density in the final magnet, and hence relative density; than those from non-milled HD powder when sieving to the same size, as seen in table 5. By milling and sieving to 45 μm the density of the resultant re-sintered magnet was increased to 7.46 g cm^{-3} compared to 7.09 g cm^{-3} for non-milled HD powder sieved to 90 μm.

These results show that decreasing the particle size of the hydrogenated NdFeB powder either by burr milling, by sieving it to 45 μm or by both processes in conjunction led to more dense re-sintered magnets. With decreasing the particle size of the HD powder, the packing arrangement of the particles during the alignment and pressing is likely to be enhanced which could be the reason for higher densities being achieved..

6.2.2 Scanning Electron Microscopy

Figure 78 shows the back-scattered electron images obtained by SEM analysis of the studied samples and the EOL VCM magnet used as starting material.

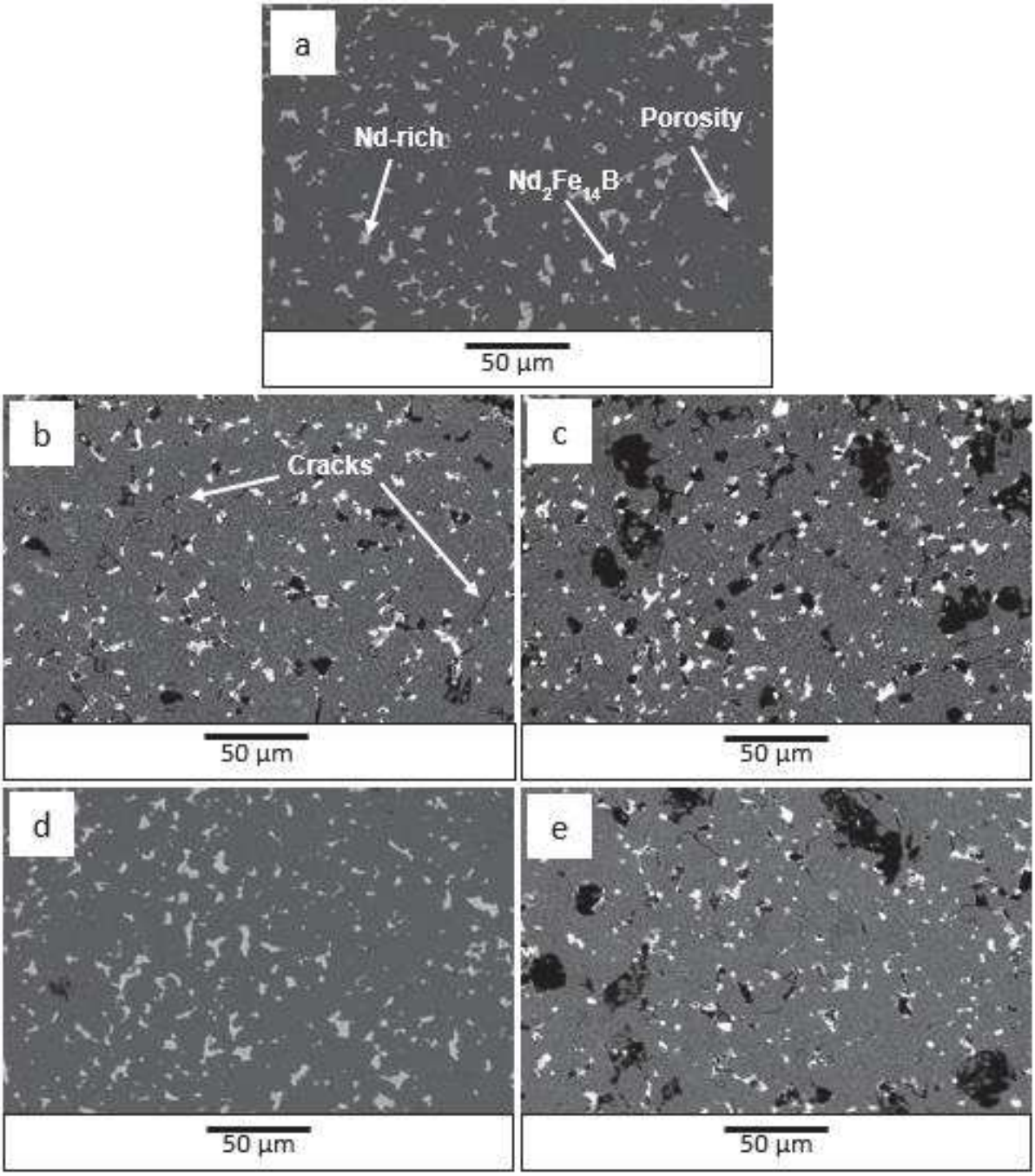

Figure 78. Back-scattered electron SEM images at 500 magnifications micrographs of (a) the EOL VCM magnet and the recycled re-sintered magnets from (b) non-milled and sieved < 45 µm, (c) non-milled and sieved < 90 µm, (d) burr milled and sieved < 45 µm and (e) burr milled and sieved < 90 µm HD powder.

As observed in table 5, the density of EOL VCM magnet is higher than that exhibited by any recycled re-sintered magnet. This difference is evident when comparing back-scattered electron images of both recycled re-sintered magnets from sieved to 90 μm HD powder, shown in figures 78(c) and 78(e), with the EOL VCM magnet used as starting material shown in figure 78(a); and even with the recycled magnet from sieved to 45 μm HD powder, shown in figures 78(b). However, the difference in density between the recycled re-sintered magnets from sieved to 45 μm HD powder, shown in figures 78(d) and the EOL VCM magnet is that small, that it is not possible to observe it in figure 78.

It is clear that more porosity is observed when larger HD particles are used to produce recycled re-sintered magnets in contrast to those produced from smaller particle sizes. These microstructural observations are supported by the values shown in table 5 and illustrate clearly the improved packing arrangement of the recycled re-sintered magnets when decreasing the particle size of the HD powder.

For all samples recycled, 78(b-e), some crack-like areas appeared along the grain boundaries, such as those indicated in figure 78(b). It could be attributed to the conjunction of two effects. On the one hand, the larger the particle size, the worse the packing arrangement and, therefore, the larger the amount of porosity. On the other hand, recycling results in an increase in the oxygen content, which decreases the amount of Nd-rich phase available for LPS during sintering. The decrease in LPS added to the increase in porosity led to porous grain boundaries that have the appearance of cracks

6.2.3 Mechanical Properties

The results of Vickers hardness HV 30 as well as the fracture toughness of the starting material and the recycled samples are presented in table 6.

Table 6. Vickers hardness HV 30 and fracture toughness for EOL VCM magnets and the recycled re-sintered magnets.

Sample	HV 30	K_{IC} [MPa $m^{1/2}$]
Starting material	604	3.13
Non-milled and 90 μm sieved	434	3.03
Burr milled and 90 μm sieved	475	3.08
Non-milled and 45 μm sieved	543	3.11
Burr milled and 45 μm sieved	567	3.12

By observing table 6 it can be concluded that recycling results in a drop in Vickers hardness when compared with the results from the EOL VCM magnet. As a consequence of the drop in density there is an increase in porosity, i.e. the amount of empty volume within the magnet, hence offering less resistance when indented. These results follow the same trend observed in density in table 5. This is due to the hardness is heavily influenced by the presence of porosity, hence increasing with decreasing the amount of porosity.

Typical Vickers hardness values of commercial sintered NdFeB magnets are between 535 and 610 HV10-40 [Ertan et al, 2013; Hu et al, 2014; Jiang et al, 2001; Wang et al, 2015], e.g. a magnet with composition $Nd_{15}Fe_{78}B_7$, very close to the commercial Neomax, $Nd_{15}Fe_{77}B_8$, accounts a Vickers hardness of 536 HV100 [Jiang et al, 2001].

Previous research have found that, when the load is above 1 kg, such parameter is of no influence in the Vickers hardness result [Chuenarrom et al, 2009; Takakuwa et al, 2014]. As a consequence, it may be possible to compare Vickers hardness results from previous studies to those obtained in this work.

Therefore, the value obtained for the EOL VCM magnet, 604 HV30, is comparable to the typical values indicated in the literature. Nonetheless, there are currently no studies either focused or including the Vickers hardness of the recycled re-sintered magnets.

The fracture toughness of recycled re-sintered magnets is lower than that of the EOL VCM magnet, as seen in table 6. This could be attributed to the cracks observed along the grain boundaries in figure 78 during SEM analysis.

Recycled re-sintered magnets from burr milled HD powder showed higher fracture toughness values than those from non-milled HD powder, as observed in table 6, when sieving was performed to the same mesh size. In addition, it is clear that when sieving to 45 μm the HD powder, either burr milled or non-milled, resulted in higher fracture toughness values than sieving it to 90 μm. All these results present the same trend as those observed in Vickers hardness as fracture toughness is greatly influenced by the density and the amount of porosity exhibited by the recycled re-sintered magnet.

As the recycled magnets contain cavities within the microstructure, the crack requires little energy expenditure to overcome it; whereas when that porosity is filled, some resistance appears, resulting in higher fracture toughness values. This inverse relationship between porosity and fracture toughness has been studied and confirmed in other sintered products, such as Fe [Shatsov et al, 2011], Mo [Sotnik et al, 2013], Al_2O_3 [Evans et al, 1972], Gd_2O_3 [Case et al, 1981], MgO [Matsushita et al, 1991] or Y_2O_3 [Rice, 1996]. However, no systematic studies have been performed on the relationship between density, porosity and fracture toughness on sintered NdFeB magnets to the authors knowledge.

Typical fracture toughness values of sintered magnets are between 2.20 and 5.50 MPa $m^{1/2}$ [Horton et al, 1996; Jiang et al, 2000; Jiang et al, 2001; Rabinovich et al, 1996; Hu et al, 2014]. This wide range of values is a consequence of the differences in composition, processing parameters and characterisation techniques employed. A magnet with composition $Nd_{15}Fe_{78}B_7$ shows a fracture toughness of 3.31 MPa $m^{1/2}$ [Rabinovich et al, 1996], which is comparable to that obtained in this study by the EOL VCM magnet, of 3.13 MPa $m^{1/2}$. Unfortunately, there are no studies including or focused on the fracture toughness of recycled re-sintered magnets.

In summary, increasing the density of the recycled re-sintered magnet, either by burr milling or by sieving, resulted in an improvement in the value of fracture toughness; although it was at every time lower than that of the EOL VCM magnet.

6.2.4 Magnetic Properties

The demagnetisation loops, measured on a permeameter at room temperature, of the EOL VCM magnets and the recycled re-sintered magnets from hydrogenated powder with different milling and sieving conditions shown as in table 4; are presented in figure 79. Table 7 shows the values of intrinsic coercivity, remanence and maximum energy product of each of the samples.

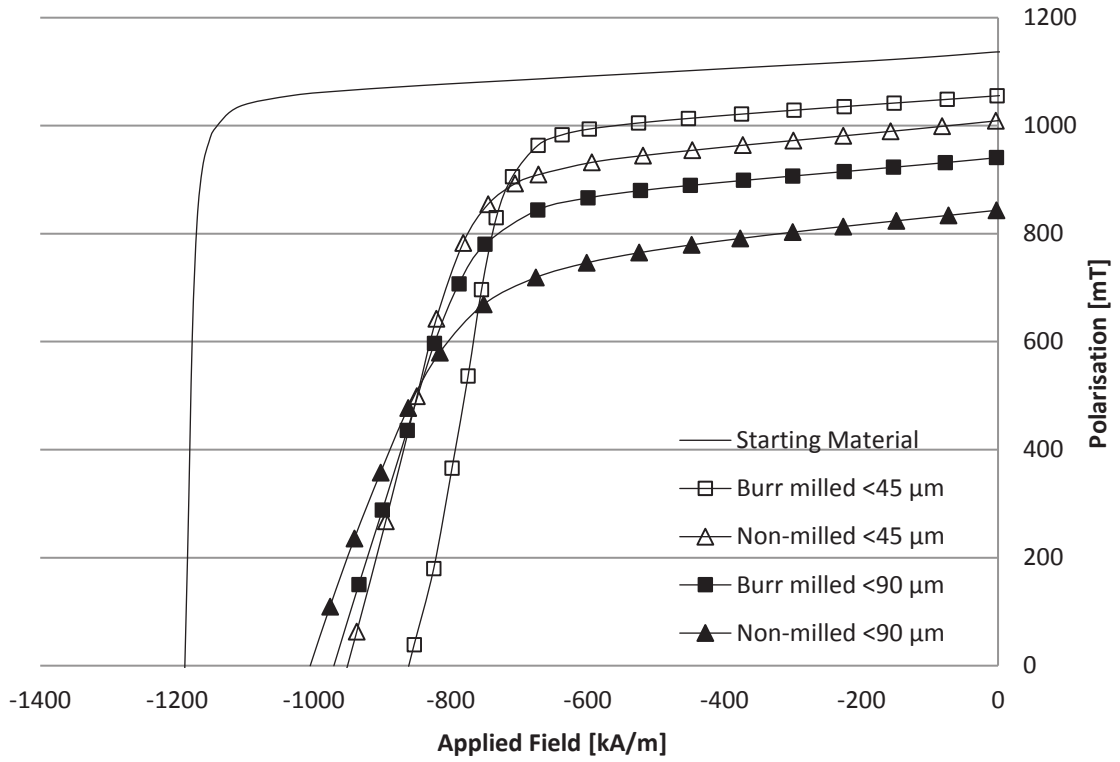

Figure 79. Demagnetisation loops of the EOL VCM magnet and the recycled re-sintered magnets with different particle sizes at room temperature.

Table 7. Magnetic properties of the EOL VCM magnet and the recycled re-sintered magnets with different particle sizes at room temperature.

Sample	Coercivity [kA m^{-1}]	Remanence [mT]	$(BH)_{max}$ [kJ m^{-3}]
Starting material	1191	1140	242
Non-milled <90 µm	1005	844	128
Burr milled <90 µm	971	942	162
Non-milled <45 µm	951	1011	189
Burr milled <45 µm	860	1059	203

Figure 79 and table 7 show that the recycled re-sintered magnets in all cases exhibit lower intrinsic coercivity, remanence and maximum energy product values at room temperature than the starting EOL VCM magnet. This reduction in magnetic properties is caused by the decrease in density of the recycled re-sintered magnets. This results in a high number of reverse domain nucleation sites at the pores within the material hence decreasing the coercivity. Moreover, the greater the porosity in the recycled magnet, the greater the non-magnetic volume in the magnet, which results in a reduction in remanence. These results are consistent with previous results which showed the same reduction in magnetic performance when recycling NdFeB magnets by re-sintering [Degri, 2013; Zakotnik et al., 2006; 2008; 2009; Li et al, 2015]. Zakotnik et al [2006; 2008; 2009] attributed the decrease in

remanence to the fact that recycled re-sintered magnets are produced from multigrained HD powder, therefore, it is unlikely that the alignment in the recycled magnet could be greater than that of the starting material.

It has been found that by decreasing the particle size to 45 μm, this led to a decrease in intrinsic coercivity but to an increase in the values of both remanence and maximum energy product at room temperature. When comparing the recycled re-sintered magnets made from non-milled <90 μm HD powder, which has the largest particle size, with those made from burr milled <45 μm HD powder, which has the smallest particle size, there is an increase in remanence of 215 mT (25.5%) and maximum energy product of 75 kJ m^{-3} (58.6%) at the expense of a reduction in intrinsic coercivity of 145 kA m^{-1} (14.4%). Therefore, decreasing the particle size of the HD powder recovers some of the magnetic performance lost due to the recycling process. The recycled re-sintered magnet from burr milled <45 μm HD powder recovered 72.2%, 92.9% and 83.9% of the intrinsic coercivity, remanence and maximum energy product when compared to the EOL VCM magnet used as starting material.

The increase in the remanence and maximum energy product indicates that better alignment of the magnetic grains is achieved with decreasing the particle size of the feedstock powder to near single crystal particles. It also implies, on the other hand, that either the larger, multigrained particles cannot rotate freely in the pulsed magnetic field, hence obtaining lower remanence values. Or, it implies that these particles are breaking apart during aligning and pressing, leading to a significant degree of misalignment. The reduction in density and increase in the level of porosity is also likely to be a major cause for the loss in remanence as there is a greater volume of non-magnetic free space.

The loss of Nd-rich GBP resulted in a reduced isolation of the $Nd_2Fe_{14}B$ matrix phase grains by forming rougher grain boundaries between these matrix grains, resulting in a decrease in the intrinsic coercivity. These results are backed up with microstructural images in section 6.2.2.

The squareness of the hysteresis of the recycled magnets is substantially reduced compared to the starting EOL VCM magnets as observed in figure 79. This indicates an increase in the misalignment

of grains with recycling. It can also be observed that the squareness is improved when decreasing the particle size of the feedstock powder, which implies better alignment is achieved, which is backed-up with the remanence results from table 7.

The demagnetisation loops of the EOL VCM magnet and the recycled re-sintered magnets from hydrogenated powder with a range of different particle sizes according to conditions shown in table 4 at 75 °C and 150 °C, are presented, respectively in figures 80 and 81.

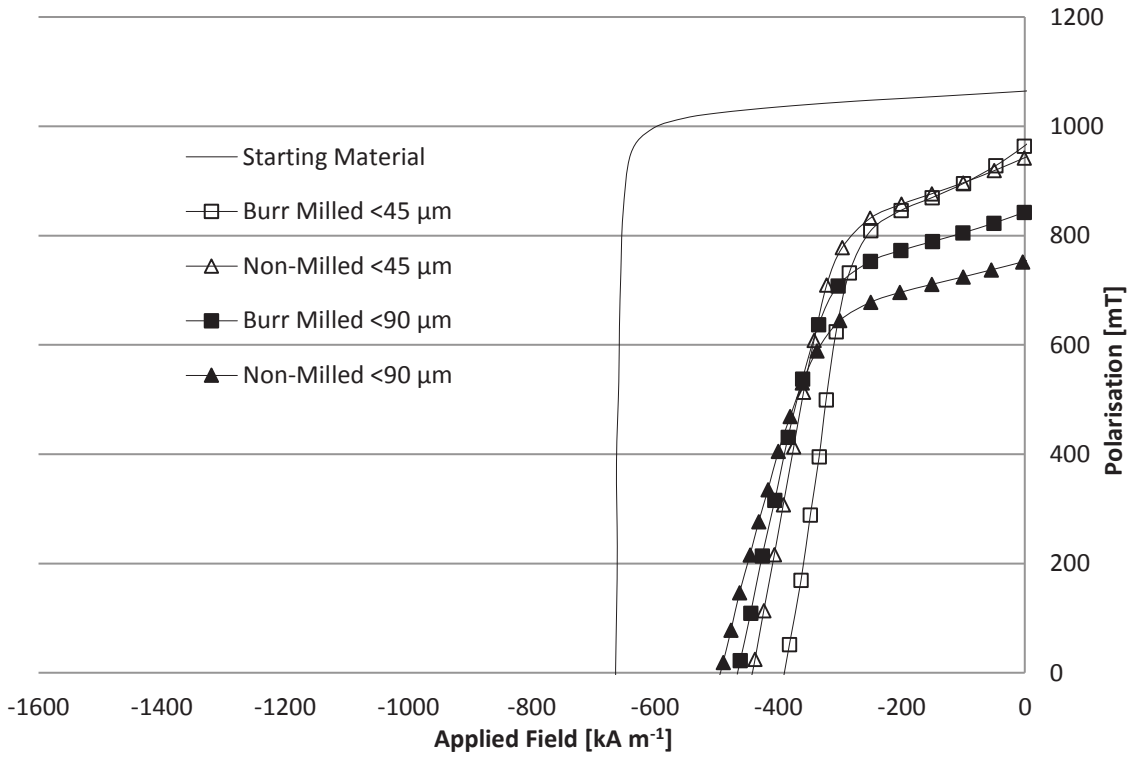

Figure 80. Demagnetisation loops of the EOL VCM magnet and the recycled re-sintered magnets with different particle sizes at 75 °C.

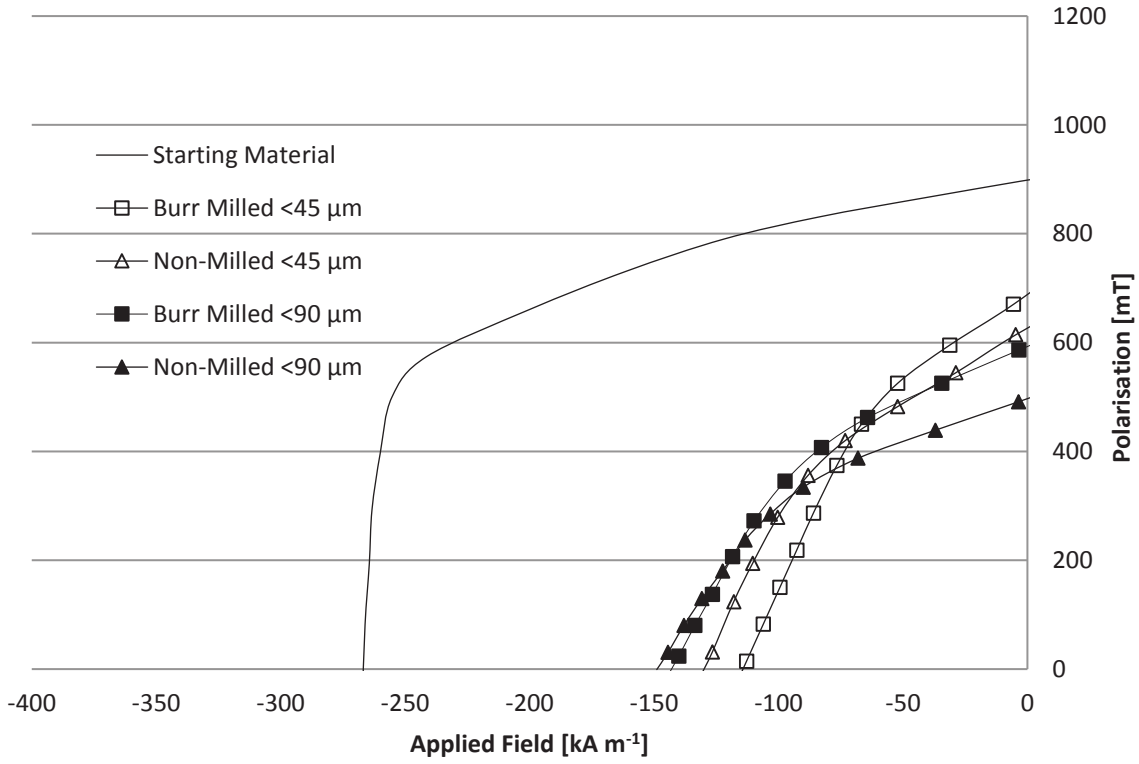

Figure 81. Demagnetisation loops of the EOL VCM magnet and the recycled re-sintered magnets with different particle sizes at 150 °C.

The results at 75 °C and 150 °C are also presented, respectively, in tables 8 and 9, including the values of intrinsic coercivity, remanence and maximum energy product. These temperatures were chosen as they are typical of the operating temperatures in wind turbines (75 °C) and in electric motors (150 °C). In addition, as these measurements were performed at 75 °C and 150 °C, respectively, the values of α and β are also included, which refer to the thermal stability of remanence and intrinsic coercivity between room temperature and the temperature at which the properties were measured.

Table 8. Magnetic properties of the EOL VCM magnet and the recycled re-sintered magnets with different particle sizes at 75 °C.

Sample	Coercivity [kA m^{-1}]	Remanence [mT]	$(BH)_{max}$ [kJ m^{-3}]	α [% $°C^{-1}$]	β [% $°C^{-1}$]
Starting material	666	1065	214	-0.120	-0.801
Non-milled <90 µm	494	748	90	-0.207	-0.924
Burr milled <90 µm	467	841	110	-0.195	-0.944
Non-milled <45 µm	444	938	128	-0.156	-0.969
Burr milled <45 µm	387	968	135	-0.131	-1.000

Table 9. Magnetic properties of the EOL VCM magnet and the recycled re-sintered magnets with different particle sizes at 150 °C.

Sample	Coercivity [kA m^{-1}]	Remanence [mT]	$(BH)_{max}$ [kJ m^{-3}]	α [% $°C^{-1}$]	β [% $°C^{-1}$]
Starting material	264	905	89	-0.158	-0.599
Non-milled <90 μm	148	498	21	-0.315	-0.655
Burr milled <90 μm	143	580	24	-0.296	-0.656
Non-milled <45 μm	128	630	25	-0.290	-0.666
Burr milled <45 μm	109	686	26	-0.271	-0.672

As with recycled re-sintered magnets tested at room temperature, it can be observed in figures 80 and 81 and in tables 8 and 9 that all the recycled re-sintered magnets showed lower values of intrinsic coercivity, remanence and maximum energy product than these exhibited by EOL VCM magnet at 75 and 150 °C.

As occurred at room temperature, it has been found that decreasing the particle size either by burr milling, by sieving it to 45 μm or by both, led to a decrease in intrinsic coercivity but to an increase in the values of both remanence and maximum energy product at 75 and 150 °C.

When comparing the recycled re-sintered magnets made from non-milled <90 μm HD powder, which has the largest particle size, with those made from burr milled <45 μm HD powder, which has the smallest particle size, there was an increase in remanence of 220 mT (29.4%) and 188 mT (37.7%) at 75 and 150 °C respectively, which led to an increase of 45 kJ m^{-3} (50%) and 5 kJ m^{-3} (23.8%) in maximum energy product respectively. That increase with decreasing the particle size occurred at the expense of a reduction in intrinsic coercivity of 107 kA m^{-1} (21.6%) and 39 kA m^{-1} (26.3%) at 75 and 150 °C respectively. Therefore, decreasing the particle size of the HD powder aids the recovery of the magnetic properties lost due to the recycling process both at room temperature and high temperatures.

At room temperature, thermal agitation is not sufficiently high to disrupt the alignment of hard the magnetic $Nd_2Fe_{14}B$ phase matrix grains but with increasing the temperature such grains starts to lose its alignment. Therefore, a degradation in both remanence and intrinsic coercivity, denoted as α and β, takes place when magnets are tested at high temperatures. In addition to the as-mentioned reduction in

properties, it can be observed that the squareness of magnets tested at 150 °C is lower than that exhibited at 75 °C, and this is lower than that observed at room temperature.

Commercial values of α are between -0.12 and -0.08% $°C^{-1}$ and only the recycled re-sintered magnet produced from burr milled and sieved to 45 μm HD powder has reached a competitive value of -0.131% $°C^{-1}$ in the range 20-75 °C.

Typical commercial values of β are between -0.60 and -0.45% $°C^{-1}$ and only the recycled re-sintered magnet produced from non-milled and sieved to 90 μm HD powder has reached a value able to compete with these, -0.655% $°C^{-1}$, in the range 20-150 °C.

The thermal stability of both remanence and intrinsic coercivity, at both temperature ranges, was deteriorated when comparing recycled re-sintered magnets with the EOL VCM sintered magnet.

The values of α in the starting EOL VCM magnets show that the remanence is much more stable in the range 20-75 °C, which implies that most of the degradation occurs in the range 75-150 °C. On the other hand, the results of β have shown the effect inverse to that occurred with α values. The thermal degradation of coercivity showed to be more stable in the 20-150 °C than in the 20-75 °C range.

In the 20-75 °C range, α improved when decreasing the particle size of the HD powder. In the same temperature range, β was deteriorated with decreasing the particle size.

In the 20-150 °C range, the values of α showed also an enhancement with decreasing the particle size as in the previous temperature range. However, the values obtained were lower compared with those obtained in the 20-75 °C range. The values of β exhibited a decrease with decreasing the particle size as occurred in the previous temperature range. Nevertheless, the values of β were higher and, hence improved significantly compared with those in the 20-75 °C range.

It should be noted that all manufactured magnets were not heat treated. In doing so, the microstructure was not modified and, as a consequence, the intrinsic coercivity was not further increased, as it was discussed in section 3.3.6.5.

6.2.5 Optical Microscopy

In figure 82 Kerr effect images obtained on an optical microscope in polarised light are shown of the perpendicular section to the c-axis of the samples studied are shown.

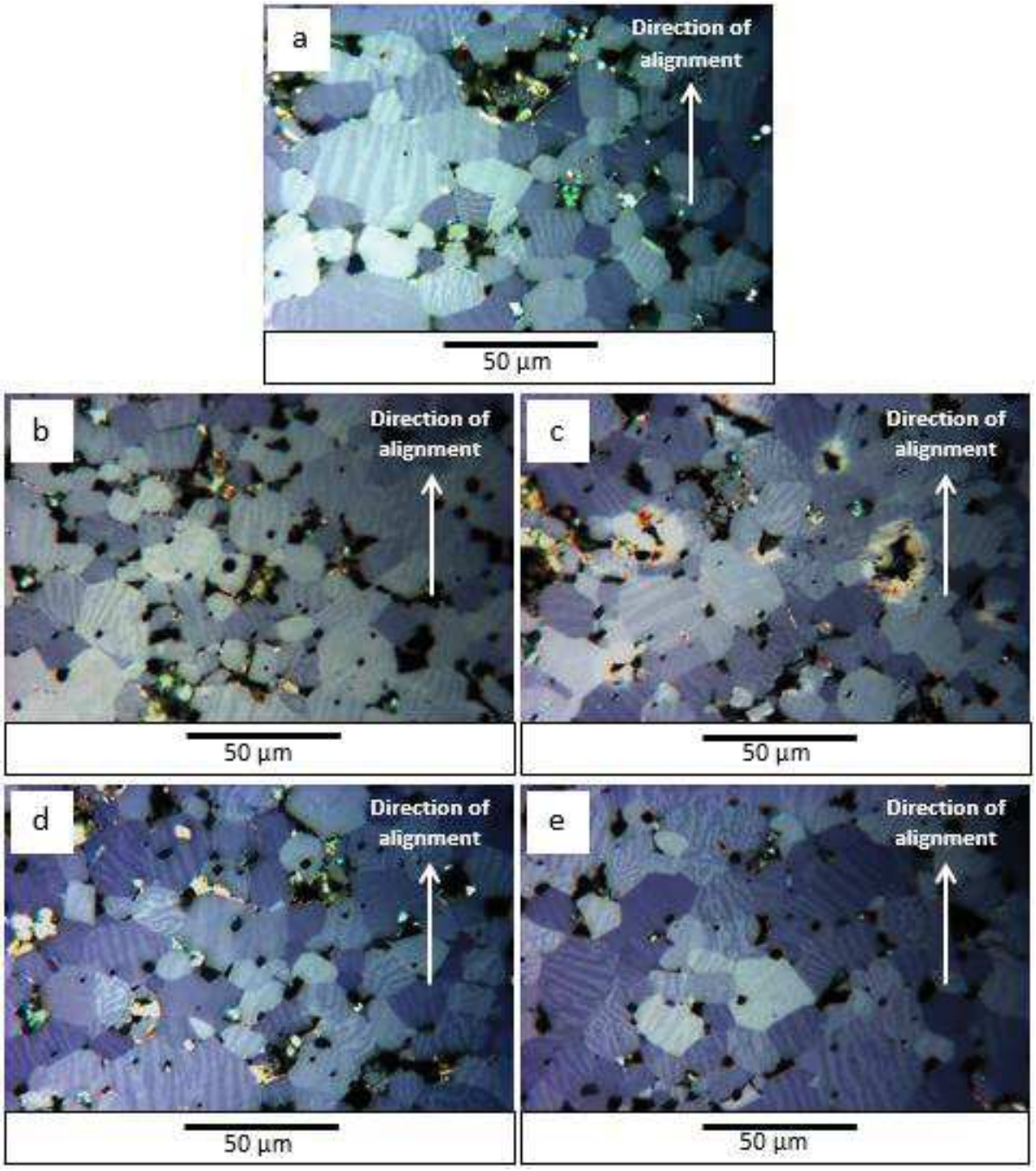

Figure 82. Kerr effect images of a transversal section perpendicular to the c-axis of (a) the EOL VCM magnet and the recycled magnets from (b) non-milled and sieved < 45 µm, (c) non-milled and sieved < 90 µm, (d) burr milled and sieved < 45 µm and (e) burr milled and sieved < 90 µm HD powder.

During Kerr effect microscopy, domains are observed as stripes when they are parallel to the direction of magnetization as NdFeB demonstrates strong uniaxial magnetocrystalline anisotropy. If there is perfect alignment, all the grains should show a striped pattern pointing in the same direction. The presence of grains with tilted stripes or a so called 'cog wheel' pattern would show that there is a degree of misalignment. Any misalignment of the grains would lead to a lowering of the remanence.

It can be observed that the EOL VCM magnet, in figure 82(a), exhibits a greater degree of alignment compared with the recycled re-sintered magnets, in figure 82(b-e). This observation is in good agreement with the results shown in figure 79 and table 7 in which the EOL VCM magnet showed higher remanence than any of the recycled re-sintered magnets.

It is clear from figure 82 that more misalignment of the grains can be observed in the recycled re-sintered magnets made from large particle size of HD powder. The magnets made from smaller particles sizes HD powder demonstrated the highest degree of alignment which is accompanied by the greater remanence as shown in figure 79. The increase in remanence could be therefore partly attributed to the enhancement in the degree of alignment. As already mentioned, it also implies, that either the larger, multigrained particles cannot rotate in the pulsed magnetic field, hence obtaining lower remanence values, or that these particles are breaking apart during aligning and pressing, leading to more misalignment of the grains.

These results are in accordance with previous studies on primary NdFeB alloys [Kawai et al, 1990; Gao et al, 1998; Cui et al, 2013], which described a sharp decrease in intrinsic coercivity and an increase in remanence and maximum energy product with the enhancement of the degree of alignment.

Gao et al [1998] attributed the increase in remanence to the enhancement in the degree of alignment whereas the decrease in intrinsic coercivity was interpreted by the starting field theory of the coercivity [Kawai et al, 1990; Gao et al, 1995].

From what it has been shown and discussed along this chapter, it is clear that it is important to reduce the particle size of the HD powder prior to re-sintering. Therefore, all powders have been burr milled and sieved to 45 μm in chapter 7.

Chapter 7. Neodymium Hydride Blending

7.1 Introduction

Powder blending of neodymium hydride into the hydrogenated NdFeB powder has been reported to be an effective approach to recover much of the magnetic performance lost during the re-sintering process [Zakotnik et al, 2009]. However, in previous work the blending of neodymium hydride was not systematically studied to map the improvement in magnetic performance.

Therefore, in this study, different percentages of neodymium hydride, shown in table 10, were added to the hydrogenated NdFeB powder. To systematically study the influence of this addition on the magnetic properties and microstructure of the resultant magnets, samples were produced with each ratio of neodymium hydride.

In spite that the dihydride form of neodymium is more stable than the trihydride form [Verdier et al, 1994], as explained in section 3.3.3.4; it requires one additional stage on preparation of the powder before blending, which makes the process more complex. In addition, it may increase the risk of contamination of the neodymium compound.

On the other hand, rare earth hydride powders are more stable than the corresponding metal forms [Mottram et al, 1999], which reduces the risk of oxygen uptake. In addition, previous research has found that using the trihydride form has led to good properties of the recycled magnets [Li et al, 2014; Liu et al, 2015; Mottram et al, 1999; Zakotnik et al, 2009].

Table 10. List of the samples produced to study the influence of blending neodymium hydride.

Starting Material	Additions
Sieved <45 µm Burr Milled HD EOL VCM Magnets	0 at% $NdH_{2.7}$
	1 at% $NdH_{2.7}$
	2 at% $NdH_{2.7}$
	3 at% $NdH_{2.7}$
	4 at% $NdH_{2.7}$
	5 at% $NdH_{2.7}$

As the best results obtained in chapter 6 were for magnets produced from burr milled and sieved HD powders below 45 μm, then that material has been used as the starting material in the present chapter.

7.2 Results and Discussion

In the present section the results of the magnets re-sintered from hydrogenated NdFeB powder blended with different percentages from 0 to 5 at% of neodymium hydride are shown and discussed.

7.2.1 Density

The density and relative density of the samples studied are shown in table 11.

Table 11. Density and relative density results of the EOL VCM magnet and the recycled re-sintered magnets blended with different $NdH_{2.7}$ contents.

Sample	Density [g cm^{-3}]	Relative density [%]
Starting material	7.59	99.98
0 at%	7.46	98.59
1 at%	7.54	99.84
2 at%	7.52	99.72
3 at%	7.50	99.68
4 at%	7.48	99.59
5 at%	7.46	99.44

Table 11 shows that recycled re-sintered magnets blended with zero neodymium hydride resulted in a decrease in density and, as a consequence, relative density, when compared with the results from the starting EOL VCM magnet. As mentioned previously, an increase in the oxygen content of the HD powder could cause partial oxidation of the Nd-rich phase, resulting in less liquid phase during sintering leading to incomplete sintering and hence an increase in porosity.

It was found that by adding 1 at% $NdH_{2.7}$ the density increased to 7.54 g cm^{-3}, however, for every additional 1 at% $NdH_{2.7}$, the density reduced linearly by 0.02 g cm^{-3}. Despite the decrease in density with additions greater than 1 at%, the relative density of all samples was above 99.44%.

The increase in density from 0 to 1 at% neodymium hydride is based on the ability of neodymium to melt, flow and fill the porosity during sintering. All samples blended with neodymium hydride showed

a higher density and relative density than that of the magnet re-sintered with zero additions, which is consistent with previous results [Degri, 2013; Mottram et al, 1999; Zakotnik et al, 2009].

The continuous decrease in density with increasing the neodymium hydride content is due to the lower theoretical density of the neodymium hydride of just 7.009 g cm^{-3} compared to the theoretical density of VCM magnets of 7.562 g cm^{-3}. Therefore, the higher the neodymium hydride content, the lower the theoretical maximum density of the resultant magnet.

7.2.2 Scanning Electron Microscopy

Figure 83 shows the back-scattered SEM images of the recycled re-sintered magnets blended with different $NdH_{2.7}$ contents.

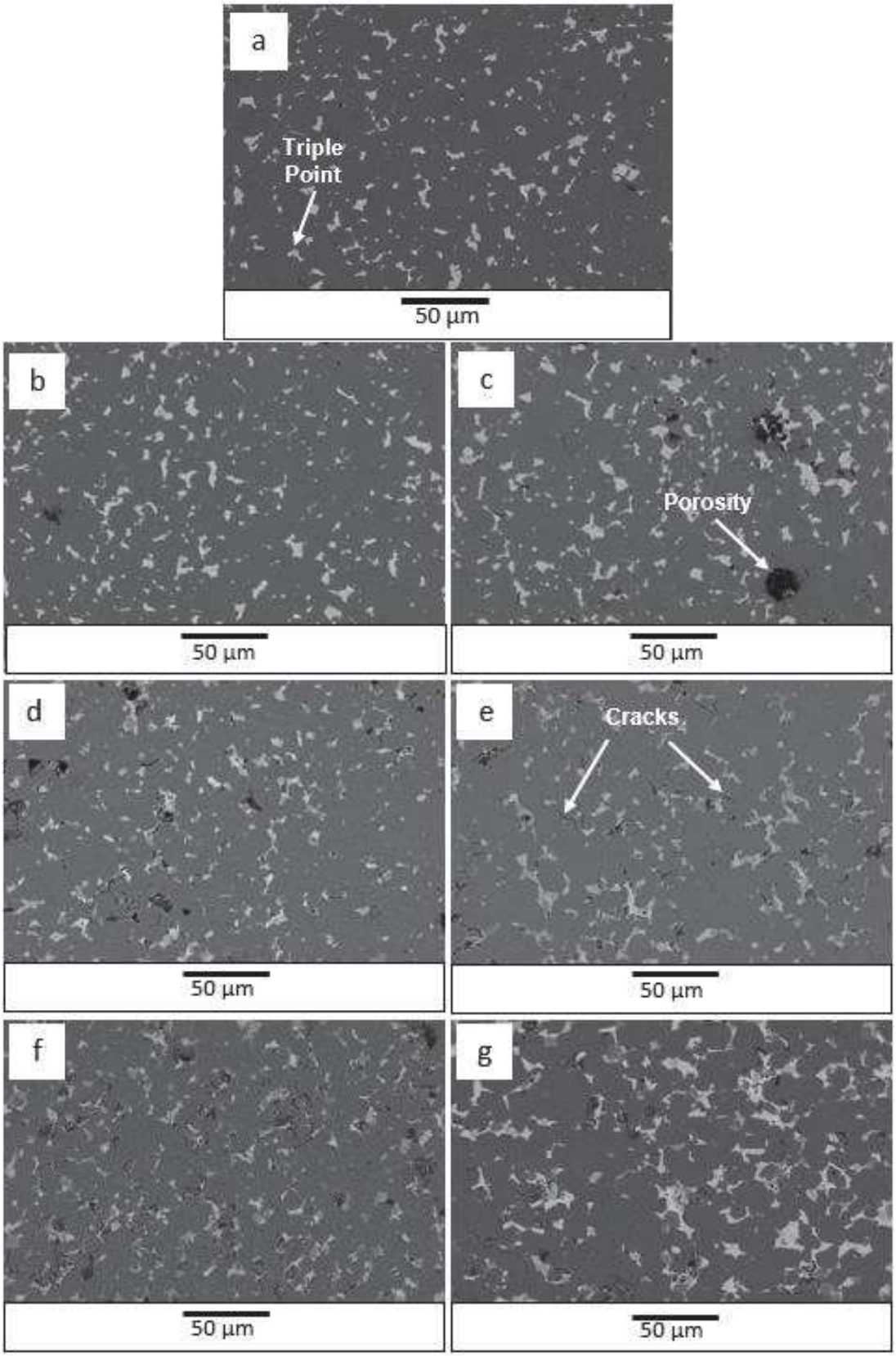

Figure 83. Back-scattered electron SEM images at 500 magnifications micrographs of (a) the EOL VCM magnet and of the recycled re-sintered magnets blended with (b) 0 at%, (c) 1 at%, (d) 2 at%, (e) 3 at%, (f) 4 at%, and (g) 5 at% neodymium hydride.

It can be observed that with increasing the amount of blended neodymium hydride, there is an enhancement in smoothing and isolation of the hard magnetic $Nd_2Fe_{14}B$ grains due to increased proportions of grain boundary phase (GBP) as previously reported by Mottram et al [1999] for primary alloys.

The BSE SEM images in figure 83 exhibit a subsequent increase in the Nd-rich phase presence with increasing neodymium hydride content. It can be observed that, with increasing neodymium hydride content, the recycled re-sintered magnets show larger triple points which evidences a heterogeneous distribution of the Nd-rich phase across the sample in all cases. This is in accordance with previous investigations [Li et al, 2014].

The GBP in figure 83 appears to be dual phase comprising the Nd-rich and a neodymium oxide phase as a consequence of the increase in oxygen. This can be better seen in figure 84.

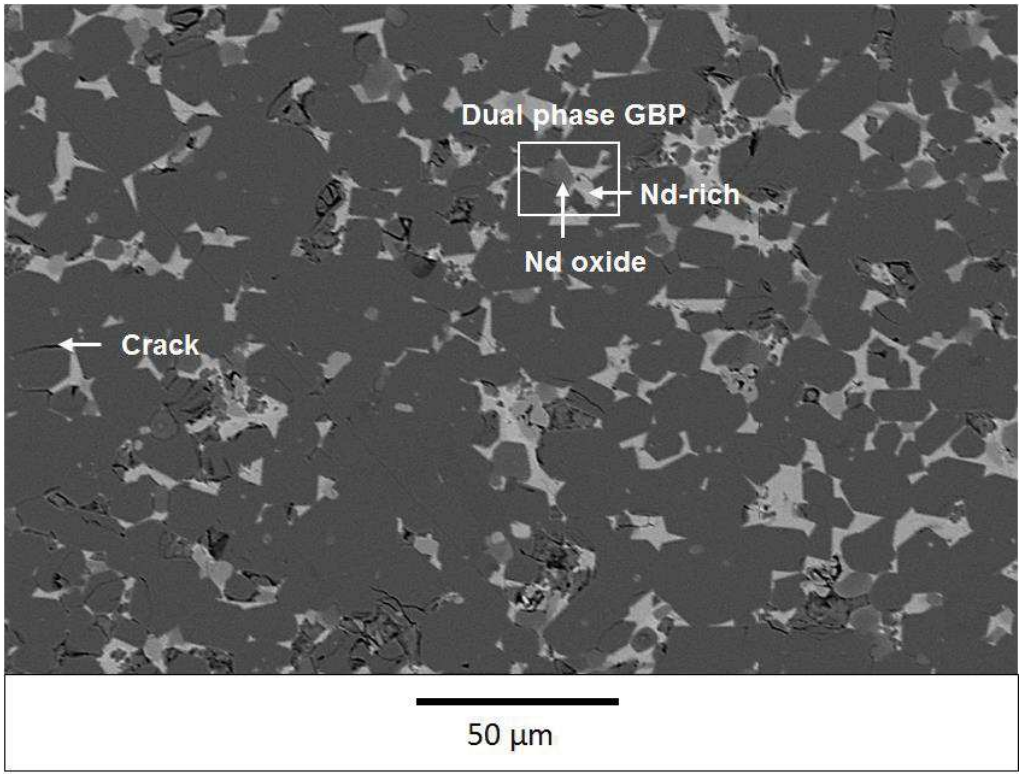

Figure 84. Back-scattered electron SEM image at 500 magnifications of the recycled re-sintered magnets blended with 5 at% neodymium hydride.

It is the first time that this dual phase GBP has been observed in BSE SEM micrographs of recycled material. The appearance of this neodymium oxide phase demonstrates the need for adding neodymium hydride in order to increase the effective amount of GBP available for liquid phase sintering. It is evident that with increasing neodymium hydride content that eventually the oxide phases become embedded in the new Nd-rich phase which leads to a reduction in cracking.

In addition, as seen from figure 83, grains seem to grow with increasing content of neodymium hydride. To study the grain size, the samples were etched using citric acid prior to image analysis; and the results are shown in table 12.

Table 12. Comparison of grain size of the recycled re-sintered magnets with increasing neodymium hydride content. All parameters expressed in μm.

Sample	Average	Maximum	Minimum	Median	Mode	Standard Deviation
EOL VCM magnet	7.71	23.07	1.36	7.42	7.50	2.83
0 at%	8.79	26.85	1.70	8.35	7.20	3.73
1 at%	8.86	22.76	1.87	8.52	8.00	3.49
2 at%	8.89	23.00	1.93	8.62	8.70	3.48
3 at%	8.95	27.76	2.01	9.64	8.00	3.45
4 at%	9.46	28.52	1.66	8.92	7.90	3.78
5 at%	12.64	38.62	2.99	11.73	9.70	5.42

From table 12 it can be concluded that grain growth occurs in recycled re-sintered magnets with increasing neodymium hydride content. The formation of larger grains during liquid phase sintering may have resulted in a worse packing arrangement and, hence, larger triple points to fill these cavities.

These results are consistent with previous studies [Degri, 2013; Li et al, 2014; Liu et al, 2015; Zakotnik et al, 2009]. Li et al [2014] found that the grain size of recycled re-sintered magnets increased with increasing blended content from 0 to 3 wt% of $(Nd_{20}Dy_{80})_{76}Co_{20}Cu_3Fe_1$ and was, in every case, higher than that exhibited by the scrap EOL VCM magnet. Liu et al [2015] reported a continuous increase in grain size with increasing content from 0 to 2 wt% of dysprosium hydride, added by powder blending, in recycled re-sintered magnets. Degri [2013] found the grain size to increase when EOL VCM magnets were recycled by powder blending with 2 at% neodymium hydride. It was reported that this increase was likely to have caused the recycled re-sintered magnets to exhibit an intrinsic coercivity value lower than that shown by the starting sintered NdFeB magnets.

Zakotnik et al [2009] reported the increase in grain size of re-sintered magnets with 0 and 1 at% neodymium hydride blended after multiple recycling cycles. The grain size of magnets blended with 1 at% was reported to increase moderately whereas those blended with 0 at% increased dramatically. This controlled increase in grain size in magnets blended with 1 at% was attributed to the formation of neodymium oxide at the grain boundaries, hindering the grain growth of recycled re-sintered magnets blended with neodymium hydride.

Nevertheless, it is the first time the grain size of final magnets is studied for systematic neodymium hydride additions.

The heterogeneous distribution of the Nd-rich can be attributed to the particle size of the neodymium hydride additions, which may have been coarse enough to hinder a homogeneous distribution. Therefore, it is suggested that preparation of neodymium hydride by further increased milling times, sieving through smaller sizes and also by using high-energy milling techniques such as jet milling, will lead to a small average particle size that could result in a more homogeneous distribution. This could also have a beneficial effect in magnetic performance as the hard magnetic grains would be better isolated at a potential lower rare earth content.

For all recycled re-sintered samples some cracks, as shown in figures 83(d) and 84, as well as in section 6.2.2, appeared along the grain boundaries. Li et al [2014] reported the appearance of cracks along grain boundaries when scrap NdFeB powders were blended with >2 at% REE-rich alloy of composition $(Nd_{20}Dy_{80})_{76}Co_{20}Cu_3Fe_1$. The formation of cracks was attributed to the desorption of hydrogen during sintering of the recycled re-sintered magnets.

7.2.3 Mechanical Properties

The Vickers hardness HV 30 and the fracture toughness of the EOL VCM magnet and the recycled re-sintered magnets with different $NdH_{2.7}$ contents are presented in table 13.

Table 13. Vickers hardness HV 30 and fracture toughness results of the EOL VCM magnets and the recycled re-sintered magnets.

Sample	HV 30	K_{IC} [MPa $m^{1/2}$]
Starting material	604	3.13
0 at%	567	3.12
1 at%	525	3.31
2 at%	499	3.41
3 at%	461	3.85
4 at%	446	3.95
5 at%	396	4.01

Table 13 shows that recycled re-sintered magnets with zero neodymium hydride led to a reduction in the Vickers hardness compared to the starting EOL VCM magnet. This decrease is likely to be due to the increase in porosity (i.e. empty volume) of the recycled magnets as previously discussed.

Recycling re-sintered magnets with increasing neodymium hydride content resulted in a linear decrease in Vickers hardness. This was attributed to the low Vickers hardness of neodymium of just 262 HV10-40 [Jiang et al, 2001], compared to that of the EOL VCM magnet of 607 HV30.

Typical Vickers hardness values of sintered NdFeB magnets are between 535 and 600 HV10-40 [Ertan et al, 2013; Hu et al, 2014; Jiang et al, 2001; Wang et al, 2015]. Therefore, the value obtained for the EOL VCM magnet, 604 HV30, is comparable to those typical values indicated in the literature. However, as mentioned in section 6.2.3, there are no studies on the Vickers hardness of recycled re-sintered magnets.

The fracture toughness of recycled re-sintered magnet with 0 at% neodymium hydride exhibited a decrease in fracture toughness compared to that of the EOL VCM magnet, as observed in table 13. This reduction was attributed to the decrease in density and, as a consequence, the increase in porosity within the magnet, which offers no resistance to crack propagation, and hence reduced fracture toughness.

By powder blending neodymium hydride into the burr milled HD powder from EOL VCM magnets resulted in an enhancement of the fracture toughness of the tested magnets. As NdFeB exhibits intergranular fracture, i.e. cracks propagate along the grain boundaries, increasing the GBP results in

an increase of the fracture toughness of the recycled magnets. The fracture toughness of pure neodymium is between 25 and 55 MPa $m^{1/2}$, which is one order of magnitude higher than the values demonstrated by NdFeB, which are typically between 2.20 and 5.50 MPa $m^{1/2}$ [Horton et al, 1996; Jiang et al, 2000; Jiang et al, 2001; Rabinovich et al, 1996; Hu et al, 2014]. As shown in figure 83, the neodymium hydride occupies the GBP and, as a consequence, increases the resistance to crack propagation, leading to greater fracture toughness compared to the EOL VCM magnet.

The fracture toughness of recycled re-sintered magnets achieved a maximum when 5 at% neodymium hydride was blended of 4.01 MPa $m^{1/2}$, which is an increase of 28.1% compared to the starting EOL VCM magnet. Commercial magnets have shown fracture toughness values between 3.90 and 4.40 MPa $m^{1/2}$ [Horton et al, 1996]. The values obtained in this work by recycled re-sintered magnets, especially for 4 and 5 at% neodymium hydride additions, are comparable to commercial primary NdFeB magnets.

There are currently no known studies on the mechanical properties of the recycled re-sintered magnets. Therefore, this study is the first such report of the impact of the re-sintering route on mechanical performance.

7.2.4 Magnetic Properties

The demagnetisation loops of the EOL VCM magnet and the recycled re-sintered magnets blended with different $NdH_{2.7}$ contents, as shown in table 10, tested at room temperature are presented in figure 85, and table 14.

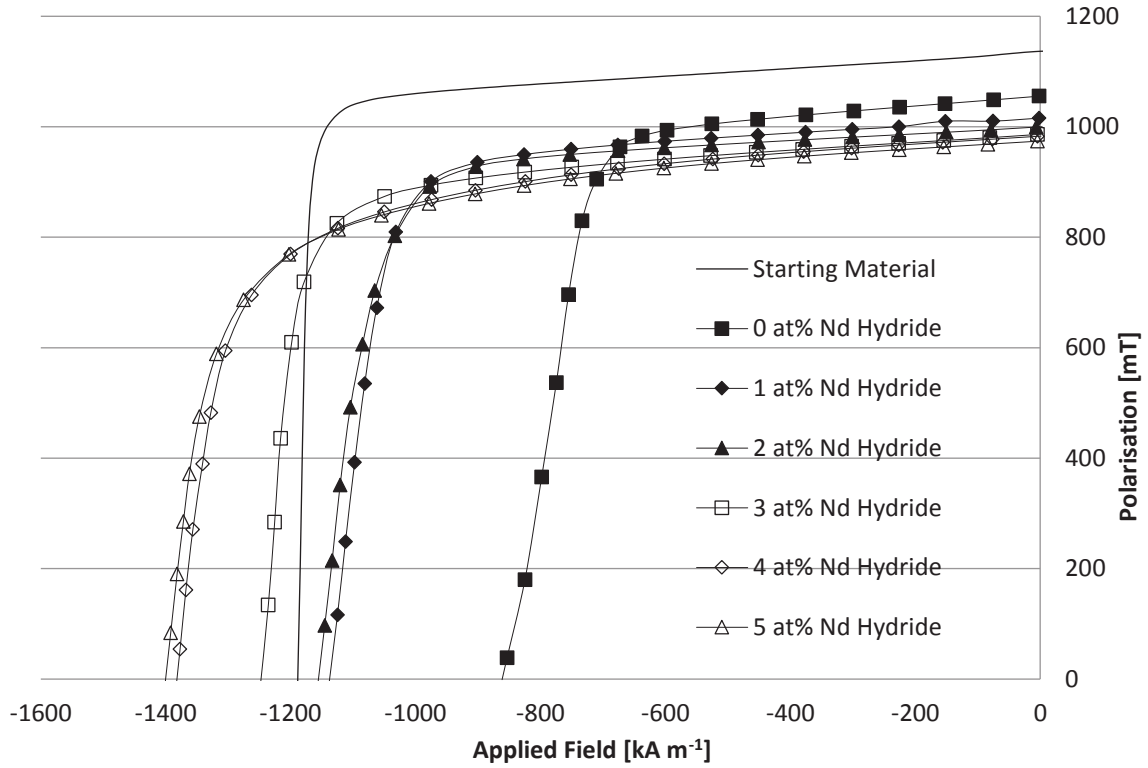

Figure 85. Demagnetisation loops of the EOL VCM magnet and the recycled re-sintered magnets blended with different $NdH_{2.7}$ contents at room temperature.

Table 14. Magnetic properties of the EOL VCM magnet and the recycled re-sintered magnets blended with different $NdH_{2.7}$ contents at room temperature.

Sample	Coercivity [kA m^{-1}]	Remanence [mT]	$(BH)_{max}$ [kJ m^{-3}]
Starting material	1191	1140	242
0 at%	860	1059	203
1 at%	1138	1016	194
2 at%	1155	999	189
3 at%	1246	987	183
4 at%	1381	984	182
5 at%	1400	975	179

Figure 85 and table 14 show that by adding no extra neodymium hydride this led to a recycled re-sintered magnet with a decrease in magnetic properties. The intrinsic coercivity, remanence and maximum energy product were reduced by 27.8%, 7.1% and 16.1% respectively, compared with the starting material. These values are in good agreement with those reported by Zakotnik et al. [2008a], which were 20%, 10% and 15% respectively. This decrease is due to multiple factors which were discussed in the previous chapter.

It has been found that increasing the amount of neodymium hydride blended led to an increase in intrinsic coercivity but to a decrease in remanence and maximum energy product of the recycled re-sintered magnets.

The remanence was expected to decrease as the proportion of hard magnetic $Nd_2Fe_{14}B$ matrix phase decreases with the addition of neodymium hydride, which is paramagnetic. This is in good agreement with previous investigations [Zakotnik et al, 2008; 2009; 2015] and follows the same trend as the degree of porosity from chapter 5. The decrease in remanence results in a subsequent drop in the value of the maximum energy product.

The subsequent addition of neodymium hydride led to an increase in intrinsic coercivity which can be attributed better smoothing and isolation of the $Nd_2Fe_{14}B$ grains due to increased proportions of GBP as previously reported by Mottram et al. [1999] in powder blending of $NdH_{2.7}$ with primary cast alloys. Unlike previous studies, in this case the neodymium hydride was added systematically up to 5 at% to optimise the proportion of GBP. In previous research using neodymium hydride, only 2 at% was added [Zakotnik et al, 2015].

The intrinsic coercivity at room temperature of the recycled re-sintered magnets blended with 3, 4 and 5 at% neodymium hydride exceeded that for the EOL VCM magnet by 4.6%, 15.9% and 17.5%, respectively. This increase in intrinsic coercivity occurred at the expense of a drop in remanence and maximum energy product. Blending 5 at% neodymium hydride, compared with 0 at% additions, resulted in an increase in intrinsic coercivity of 62.8% at the expense of a reduction in remanence of 7.9% and in maximum energy product of 11.8%. This is in agreement with previous results by Zakotnik et al [2015] who blended either 0.5, 2 or 3 at% of $(Nd_{0.22}Dy_{0.78})(Co_{0.84}Cu_{0.12}Fe_{0.04})_{0.84}$, with EOL NdFeB prior to HD, to increase the intrinsic coercivity at the expense of both the remanence and the maximum energy product.

The demagnetisation loops of the EOL VCM magnet and the recycled re-sintered magnets blended with $NdH_{2.7}$ from 0 to 5 at% were also tested at 75 and 150 °C, and they are presented respectively in figures 86 and 87.

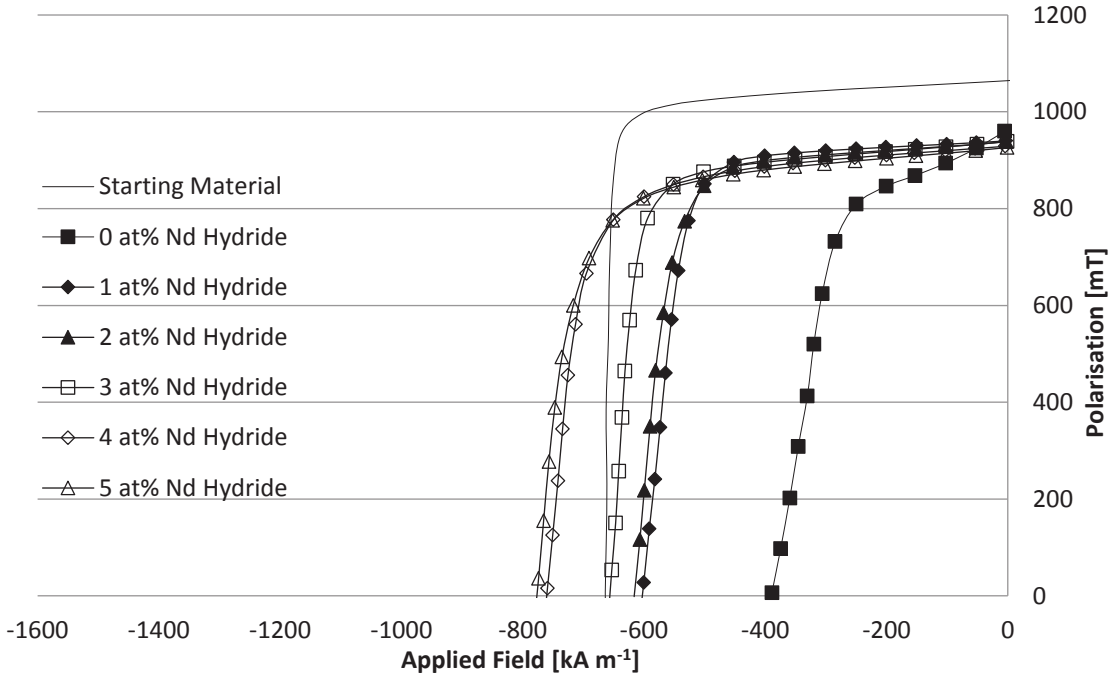

Figure 86. Demagnetisation loops of the EOL VCM magnet and the recycled re-sintered magnets blended with different $NdH_{2.7}$ contents at 75 °C.

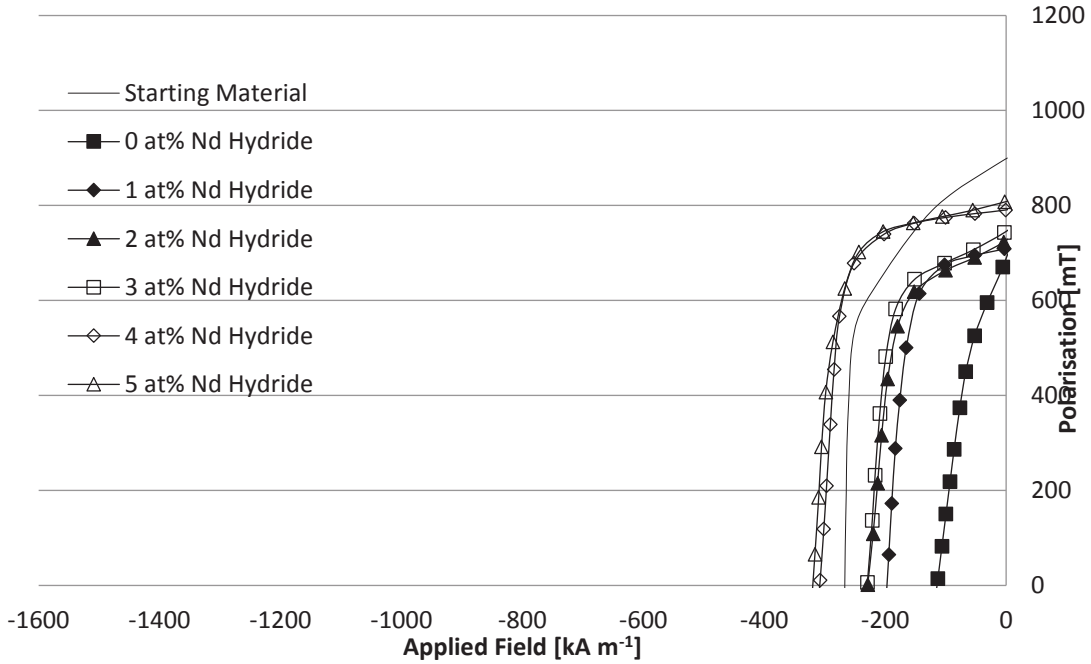

Figure 87. Demagnetisation loops of the EOL VCM magnet and the recycled re-sintered magnets blended with different $NdH_{2.7}$ contents at 150 °C.

The results at 75 °C and 150 °C are also presented, respectively, in tables 15 and 16, including the values of intrinsic coercivity, remanence and maximum energy product. In addition, as these measurements were performed at 75 °C and 150 °C, respectively, the values of α and β, which refer to the thermal stability of remanence and intrinsic coercivity between room temperature and the temperature at which the properties were measured, are also included.

Table 15. Magnetic properties of the EOL VCM magnet and the recycled re-sintered magnets blended with different $NdH_{2.7}$ contents at 75 °C.

Sample	Coercivity [kA m^{-1}]	Remanence [mT]	$(BH)_{max}$ [kJ m^{-3}]	α [% $°C^{-1}$]	β [% $°C^{-1}$]
Starting material	666	1065	214	-0.120	-0.801
0 at%	387	968	135	-0.156	-1.000
1 at%	602	940	174	-0.136	-0.862
2 at%	612	938	162	-0.111	-0.856
3 at%	655	936	161	-0.102	-0.855
4 at%	760	929	157	-0.094	-0.817
5 at%	779	925	155	-0.093	-0.806

Table 16. Magnetic properties of the EOL VCM magnet and the recycled re-sintered magnets blended with different $NdH_{2.7}$ contents at 150 °C.

Sample	Coercivity [kA m^{-1}]	Remanence [mT]	$(BH)_{max}$ [kJ m^{-3}]	α [% $°C^{-1}$]	β [% $°C^{-1}$]
Starting material	264	905	89	-0.158	-0.599
0 at%	109	686	26	-0.271	-0.672
1 at%	196	709	53	-0.232	-0.637
2 at%	229	726	65	-0.210	-0.618
3 at%	246	750	75	-0.185	-0.617
4 at%	299	775	93	-0.163	-0.603
5 at%	320	809	99	-0.131	-0.593

One of the most important issues of magnets for motor applications is thermal stability. Such components are often exposed to severe thermal conditions which may vary from 75 °C in wind turbines to 150 °C in automotive motors. Therefore, the thermal stability of remanence (α) and coercivity (β) are very important parameters for motor designers and engineers.

Values of α improved in both studied temperature ranges with increasing neodymium hydride content. It must be noted that α was higher in the range 20-75 °C for all samples, hence evidencing that samples are more thermally stable in that range. On the other hand, it implies that most of the degradation in remanence occurs in the range 75-150 °C.

Commercial values of α are typically between -0.12 and -0.08% $°C^{-1}$. Samples with neodymium hydride contents between 2 and 5 at% exhibit an α very similar to that of commercial magnets in the range 20-75 °C, reaching a maximum of -0.093% $°C^{-1}$ when 5 at% neodymium hydride is blended. Between 2 and 5 at% neodymium hydride, the recycled magnets showed an α superior to that exhibited by the EOL VCM magnet, of -0.120% $°C^{-1}$. However, in the range of temperatures 20-150 °C, only the re-sintered magnet blended with 5 at% neodymium hydride yielded an α value, of -0.131% $°C^{-1}$, comparable to commercial sintered magnets. At 5 at% neodymium hydride, the α value of the recycled magnet surpassed that of the EOL VCM magnet, of -0.158% $°C^{-1}$ and hence exhibiting a better thermal stability of remanence in both temperature ranges than the EOL VCM magnet.

The thermal stability of coercivity was enhanced in both temperature ranges with increasing neodymium hydride content.

Typical commercial values of β are typically between -0.60 and -0.45% $°C^{-1}$, only the recycled re-sintered magnet with 5 at% neodymium hydride fitted into this criteria, exhibiting a β value of -0.593% $°C^{-1}$ in the range 20-150 °C which, in addition, exceeds that shown by the EOL VCM magnet, of -0.599% $°C^{-1}$. Nonetheless, recycled re-sintered magnets blended with between 2 and 4 at% neodymium hydride were reasonably close to those values from both commercial and EOL VCM magnets as they showed β values between -0.618 and -0.603% $°C^{-1}$.

As opposed to room temperature measurements, it can be observed from figures 86 and 87 and tables 15 and 16 that not all recycled re-sintered magnets blended with neodymium hydride exhibited lower intrinsic coercivity values than those exhibited by EOL VCM magnet at 75 and 150 °C. It can be observed that, at both testing temperatures, the intrinsic coercivity of recycled re-sintered magnets blended with 4 and 5 at% neodymium hydride exceeded that of the starting EOL VCM magnets by 13.3 to 21.1%.

As with room temperature measurements, it can be observed in figures 86 and 87 and tables 15 and 16 that all recycled re-sintered magnets showed lower values of remanence than those exhibited by EOL VCM magnet at 75 and 150 °C.

At both 75 and 150 °C the intrinsic coercivity increased with neodymium hydride content as seen in figures 86 and 87 and in tables 15 and 16. The remanence at 75 °C decreased with increasing neodymium hydride content whereas the maximum energy product peaked at 1 at% neodymium hydride addition and then decreased. At 150 °C, in contrast, the remanence and the maximum energy product increased linearly as a consequence of the different thermal stability of each material. The intrinsic coercivity, remanence and maximum energy product decreased with increasing temperature as thermal agitation becomes sufficiently high to disrupt the alignment of the material.

Blending 3 at% neodymium hydride leads to an increase in relative density, coercivity, α, β and fracture toughness; however a reduction in remanence, maximum energy product and Vickers hardness in the recycled magnets compared with those blended with zero neodymium hydride. This amount of neodymium hydride recovers the intrinsic coercivity of the starting EOL VCM magnet.

It should be noted that all manufactured magnets were not heat treated, as mentioned in section 5.2.7. Nevertheless, performing a heat treatment on as-sintered magnets is highly beneficial in order to further increase the value of intrinsic coercivity, as it was discussed 3.3.6.5. Therefore, investigating the effect of heat treatments on the microstructure and both magnetic and mechanical properties of recycled Nd-Fe-B magnets is of great interest.

Chapter 8. Separation

8.1 Introduction

The starting material in this study is EOL VCM magnets whose oxygen content is between 1600 and 6000 ppm mainly entrained in the grain boundary Nd-rich phase [Namkung et al, 2011; Nothnagel et al, 1991; USITC, 1996]. To recycle them, the HD process has been demonstrated to be a suitable technique to break down the EOL VCM magnets into friable powder as discussed in section 4.1.6. Although many of the impurities such as Ni can be removed, the oxygen can only be extracted by passing the material through a separation system.

The focus of this chapter is to efficiently separate the oxidised grain boundary phase using mechanical means. Despite the fact that there are several stable NdFeB phases, the main two present in a magnet are: (1) a hard magnetic matrix phase, with a grain size at around 10 μm [Kaneko et al, 1994] and a composition near to $Nd_2Fe_{14}B$; and (2) a Nd-rich grain boundary phase (GBP), which is where the oxygen is concentrated, which is below 2 μm. On processing in hydrogen, the two phases cleave away from each other. As the two main phases have different sizes and densities it may be possible to strip out the oxidised Nd-rich phase from the matrix phase. The ultimate aim is to use the purified matrix phase to produce new magnets.

If the Nd-rich phase could be efficiently separated from the $Nd_2Fe_{14}B$, then the remaining powder would have a composition close to the stoichiometric composition which, by blending with fresh neodymium, could lead to a recycled magnet with properties equal to the starting material. The composition of the $Nd_2Fe_{14}B$ phase is $Nd_{11.8}Fe_{82.3}B_{5.9}$ in at% and $Nd_{26.7}Fe_{72.3}B_1$ in wt%.

In order to separate the fine GBP particles from the matrix phase, two separation methods have been investigated. The first technique used a hydrocyclone separator whose working principle is based on the differences in particle size and density, in this case between the Nd-rich and the $Nd_2Fe_{14}B$ matrix

grains. The second separation method used was based on wet low-intensity magnetic separation which uses the differences in magnetic susceptibility between the GBP and the $Nd_2Fe_{14}B$ matrix grains.

8.2 Hydrocyclone Separation. Results and Discussion

In the present section the results of hydrocyclone separation using HD powder from EOL VCM magnets, either burr milled or non-milled, are shown and discussed.

8.2.1 Introduction

As mentioned in section 5.3, two different input feeds were studied: non-milled and burr milled HD powder from EOL VCM magnets. The schematic of the three cycle hydrocyclone separation stages for both input feeds is shown in figure 88 accompanied by the masses of the underflow (UF) and overflow (OF) fractions obtained as well as the masses of powder before each cycle.

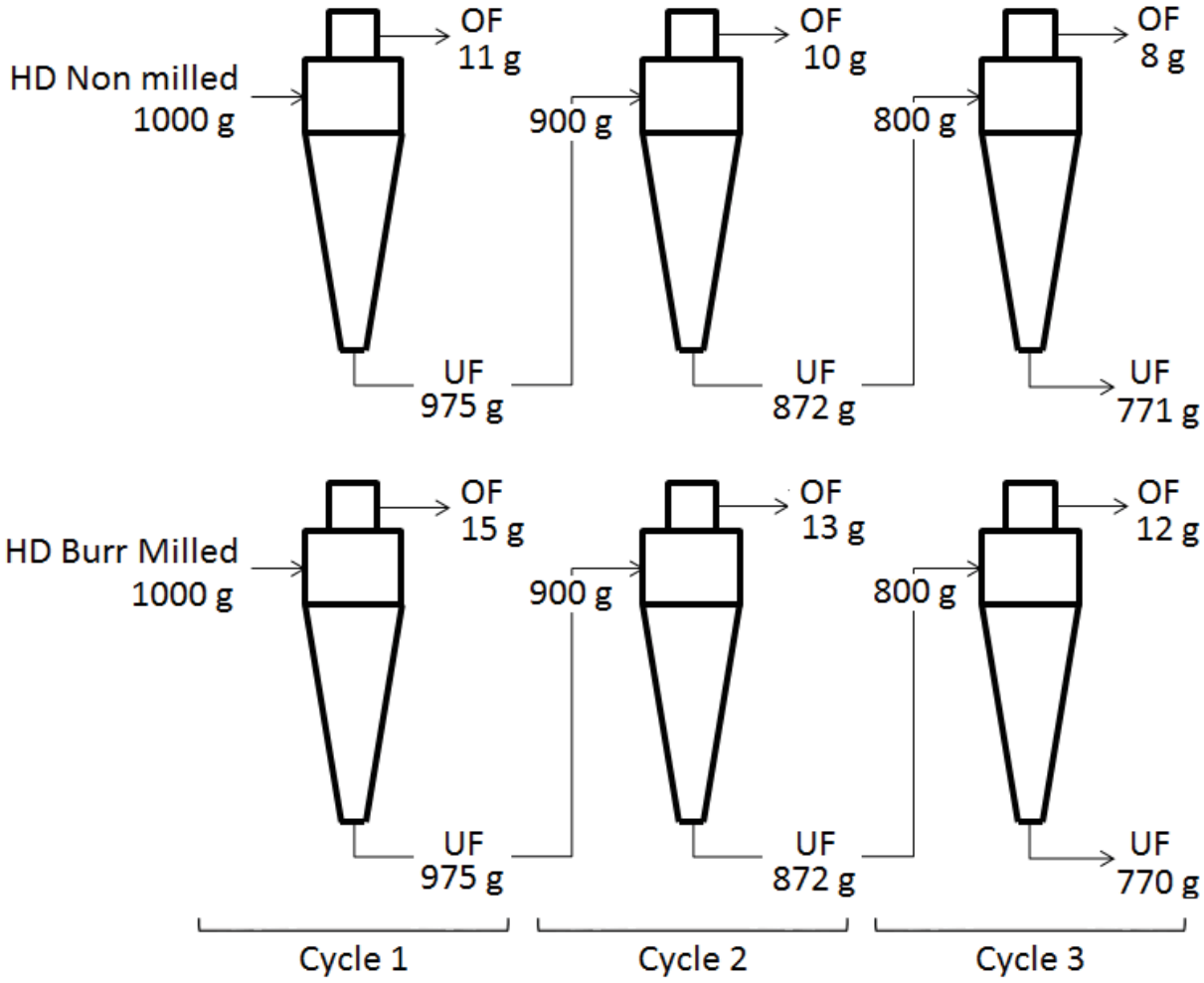

Figure 88. Schematic of the three cycle hydrocyclone separation using two different input feeds, with the mass from each fraction and the starting powder of each cycle.

The feed is introduced and separated into two fractions. The UF is expected to be predominantly composed of $Nd_2Fe_{14}B$ matrix hydride phase particles whereas the OF is expected to be made mainly of GBP particles. This technique is never 100% effective; therefore it may be likely to have matrix hydride particles in the OF and GBP particles in the UF. As the idea is to strip out the GBP particles from the matrix phase, then the UF from the first run is used as input feed in the second run and so on; which should lead to further purification, as shown in figure 88.

In figure 88 it can be observed that the mass of the OF after each cycle is subsequently decreased for both starting feedstocks. This indicates that separation may be taking place and, also, that further passes through the hydrocyclone may lead to even lower OF masses. This may result in lower GBP concentrations in the UF but also in losses of the matrix hydride phase as some of these particle would be present in the OF.

It can be observed that the material input is not equal to the material output. These losses are due to the fine material may be stuck in the walls of the pipes and the walls of the tub; as well as in the elbows, where the flow is turbulent. Using non-milled HD powder the losses were of 14 g (1.4 wt%), 18 g (2.0 wt%) and 21 g (2.5 wt%) after the 1^{st}, 2^{nd} and 3^{rd} hydrocyclone separation runs; whereas using burr milled feedstock they were, respectively, of 10 g (1.0 wt%), 15 g (1.6 wt%) and 18 g (2.2 wt%). As can be observed, these losses are low and are always below 2.5 wt% although they are not negligible.

All of the materials generated during the hydrocyclone separation trials were analysed using different techniques to systematically study the process and its effectiveness.

8.2.2 Scanning Electron Microscopy

Back-scattered electron images of the UF and OF powder after cyclic hydrocyclone separation are shown using either non-milled, in figure 89, or burr milled, in figure 90, HD powder from EOL VCM magnets as input feed.

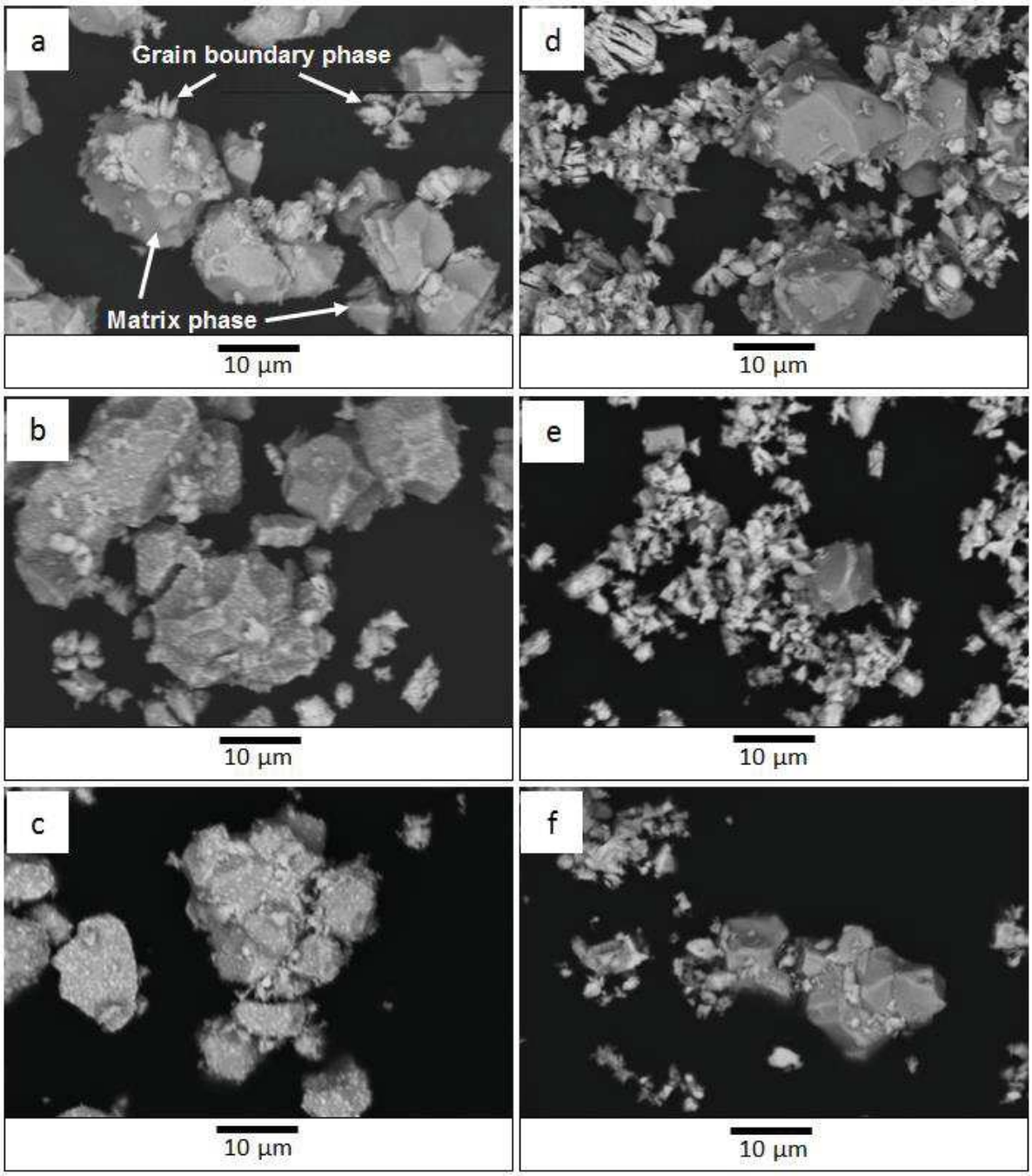

Figure 89. Back-scattered electron images of (a-c) underflow and (d-f) overflow powder from non-milled HD powder after the (a,d) 1st, (b,e) 2nd, and (c,f) 3rd cycle of hydrocyclone separation.

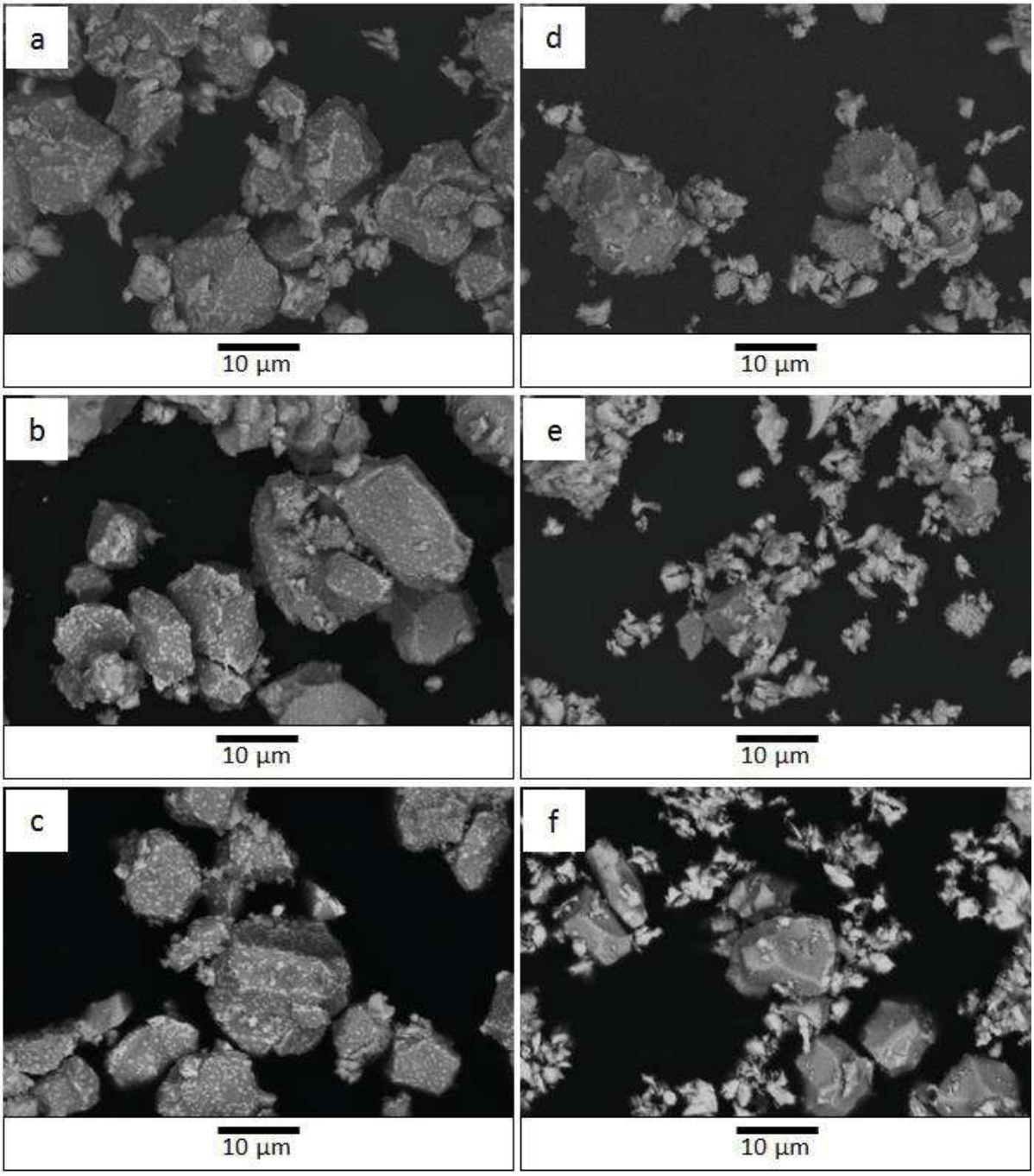

Figure 90. Back-scattered electron images of (a-c) underflow and (d-f) overflow powder from burr milled HD powder after the (a,d) 1st, (b,e) 2nd, and (c,f) 3rd cycle of hydrocyclone separation.

After each cycle of hydrocyclone separation, for both input feeds, it can be observed that the OF is richer in smaller particles than the UF. EDX showed that the small particles are richer in Nd and O than the large particles. This indicates that there is more GBP in the OF and that some separation has occurred between the two targeted streams as observed in figures 89 and 90.

Underflow Fraction

The UF in both figures appeared to be composed mainly of matrix hydride phase particles, which are >10 μm. There were, in addition, two types of smaller particles: (1) particles with a nanometric size; and (2) particles <2 μm and larger than nanometric. The nanometric particles are bound to the surface of the matrix hydride phase particles as a consequence of the triboelectric charges. These particles are suggested to be from the thinnest grain boundaries and, as they are very fine particles, they are not likely to be liberated from the surface easily [Dobbins et al, 2009]. The non-nanometric <2 μm particles are coarser and, as a consequence, they are more easily extracted despite the triboelectric charges. They are likely to be GBP from the triple points between matrix grains.

Overflow Fraction

The OF fractions in both figures appeared to be composed of both GBP and matrix hydride phase particles in a more even ratio. The OF fraction also presented the same three particles, but in different proportions. The matrix hydride phase particles present in this fraction are, in general terms, smaller than the UF average. As they were smaller, then they were able to move towards the inner vortex of the hydrocyclone during separation. This would lead to some yield loss of the matrix hydride phase.

Number of Cycles

In figures 89 and 90 the influence of the number of cycles on the UF can be observed. It can be seen that in all cases matrix hydride phase particles with nanometric GBP particles bound to the surface are present. The main difference from one cycle to the following, after visual inspection, is the decrease in non-nanometric <2 μm GBP particles with increasing the number of cycles performed. The UF after the third cycle exhibits a good degree of separation when compared with the UF after the first cycle in both figures. This indicates the improvement in efficiency of the separation with increasing the number of cycles performed. In contrast, the OF shows no trend with each cycle of separation

Milling Status

From figures 89 and 90 it is hard to determine if the milling status of the HD input feed, have had any major influence on the separation process. It may be possible to state that the UF powder in figure 90(c), produced using burr milled input feed, exhibits a lower quantity of GBP particles than that shown in figure 89(c), produced using non-milled input feed. Nevertheless, quantitative measurements are required to discern the influence of the milling status of the hydrogenated NdFeB powder in the separation yield.

8.2.3 Thermal Desorption

Starting Material

In order to determine the changes in hydride state of the powder before hydrocyclone separation, both input feeds were analysed by thermal desorption in order to study the influence of exposure to air. Results appear in figures 91 and 92.

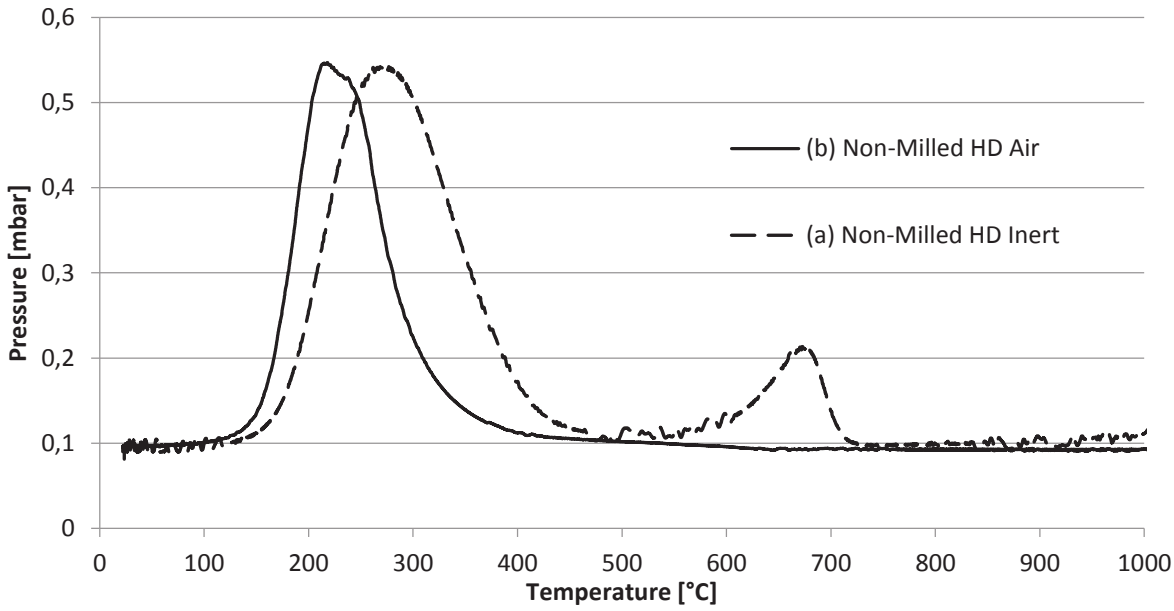

Figure 91. Thermal desorption trace of the HD non-milled powder from EOL VCM magnet as input feed (a) inertly loaded and (b) exposed to air.

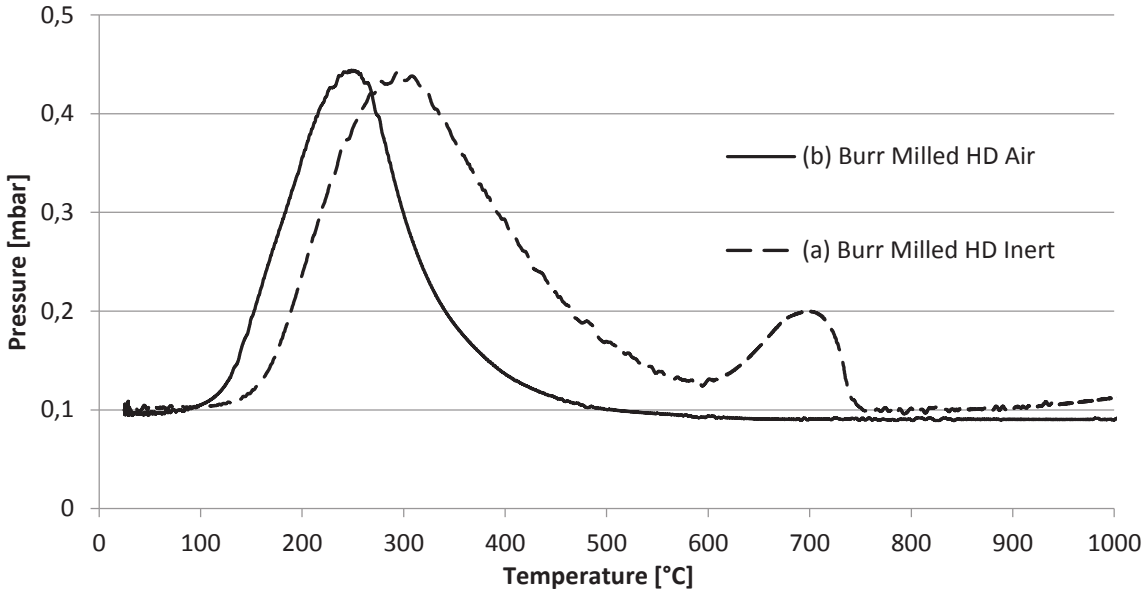

Figure 92. Thermal desorption trace of the HD burr milled powder from EOL VCM magnet as input feed (a) inertly loaded and (b) exposed to air.

In figures 91 and 92 it can be observed that the inertly loaded HD powder, either non-milled or burr milled, showed two main peaks; whereas powder exposed to air showed only one peak. This is characteristic of a hydrogenated NdFeB alloy, as seen in figure 34, where the peaks represents hydrogen desorption from the matrix and the GBP.

The air exposed samples exhibited no peak above 600 °C, hence either all or most of the Nd-rich GBP has not desorbed hydrogen with increasing the temperature. This was due to oxide or hydroxide formation in the Nd-rich phase when exposed to air after HD. Verdier et al [1994] observed by XRD that the Nd-rich GBP of hydrogenated NdFeB sintered magnets formed neodymium hydroxide when exposed to air. Therefore, the Nd-rich phase is likely to have hydrated, forming neodymium hydroxide in the HD powder.

The thermal desorption trace of neodymium hydroxide is shown in figure 93. It can be observed that it is composed by a main peak at about 120 °C, which starts at 50 °C, and a second peak at 250 °C with a right shoulder at about 350 °C.

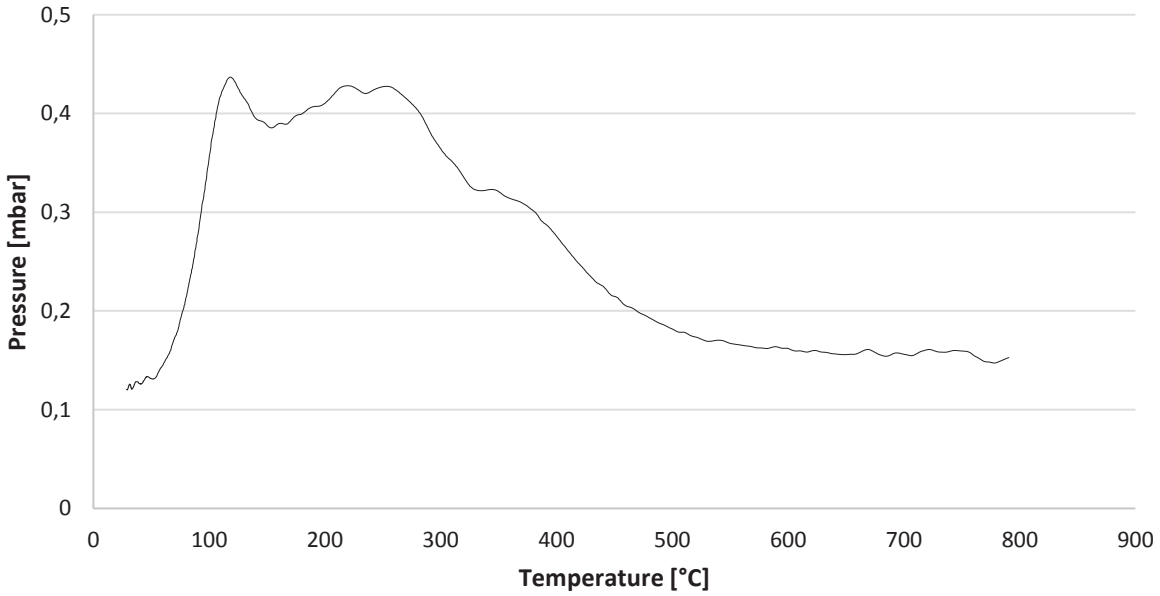

Figure 93. Thermal desorption trace of neodymium hydroxide.

Exposing the HD powder to air showed to shift the thermal desorption trace to the left, to lower temperatures. In figure 91 the peak shifted 55 °C to the left, whereas in figure 92 the peak shifted 60 °C to the left. This may indicate the formation of neodymium hydroxide at the expense of the neodymium from the GBP. Therefore, the shoulder that appeared on the right hand side of the main desorption peak, which is due to the partial hydrogen desorption of the Nd-rich phase from $NdH_{2.7}$ into NdH_2, is lost.

Comparing the influence of milling on thermal desorption traces shows that burr milling the HD powder resulted in peaks shifted to the right and significantly broader than those from non-milled HD powder, as shown in figures 91 and 92. Inertly loaded burr milled HD powder peaked at 305 °C and at 705 °C, whereas non-milled HD powder peaked at 275 °C and at 680 °C, respectively.

Underflow Fraction

In spite of the fact that underflow and overflow fraction were generated after each hydrocyclone separation; the UF is more important as it contains the matrix phase that would be further purified and processed into recycled re-sintered magnets. Therefore, thermal desorption traces from UF fractions

using both input feeds are respectively presented in figures 94 and 95. All thermal desorption traces from all fractions are included in the Appendix.

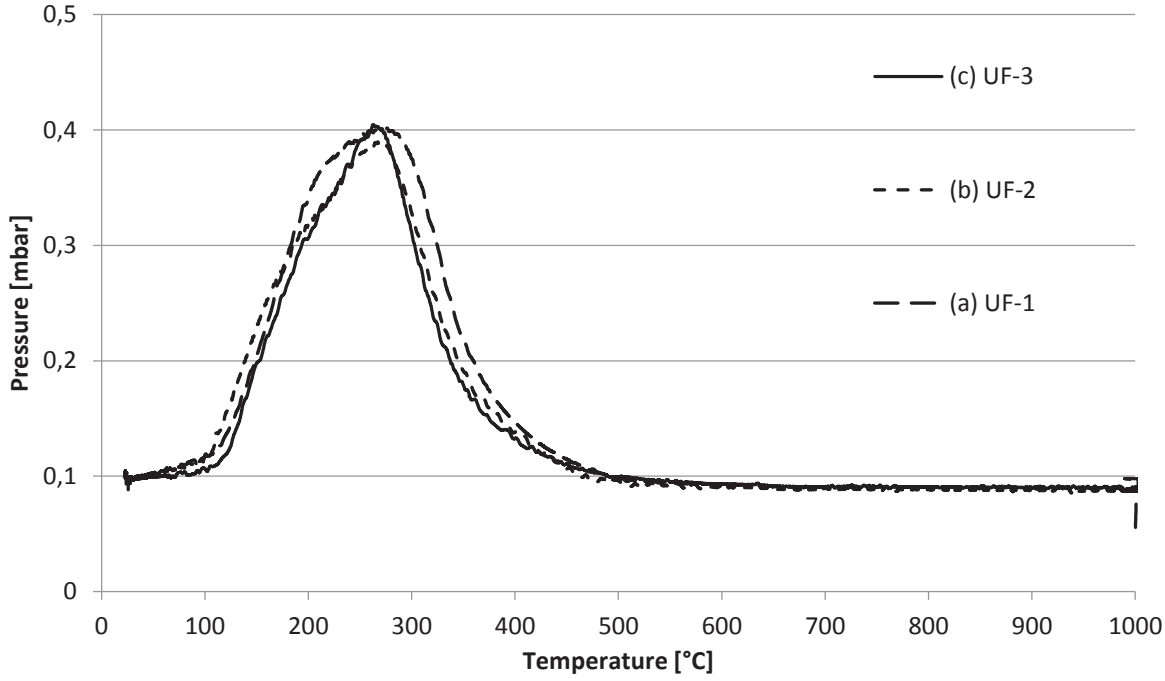

Figure 94. Thermal desorption trace of the UF powder after the (a) 1st, (b) 2nd, and (c) 3rd cycle of hydrocyclone separation using HD non-milled powder from EOL VCM magnet as input feed.

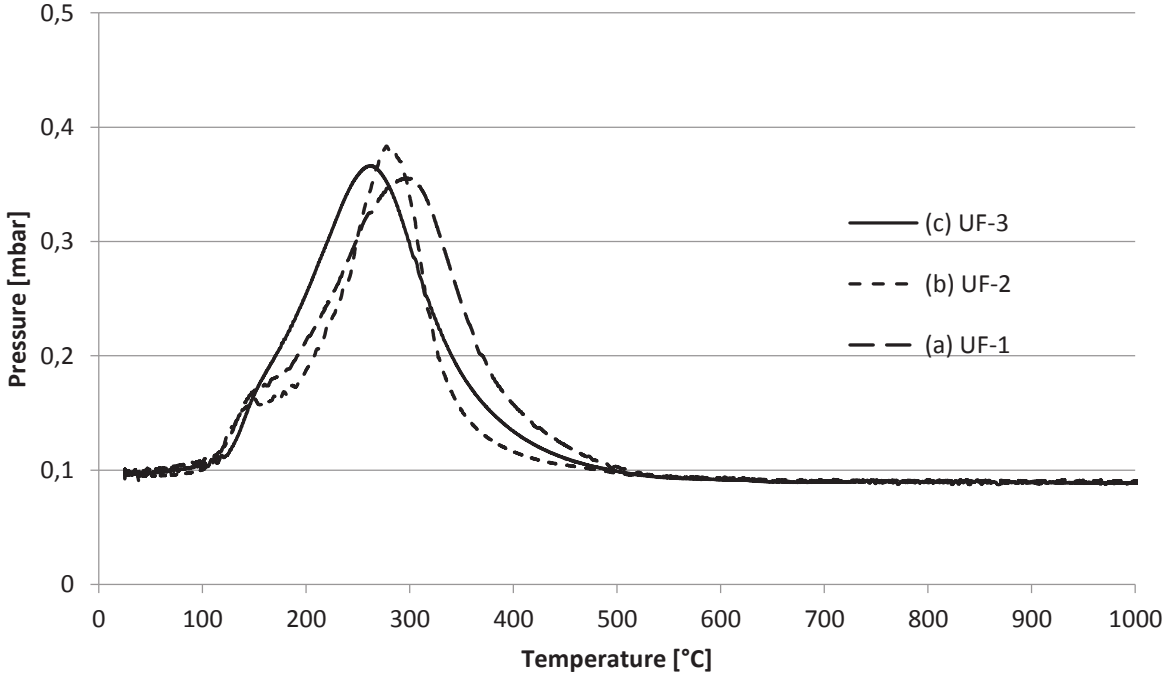

Figure 95. Thermal desorption trace of the UF powder after the (a) 1st, (b) 2nd, and (c) 3rd cycle of hydrocyclone separation using HD burr milled powder from EOL VCM magnet as input feed.

Both figures 94 and 95 lacked a second peak at 600 °C, which indicates either removal or oxidation/hydration of the GBP.

It can be observed in figure 94 that the temperature of the main desorption peak remains roughly within the same temperature range between each cycle. The shoulder which appeared at the left side of the main desorption peak in figure 94(a) decreased in intensity after the first cycle and, afterwards, it becomes difficult to discern whether it has decreased in intensity or not with increasing number of cycles.

In figure 95 it can be observed that with increasing the number of cycles, the temperature of the desorption peak shifted to the left, reaching after the 1st, 2nd and 3rd cycle of hydrocyclone separation temperatures of 305, 285 and 275 °C respectively. In addition, the shoulder that appeared between 150 and 155 °C was reduced in intensity with increasing the number of cycles of hydrocyclone separation which may indicate removal of the GBP, which is likely to be neodymium hydroxide.

Comparison of both figures does show that there are differences in the desorption behaviour depending on the milling status of the powder. After all cycles, the temperature of the main desorption peak was higher when HD powder was burr milled compared to the non-milled; as occurred in the HD powder before hydrocyclone separation.

The desorption of the $Nd_2Fe_{14}B$ phase consists on a sharp peak centred on 150 °C [Williams et al 1991]; whereas the desorption of an oxidised NdFeB magnet has been shown to peak at 280 °C [Degri, 2014]. Therefore, the shifting to lower temperatures of the main desorption peak of UF powders with increasing the number of cycles may be attributed to a decrease in the GBP as it may have been either removed or formed oxides or hydroxides.

In summary, thermal desorption studies have been useful to determine that the milling status has an influence in the resultant powder; however, such difference is not substantial. The peak temperature shifted to the left with increasing the number of cycles as a consequence of the subsequent separation of phases with increasing number of cycles.

8.2.4 X-Ray Diffraction

To determine the crystal structure of the separated powder, X-ray diffraction was performed on powder form in each stream. The phases were then quantified. All X-ray diffraction patterns are individually shown in the Appendix covering 2θ angles from 15 to 90° in which all phases are identified. The XRD pattern of an EOL VCM magnet is shown in figure 96. The XRD traces of the UF using both feedstocks are studied and presented in figures 97 and 98.

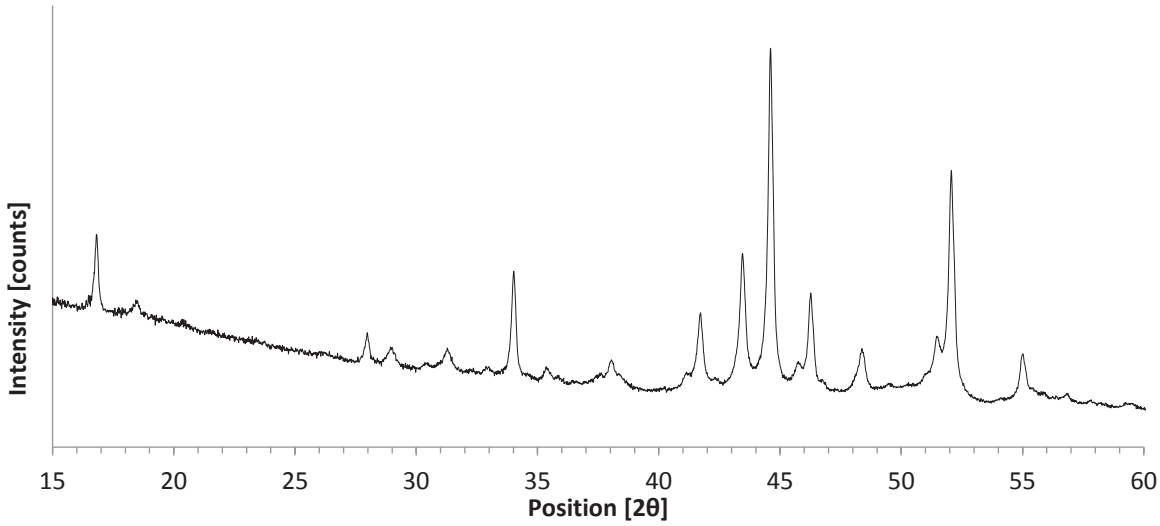

Figure 96. X-ray diffraction pattern of a solid EOL VCM magnet. All peaks correspond to $Nd_2Fe_{14}B$.

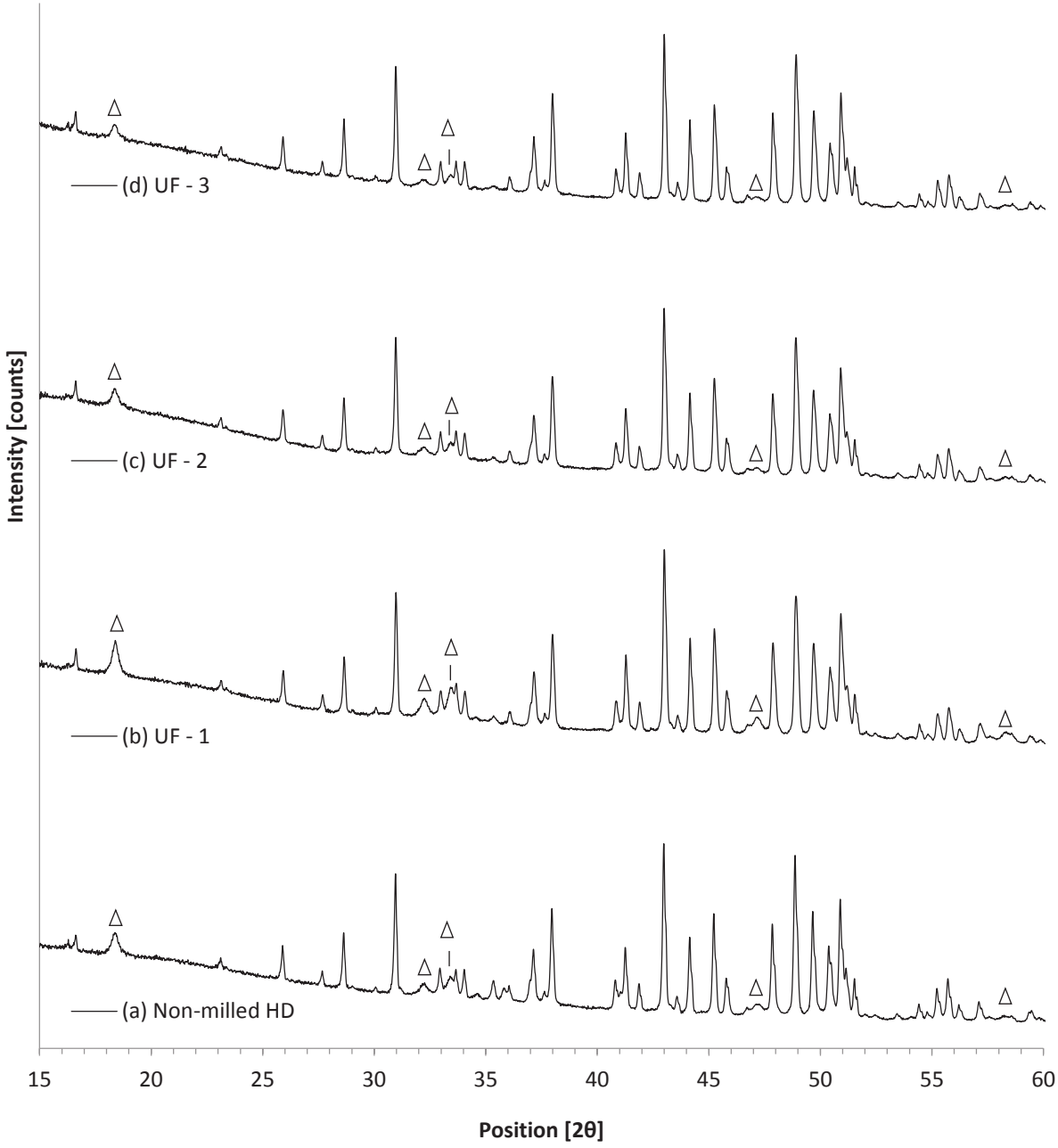

Figure 97. X-ray diffraction patterns of (a) non-milled powder from HD EOL VCM magnet, and the underflow powder after the (b) 1st, (c) 2nd, and (d) 3rd cycle of hydrocyclone separation using HD non-milled from EOL VCM magnet as input feed. Peaks identified with a triangle correspond to neodymium hydroxide; the rest correspond to matrix hydride phase.

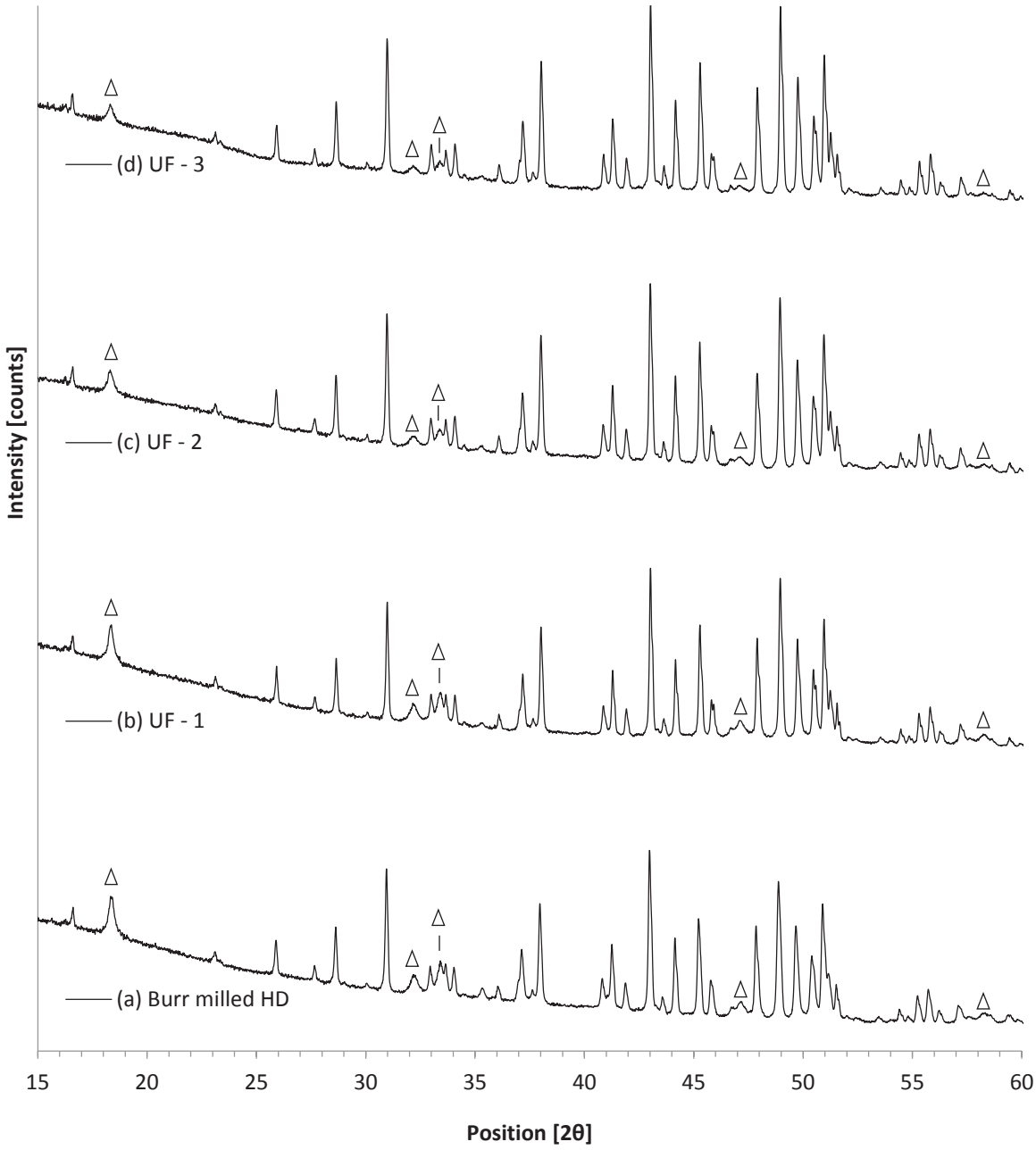

Figure 98. X-ray diffraction patterns of (a) burr milled powder from HD EOL VCM magnet, and the underflow powder after the (b) 1st, (c) 2nd, and (d) 3rd cycle of hydrocyclone separation using HD burr milled from EOL VCM magnet as input feed. Peaks identified with a triangle correspond to neodymium hydroxide; the rest correspond to matrix hydride phase.

The phases identified to be present were the matrix phase ($Nd_2Fe_{14}B$), neodymium oxide (Nd_2O_3), matrix phase hydride ($Nd_2Fe_{14}BH_x$) and neodymium hydroxide ($Nd(OH)_3$). It was immediately evident that the matrix hydride phase is clearly identifiable by X-ray diffraction in the UF; which means to a large extent that this phase does not decompose on exposure to hydrocyclone. This signifies that this

phase is still intact after exposure to water and atmosphere at 80 °C. This is quite remarkable given the small particle size of the $Nd_2Fe_{14}B$ and the harsh environment which it was exposed to.

In table 17 the phase quantification results from XRD traces are presented for all the samples produced on the three cycle hydrocyclone separation process. The powder from the OF fraction after the third cycle from HD burr milled input feed as the sample was contaminated after the flask containing it was broken. It was not possible to obtain such sample again as it would have entailed repeating the whole batch of cyclic hydrocyclone separations again.

Table 17. X-ray diffraction phase quantification of all the samples produced on the performance of three cycles hydrocyclone separation.

Sample		$Nd_2Fe_{14}B$	Nd_2O_3	$Nd_2Fe_{14}BH_x$	$Nd(OH)_3$
VCM magnet		99.3	0.7	n/d	n/d
Non-milled HD NdFeB magnet	Air	0.8	1.2	88.9	9.1
	UF - 1	n/d	n/d	91.3	8.7
	UF - 2	n/d	n/d	96.0	4.0
	UF - 3	n/d	n/d	97.1	2.9
	OF -1	n/d	n/d	59.6	40.4
	OF - 2	n/d	n/d	20.4	77.6
	OF - 3	n/d	n/d	50.2	49.8
Burr milled HD NdFeB magnet	Air	n/d	n/d	89.3	10.7
	UF - 1	n/d	n/d	89.5	10.5
	UF - 2	n/d	n/d	91.1	8.9
	UF - 3	n/d	n/d	94.2	5.8
	OF - 1	n/d	n/d	25.3	74.7
	OF - 2	n/d	n/d	31.9	68.1
	OF - 3	Contaminated			

n/d – not detected

As the intensity of the $Nd_2Fe_{14}BH_x$ peaks is so similar from one fraction to another it is more appropriate, from a comparative perspective, to focus on the peaks from neodymium hydroxide. These peaks are centred at 18.35, 32.20, 33.40, 47.10 and 58.20 2θ angles As the target is to obtain an oxygen free powder for further reprocessing by re-sintering into a new magnet, it is fundamental to study and evaluate the effectiveness of separation by observing the evolution of the UF from both feedstocks.

Starting Material

Although the XRD spectra of both starting feedstocks should be the same, they are not. It can be observed that neodymium hydroxide peaks are more intense in the burr milled HD powder than in its non-milled counterpart. It indicates that decreasing the particle size of the input feed results in an increase in the specific area and reactivity of the powder. Therefore, qualitatively speaking, a larger amount of neodymium from the GBP reacts leading to more intense neodymium hydroxide peaks. This was later confirmed by phase quantification, in table 17, showing that the non-milled HD powder had just 9.1 wt% neodymium hydroxide whereas the burr milled contained 10.7 wt%.

Number of Cycles

For both feedstocks, it can be observed in table 17 that the proportion of neodymium hydroxide in the UF is reduced on successive cycles on the hydrocyclone. The neodymium hydroxide content showed a subsequent decrease, reaching 8.7, 4.0 and 2.9 wt% after the 1st, 2nd and 3rd cycle using non-milled feedstock. The use of burr milled feedstock resulted in neodymium hydride contents, respectively, of 10.5, 8.9 and 5.8 wt%. This is corroborated by figures 97 and 98, in which a reduction in intensity of the neodymium hydroxide peaks is observed on successive cycles.

Conversely, the matrix hydride in the UF is concentrated with increasing number of cycles, hence evidencing separation. The matrix hydride content of the UF yielded 91.3, 96.0 and 97.1 wt% after the 1st, 2nd and 3rd cycle using non-milled feedstock. When burr milled feedstock was utilised, the matrix hydride content was, respectively, 89.5, 91.1 and 94.2 wt%.

In contrast with the UF, no trend is observed in the composition of the OF with increasing number of cycles of hydrocyclone separation. The OF showed, for both input feeds, more intense neodymium hydroxide peaks than the UF at all 2θ angles as can be observed in the individual XRD traces included in the Appendix. This agreed with phase quantification results in table 17 which showed that the OF contained a larger content of neodymium hydroxide, over 40 wt%, and also a much lower content of

matrix hydride, below 60 wt%. These results evidenced that the OF is composed by both small particles of matrix hydride but also a great proportion of GBP.

Matrix Hydride to Neodymium Hydroxide Ratio

The matrix hydride to neodymium hydroxide ratio of the UF, using the non-milled input feed, after the 1st, 2nd and 3rd cycle is, respectively, 10.49, 24.00 and 33.48. When burr milled feedstock was used, this ratio was of 8.53, 10.24 and 16.24.

Although the ideal ratio of matrix hydride to neodymium hydroxide would be infinite, in the case of a fraction free of neodymium hydroxide (UF in this study), this would be never achieved. This occurs as a consequence of the triboelectric charges generated that cause the fine paramagnetic neodymium hydroxide particles to adhere to the ferromagnetic matrix hydride particles [Dobbins et al, 2009].

The matrix hydride to neodymium hydroxide ratio of the OF yielded values of 1.47, 0.26 and 1.01 after the 1st, 2nd and 3rd cycle respectively using the non-milled input feed; whereas for burr milled feedstock the ratios were, respectively, of 0.34 and 0.47 as the sample after the 3rd cycle was contaminated. All these ratios are more than 5 times lower than those of both input feeds, which were of 9.77 and 8.34 respectively for the non-milled and burr milled.

Milling Status

It should be noted in table 17 that, in the UF, there is a lower quantity of the matrix hydride at the expense of a higher neodymium hydroxide content for the burr milled feedstock when compared to the non-milled. This may indicate that milling decreases the particle size of both the matrix and the GBP. Therefore, the smaller the particle size of the GBP, the more difficult to extract as a consequence of the triboelectric charges. This was corroborated by the matrix hydride to neodymium hydroxide ratios of both feedstocks. Nevertheless, this effect of the milling status may be supressed by increasing the number of passes of the material through the hydrocyclone.

To sum up, the fact that the matrix hydride phase is still intact after exposure to water and atmosphere at 80 °C is remarkable as it does not decompose as observed in XRD spectra. The neodymium hydride content was reduced and the matrix hydride phase was concentrated in the UF with increasing number of cycles. This, added to previous SEM and thermal desorption results, point to the fact that separation is effectively taking place.

Using non-milled HD powder as the input feed resulted in higher matrix hydride contents, lower neodymium hydride contents and higher ratios than using burr milled HD powder at all cycles. It may be possible that decreasing the particle size resulted in the comminution of the GBP, hence increasing the proportion of fine paramagnetic GBP. As a consequence of triboelectric charges, it make it more difficult to separate a greater proportion of the fine GBP. It should be noted that XRD has significant error associated with quantitative analysis. For this reason further more detailed and accurate XRF (see section 8.2.5) and ICP-OES (see section 8.2.6) analysis were carried out on these separated fractions.

8.2.5 X-Ray Fluorescence Spectroscopy

To determine more accurately the composition of the feedstocks, UF and OF fractions obtained during hydrocyclone separation, X-ray fluorescence spectroscopy was employed. A more detailed composition of the fractions studied shown in figure 88 is given in the Appendix of this thesis. A shortened version of these is shown in figures 99 and 100, where the Fe and the ΣREEs content from X-ray fluorescence spectroscopy of the input feeds, the UF and the OF samples, are presented, except the OF-3 from burr milled powder due to contamination.

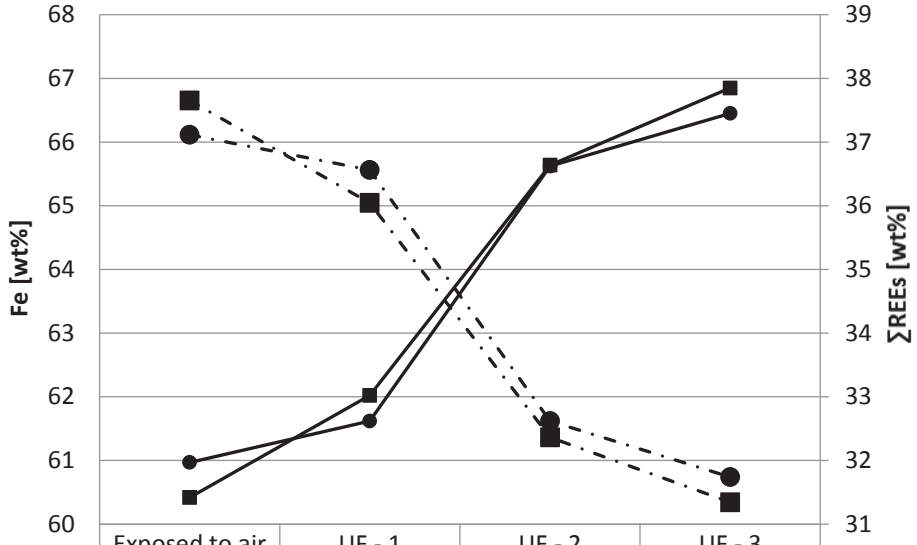

	Exposed to air	UF - 1	UF - 2	UF - 3
Fe Non-Milled	60,97	61,62	65,62	66,45
Fe Burr Milled	60,42	62,02	65,64	66,85
REE Non-Milled	37,11	36,56	32,62	31,74
REE Burr Milled	37,65	36,05	32,37	31,35

Figure 99. X-ray fluorescence spectroscopy results of Fe and ΣREEs expressed in wt% from the input feed and the UF of three cycles of hydrocyclone separation.

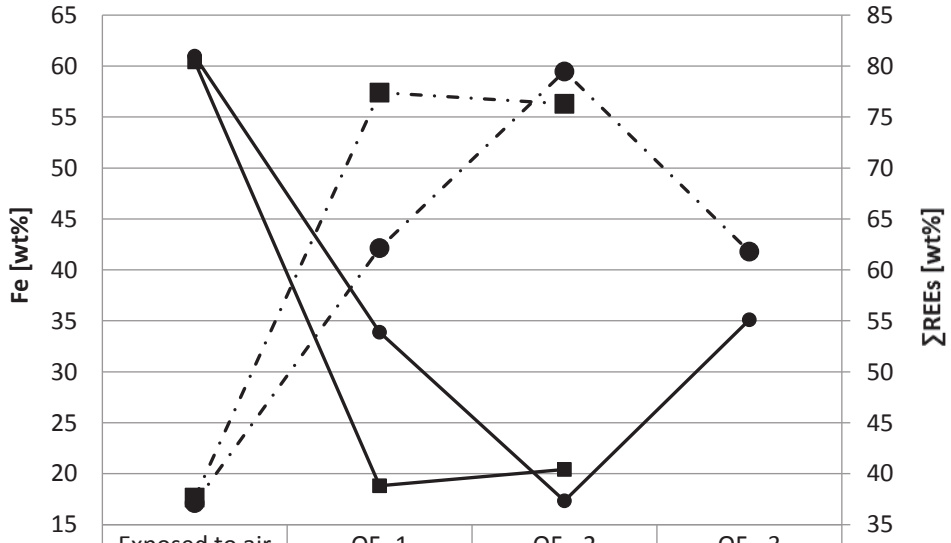

	Exposed to air	OF -1	OF - 2	OF - 3
Fe Non-Milled	60,97	33,90	17,34	35,11
Fe Burr Milled	60,42	18,82	20,43	
REE Non-Milled	37,11	62,14	79,48	61,79
REE Burr Milled	37,65	77,40	76,30	

Figure 100. X-ray fluorescence spectroscopy results of Fe and ΣREEs expressed in wt% from the input feed and the OF of three cycles of hydrocyclone separation. OF-3 from burr milled feedstock was contaminated

The main aim of subjecting HD powder, either non-milled or burr milled, to separation is to extract all the GBP in order to have a clean fraction based on the $Nd_2Fe_{14}B$ matrix phase, of composition $Nd_{26.7}Fe_{72.3}B_{1.0}$, in wt%, as already mentioned in section 8.1. Therefore, this is the desired composition of the UF fraction and the Fe is wanted to be as close as possible to 72.3 wt% as it is the maximum theoretical value that can be achieved. To evaluate the separation efficiency, the ratio of iron to total rare earth elements, Fe/ΣREEs, is a suitable indicator.

Starting Material

In spite of the similarity between the compositions of both feedstocks, they are not identical. The starting non-milled HD powder exhibited a higher Fe, and lower Nd content than the burr milled. The Fe/ΣREEs ratio of both the non-milled and the burr milled HD powder was 1.64 and 1.60, respectively, which is far from the 2.71 given by the stoichiometric $Nd_2Fe_{14}BH_x$.

Number of Cycles

For both feedstocks, the Fe content of the UF increased with each cycle of hydrocyclone separation. Conversely, Nd showed a subsequent decrease; which indicates that the matrix hydride concentration increased as the GBP was extracted after every cycle.

The Fe content of the UF after the 1st, 2nd and 3rd cycles was of 61.62, 65.62 and 66.45 wt%, respectively, when non-milled feedstock was used. However, when burr milled feed was used, these values were of 62.02, 65.64 and 66.85 wt%. On the other hand, the Nd content after the 1st, 2nd and 3rd cycles reached 36.56, 32.62 and 31.74 wt%, respectively, when non-milled feedstock was used. However, when burr milled feed was used, these values were of 36.05, 32.37 and 31.35 wt%.

For both input feeds the OF showed higher Nd and lower Fe contents than the UF at all cycles, which is in good agreement with XRD results shown in section 8.2.4.

For the OF powder using the non-milled input feed, the content of Fe was below 36 wt% whereas the Nd and ΣREEs content were over 59 and 61 wt%, respectively, at any cycle of hydrocyclone

separation. When the burr milled feedstock was used, the Fe content was kept under 21 wt% and the Nd and ΣREEs content were higher than 74 and 76 wt%, respectively, at any cycle of hydrocyclone separation. These results suggest that the separation between both targeted phases was effective when compared with the composition of both the input feed and the EOL VCM magnet. Nevertheless, as shown in figure 100, no clear trend is observed in the OF results.

Iron to Total Rare Earth Elements Ratio

The Fe/ΣREEs ratio of the UF using non-milled feedstock after the 1st, 2nd and 3rd cycle is, respectively, 1.69, 2.01 and 2.09; whereas for the burr milled feed, these values were of 1.72, 2.03 and 2.13. Although the target ratio is of 2.71 from the stoichiometric $Nd_2Fe_{14}B$, this would be never achieved as a consequence of the triboelectric charges. In addition, the stoichiometric cannot be achieved because the EOL VCM magnets contain a large number of alloying elements.

Such ratio of the OF using non-milled feedstock after the 1st, 2nd and 3rd cycles was, respectively, of 0.55, 0.22 and 0.57; whereas using burr milled feed, values of 0.24 and 0.27 were obtained. These ratios are much lower than that of the input feeds, 1.64 and 1.60 respectively; or that from the VCM magnet, of 1.68, hence demonstrating the enrichment in ΣREEs in the OF, which implies the effectiveness of hydrocyclone separation.

Milling Status

From composition and ratio results it is clear that better results are obtained when the burr milled feedstock is used. Nevertheless, the differences observed between both feedstocks are not substantial enough as to declare one specific milling status better than the other. Therefore, further investigation is required.

To sum up, the use of burr milled HD powder as input feed resulted in higher Fe contents, lower Nd contents and higher Fe/ΣREEs ration than the use of non-milled HD powder at all cycles. These results contradict those from XRD phase quantification. It does not mean that either XRD phase

quantification or XRF results are wrong, but complimentary. As the theoretical basis of each technique is different, there are a number of reasons why the results do not match. XRD quantifies the amount of a certain crystal structure whereas XRF measures the total amount of a certain element in the sample. Therefore, XRD is more likely to introduce errors and miscalculations.

It may be possible that with decreasing the average particle size of the input feed by burr milling, the powder increased its specific area, hence aiding neodymium to separate from the matrix and flow more freely towards the inner vortex. Therefore, a larger proportion of GBP was extracted in the OF fraction, which resulted in a cleaner UF fraction when using burr milled HD powder than when using non-milled HD powder.

8.2.6 Inductively Coupled Plasma – Optical Emission Spectrometry

As a consequence of the disagreement between XRF and XRD phase quantification results, inductively coupled plasma – optical emission spectrometry was used to corroborate the compositional analysis. The Fe and ΣREEs results from ICP-OES are presented in figures 101 and 102. Full results of ICP-OES are presented in the Appendix.

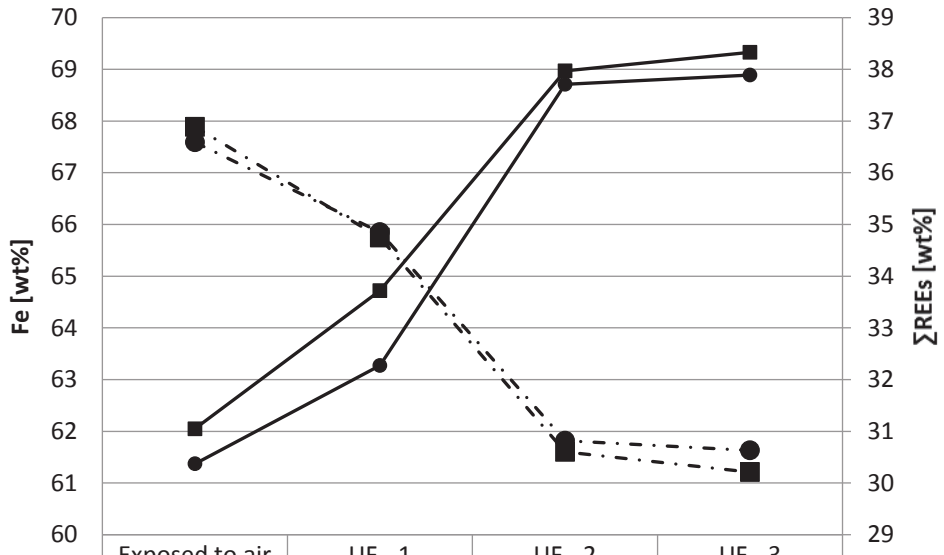

	Exposed to air	UF - 1	UF - 2	UF - 3
Fe Non-Milled	61,37	63,27	68,71	68,89
Fe Burr Milled	62,05	64,72	68,97	69,33
REE Non-Milled	36,59	34,85	30,82	30,63
REE Burr Milled	36,89	34,75	30,60	30,21

Figure 101. Inductively coupled plasma – optical emission spectrometry results of Fe and ΣREEs expressed in wt% from the input feed and the UF of three cycles of hydrocyclone separation.

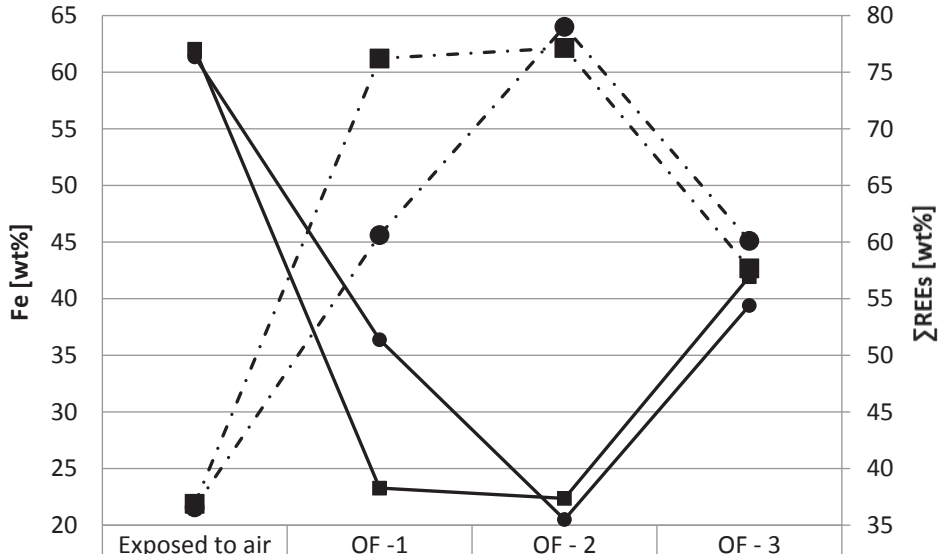

	Exposed to air	OF -1	OF - 2	OF - 3
Fe Non-Milled	61,37	36,38	20,50	39,40
Fe Burr Milled	62,05	23,29	22,36	41,95
REE Non-Milled	36,59	60,62	79,02	60,12
REE Burr Milled	36,89	76,22	77,15	57,68

Figure 102. Inductively coupled plasma – optical emission spectrometry results of Fe and ΣREEs expressed in wt% from the input feed and the OF of three cycles of hydrocyclone separation.

Starting Material

As previously observed by XRD and XRF, the compositions of both input feeds are very similar. However, the non-milled HD powder exhibited a higher Nd content whereas the burr milled HD powder showed a larger Fe content. The Fe/ΣREEs ratio of both feedstocks was of 1.68, which is lower than that exhibited by the EOL VCM magnet of 1.75.

Number of Cycles

For both feeds, the Fe content of the UF increased with each cycle. Conversely, Nd demonstrated a subsequent reduction. On the other hand, the OF, for both feeds, showed higher Nd and lower Fe contents than the UF at all cycles. This indicates that the matrix hydride concentration increased as the GBP was being extracted, which endorses previous results in the present chapter.

The Fe content of the UF was of 63.27, 68.71 and 68.89 wt%, respectively, after the 1st, 2nd and 3rd cycle when non-milled feedstock was used. However, when burr milled feed was used, these values reached 64.72, 68.97 and 69.33 wt%. On the other hand, the Nd content after the 1st, 2nd and 3rd cycles was of 34.85, 30.82 and 30.63 wt%, respectively, when non-milled feedstock was used. However, when burr milled feed was used, these values were of 34.75, 30.60 and 30.21 wt%.

For the OF powder using the non-milled input feed, the content of Fe was below 40 wt% whereas the ΣREEs content was over 60 wt%, respectively, at any cycle of hydrocyclone separation. When the burr milled feedstock was used, the Fe content was kept under 42 wt% and the ΣREEs content was higher than 58 wt%, respectively, at any cycle of hydrocyclone separation. Nevertheless, as shown in figure 102, no clear trend is observed in the OF results.

These results are in accordance with those from XRF in section 8.2.1; however, slightly higher in Fe and lower in Nd and total rare earth content. This may also change the iron to rare earth elements ratio by increasing it further. These differences in values from XRF to ICP-OES lay on the theoretical differences between both techniques.

Iron to Rare Earth Elements Ratio

The Fe/ΣREEs ratio of the UF using non-milled feedstock after the 1st, 2nd and 3rd cycle is, respectively, 1.81, 2.23 and 2.25; whereas for the burr milled feed, these values were of 1.86, 2.25 and 2.29.

Such ratio of the OF using non-milled feedstock after the 1st, 2nd and 3rd cycles was, respectively, of 0.60, 0.26 and 0.65; whereas using burr milled feed, values of 0.31, 0.29 and 0.73 were obtained. These ratios are much lower than that of the input feeds, 1.68 both; or that from the VCM magnet, of 1.75, hence demonstrating the enrichment in ΣREEs in the OF.

Milling Status

The use of burr milled feeds has led to higher Fe concentrations and, hence, lower Nd contents compared with the non-milled feedstock, corroborating XRF results. Nevertheless, the differences between both milling status are not substantial hence being possible to consider both feedstocks acceptable. In addition, this effect of the milling status may be supressed by increasing the number of passes of the material through the hydrocyclone, which needs to be further investigated in the future.

To sum up, the use of burr milled HD powder as input feed resulted in higher Fe concentrations, lower Nd contents and higher Fe/ΣREEs ratios than when using the non-milled HD powder. These results endorse those from XRF and contradict those from XRD phase quantification.

8.3 Wet Low-Intensity Magnetic Separation. Results and Discussion

In the present section the results of wet low-intensity magnetic separation using HD powder from EOL VCM magnets, either burr milled or non-milled, are shown and discussed.

8.3.1 Introduction

The schematic of the wet low intensity magnetic separation (WLIMS) for both input feeds is shown in figure 103 showing, in addition the mass of each fraction. The magnetic fraction (MF) is expected to

be composed mainly of the ferromagnetic matrix phase; and the paramagnetic non-magnetic fraction (NMF) mainly of GBP. The aim was to obtain the MF consisting predominantly of $Nd_2Fe_{14}B$ particles free of oxidised compounds present in the GBP.

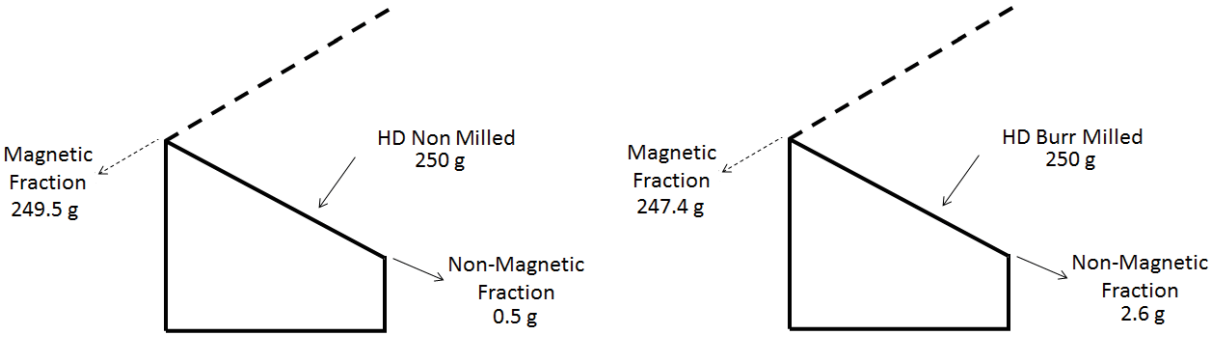

Figure 103. Schematic of the wet low intensity magnetic separation using two different input feeds: non-milled and burr milled HD powder from EOL VCM magnets. The dashed lines represents the tilting of the slope in order to collect the magnetic fraction as explained in chapter 5.

All products used and obtained during WLIMS were analysed using different techniques to systematically study the process and its effectiveness.

The masses obtained in the NMF observed in figure 103 when trying this separation method from both feeds were significantly lower compared to hydrocyclone separation. In this separation method the milling status appears to be critical to the quantity of powder of NMF. The decrease in particle size allowed GBP particles to flow more freely, hence increasing the amount of this phase.

8.3.2 Scanning Electron Microscopy

Back-scattered electron images of both the magnetic and the non-magnetic fraction after WLIMS are shown in figure 104 using either non-milled or burr milled HD powder from EOL VCM magnets as input feed.

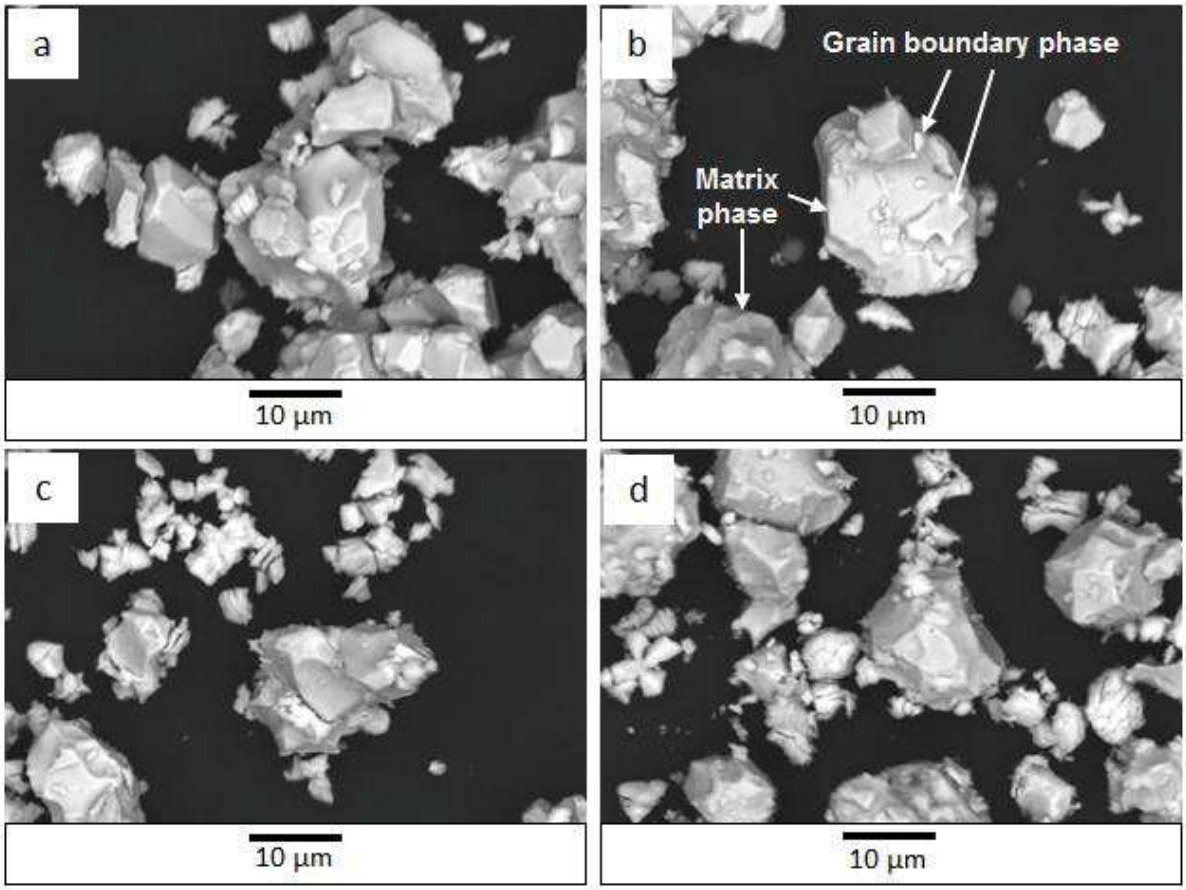

Figure 104. Back-scattered electron images at 2000 magnifications of (a,b) magnetic and (c,d) non-magnetic fraction after WLIMS using (a,c) non-milled and (b,d) burr milled HD powder as input feed.

Unlike hydrocyclone separation, WLIMS shows almost no separation between the two targeted streams, as can be observed in figure 104. The BSE SEM images exhibit a low degree of separation although a tiny difference between the MF powder, shown in figure 104(a) and (b), and the NMF powder, shown in figure 104(c) and (d) is perceptible in the amount of GBP particles.

It is hard to determine, from the BSE SEM images, if the milling status of the HD powder, either burr milled or non-milled, have had any effect on the separation yield. Nonetheless, it can be observed that in all streams a large amount of GBP is present bound to the surface of the matrix hydride particles.

8.3.3 X-Ray Diffraction

XRD was performed to identify which phases are present in each stream and to quantify such phases. All X-ray diffraction patterns are individually shown in the Appendix covering 2θ angles from 15 to 90° in which all phases are identified.

Two streams were produced after each WLIMS, NMF and MF, with the latter hopefully containing the matrix phase. The XRD patterns of the VCM magnet and both investigated fractions are presented, respectively, in figures 105, 106 and 107.

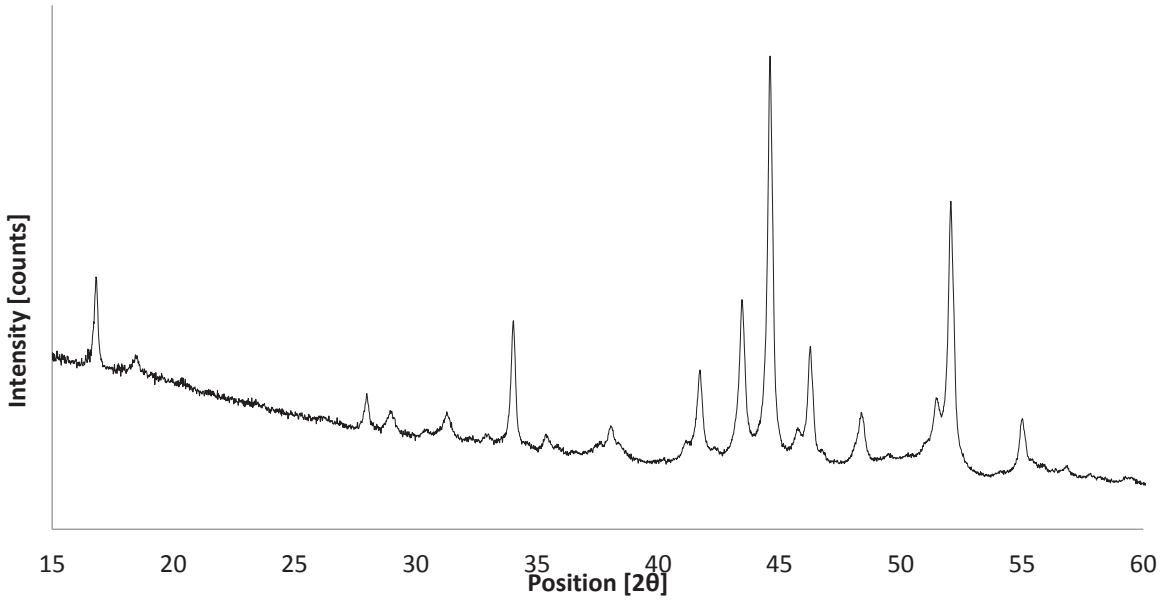

Figure 105. X-ray diffraction pattern of the EOL VCM magnet used as starting material in this project.

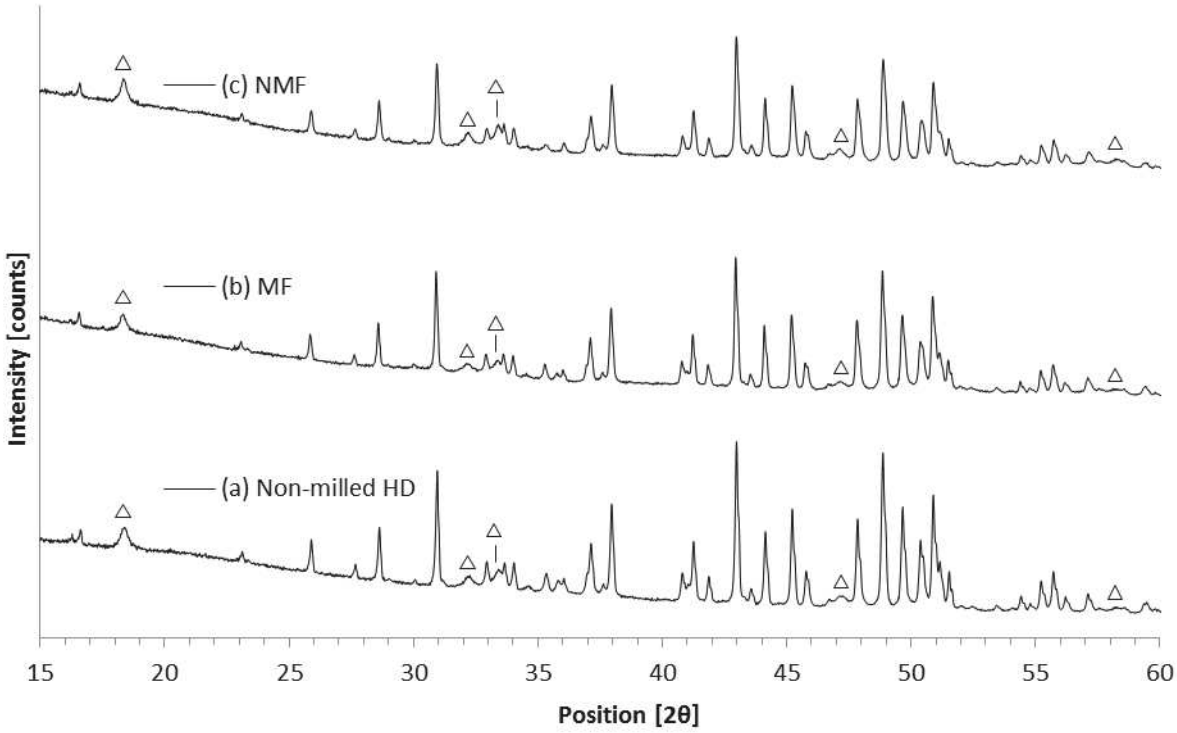

Figure 106. X-ray diffraction patterns of (a) non-milled powder from HD EOL VCM magnet, and the (b) MF and (c) NMF after WLIMS using HD non-milled as input feed. Peaks identified with a triangle correspond to neodymium hydroxide; the rest correspond to matrix hydride phase.

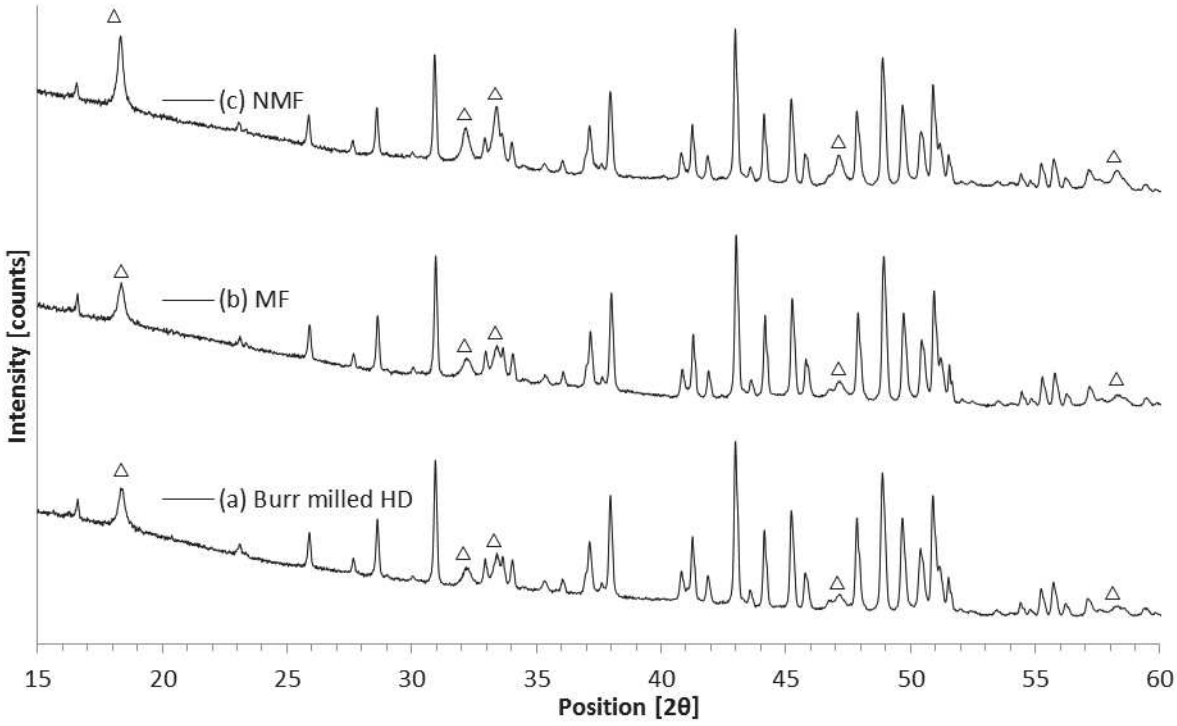

Figure 107. X-ray diffraction patterns of (a) burr milled powder from HD EOL VCM magnet, and the (b) MF and (c) NMF after WLIMS using HD burr milled input feed. Peaks identified with a triangle correspond to neodymium hydroxide; the rest correspond to matrix hydride phase.

In table 18 the phase quantification results from XRD traces are presented for all samples produced on the WLIMS. The phases present were the matrix phase ($Nd_2Fe_{14}B$), neodymium oxide (Nd_2O_3), matrix phase hydride ($Nd_2Fe_{14}BH_x$) and neodymium hydroxide ($Nd(OH)_3$).

Table 18. X-ray diffraction phase quantification results of all the samples produced on the performance of WLIMS expressed in wt%.

Sample		$Nd_2Fe_{14}B$	Nd_2O_3	$Nd_2Fe_{14}BH_x$	$Nd(OH)_3$
VCM magnet		99.3	0.7	n/d	n/d
Non-milled HD powder	Air	n/d	n/d	89.1	10.9
	MF	n/d	n/d	89.3	10.7
	NMF	n/d	n/d	86.9	13.1
Burr milled HD powder	Air	n/d	n/d	88.8	11.2
	MF	n/d	n/d	89.6	10.4
	NMF	n/d	n/d	79.8	17.2

n/d – not detected

Starting Material

The XRD patterns of the burr milled and the non-milled powder can be observed from figures 106(a) and 106(a), showing that the burr milled feedstock exhibited more intense neodymium hydroxide peaks. The phase quantification in table 18 shows that the non-milled input feed had reached 10.9 wt% neodymium hydride whereas the burr milled contained 11.2 wt%, which is a tiny difference which can be neglected given the error associated with XRD phase quantification analysis.

Non-Milled HD Input Feed

The NMF was richer in neodymium hydride than the MF and the input feed; whereas the MF showed larger matrix hydride concentration than the NMF and the input feed. Nevertheless, the matrix hydride content of the MF is of 89.3 wt% which, compared to the 89.1 wt% of the feedstock, is a tiny, and almost negligible, enhancement. Given the small amount of material separated in the NMF shown in figure 103, it is evident that minor or no enhancements may be achieved.

The matrix hydride to neodymium hydroxide ratios of the feedstock, the MF and the NMF are, respectively, of 8.17, 8.34 and 6.63. The ratio of the MF is far away from those obtained during

hydrocyclone which, as described in section 8.1.4, ranged from 10.49-33.48 for the UF; whereas the ratio of the NMF is much higher than those in the hydrocyclone which were below 1.50 for the OF. The tiny improvement in matrix hydride added to the fact that ratios are poor compared to those from hydrocyclone separation and that the amount of separated NMF is minuscule; reveal that this method is not effective for the separation of both targeted phases.

As the powder was not milled, then most GBP particles were not liberated and were unable to flow freely, hence hindering their effective separation. In addition, some of those particles which were able to flow through the apparatus were rub together creating triboelectric charges that caused fine paramagnetic powder to adhere to ferromagnetic particles, inhibiting separation.

Burr Milled HD Input Feed

There was an increase in neodymium hydroxide from 10.1 wt% in the MF to 17.2 wt% in the NMF; being higher than that in the input feed, of 11.2 wt%. In addition, the matrix hydride content decreased from 88.8 wt% in the input feed to 79.8 in the NMF, but increased to 89.9 in the MF.

This feedstock, compared with the non-milled, has resulted in a MF richer in matrix hydride. However, an improvement of 1.1 wt% may not be significant enough when compared to hydrocyclone separation results. In addition, this feedstock has led to a NMF richer in neodymium hydroxide. This has been possible given the fact that HD powder was milled, hence aiding the paramagnetic GBP particles to flow freely in a larger proportion than when powder non-milled was used. This has enabled obtaining 5 times more powder as observed in figure 103.

The matrix hydride to neodymium hydroxide ration in the NMF was of 4.63. Although it is lower than that of the input feed, 8.35, it is still away from those showed in section 8.2 in hydrocyclone separation which ranged from 0.34 to 0.47 in the OF. Such ratio in the MF was of 8.9, which is better than in the feedstock, but lower when compared with the hydrocyclone results in section 8.2.4, which reached a maximum of 16.24

To sum up, the MF appears to be richer in matrix hydride and the NMF richer in neodymium hydroxide than the starting feed for both feedstocks. In addition, burr milling the feedstock prior to separation has led to improved separation yields. Nonetheless, such improvements are small and further detailed and accurate compositional measurements are required by XRF (see section 8.3.4) and ICP-OES (see section 8.3.5).

8.3.4 X-Ray Fluorescence Spectroscopy

In order to clarify the results and trends observed from XRD results in section 8.3.3, XRF has been performed in all samples. In table 19 the results are presented except the NMF from non-milled feedstock as the quantity of powder collected, of just 0.5 g, was not enough to obtain a reliable, trustworthy result from XRF analysis.

Table 19. X-ray fluorescence spectroscopy results expressed in wt% from all the samples on the performance of three cycles hydrocyclone separation. MF refers to the magnetic fraction and NMF to the non-magnetic fraction collected.

Sample		Fe	Nd	Dy	Nb	Si	Pr	Gd	Sn	Al	ΣREEs
VCM magnet		61.54	34.87	1.38	0.64	0.39	0.22	0.21	0.17	0.11	36.68
Non-milled HD powder	Air	60.97	35.23	1.42	0.64	0.39	0.23	0.23	0.21	0.12	37.11
	MF	61.04	35.19	1.34	0.63	0.39	0.21	0.22	0.25	0.15	35.96
	NMF	Not measured									
Burr milled HD powder	Air	60.42	35.84	1.39	0.65	0.40	0.19	0.23	0.23	0.11	37.65
	MF	61.18	35.31	1.34	0.60	0.38	0.23	0.20	0.17	0.11	37.08
	NMF	52.74	43.37	1.40	0.88	0.47	0.38	0.16	0.13	0.05	45.31

Starting Material

The non-milled feed exhibited a larger content in Fe, Dy and Pr, whereas the burr milled showed a higher quantity of Nd. The Fe/ΣREEs ratio of both the non-milled and the burr milled input feeds is of 1.64 and 1.60 respectively, which is lower than that exhibited by the VCM magnet of 1.68.

Non-Milled HD Input Feed

The Fe content of the MF increased and was consistently accompanied by a decrease in Nd and ΣREEs. It suggests that some separation is taking place, although that does not imply the separation was effective. In addition, the Fe content in the MF is lower than that showed by the VCM magnet.

The Fe/ΣREEs ratio of the MF is 1.65, which is better than the input feed, 1.64, but still far away from that of the stoichiometric $Nd_2Fe_{14}B$, 2.71. In addition, it is lower than any cycle of hydrocyclone separation using non-milled HD powder, which reached 1.69, 2.01 and 2.09 after the first, second and third cycle as shown in section 8.2.

Despite the enhancement in Fe and Nd content as well as in the Fe/ΣREEs ratio, which suggests that some separation is taking place, the resultant powder exhibits no improvement compared to the VCM magnet. This agrees with XRD results showing the inability of separation of the matrix hydride from the GBP.

Burr Milled HD Input Feed

The MF showed an increase in the Fe content whereas the NMF exhibited an enrichment in Nd when compared to the input feed. This suggests that separation is occurring and is enhanced when compared with results using non-milled input feed, which agrees with the XRD results from section 8.3.3.

The NMF exhibited a Fe/ΣREEs ratio of 1.16, which is lower than that of the input feed, 1.60, but higher than hydrocyclone separation using non-milled HD powder, which achieved 0.24 and 0.27 after the first and second cycle as shown in section 8.2.

The MF exhibited a higher Fe and lower Nd content than the input feed and the NMF, but did not overcome those values of the VCM magnet. It showed a Fe/ΣREEs ratio of 1.65, an increase of 0.05 compared to the input feed but lower than that of the VCM magnet, 1.68. It was lower than any cycle of hydrocyclone separation using non-milled HD powder, which reached 1.72, 2.02 and 2.13 after the 1^{st}, 2^{nd} and 3^{rd} cycle.

To sum up, it appears to be more effective to use burr milled HD powder instead of non-milled HD as input feed as it is possible to yield lower Nd contents, higher Fe contents and higher Fe/ΣREEs ratios in the MF. This occurs as a consequence of the decrease in average particle size, allowing particles to flow better through the separating apparatus. The results obtained endorse those from XRD as the MF obtained is better than the feedstock. Despite the fact that some separation is taking place, results have evidenced that WLIMS is not effective enough to overcome the composition of the EOL VCM magnets.

8.3.5 Inductively Coupled Plasma – Optical Emission Spectrometry

In addition, inductively coupled plasma – optical emission spectrometry was used to corroborate the results obtained by XRF. The results from ICP-OES are presented in table 20 except for the NMF after WLIMS from burr milled HD powder input feed as it was contaminated.

Table 20. Inductively coupled plasma – optical emission spectrometry results from all the samples after WLIMS.

Sample		Fe	Nd	Dy	Nb	Si	Pr	Gd	Sn	Al	ΣREEs
VCM magnet		61.92	34.21	0.95	0.06	0.60	0.24	0.05	0.06	1.91	35.45
Non-milled HD powder	Air	61.37	35.31	1.01	0.06	0.14	0.22	0.05	0.06	1.79	36.59
	MF	61.81	35.14	0.98	0.09	0.19	0.44	0.01	0.06	1.29	36.57
	NMF	60.66	36.13	1.09	0.06	0.14	0.48	0.01	0.06	1.38	37.71
Burr milled HD powder	Air	61.05	35.82	1.10	0.06	0.11	0.49	0.01	0.11	1.28	37.42
	MF	61.83	35.00	1.01	0.09	0.14	0.46	0.07	0.06	1.34	36.55
	NMF	Contaminated									

Starting Material

The Fe/ΣREEs ratio of both the non-milled and the burr milled HD powder was of 1.63 and 1.68 respectively, which is lower than that exhibited by the VCM magnet of 1.75. These results are in the same range as those from XRF shown in section 8.3.4, although there are some differences due to the nature of each technique.

Non-Milled HD Input Feed

Using the non-milled the input feed, led to an increase in the Fe content in the MF, and a decrease in the NMF compared to the input feed. This variation in Fe content was consistently accompanied by a decrease in the Nd content in the MF and an increase in the NMF. It suggests that some separation is occurring.

The NMF showed a Fe/ΣREEs ratio of 1.61, which is very close to that of the MF, 1.69; hence separation is occurring but is hindered. Both are below that of the VCM magnet, 1.75.

Burr Milled HD Input Feed

Using the burr milled input feed, showed an increase in the Fe content in the MF and a decrease in Nd compared to the input feed. However, the Fe content is still lower than in the VCM magnet hence showing that the separation is not effective although is taking place. These results are in good agreement with those from XRF shown in section 8.3.4

The Fe/ΣREEs ratio of the MF is 1.69, which is better than the input feed, 1.63, but not as much as that of the VCM magnet, 1.75, and still far away from that of the stoichiometric $Nd_2Fe_{14}B$, 2.71.

It results to be more effective to use burr milled HD powder instead of non-milled HD as input feed as it is possible to yield, lower Nd contents, higher Fe contents and higher Fe/ΣREEs ratios.

To summarise, ICP-OES results confirmed the trends shown by XRD and XRF measurements, however the figures varied slightly due to the nature of each measurement technique. The burr milled powder resulted in better separation efficiency than the non-milled powder, however the results were inferior to the EOL VCM magnet. In addition, the results were significantly inferior to those from hydrocyclone separation evidencing this technique is ineffective as a whole for this application.

Chapter 9. Re-Sintering Hydrocyclone Separated Powder

9.1 Introduction

Powders produced in chapter 8 obtained after 3 cycles of hydrocyclone separation using burr milled HD powder from EOL VCM magnets were processed into new magnets. This powder was re-sintered after blending with 0, 5, 6 or 7 at% $NdH_{2.7}$, aligning and pressing.

As mentioned in section 3.2.6, the $Nd_2Fe_{14}B$ phase constitutes about 82 to 85 % of the total and the Nd-rich occupies approximately 10 % of the volume [Corfield, 2003]. Added to the two different compositions of the Nd-rich phase, $Nd_{75}Fe_{25}$ and $Nd_{95}Fe_5$ at% mentioned in section 3.2.4 [Tang et al, 1988a, 1988b; Ramesh et al, 1987]; it is then possible to calculate the two values of neodymium hydride required to fully replace the GBP in a NdFeB magnet; which are 5.32 and 6.39 wt%. As a consequence, 5, 6 and 7 at% $NdH_{2.7}$ were chosen to be added to EOL VCM magnets.

The extraction of the oxidised particles from the HD powder has proved to be an interesting process performed by hydrocyclone separation, with a moderate degree of separation.

To close the recycling loop, hydrocyclone separated powder was used to produce a recycled magnet. This was done by aligning, pressing and, finally, re-sintering of these powders into magnets.

The powder from hydrocyclone separation after three cycles using burr milled HD powder from EOL VCM magnets is used as the starting material. It exhibited the highest Fe content of all studied fractions in chapter 8, according to XRF and ICP, and its composition was therefore the closest to the stoichiometric $Nd_2Fe_{14}B$. As already explained in chapter 8, the maximum theoretical content of Fe in the UF is of 72.3 wt% and, as a consequence, the UF sample with the highest Fe content may be considered as the sample with the closest composition to that of the stoichiometric.

On the other hand, the best recycled re-sintered magnets obtained in chapters 6 and 7 were the result of blending, respectively, 0 and 5 at% neodymium hydride with the burr milled <45 μm powder from HD of EOL VCM magnets. These will be used as a reference for comparison.

The main aim was to produce a magnet without oxygen as it hinders recycling and achieving good magnetic properties. Hydrocyclone separation was used to strip out the oxidised GBP present on the powder. Afterwards, the hydrocyclone separated powder was blended with 0, 5, 6 or 7 at% neodymium hydride for production of re-sintered magnets in an attempt to replace the GBP extracted during hydrocyclone separation and to optimise its content.

9.2 Results and Discussion

The results of re-sintering hydrocyclone separated powder into magnets, with or without neodymium hydride, are presented and discussed in this section.

9.2.1 Scanning Electron Microscopy

Figure 108 shows the back-scattered SEM images of the recycled re-sintered magnets from hydrocyclone separated powder blended with 0, 5, 6 and 7 at% $NdH_{2.7}$, the EOL VCM magnet and the conventionally recycled re-sintered magnets blended with 0 and 5 at% $NdH_{2.7}$.

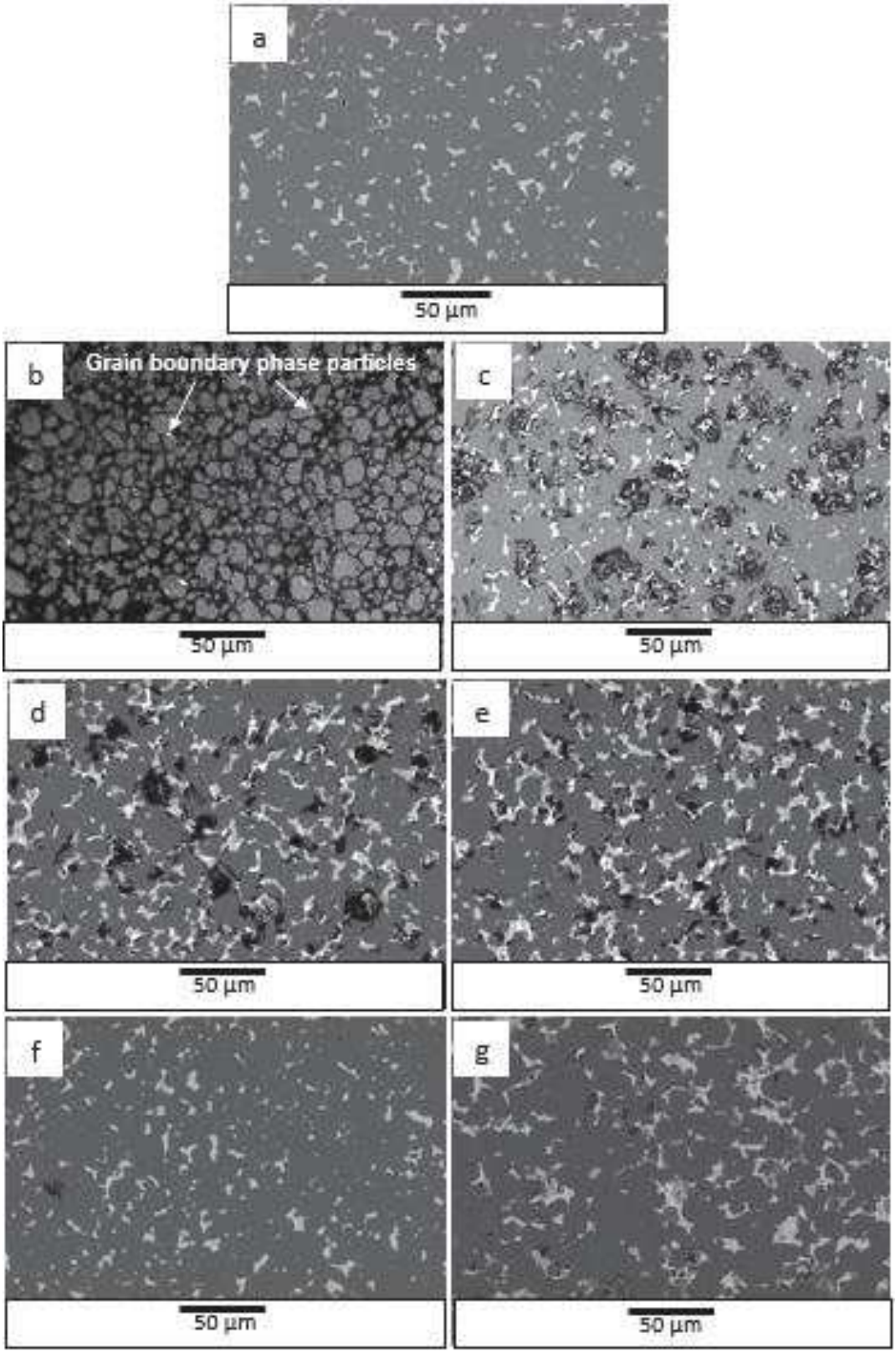

Figure 108. Back-scattered electron SEM images at 500 magnifications micrographs of (a) EOL VCM magnet, (b-e) recycled re-sintered magnets from hydrocyclone separated powder blended with (b) 0 at%, (c) 5 at%, (d) 6 at% and (e) 7 at% neodymium hydride; and from conventionally recycled re-sintered magnets blended with (f) 0 at% and (g) 5 at% neodymium hydride.

Recycling hydrocyclone separated powder without neodymium hydride resulted in a magnet which is not fully dense, as can be observed in figure 108(b). It can be observed some white spots on the surface of the $Nd_2Fe_{14}B$ matrix particles which can be observed more in detail in figure 109.

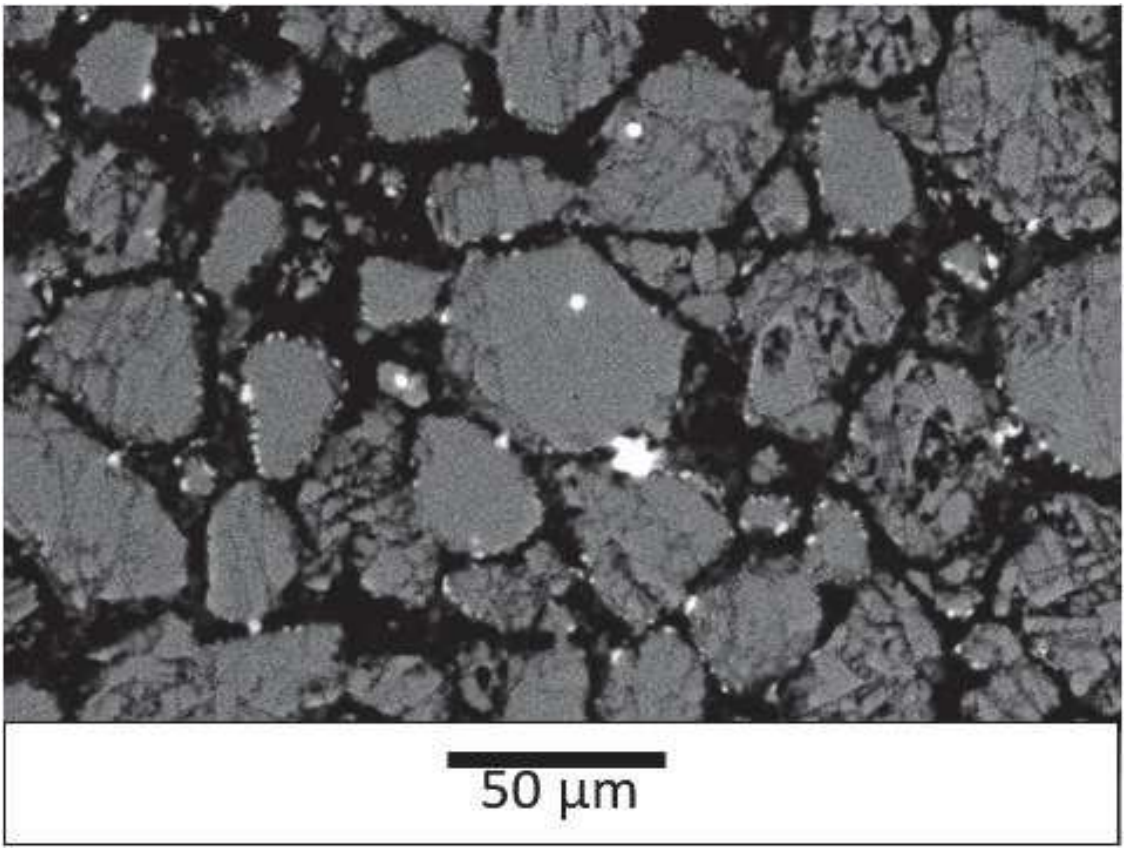

Figure 109. Back-scattered electron SEM image at 2000 magnifications micrographs of recycled re-sintered magnet from hydrocyclone separated powder blended with 0 at% neodymium hydride.

In figure 109, it can be observed some white spots on the surface of the $Nd_2Fe_{14}B$ matrix particles, which correspond to oxygen-rich grain boundary phase particles that were not separated as a consequence of the triboelectric charges generated along the recycling process. These spots showed by EDX to contain 5.02 wt% oxygen, 84.14 wt% Nd and just 10.84 wt% Fe, in contrast to the matrix grains which contained 71.37 wt% Fe, 28.63 wt% Nd and were free from oxygen. Due to the lack of GBP the resultant recycled re-sintered magnet exhibited no magnetisation.

When 0 at% neodymium hydride was blended, it can be observed that magnets produced using the conventional powder metallurgy route, figure 108(f), reached higher density than those produced from

hydrocyclone separated powder, figure 108(b). The main reason for this difference is the effective GBP present during re-sintering. In the case of magnets produced in chapter 7, the neodymium hydride blended was added to that which was already present in the EOL VCM magnet. However, in the case of magnets recycled from hydrocyclone separated powder, the neodymium hydride blended is the only effective GBP present during re-sintering. Therefore, if no neodymium hydride is added, the magnet will have little to no GBP and hence will not achieve full density.

In figure 108(c) it can be observed that blending neodymium hydride with the hydrocyclone separated powder led to a decrease in porosity, which means an increase in density, when compared with figure 108(b) in which zero neodymium hydride was blended.

Moreover, it can be seen that when 5 at% neodymium hydride was blended, the magnets produced using the conventional powder metallurgy route, figure 108(g), reached higher density than those produced from hydrocyclone separated powder, figure 108(c). Therefore, full density was not achieved on magnets from hydrocyclone separated powder blended with 5 at% neodymium hydride. As already stated, this difference arises from the quantity of effective, non-oxidised GBP in the powder before re-sintering.

The back-scattered images in figure 108(c-e) exhibit a subsequent increase in the Nd-rich phase presence with increasing neodymium hydride content. Figures 108(d) and 108(e) show that increasing the neodymium hydride content results in an decrease in porosity and hence an increase in density. It can be observed in figures 108(c-e) that the magnets are not fully dense and they show a number of local inhomogeneous areas with porosity. It implies that the amount of neodymium hydride blended was not enough to achieve full density.

GBP in figure 108 appears to be a dual phase comprising the Nd-rich and a neodymium oxide phase as a consequence of the increase in oxygen. This can be better seen in figure 109.

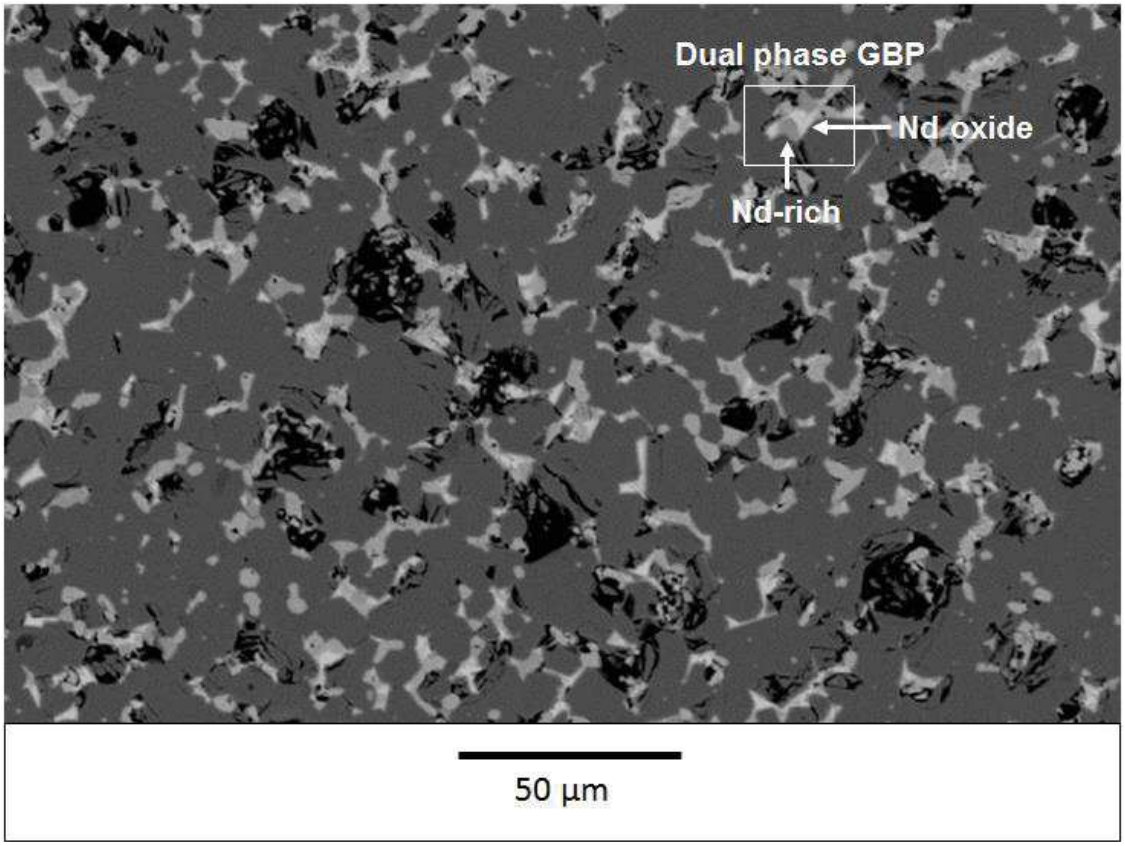

Figure 109. Back-scattered electron SEM image at 500 magnifications of the recycled re-sintered magnets from hydrocyclone separated powder blended with 6 at% neodymium hydride.

The increase in oxygen during recycling has been previously reported to form neodymium oxide at grain boundaries and triple points by Meakin et al [2016] and Zakotnik et al [2009]. The formation of this dual phase GBP was also observed in chapter 7 with increasing the neodymium hydride blended content.

9.2.2 Density

The density and relative density, which is the ratio between the experimental density and the theoretical density in percentage, of the samples studied are shown in table 21.

Table 21. Density and relative density results of the EOL VCM magnet and the recycled re-sintered magnets from hydrocyclone separated powder blended with 0, 5, 6 and 7 at% $NdH_{2.7}$ contents.

Sample	Density [g cm^{-3}]	Relative density [%]
Starting material	7.59	99.98
Separated + 0 at%	5.03	66.48
Separated + 5 at%	6.98	93.06
Separated + 6 at%	7.10	94.60
Separated + 7 at%	7.24	96.56
0 at%	7.46	98.59
5 at%	7.46	99.44

Table 21 shows that recycled re-sintered magnets blended with zero neodymium hydride exhibit a much lower density, 5.03 g cm^{-3}, and also relative density, 66.48%, than that from the starting EOL VCM magnet. As observed in chapter 8, powder after three cycles of hydrocyclone separation using burr milled HD powder as input feed showed a high matrix hydride content as well as a high Fe content, according to XRD phase quantification XRF and ICP-OES. Therefore, most of the GBP was successfully extracted. As a consequence, during re-processing of this powder into a new magnet, it lacked the presence of Nd-rich phase, and hence no liquid phase was generated when re-sintered. It resulted in a magnet which was not fully dense and, thus, showed no magnetisation at all when pulse magnetised.

Neodymium hydride was blended into the hydrocyclone separated powder in an attempt to allow liquid phase during re-sintering and hence obtain a fully dense recycled magnet. It can be observed that density increased linearly with the amount of neodymium hydride blended. These results endorse observations from section 9.2.1 in which a decrease in porosity was observed with increasing the amount of neodymium hydride. Although full density was not reached in any case, much better results than when no neodymium hydride was blended have been achieved. The introduction of fresh neodymium to replace the extracted GBP is a valid technique to enhance LPS and to yield higher

density values. It implies that the amount of neodymium hydride blended was not enough to achieve full density by melting and filling the pores and cavities during LPS.

The densities of the magnets recycled using the conventional powder metallurgy route showed in chapter 7 blended with 0 and 5 at% neodymium hydride are also shown in table 21. Both show that the magnets produced using the conventional powder metallurgy route reached higher density and relative density than those produced from hydrocyclone separated powder.

In the case of the magnets produced in chapter 7, the neodymium hydride blended was added to the GBP previously present in the EOL VCM magnet. Whilst in the case of the magnet recycled from hydrocyclone separated powder, the neodymium hydride blended was the only effective, non-oxidise GBP present during re-sintering.

9.2.3 Magnetic Properties

The demagnetisation loops of the EOL VCM magnet and the recycled re-sintered magnets from hydrocyclone separated powder blended with 5, 6 and 7 at% $NdH_{2.7}$, along with the recycled re-sintered magnets from HD powder blended with 0 and 5 at% neodymium hydride (from chapters 6 and 7) are presented in figure 110 in order to compare both recycling routes. The results at room temperature are also presented in table 22, including the values of intrinsic coercivity, remanence and maximum energy product.

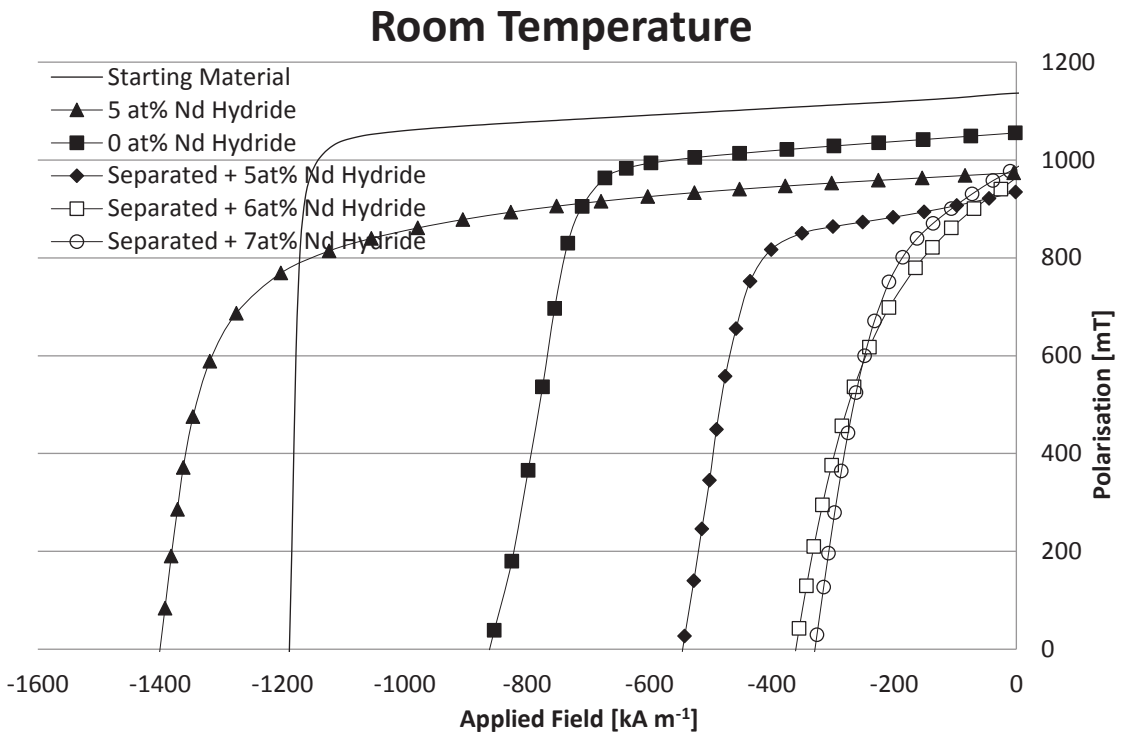

Figure 110. Demagnetisation loops of the EOL VCM magnet, the recycled re-sintered magnets from hydrocyclone separated powder blended with 5 at% $NdH_{2.7}$, and the conventionally recycled re-sintered magnets blended with 0 and 5 at% $NdH_{2.7,}$ at room temperature.

Table 22. Magnetic properties of the EOL VCM magnet, the recycled re-sintered magnets from hydrocyclone separated powder blended with 5 at% $NdH_{2.7}$, and the conventionally recycled re-sintered magnets blended with 0 and 5 at% $NdH_{2.7,}$ at room temperature.

Sample	Coercivity [kA m^{-1}]	Remanence [mT]	$(BH)_{max}$ [kJ m^{-3}]
Starting material	1191	1140	242
Separated + 0 at%	0	0	0
Separated + 5 at%	545	934	146
Separated + 6 at%	358	962	112
Separated + 7 at%	331	982	103
0 at%	860	1059	203
5 at%	1400	975	179

Table 22 shows that recycled re-sintered magnets from hydrocyclone separated powder with 0 at% neodymium hydride exhibited no magnetisation. This occurred as a consequence of the incomplete sintering due to the lack of Nd-rich phase, which led to poor density. As it showed no magnetisation, it has not been included in figure 110, as it would have appeared as a single spot at the origin of the chart.

It should be noted that this recycling route is different from the conventional powder metallurgy route used in chapter 7, in which the neodymium hydride blended was added to the GBP already present in the EOL VCM magnet. In the case of the magnet recycled from hydrocyclone separated powder, the neodymium hydride blended was the only effective non-oxidised GBP present during re-sintering. It explains why both magnets blended with 0 at% neodymium hydride in table 22 differ in magnetic properties.

Recycled re-sintered magnet from hydrocyclone separated powder blended with 5 at% neodymium hydride exhibited a typical hard ferromagnetic hysteresis loop. This magnet showed lower magnetic properties than the EOL VCM magnet. This reduction is a consequence of the decrease in density shown in table 21.

Porosity is present because, as suggested in section 9.2.1, the amount of neodymium hydride blended was insufficient to replace all the oxygen-rich GBP that was extracted. Therefore, it was not possible to achieve full density by melting and filling the pores and cavities during LPS. That lack of GBP present during sintering resulted in $Nd_2Fe_{14}B$ matrix grains being not homogeneously covered by a smooth layer of GBP, which finally caused a sharp decrease in intrinsic coercivity.

The reduction in density of the recycled re-sintered magnet means that a large amount of non-magnetic volume exists as a consequence of the presence of porosity. Therefore, the proportion of $Nd_2Fe_{14}B$ matrix grains within the magnet decreased, causing a reduction in the remanence exhibited by the final magnet. As a consequence of the reduction in both remanence and intrinsic coercivity, the maximum energy product of recycled re-sintered magnets from hydrocyclone powder blended with 5 at% neodymium hydride was also reduced.

When recycled re-sintered magnets from hydrocyclone separated powder blended with 5 at% neodymium hydride are compared with recycled re-sintered magnets blended with 5 at% neodymium hydride produced using the conventional powder metallurgy route, it can be seen that the former exhibits a decrease in intrinsic coercivity, remanence and maximum energy product of 61.1%, 4.2%

and 18.4%, respectively. The contrast between the differences in intrinsic coercivity and remanence of both recycled re-sintered magnets indicates the key role that Nd-rich GBP plays. In addition, it highlights the fact that the $Nd_2Fe_{14}B$ matrix phase remained intact after being subjected to hydrocyclone separation, hence exhibiting a good remanence.

When higher quantities of neodymium hydride were blended, 6 and 7 at%, the intrinsic coercivity and maximum energy product decreased whereas the remanence increased. The increase in remanence can be explained by the increase in density hence having lower amounts of pores that are now filled by GBP, matrix grains or both. Therefore, remanence of the magnet increases with increasing the neodymium hydride blended. However, the intrinsic coercivity decrease is a controversial result as it contradicts the enhancement in density. This may be attributed to the partial oxidation of the GBP at a late stage of sintering so both densification and a decrease in coercivity may be compatible.

The demagnetisation loops of the EOL VCM magnet and the recycled re-sintered magnets from hydrocyclone separated powder blended with 5 at% $NdH_{2.7}$, and the conventionally recycled re-sintered magnets blended with 0 and 5 at% $NdH_{2.7,}$ tested at 75 °C and 150 °C are presented, respectively, in figures 111 and 112. Magnets blended with 6 and 7 at% neodymium hydride were not tested at high temperature due to the poor performance demonstrated at room temperature.

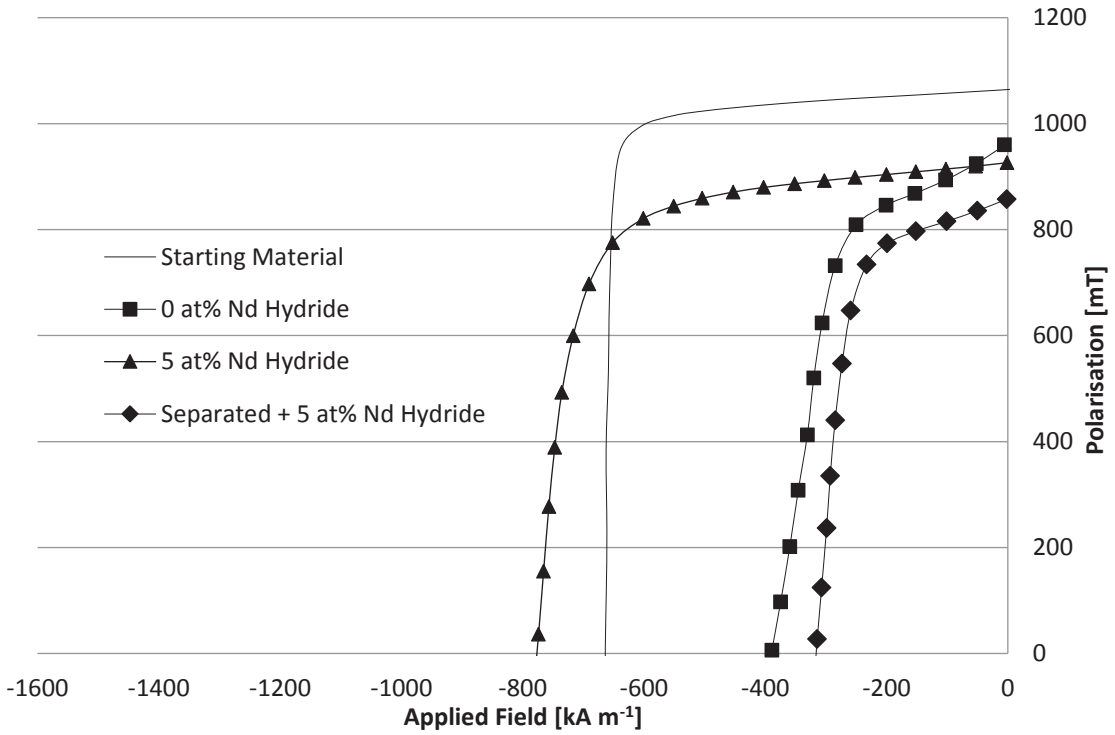

Figure 111. Demagnetisation loops of the EOL VCM magnet, the recycled re-sintered magnets from hydrocyclone separated powder blended with 5 at% $NdH_{2.7}$, and the conventionally recycled re-sintered magnets blended with 0 and 5 at% $NdH_{2.7}$, at 75 °C.

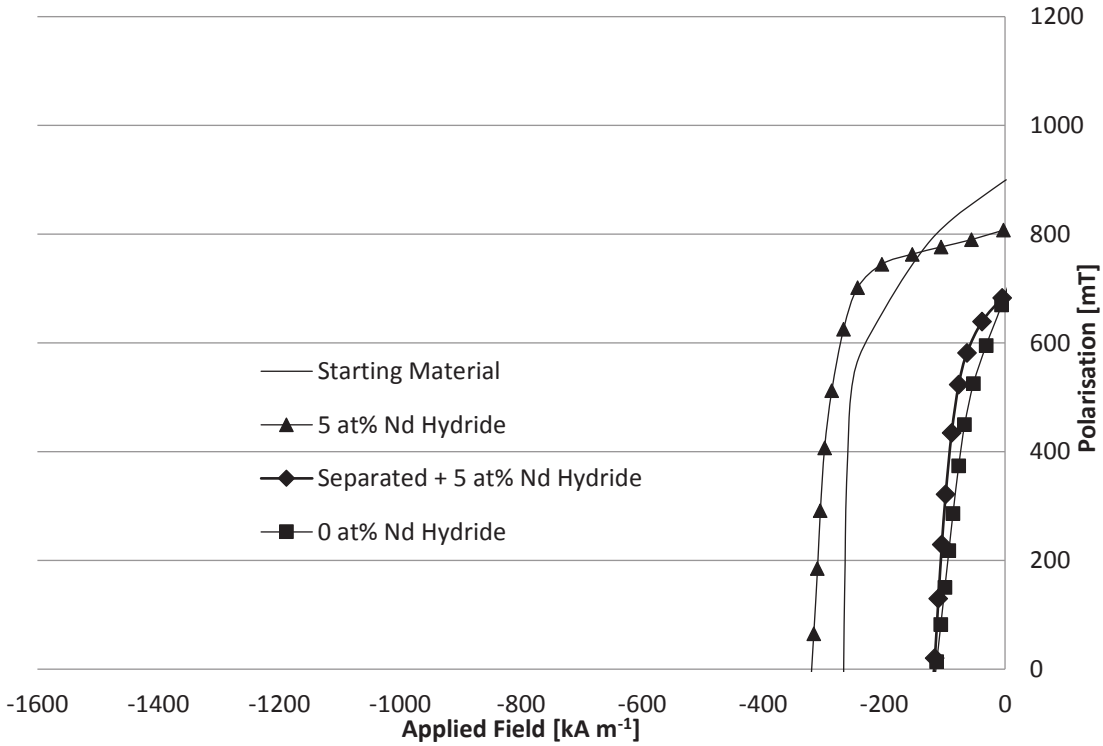

Figure 112. Demagnetisation loops of the EOL VCM magnet, recycled re-sintered magnets from hydrocyclone separated powder blended with 5 at% $NdH_{2.7}$, and the conventionally recycled re-sintered magnets blended with 0 and 5 at% $NdH_{2.7}$, at 150 °C.

The results at 75 °C and 150 °C are also presented, respectively, in tables 23 and 24, including the values of intrinsic coercivity, remanence and maximum energy product. In addition, as these measurements were performed at 75 °C and 150 °C, respectively, the values of α and β are also included. They respectively refer to the thermal stability of remanence and intrinsic coercivity between room temperature and the temperature at which the properties were measured.

Table 23. Magnetic properties of the EOL VCM magnet, the recycled re-sintered magnets from hydrocyclone separated powder blended with 5 at% $NdH_{2.7}$, and the conventionally recycled re-sintered magnets blended with 5 at% $NdH_{2.7,}$ at 75 °C.

Sample	Coercivity [kA m^{-1}]	Remanence [mT]	$(BH)_{max}$ [kJ m^{-3}]	α [% $°C^{-1}$]	β [% $°C^{-1}$]
Starting material	666	1065	214	-0.120	-0.801
Separated + 5 at%	315	858	106	-0.148	-0.767
5 at%	779	925	155	-0.093	-0.806

Table 24. Magnetic properties of the EOL VCM magnet, the recycled re-sintered magnets from hydrocyclone separated powder blended with 5 at% $NdH_{2.7}$, and the conventionally recycled re-sintered magnets blended with 5 at% $NdH_{2.7,}$ at 150 °C.

Sample	Coercivity [kA m^{-1}]	Remanence [mT]	$(BH)_{max}$ [kJ m^{-3}]	α [% $°C^{-1}$]	β [% $°C^{-1}$]
Starting material	264	905	89	-0.158	-0.599
Separated + 5 at%	117	685	32	-0.205	-0.604
5 at%	320	809	99	-0.131	-0.593

As with room temperature measurements, it has been shown in figures 111 and 112 that the influence of the reduction in density is high. It resulted in sharp reductions in intrinsic coercivity, remanence and maximum energy product of 52.7%, 19.4% and 50.5%, respectively, when compared to the EOL VCM magnets at 75 °C and of 55.7%, 24.3% and 64.0%, respectively at 150 °C.

This sharpening of reduction also appeared when comparing both recycled re-sintered magnets blended with 5 at% neodymium hydride produced from conventional recycling routes. These reductions were of 59.6%, 7.2% and 31.6% in intrinsic coercivity, remanence and maximum energy product, respectively, at 75 °C; and of 63.4%, 15.3% and 67.7% at 150 °C.

In these comparisons the sharpening effect is not only due to the influence of the reduction in density, but also to the thermal stability behaviour of the recycled re-sintered magnets. At room temperature, thermal agitation is not sufficiently high to disrupt the alignment of hard magnetic $Nd_2Fe_{14}B$ phase matrix grains but with increasing the temperature the magnet starts to lose its alignment.

The thermal stability of remanence and intrinsic coercivity, were obtained in the range 20-75 °C and 20-150 °C. In the former range, α and β exhibited by the recycled re-sintered magnets from hydrocyclone separated powder blended with 5 at% neodymium hydride were, -0.148 and -0.767% $°C^{-1}$ respectively; whereas in the latter range, they respectively were, -0.205 and -0.604% $°C^{-1}$. The differences in α from one temperature range to another mean that in the 20-75 °C range the remanence is much more stable that in the 20-150 °C range. This implies that most of the degradation in remanence occurs in the 75-150 °C range. The results of β in both ranges have shown the inverse effect to that with α. The intrinsic coercivity degradation resulted to be more stable in the 20-150 °C range than in the 20-75 °C range.

Recycled re-sintered magnets from hydrocyclone separated powder blended with 5 at% neodymium hydride have shown α values in both temperature ranges worse than those exhibited by the EOL VCM magnets. Nonetheless, β values were comparable in both temperature ranges.

When comparing both recycled re-sintered magnets blended with 5 at% neodymium hydride produced from different recycling routes, it can be seen in table 24 that magnets recycled using the conventional powder metallurgy route achieved superior α and β values in the range 20-150 °C.

In summary it has been shown that it is possible to produce hard magnetic recycled re-sintered magnets from hydrocyclone separated powder by blending neodymium hydride to replace the separated GBP. Although the magnetic properties are much lower than those of the starting EOL VCM magnets there is scope for this to be an effective route for recycling sintered NdFeB magnets by optimising the blending of $NdH_{2.7}$ to achieve full density as well as the hydrocyclone separation process.

All manufactured magnets were not heat treated as mentioned in section 5.2.7. Nevertheless, as already discussed in 3.3.6.5, performing heat treatments lead to an increase in the intrinsic coercivity.

Chapter 10. Conclusions

As shown in chapter 6, by decreasing the particle size of the hydrogenated neodymium-iron-boron (NdFeB) powder by milling and sieving through a 45 μm sieve it is possible to increase the remanence in the final NdFeB magnet compared to larger particle sizes. Therefore, it is necessary to further reduce the polycrystalline NdFeB powder to near single crystals in order to get the best magnetic properties. As a consequence, the hydrogen decrepitated (HD) powder will need to be jet milled prior to re-sintering, which will lead to an increase in the cost and energy consumption for recycling.

The magnetic properties of the recycled magnets without additions were not at the same level as the starting voice coil motor (VCM) magnets. This is likely to be due to incomplete sintering as a consequence of an increase in oxygen in the secondary material. In order to alleviate this effect and reach higher magnetic properties, it is necessary to blend with an element or alloy that enhances liquid phase during sintering.

Blending 1-5 at% neodymium tri-hydride was an effective method to recover the coercivity at the expense of a small reduction in remanence and maximum energy product. When extra rare earth is added to the magnets then the remanence falls as a larger non-ferromagnetic fraction is present in the magnet. With additions of 3 at% neodymium hydride the coercivity of the recycled magnets can be recovered to the level of starting material; and even surpassed when neodymium hydride contents above 3 at% are achieved. The neodymium used for blending, added in tri-hydride form, was primary material; hence increasing the price of the recycled magnet. It also leaves the recycling process open to supply restrictions from the primary producers if only on a small scale. However, at present primary neodymium prices are relatively low (£39 per kg of Nd metal [Shanghai Metals Market, 2016]). Therefore, the increase in cost of the recycled magnet would not be significant, below £3.

An approach to overcome this is to further extract the oxygen-rich grain boundary phase and then blend fresh Nd back into the magnets to completely replace the grain boundary phase. If oxygen is not removed, then the magnetic properties will deteriorate with each recycling cycle [Zakotnik et al, 2009]. This has been performed by wet low-intensity magnetic separation and hydrocyclone separation.

Wet low-intensity magnetic separation was demonstrated to be an ineffective method to separate the hard magnetic matrix phase from the oxygen-rich non-magnetic grain boundary phase as a consequence of the triboelectric charge built-up due to friction between both fractions.

Hydrocyclone, in contrast, showed promising separations with increasing number of passes through the system. On each pass an increase in the amount of matrix phase in the underflow (UF) was observed. Further passes are required on the hydrocyclone in order to maximise the separation and to obtain a UF as close as possible to stoichiometric $Nd_2Fe_{14}B$. The hydrocyclone process is a simple technique which is used commonly for mineral processing, making it a good candidate for further upscaling in a flow sheet for recycling of NdFeB scrap.

The separated matrix phase particles were shown to be mostly intact after exposure to water and air at 80 °C, which is perhaps surprising, given the fine particle size of the hydrogenate NdFeB powder. In addition, the use of an inert gas as separation media such as nitrogen in a jet mill may be of further interest to optimise the separation of both fractions.

Further recycling of hydrocyclone separated powder by blending neodymium hydride into re-sintered magnets may be an alternative to conventional recycling. Magnets achieved good remanence but low coercivity values. However, as the neodymium blended was not recycled but from primary production, this process is not using 100 % recycled material.

In another project at the University of Birmingham, Jönsson et al [2016a, 2016b] have investigated the possibility of separating pure neodymium hydride from the rest of the NdFeB elements. If successful, this will be blended back in to the hydrogenated NdFeB powder. If successful, then this will lead to a 100 % recycled magnet.

In addition, this thesis is the first report on the impact of the re-sintering route on the mechanical properties of the recycled magnets. Vickers hardness was found to decrease in every recycled magnet, whereas fracture toughness decreased when no alloying elements were added, and increased when neodymium hydride was blended, reaching 4.01 MPa $m^{1/2}$ when 5 at% $NdH_{2.7}$ was blended.

Chapter 11. Future Work

- Study of the influence of different milling techniques, such as jet milling on the comminution of the HD powder and, consequently, on the properties of the recycled re-sintered magnet.
- Investigate the particle size distribution of the HD powder prior sintering in an attempt to correlate it to the magnetic properties of the recycled re-sintered magnet; and relate it to the comminution technique employed. This could be studied using laser diffraction with the particles dispersed in a protective liquid media.
- Assessment of the powder after hydrocyclone separation performed cyclically more than 3 times in order to increase the purification of the matrix phase in the UF.
- Study of the potential use of nitrogen as a separation media during hydrocyclone using a jet mill with particle size classifier in order to eliminate the adverse effects of water on the HD powder.
- Investigate decreasing the particle size of the neodymium hydride further either by increasing milling times or by changing the milling technique, in an attempt to obtain a more homogeneous distribution of the Nd-rich grain boundary phase across the magnet.
- Study the effect of blending other rare earth hydrides such as Tb or Dy and investigate its impact on magnetic and mechanical properties; as they exhibit the highest anisotropy field of all $RE_2Fe_{14}B$ compounds.
- Evaluation of the corrosion resistance of these recycled re-sintered magnets using environmental accelerated testing, e.g. 80 °C at 80 % humidity.
- Assessment of the impact of heat treating/annealing the recycled re-sintered magnets, varying both the heat treatment temperature and hold time on magnetic and mechanical properties of the final magnets.

- Investigate the oxygen content of the recycled re-sintered magnets from hydrocyclone separated powder after different number of runs; and correlate it to the microstructures and magnetic properties exhibited by those.
- The effect of blending neodymium from secondary sources into hydrogenated NdFeB scrap powder. More specifically, hydrogen disproportionated powder after milling [Jönsson et al, 2016a; 2016b].

Appendix

Thermal Desorption Traces from Chapter 8

Non-milled hydrogen decrepitated voice coil motor magnet powder air-tight

Non-milled hydrogen decrepitated voice coil motor magnet powder exposed to air

Burr milled hydrogen decrepitated voice coil motor magnet powder air-tight

Burr milled hydrogen decrepitated voice coil motor magnet powder exposed to air

Underflow powder after 1 cycle of hydrocyclone separation using non-milled HD VCM powder

Underflow powder after 2 cycles of hydrocyclone separation using non-milled HD VCM powder

Underflow powder after 3 cycles of hydrocyclone separation using non-milled HD VCM powder

Overflow powder after 1 cycle of hydrocyclone separation using non-milled HD VCM powder

Overflow powder after 2 cycles of hydrocyclone separation using non-milled HD VCM powder

Overflow powder after 3 cycles of hydrocyclone separation using non-milled HD VCM powder

Underflow powder after 1 cycle of hydrocyclone separation using burr milled HD VCM powder

Underflow powder after 2 cycles of hydrocyclone separation using burr milled HD VCM powder

Underflow powder after 3 cycles of hydrocyclone separation using burr milled HD VCM powder

Overflow powder after 1 cycle of hydrocyclone separation using burr milled HD VCM powder

Overflow powder after 2 cycles of hydrocyclone separation using burr milled HD VCM powder

Overflow powder after 3 cycles of hydrocyclone separation using burr milled HD VCM powder

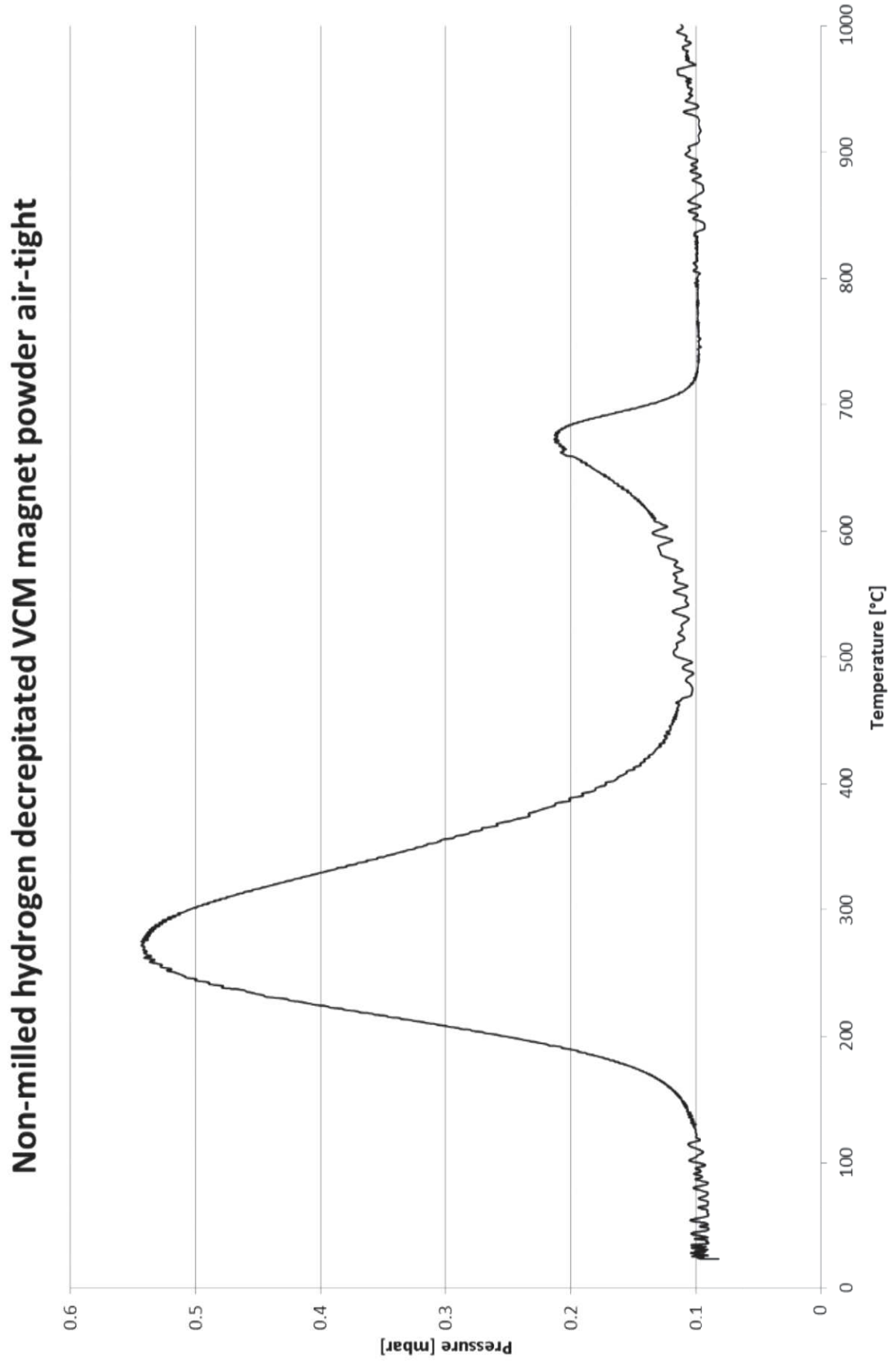
Non-milled hydrogen decrepitated VCM magnet powder air-tight
Pressure [mbar]
0.6
0.5
0.4
0.3
0.2
0.1
0
Temperature [°C]
0
100
200
300
400
500
600
700
800
900
1000

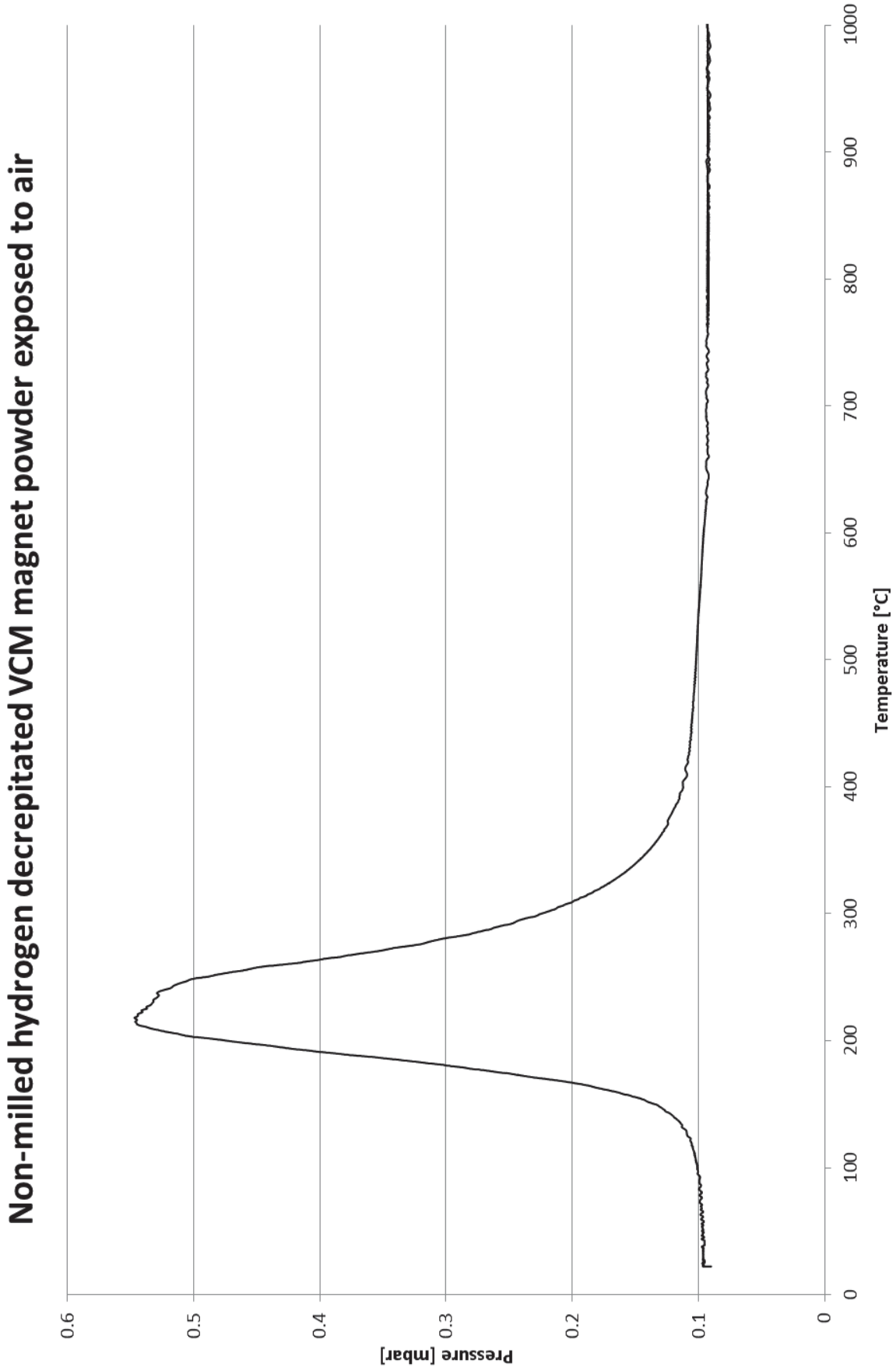
Non-milled hydrogen decrepitated VCM magnet powder exposed to air
Pressure [mbar]
0.6
0.5
0.4
0.3
0.2
0.1
0
0
100
200
300
400
500
600
700
800
900
1000
Temperature [°C]

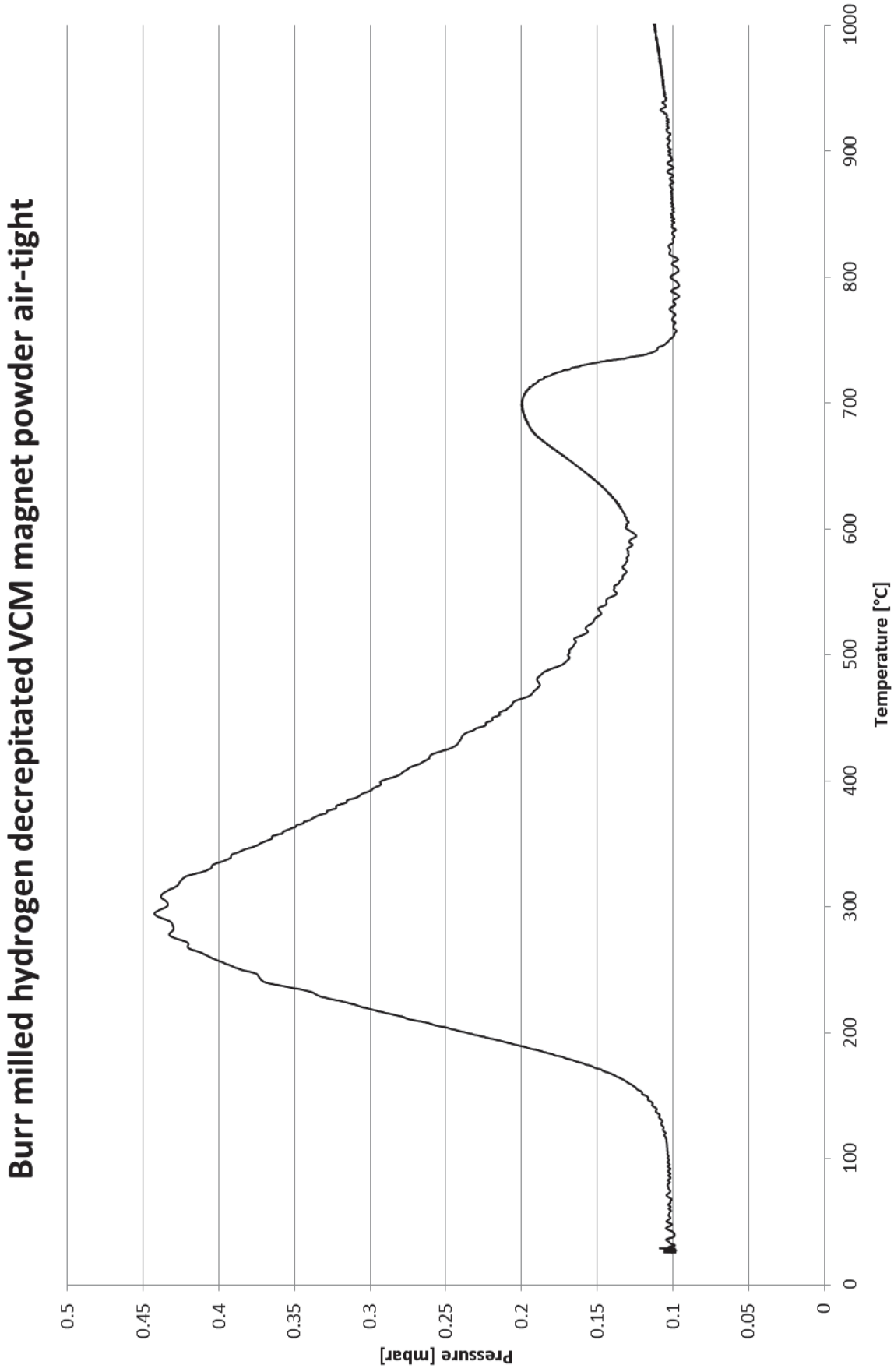
Burr milled hydrogen decrepitated VCM magnet powder air-tight
Pressure [mbar]
0.5
0.45
0.4
0.35
0.3
0.25
0.2
0.15
0.1
0.05
0
Temperature [°C]
0
100
200
300
400
500
600
700
800
900
1000

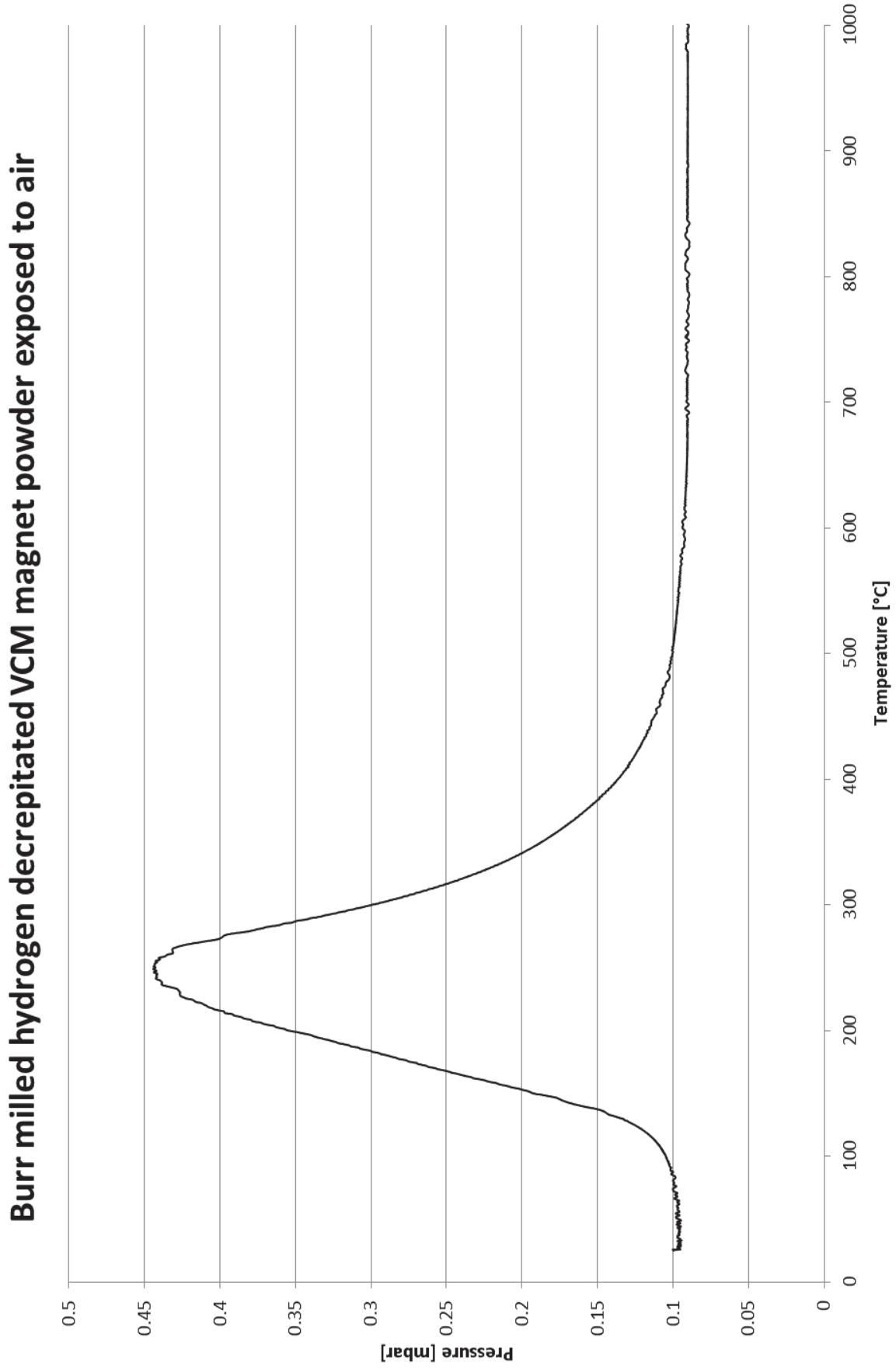
Burr milled hydrogen decrepitated VCM magnet powder exposed to air
Pressure [mbar]
0.5
0.45
0.4
0.35
0.3
0.25
0.2
0.15
0.1
0.05
0
Temperature [°C]
0
100
200
300
400
500
600
700
800
900
1000

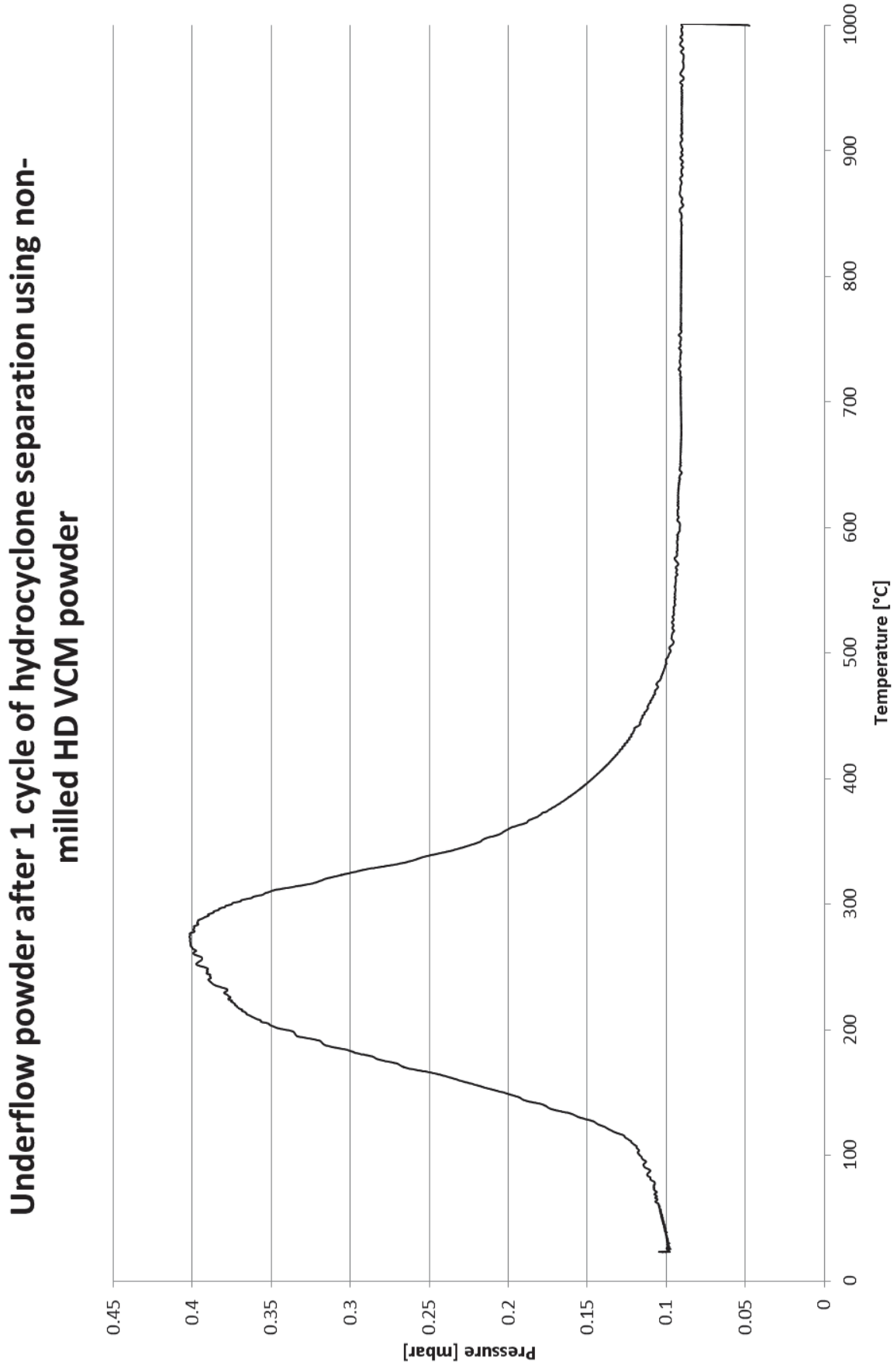
Underflow powder after 1 cycle of hydrocyclone separation using non-milled HD VCM powder
Pressure [mbar]
0.45
0.4
0.35
0.3
0.25
0.2
0.15
0.1
0.05
0
Temperature [°C]
0
100
200
300
400
500
600
700
800
900
1000

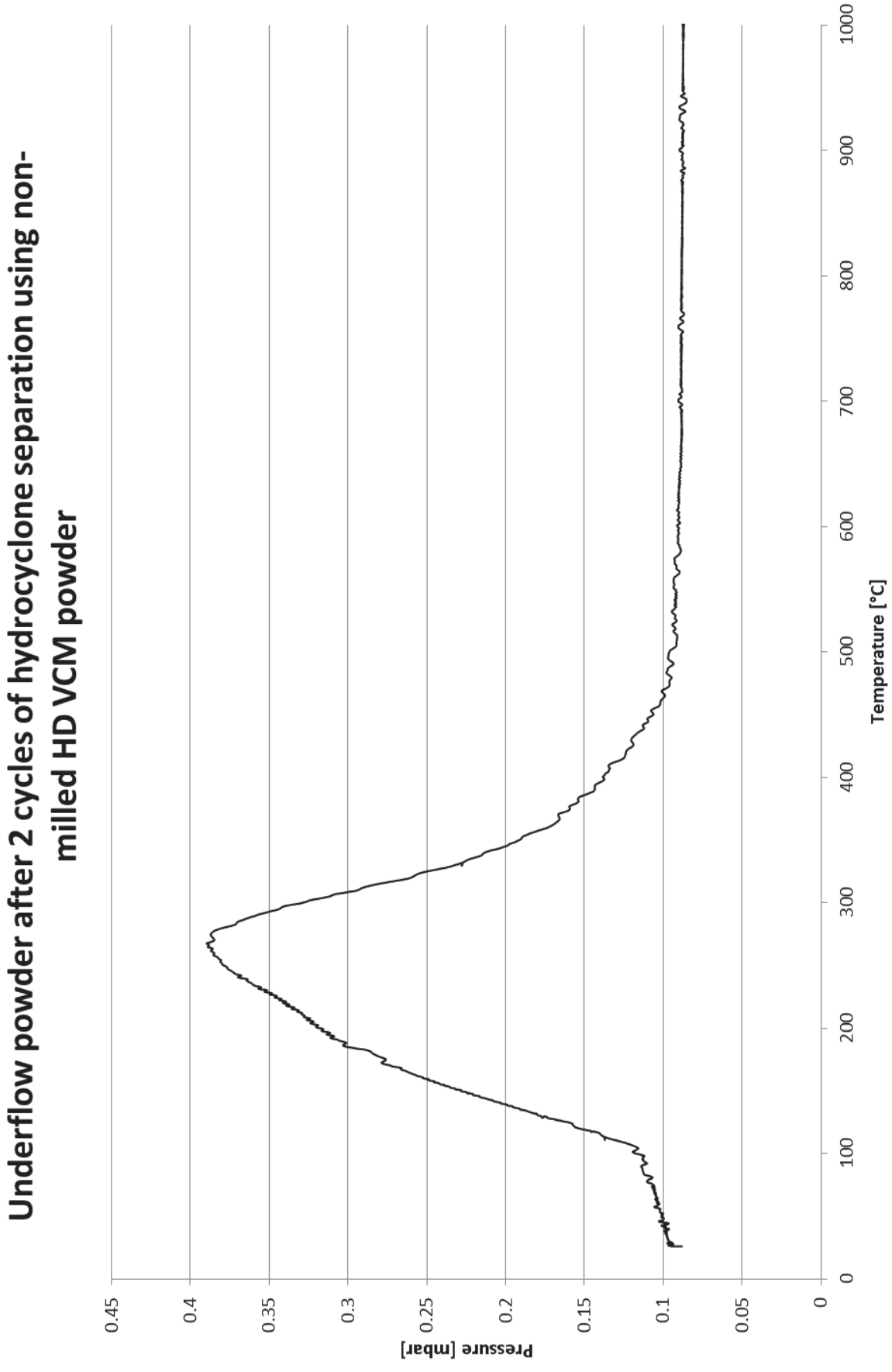
Underflow powder after 2 cycles of hydrocyclone separation using non-milled HD VCM powder
Pressure [mbar]
0.45
0.4
0.35
0.3
0.25
0.2
0.15
0.1
0.05
0
Temperature [°C]
0
100
200
300
400
500
600
700
800
900
1000

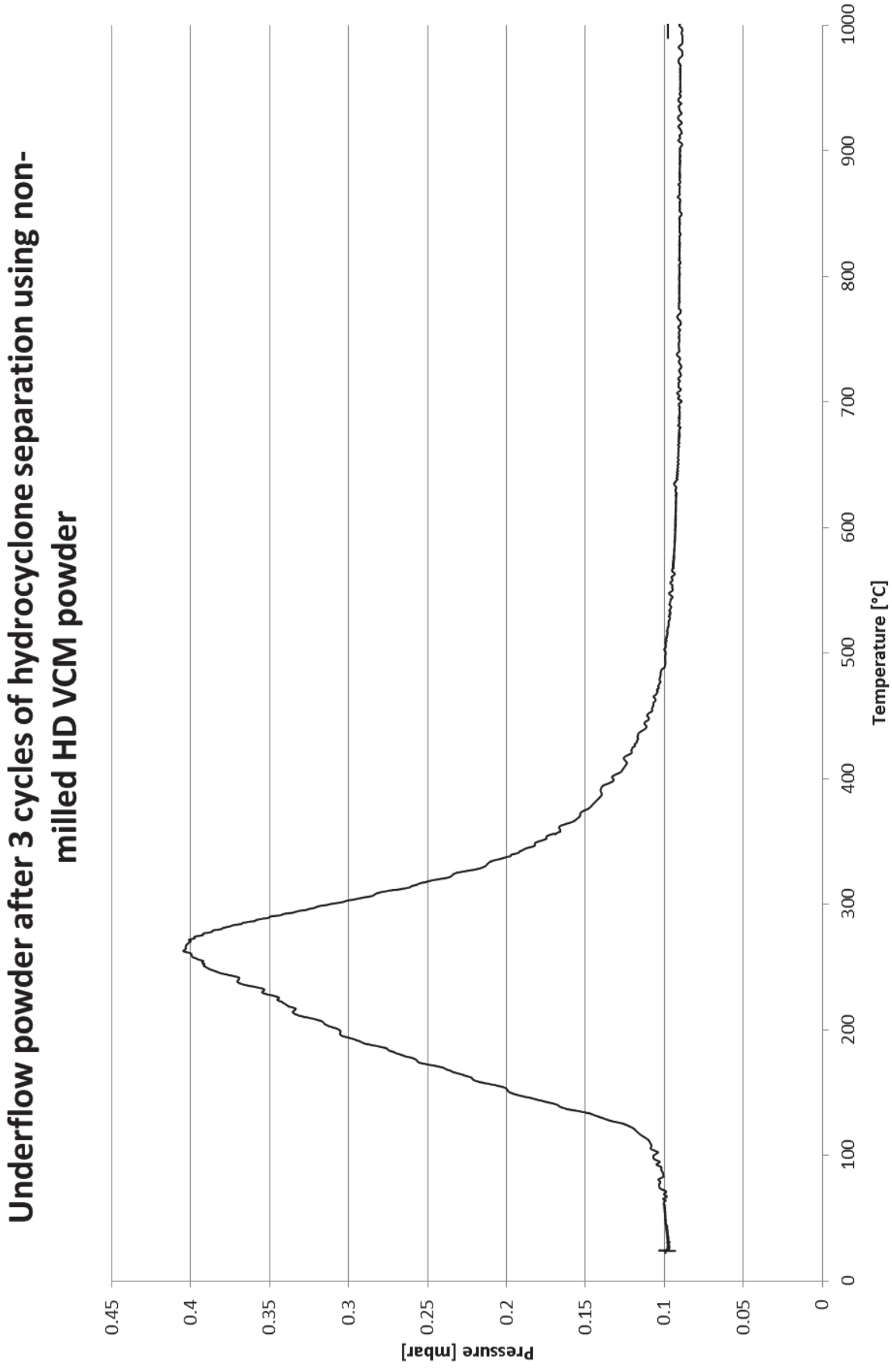
Underflow powder after 3 cycles of hydrocyclone separation using non-milled HD VCM powder
Pressure [mbar]
0.45
0.4
0.35
0.3
0.25
0.2
0.15
0.1
0.05
0
Temperature [°C]
0
100
200
300
400
500
600
700
800
900
1000

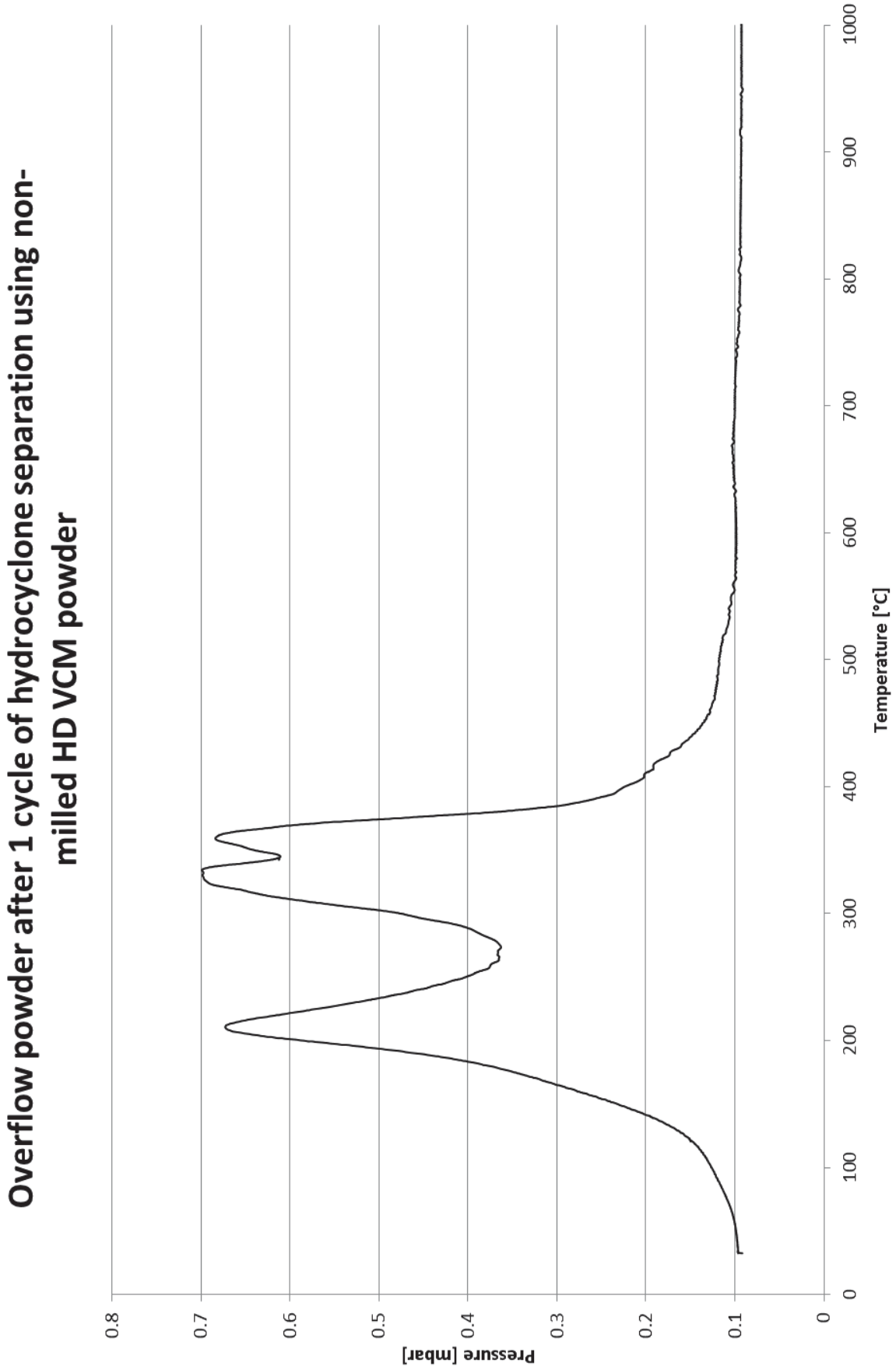
Overflow powder after 1 cycle of hydrocyclone separation using non-milled HD VCM powder
Pressure [mbar]
0.8
0.7
0.6
0.5
0.4
0.3
0.2
0.1
0
Temperature [°C]
0
100
200
300
400
500
600
700
800
900
1000

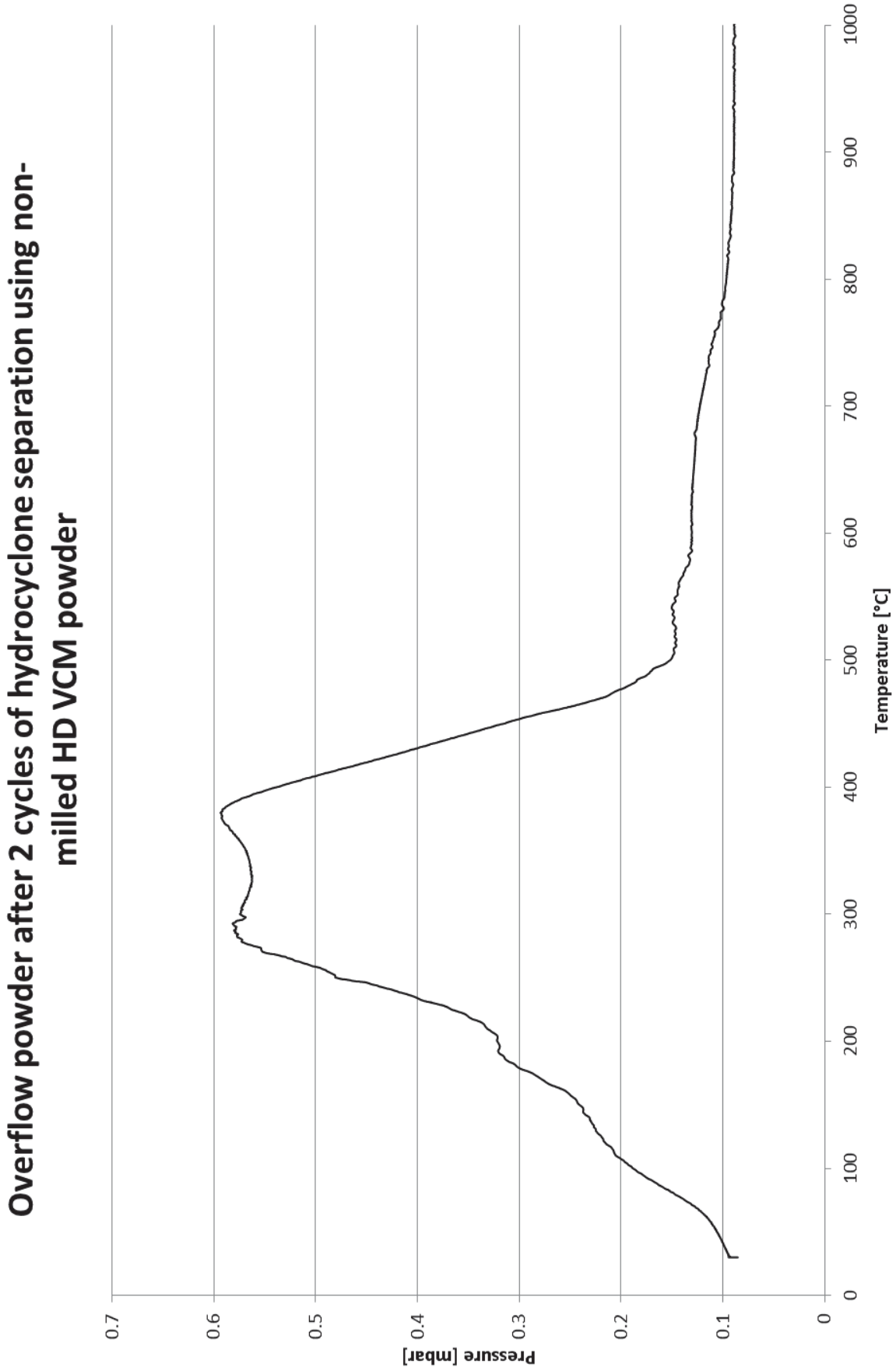
Overflow powder after 2 cycles of hydrocyclone separation using non-milled HD VCM powder
Pressure [mbar]
0.7
0.6
0.5
0.4
0.3
0.2
0.1
0
Temperature [°C]
0
100
200
300
400
500
600
700
800
900
1000

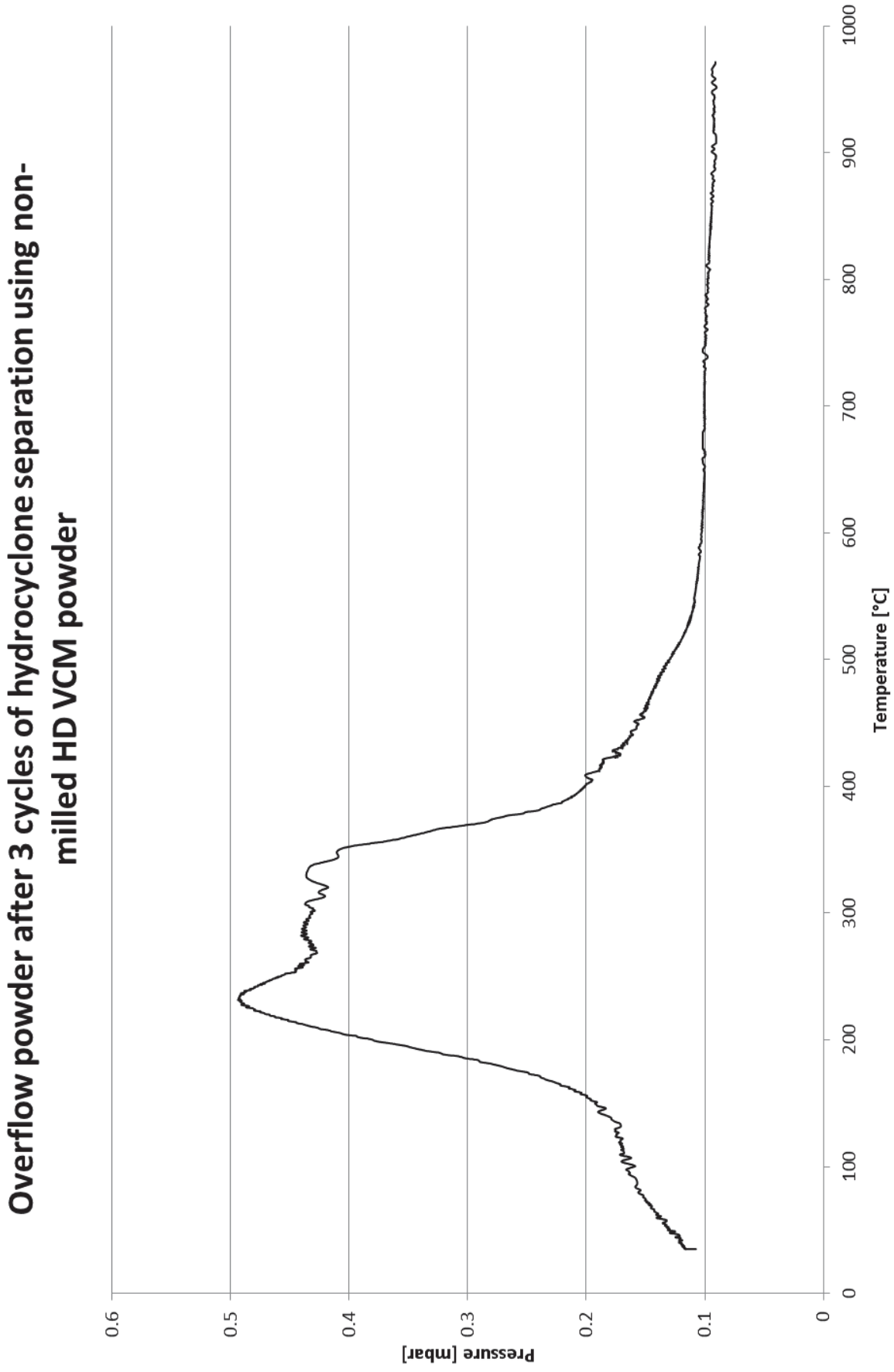
Overflow powder after 3 cycles of hydrocyclone separation using non-milled HD VCM powder
Pressure [mbar]
0.6
0.5
0.4
0.3
0.2
0.1
0
Temperature [°C]
0
100
200
300
400
500
600
700
800
900
1000

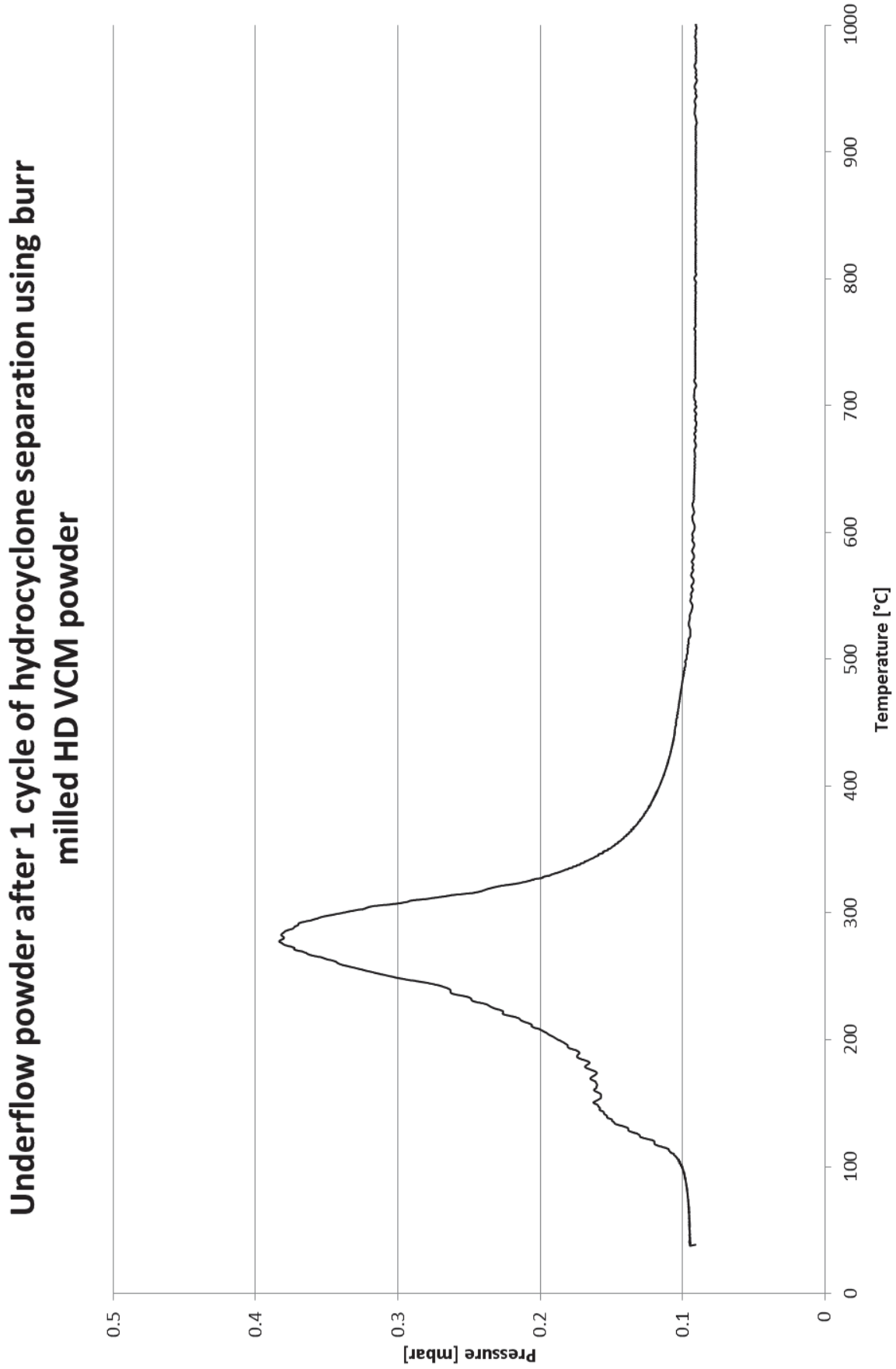
Underflow powder after 1 cycle of hydrocyclone separation using burr milled HD VCM powder
Pressure [mbar]
0.5
0.4
0.3
0.2
0.1
0
Temperature [°C]
0
100
200
300
400
500
600
700
800
900
1000

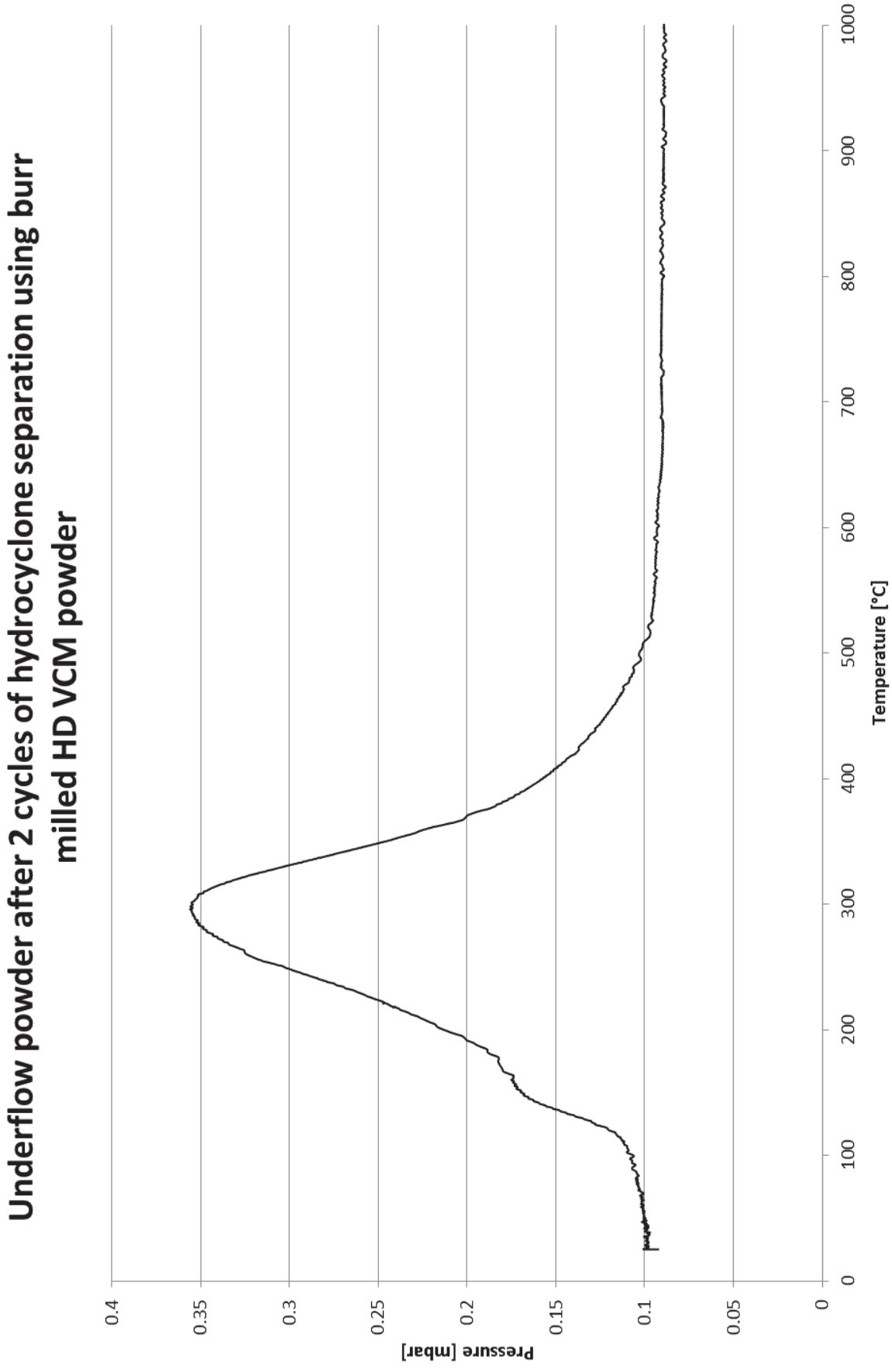
Underflow powder after 2 cycles of hydrocyclone separation using burr milled HD VCM powder
Pressure [mbar]
0.4
0.35
0.3
0.25
0.2
0.15
0.1
0.05
0
Temperature [°C]
0
100
200
300
400
500
600
700
800
900
1000

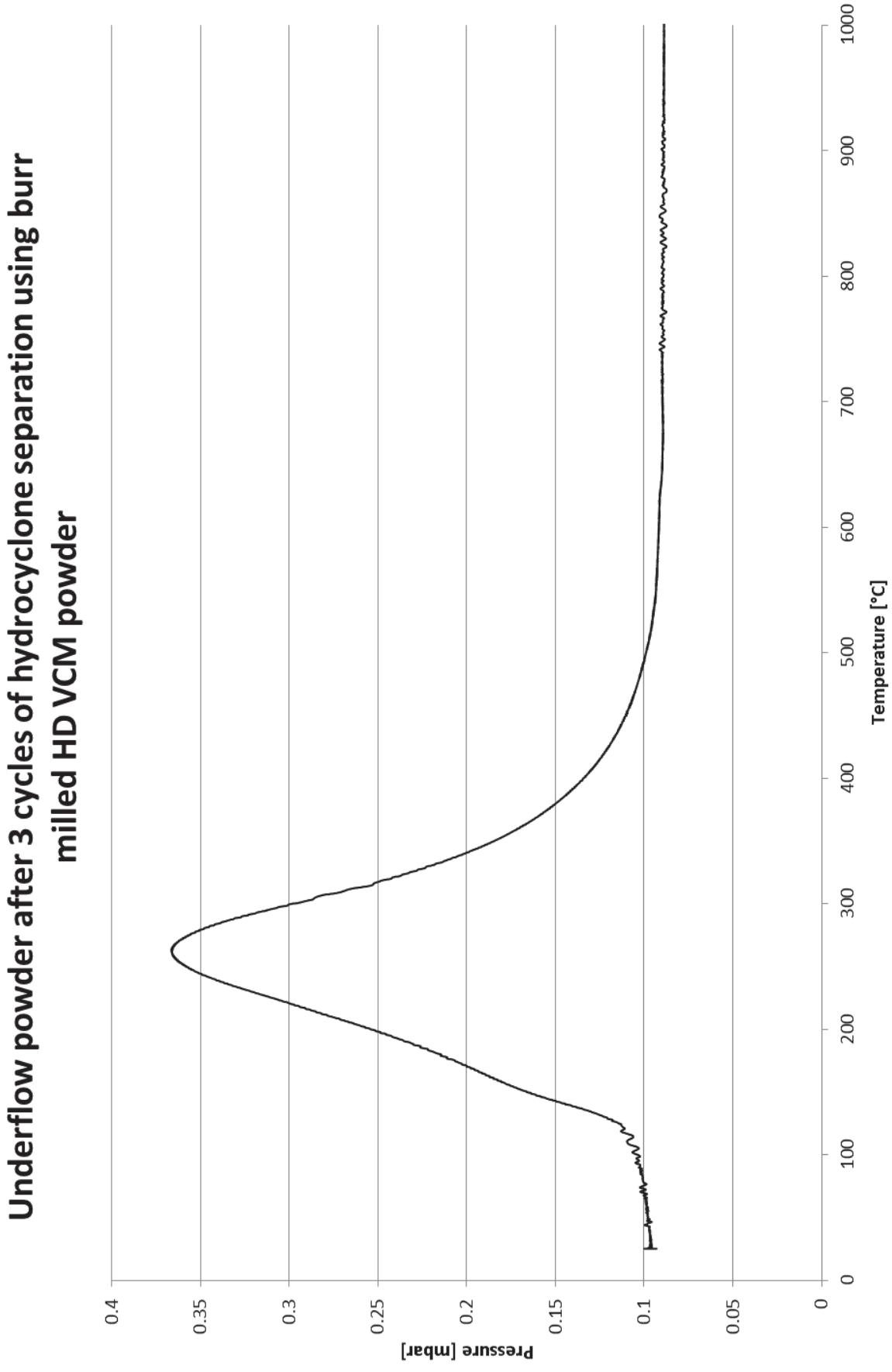
Underflow powder after 3 cycles of hydrocyclone separation using burr milled HD VCM powder
Pressure [mbar]
0.4
0.35
0.3
0.25
0.2
0.15
0.1
0.05
0
Temperature [°C]
0
100
200
300
400
500
600
700
800
900
1000

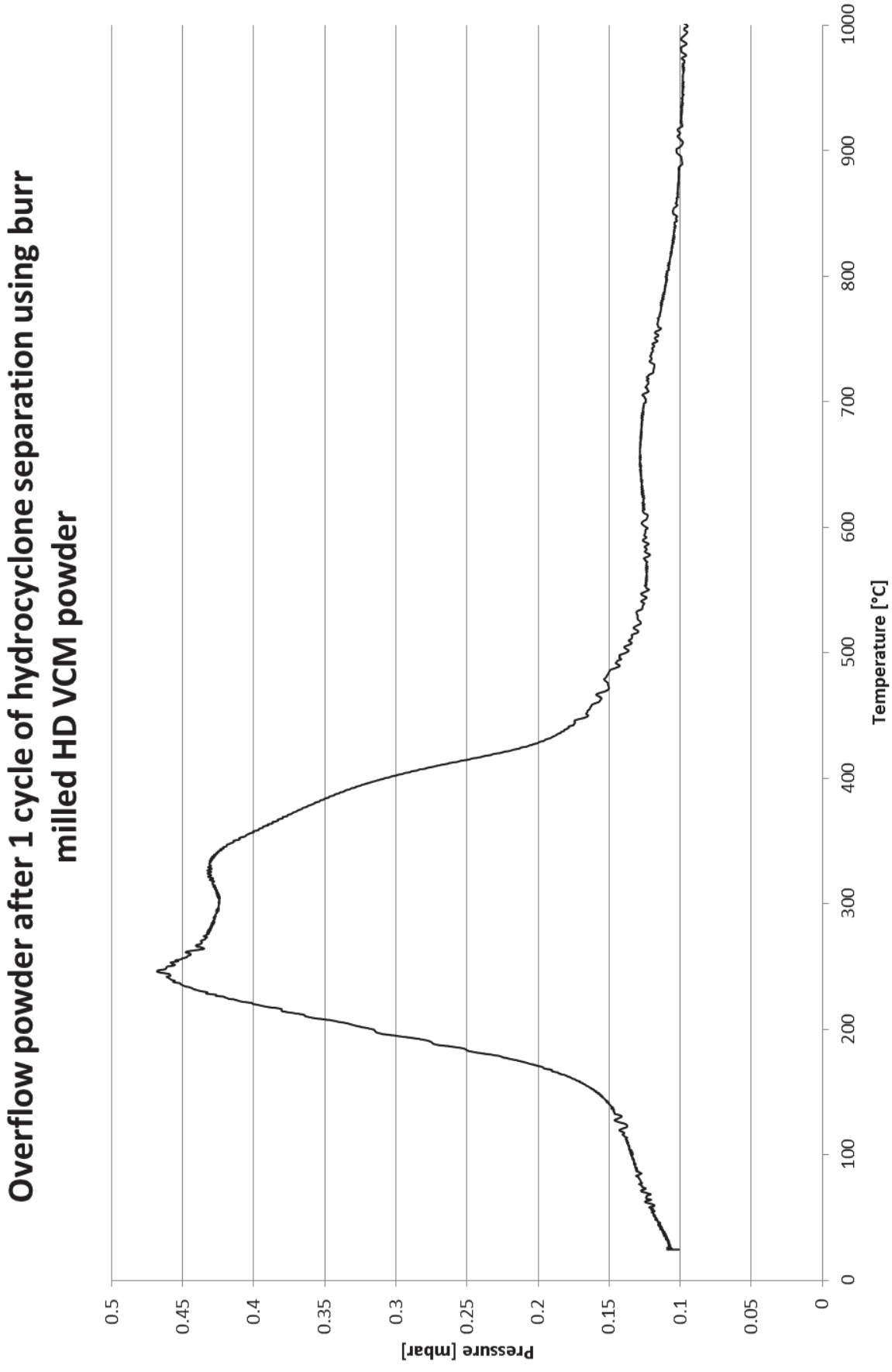
Overflow powder after 1 cycle of hydrocyclone separation using burr milled HD VCM powder
Pressure [mbar]
0.5
0.45
0.4
0.35
0.3
0.25
0.2
0.15
0.1
0.05
0
Temperature [°C]
0
100
200
300
400
500
600
700
800
900
1000

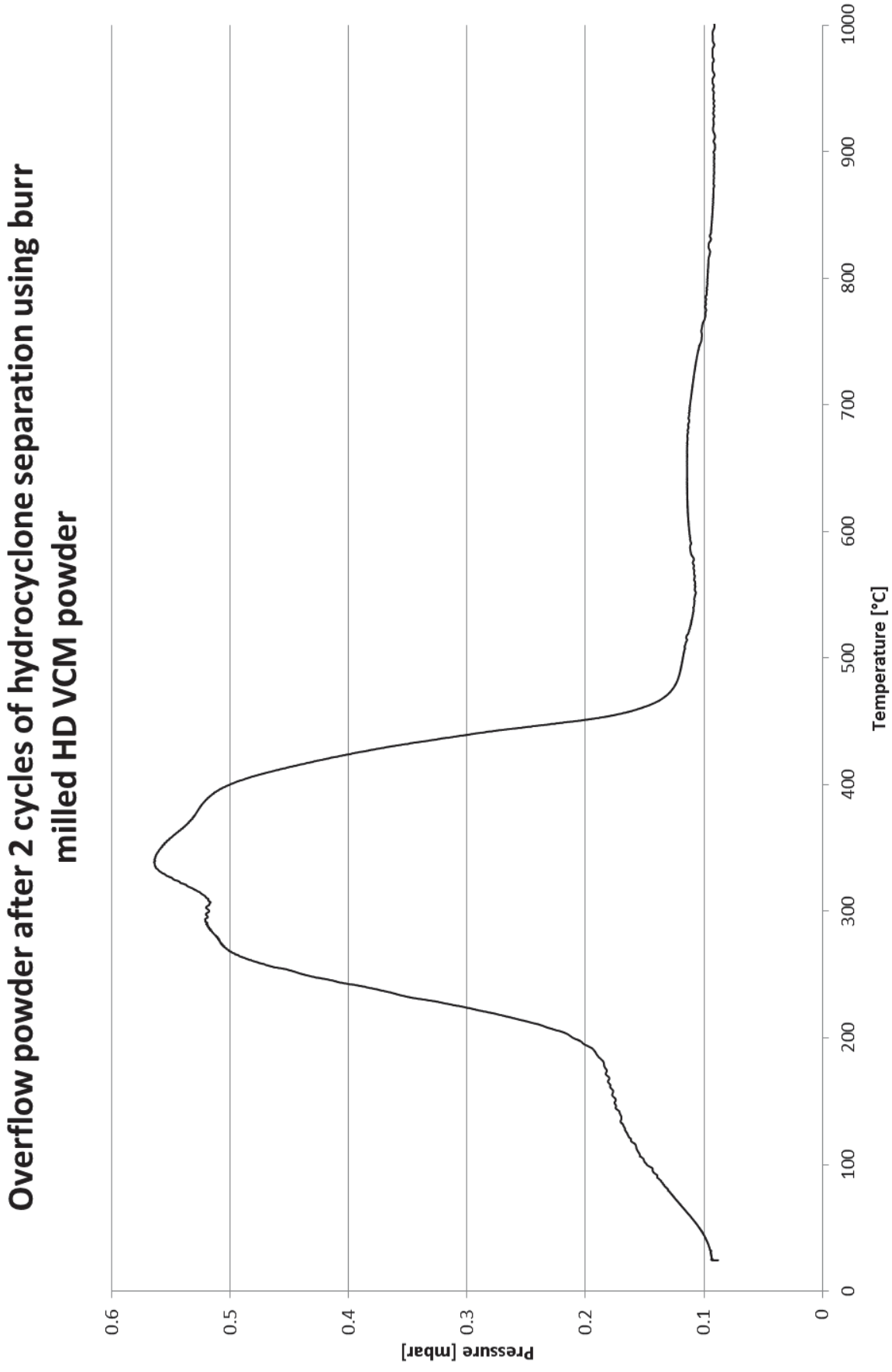
Overflow powder after 2 cycles of hydrocyclone separation using burr milled HD VCM powder
Pressure [mbar]
0
0.1
0.2
0.3
0.4
0.5
0.6
Temperature [°C]
0
100
200
300
400
500
600
700
800
900
1000

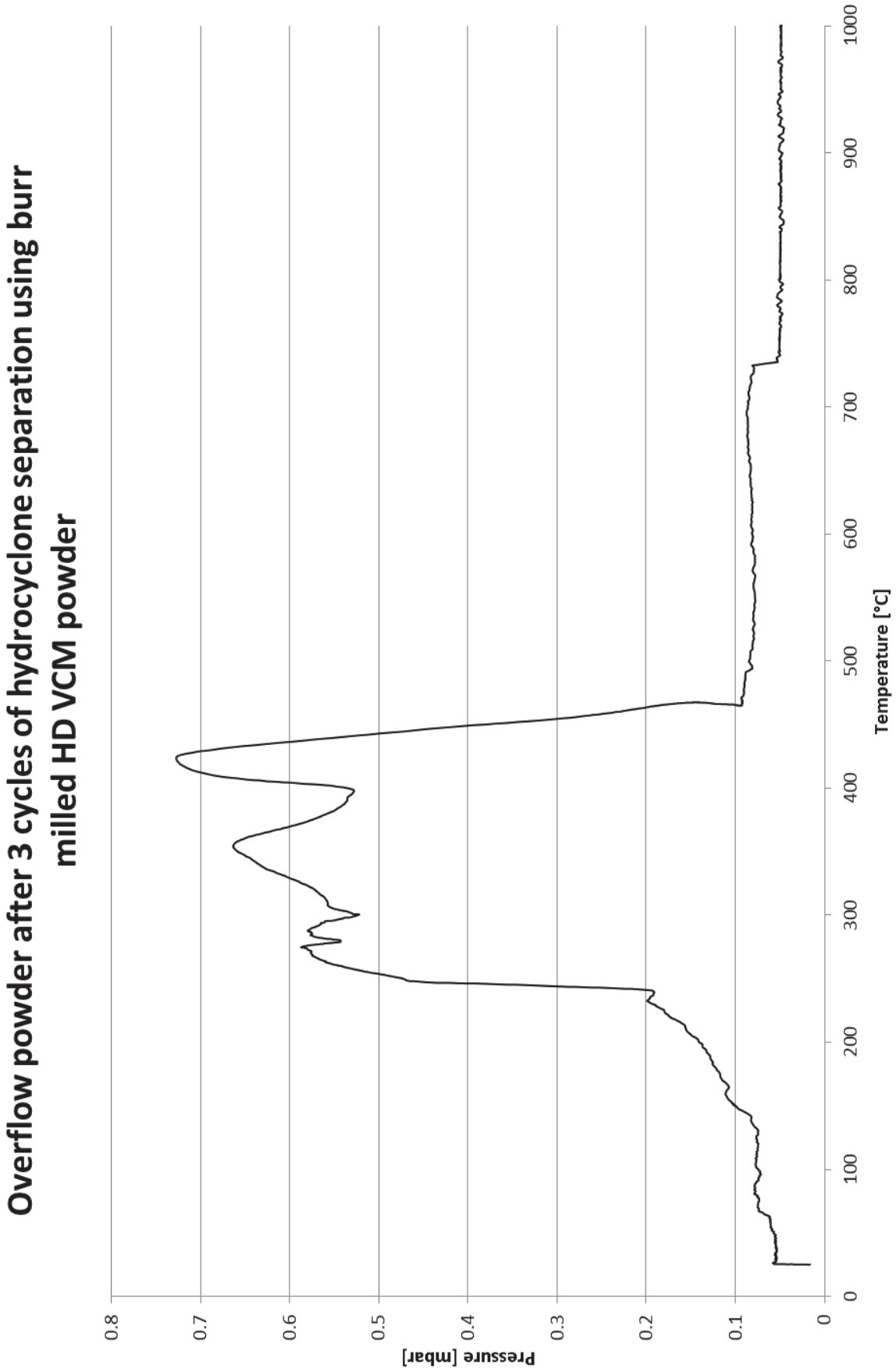
Overflow powder after 3 cycles of hydrocyclone separation using burr milled HD VCM powder
Pressure [mbar]
0.8
0.7
0.6
0.5
0.4
0.3
0.2
0.1
0
Temperature [°C]
0
100
200
300
400
500
600
700
800
900
1000

X-Ray Diffraction Patterns from Chapter 8

Nickel decoated voice coil motor magnet

Non-milled hydrogen decrepitated voice coil motor magnet powder

Burr milled hydrogen decrepitated voice coil motor magnet powder

Underflow powder after 1 cycle of hydrocyclone separation using non-milled HD VCM powder

Underflow powder after 2 cycles of hydrocyclone separation using non-milled HD VCM powder

Underflow powder after 3 cycles of hydrocyclone separation using non-milled HD VCM powder

Overflow powder after 1 cycle of hydrocyclone separation using non-milled HD VCM powder

Overflow powder after 2 cycles of hydrocyclone separation using non-milled HD VCM powder

Overflow powder after 3 cycles of hydrocyclone separation using non-milled HD VCM powder

Underflow powder after 1 cycle of hydrocyclone separation using burr milled HD VCM powder

Underflow powder after 2 cycles of hydrocyclone separation using burr milled HD VCM powder

Underflow powder after 3 cycles of hydrocyclone separation using burr milled HD VCM powder

Overflow powder after 1 cycle of hydrocyclone separation using burr milled HD VCM powder

Overflow powder after 2 cycles of hydrocyclone separation using burr milled HD VCM powder

Magnetic fraction after wet low-intensity magnetic separation using non-milled HD VCM powder

Non-magnetic fraction after wet low-intensity magnetic separation using non-milled HD VCM powder

Magnetic fraction after wet low-intensity magnetic separation using burr milled HD VCM powder

Non-magnetic fraction after wet low-intensity magnetic separation using burr milled HD VCM powder

The legend for all the traces is the following:

- □ $Nd_2Fe_{14}B$
- ○ Nd_2O_3
- △ $Nd_2Fe_{14}BH_x$
- ◇ $Nd(OH)_3$
- ✚ Fe
- ✖ FeB_2

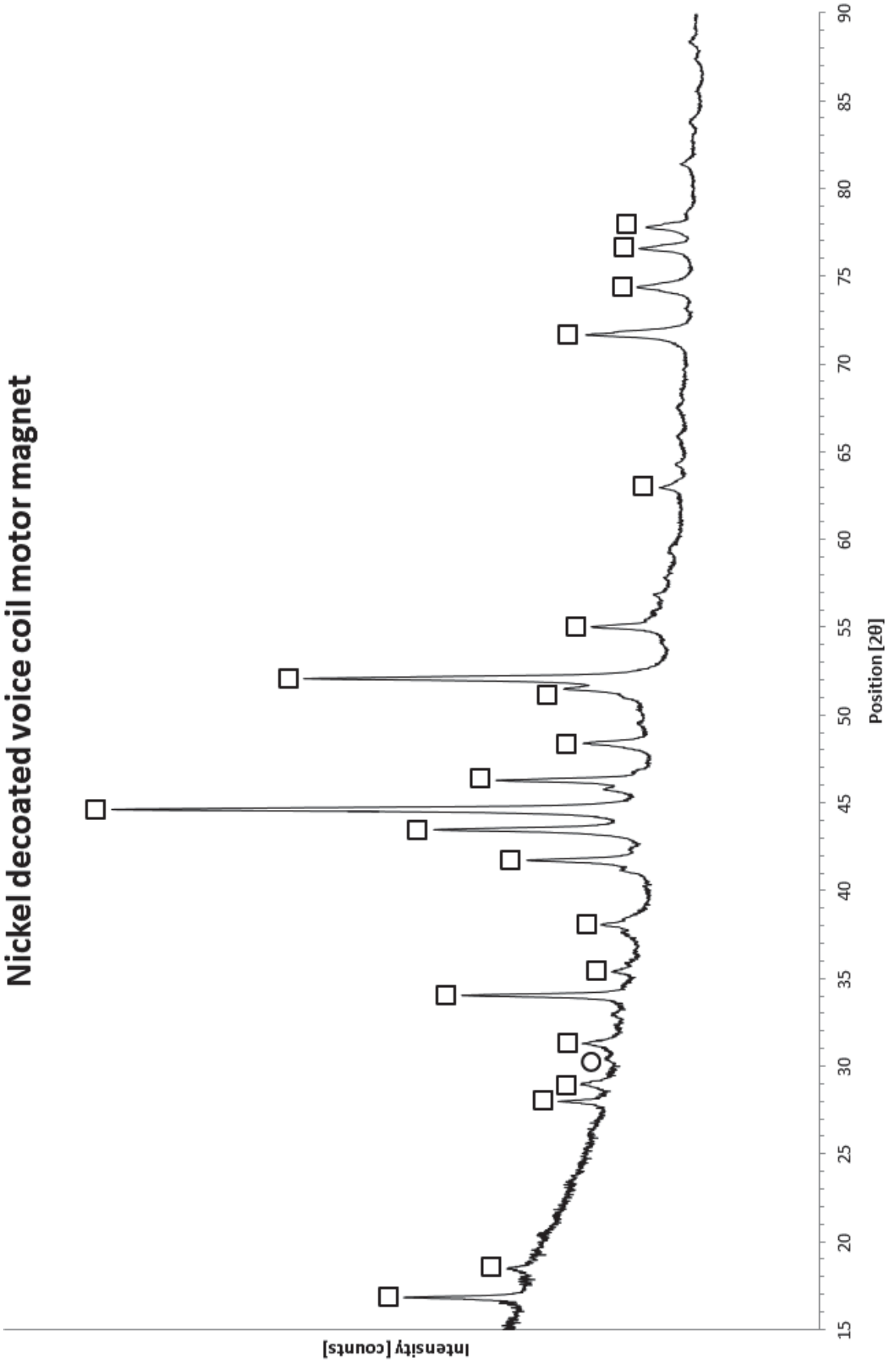
Nickel decoated voice coil motor magnet
Intensity [counts]
Position [2θ]
15
20
25
30
35
40
45
50
55
60
65
70
75
80
85
90

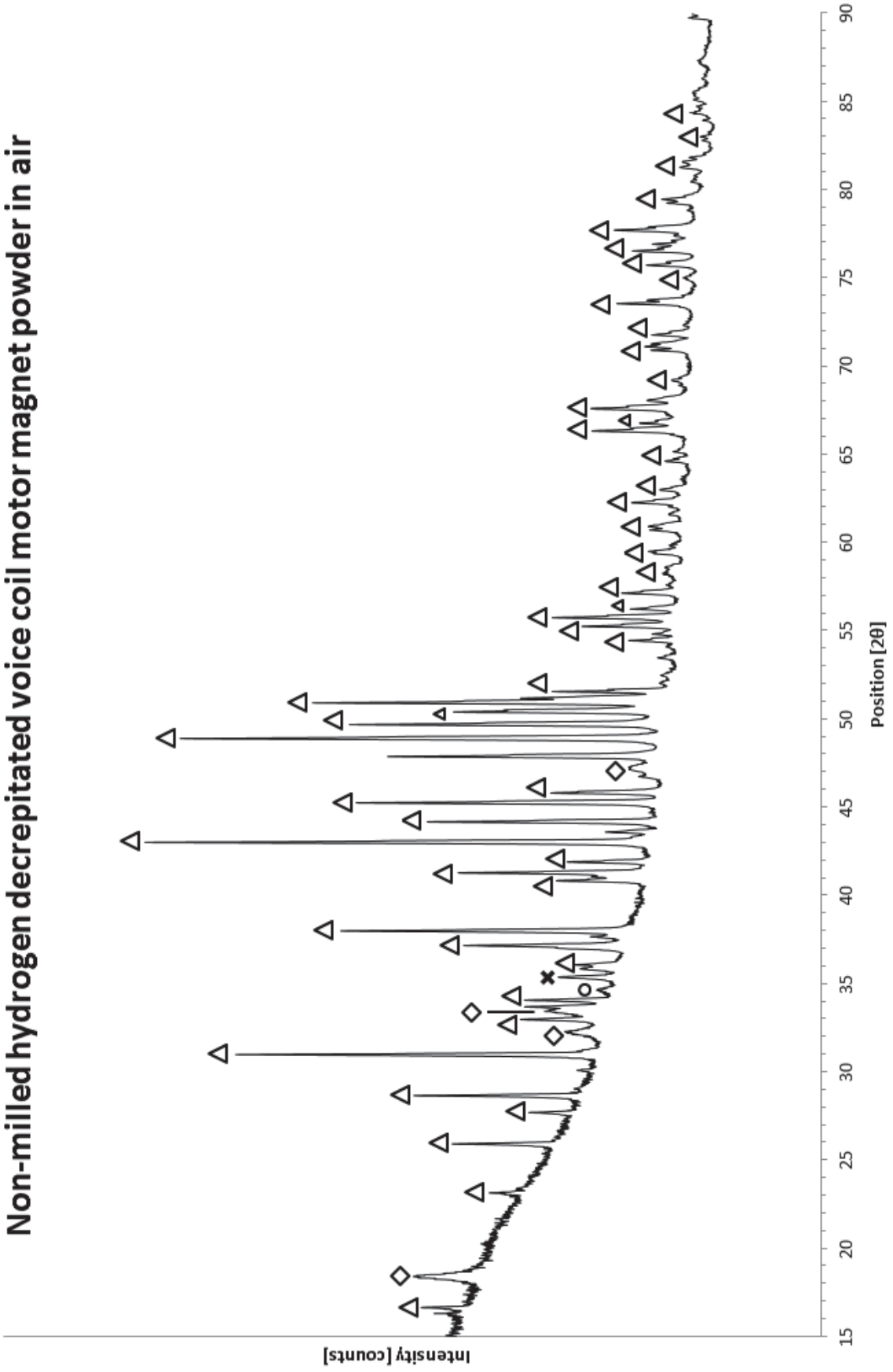
Non-milled hydrogen decrepitated voice coil motor magnet powder in air
Intensity [counts]
Position [2θ]
15
20
25
30
35
40
45
50
55
60
65
70
75
80
85
90

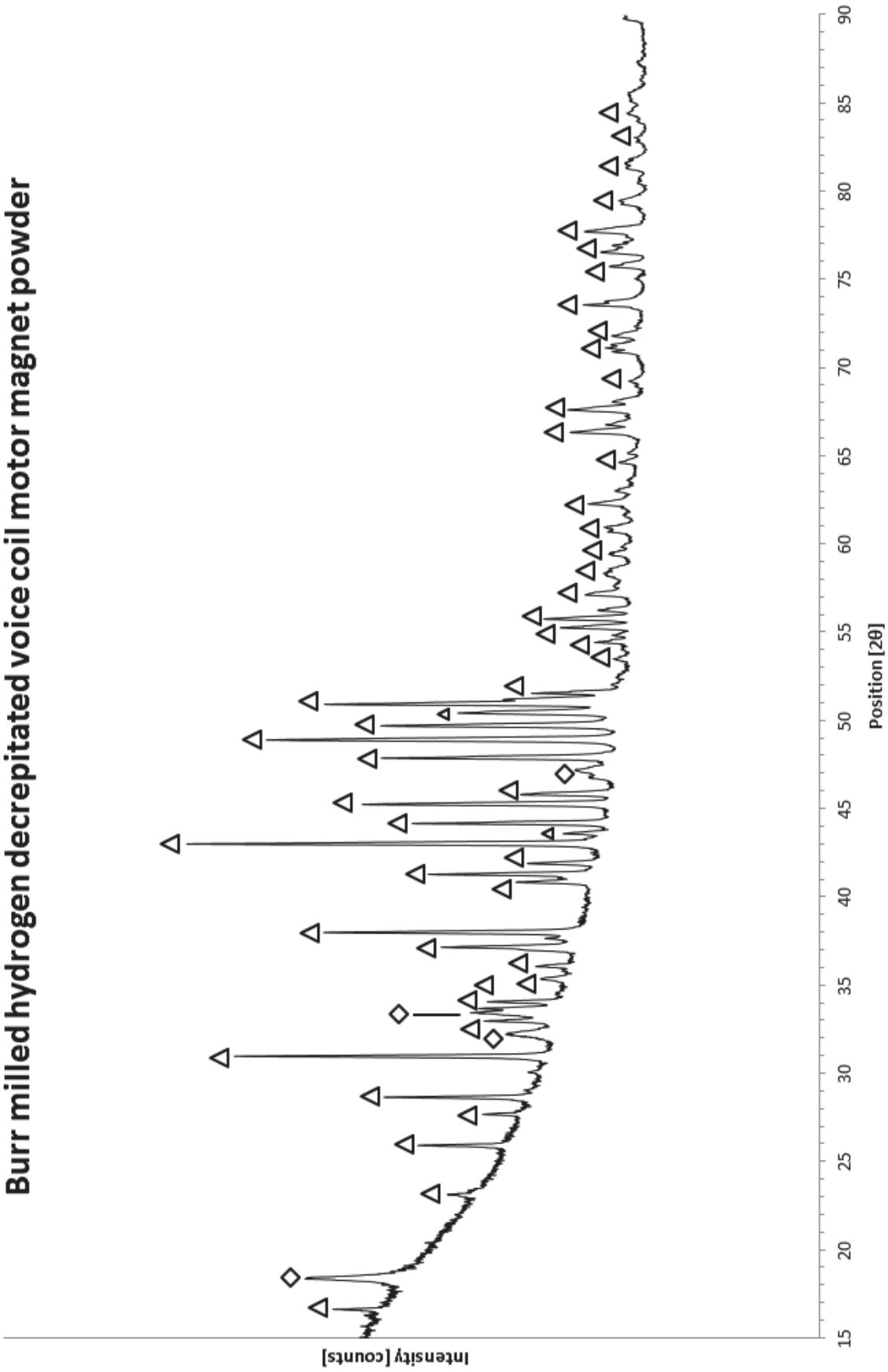
Burr milled hydrogen decrepitated voice coil motor magnet powder
Intensity [counts]
Position [2θ]
15
20
25
30
35
40
45
50
55
60
65
70
75
80
85
90

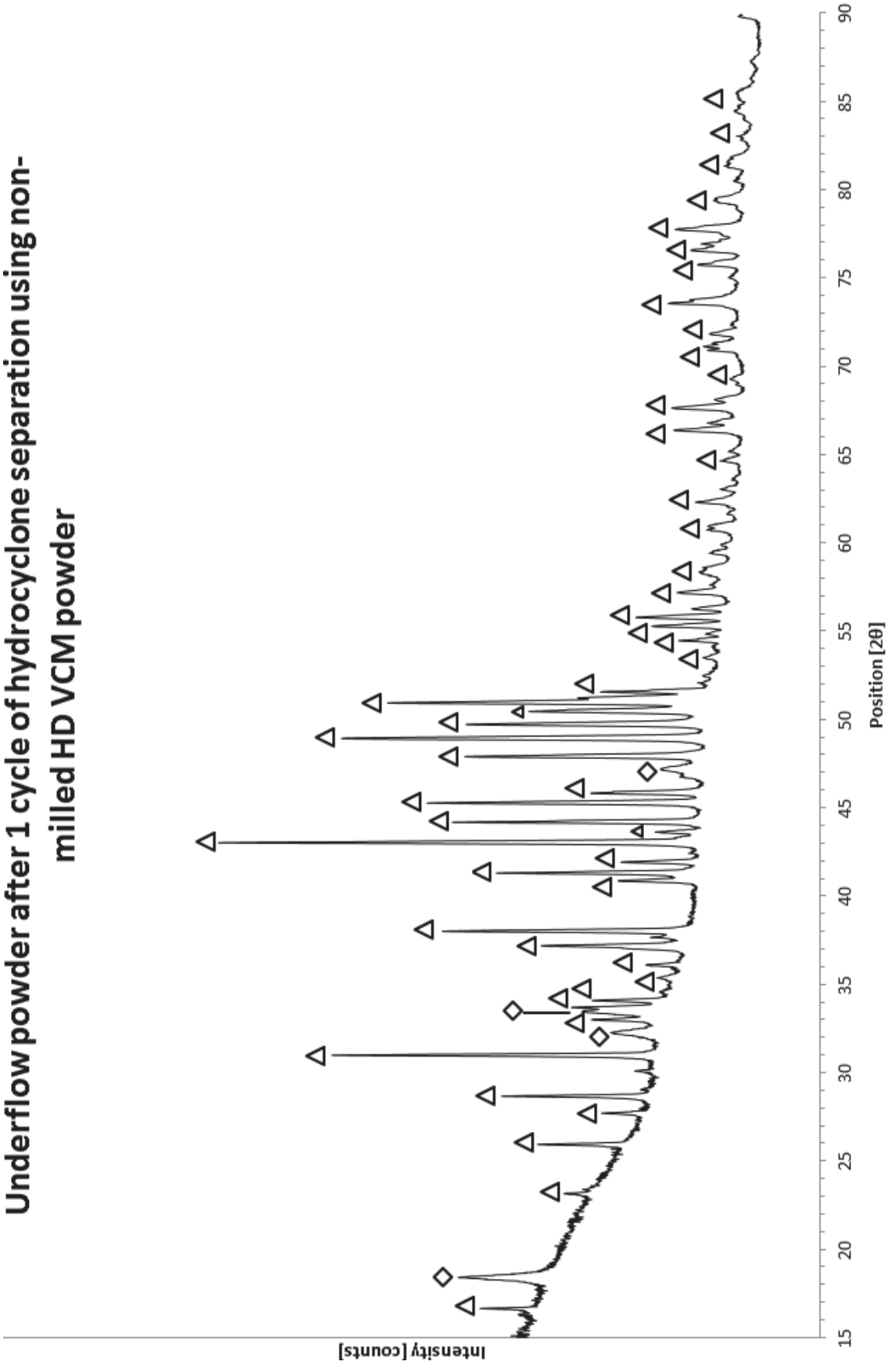
Underflow powder after 1 cycle of hydrocyclone separation using non-milled HD VCM powder
Intensity [counts]
Position [2θ]
15
20
25
30
35
40
45
50
55
60
65
70
75
80
85
90

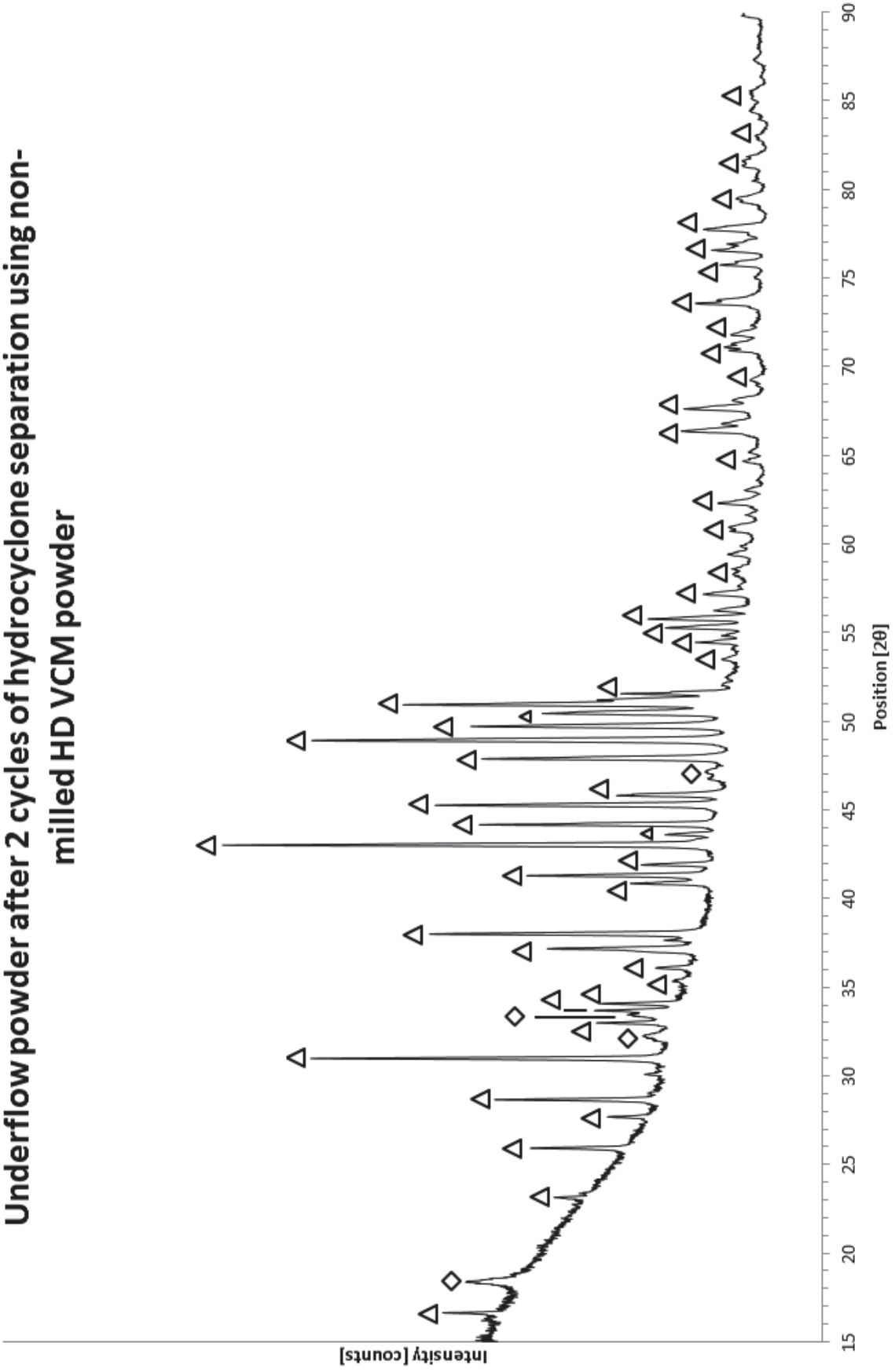
Underflow powder after 2 cycles of hydrocyclone separation using non-milled HD VCM powder
Intensity [counts]
Position [2θ]
15
20
25
30
35
40
45
50
55
60
65
70
75
80
85
90

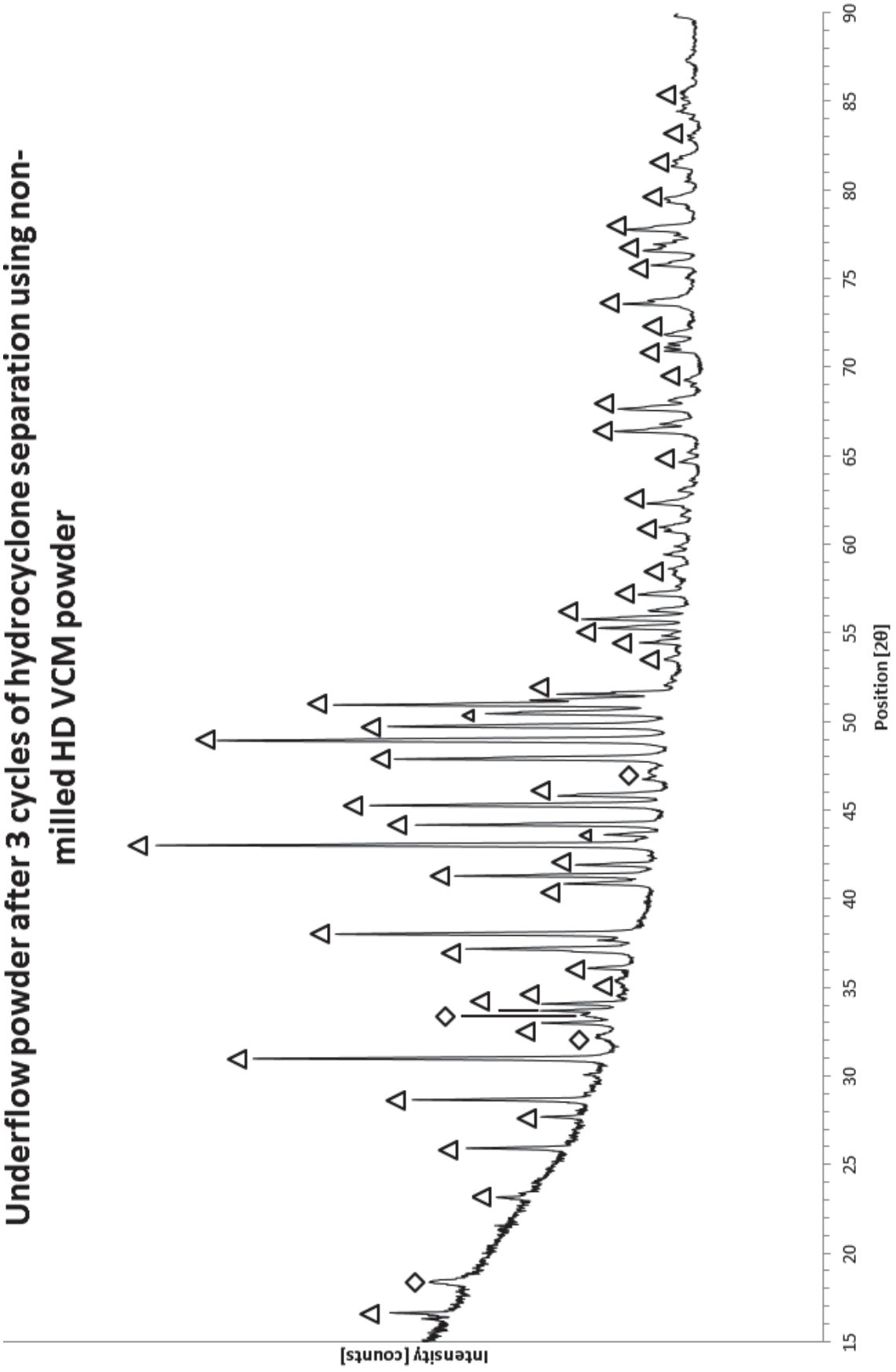
Underflow powder after 3 cycles of hydrocyclone separation using non-milled HD VCM powder
Intensity [counts]
Position [2θ]
15
20
25
30
35
40
45
50
55
60
65
70
75
80
85
90

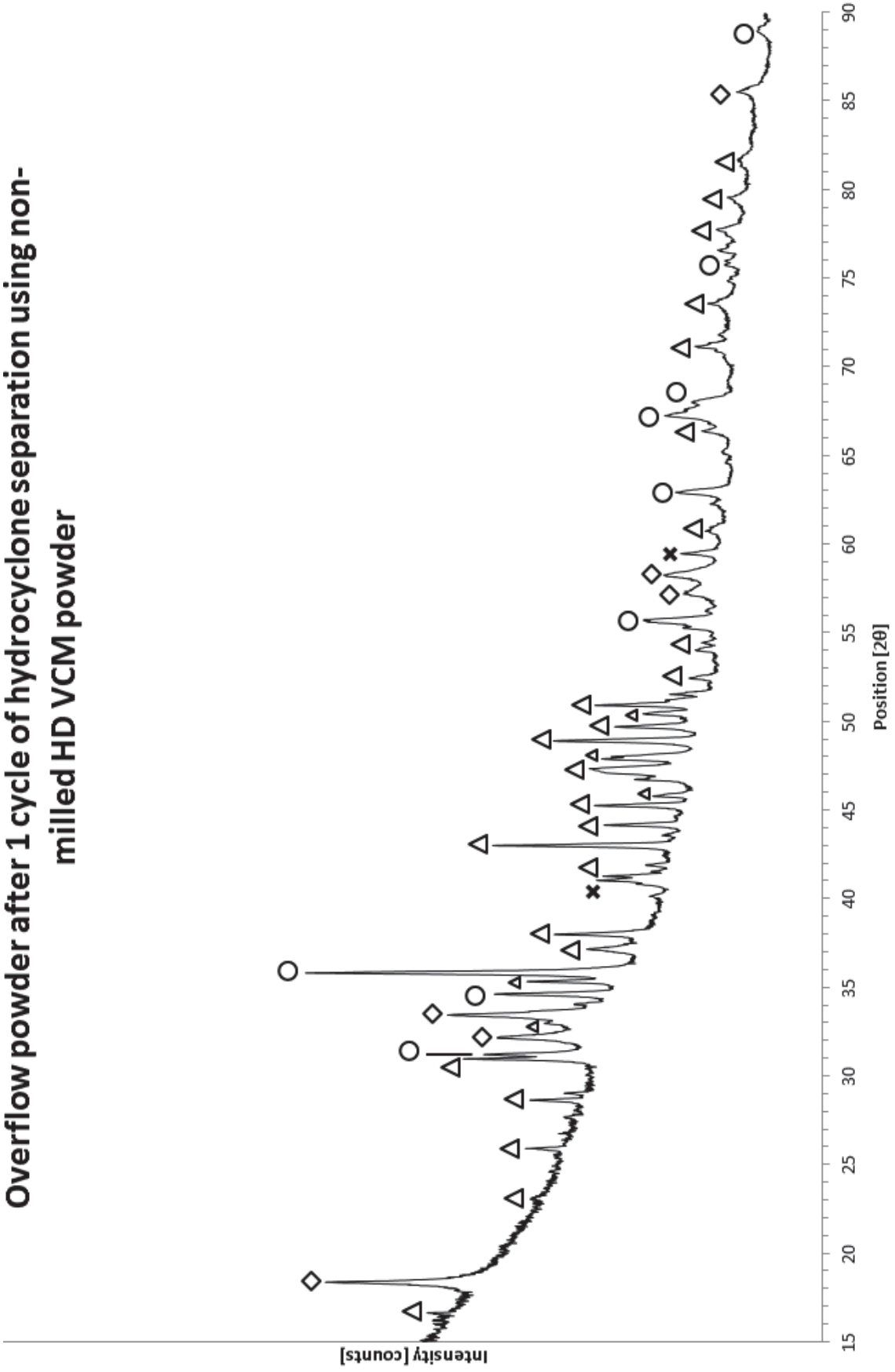
Overflow powder after 1 cycle of hydrocyclone separation using non-milled HD VCM powder
Intensity [counts]
Position [2θ]
15
20
25
30
35
40
45
50
55
60
65
70
75
80
85
90

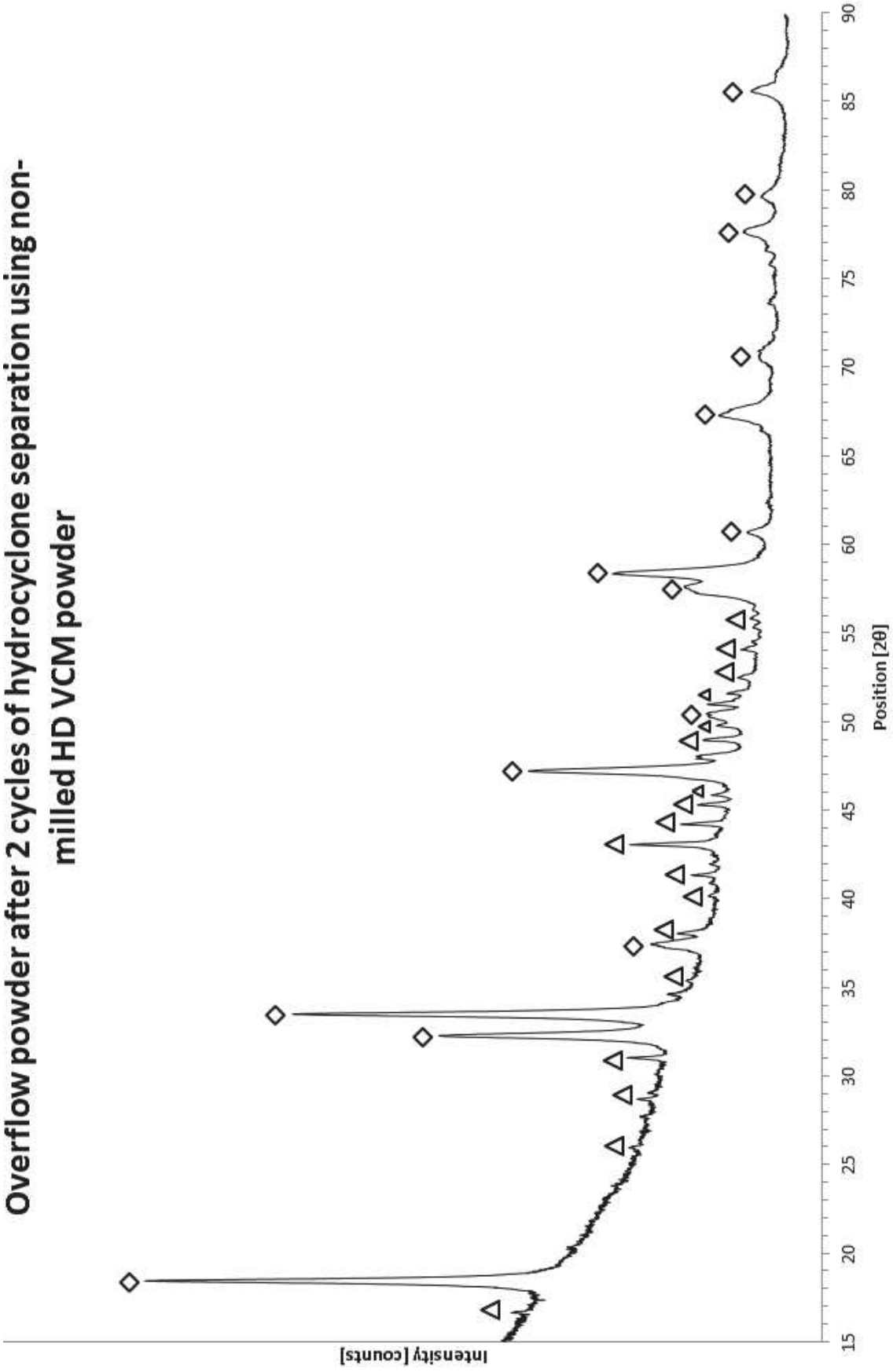
Overflow powder after 2 cycles of hydrocyclone separation using non-milled HD VCM powder
Intensity [counts]
Position [2θ]
15
20
25
30
35
40
45
50
55
60
65
70
75
80
85
90

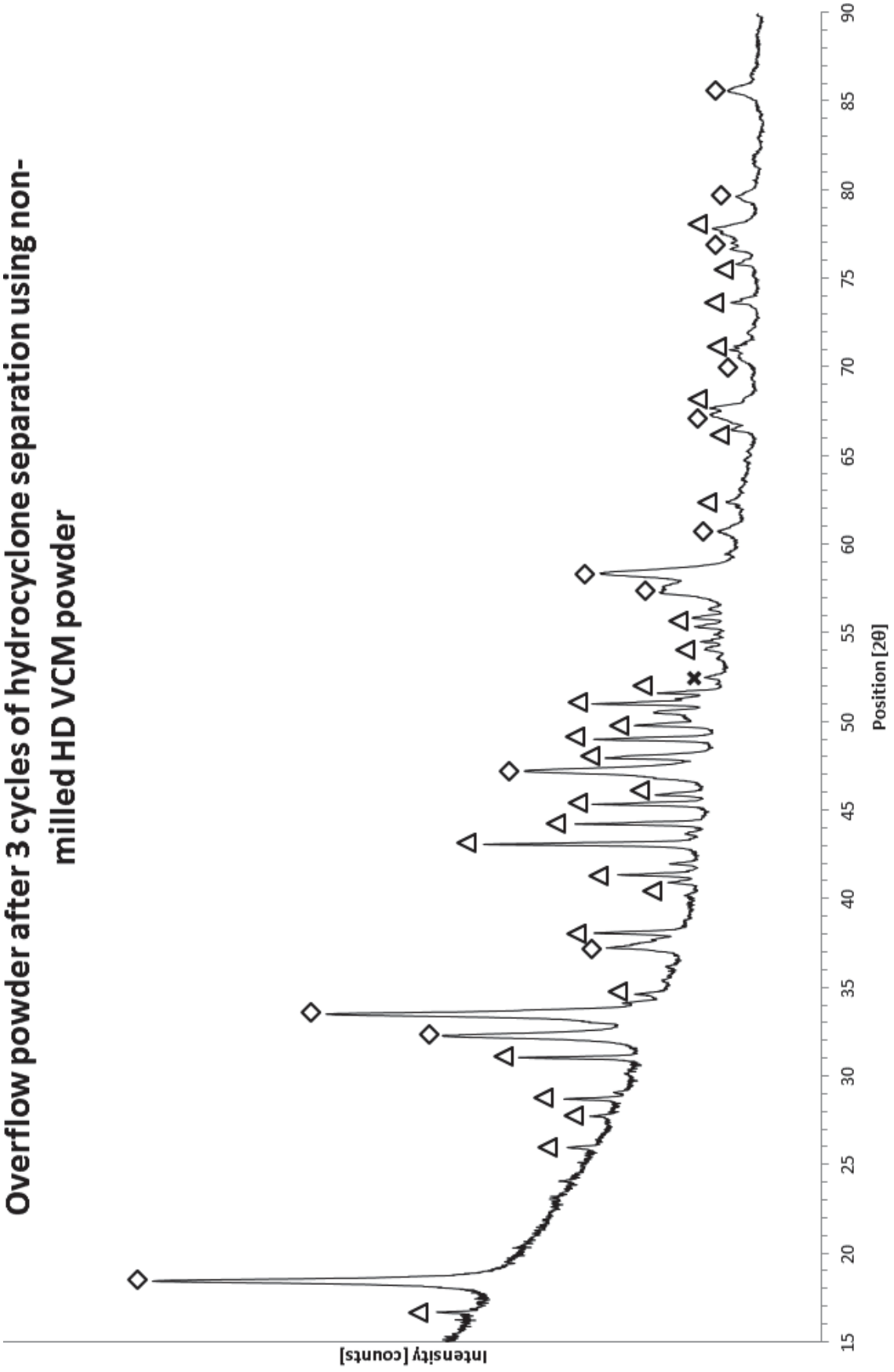
Overflow powder after 3 cycles of hydrocyclone separation using non-milled HD VCM powder
Intensity [counts]
Position [2θ]
15
20
25
30
35
40
45
50
55
60
65
70
75
80
85
90

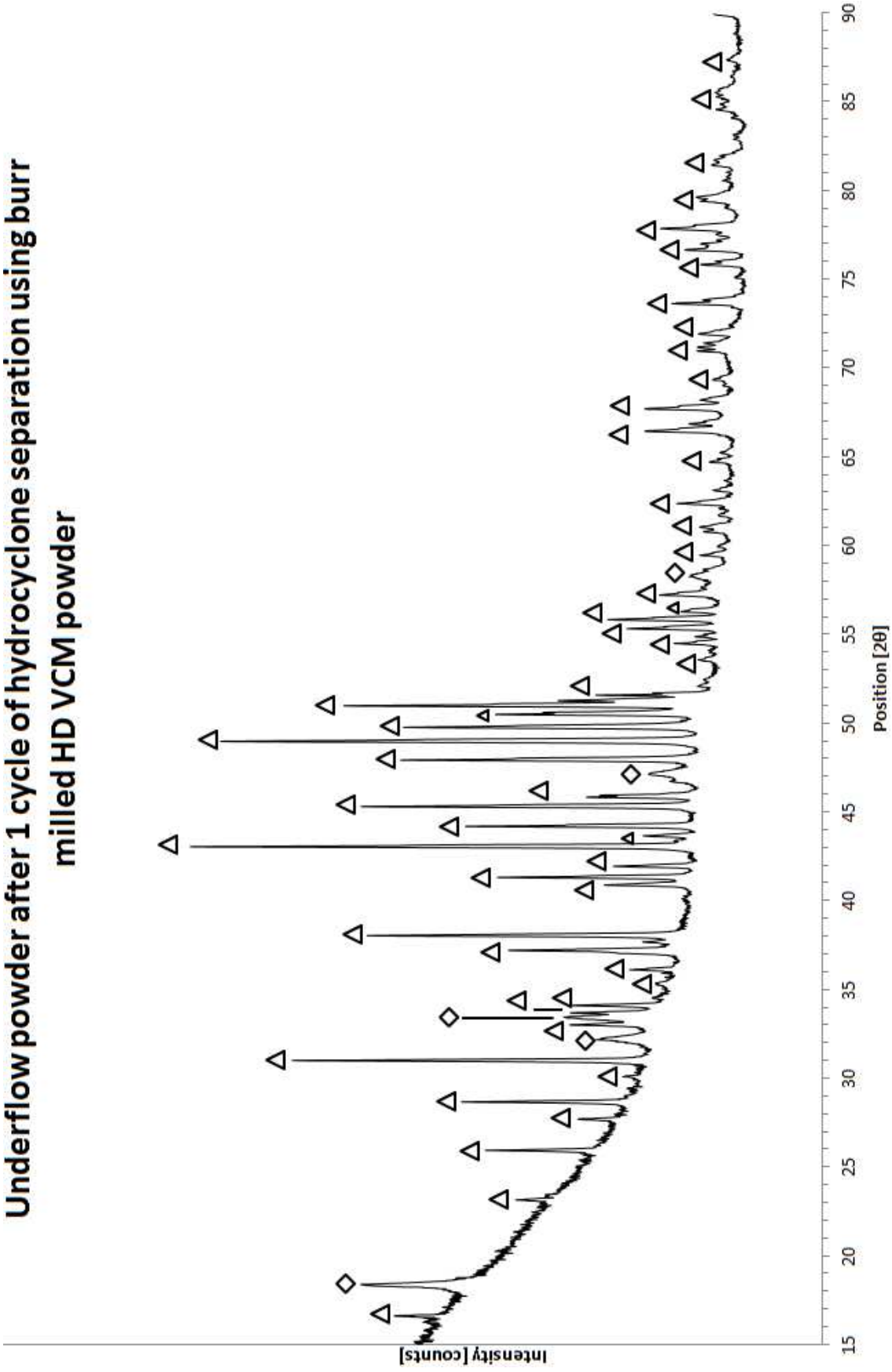
Underflow powder after 1 cycle of hydrocyclone separation using burr milled HD VCM powder
Intensity [counts]
Position [2θ]
15
20
25
30
35
40
45
50
55
60
65
70
75
80
85
90

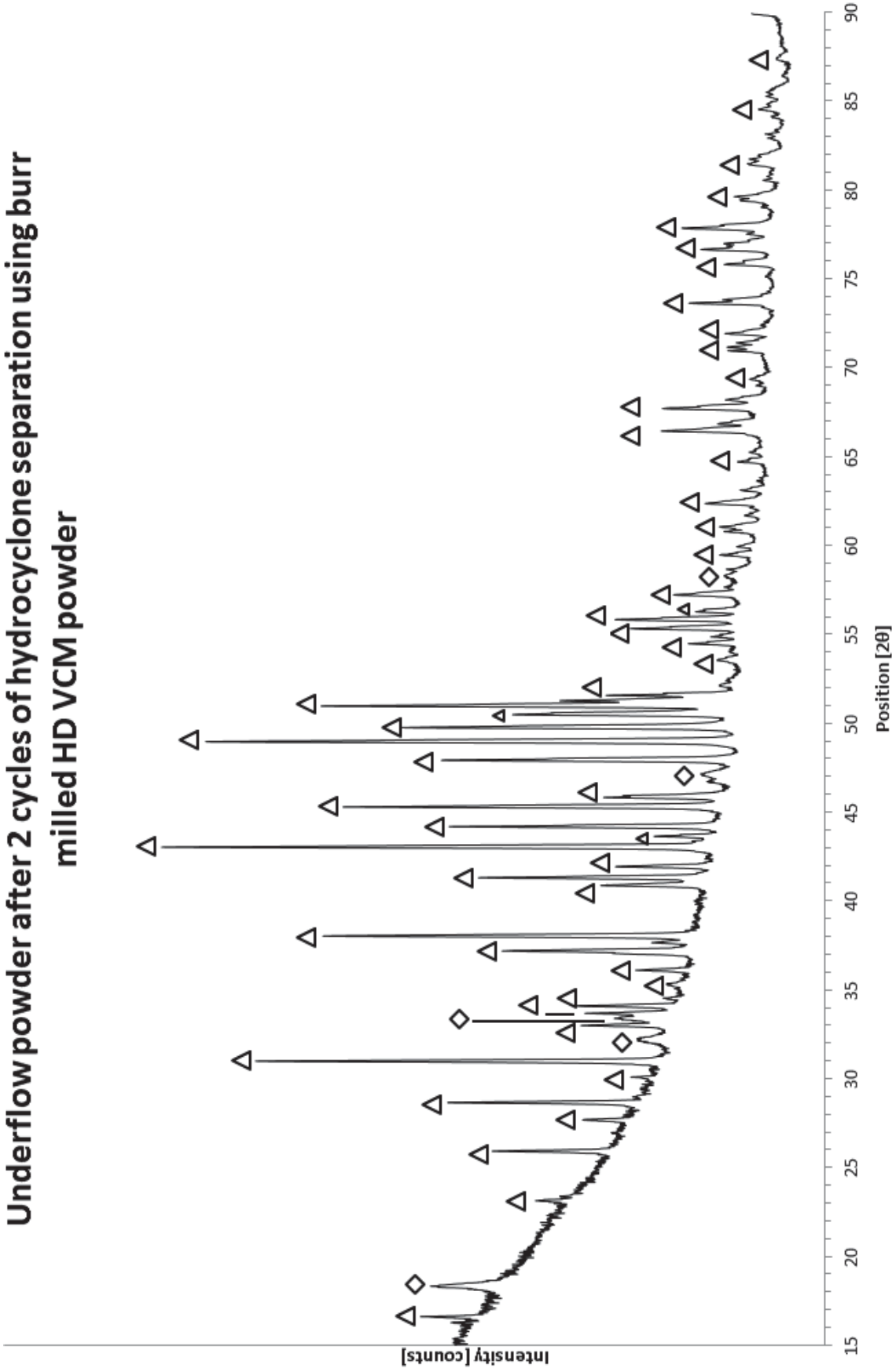
Underflow powder after 2 cycles of hydrocyclone separation using burr milled HD VCM powder
Intensity [counts]
Position [2θ]
15
20
25
30
35
40
45
50
55
60
65
70
75
80
85
90

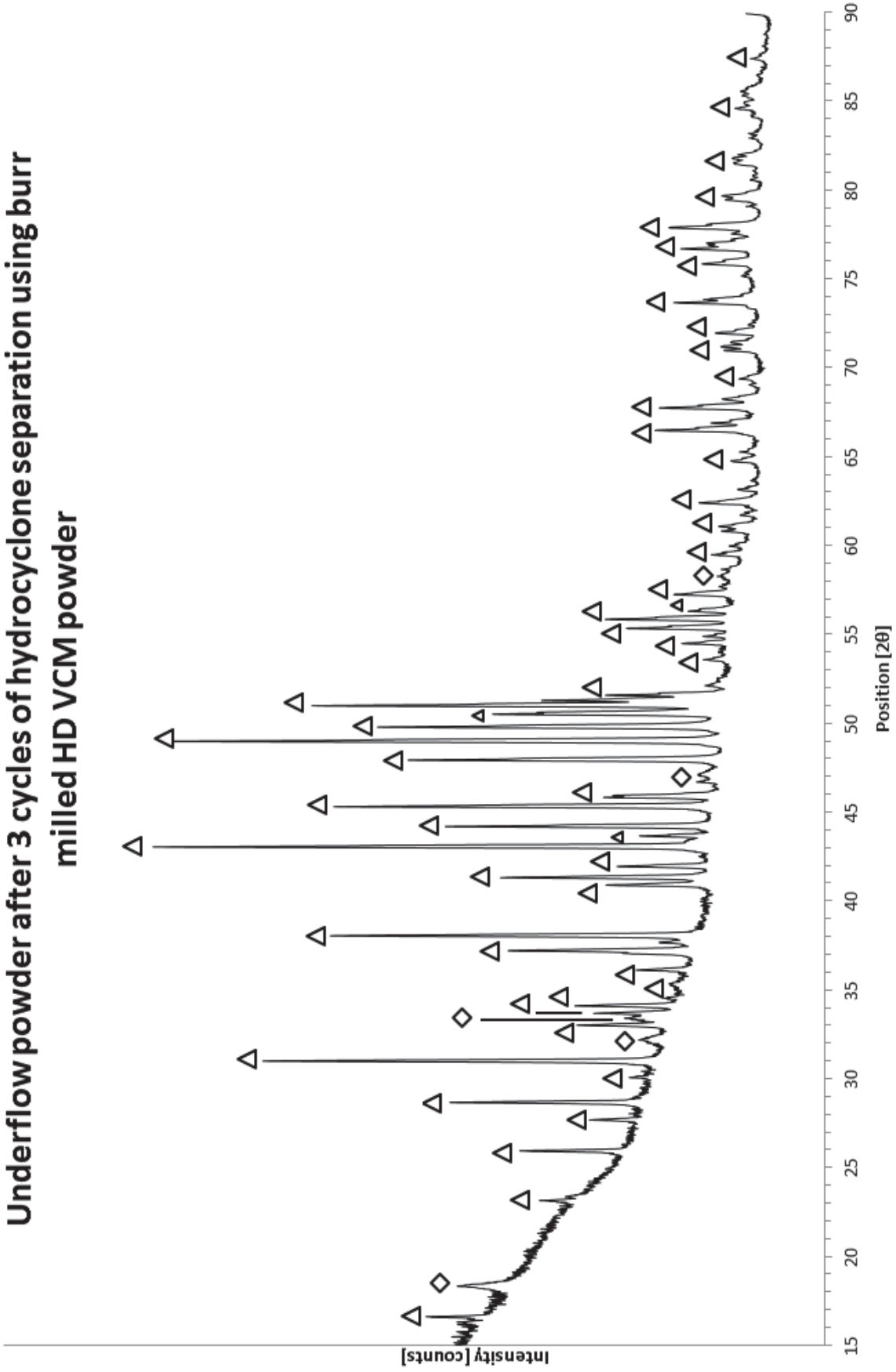
Underflow powder after 3 cycles of hydrocyclone separation using burr milled HD VCM powder
Intensity [counts]
Position [2θ]
15
20
25
30
35
40
45
50
55
60
65
70
75
80
85
90

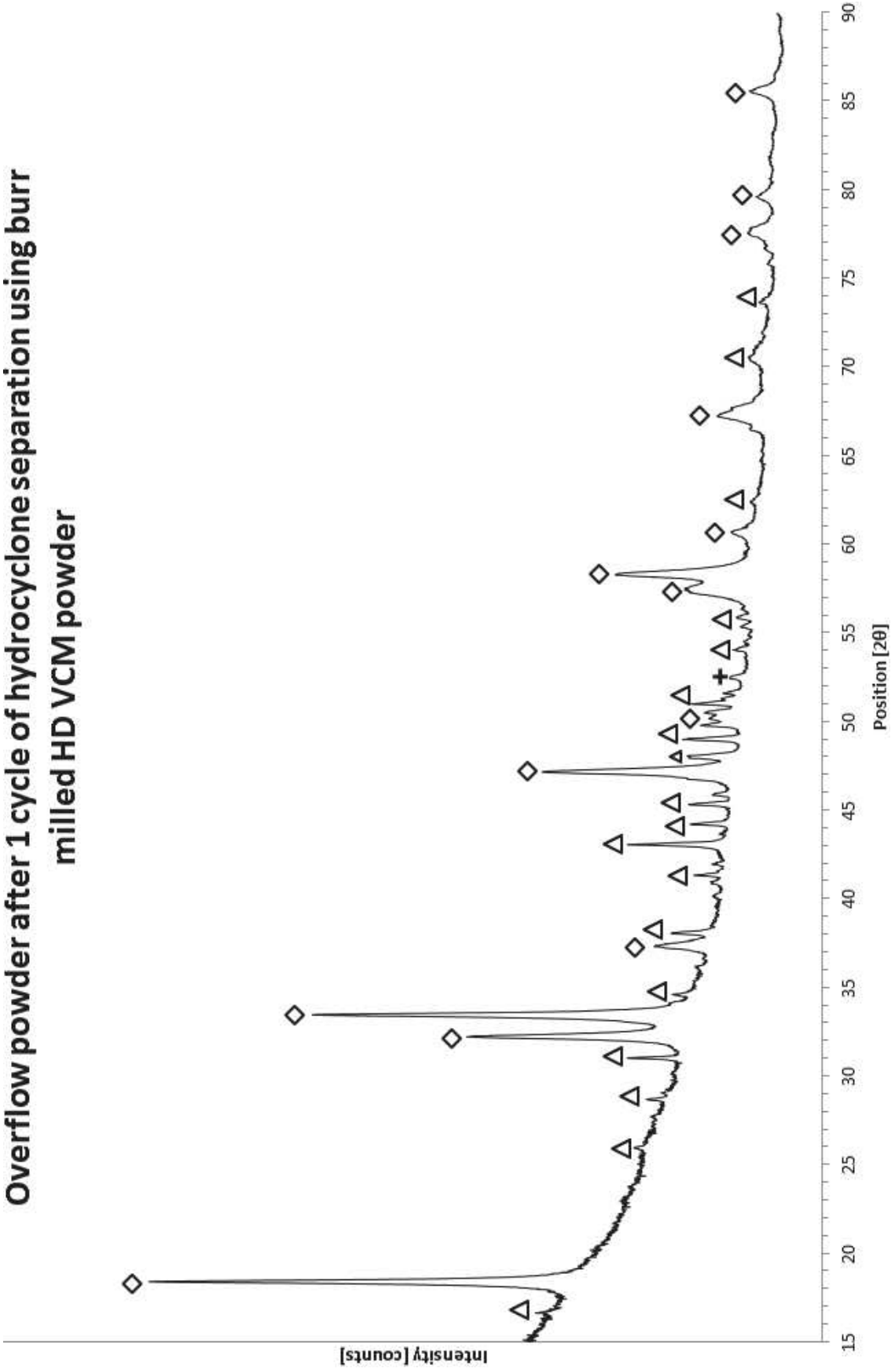
Overflow powder after 1 cycle of hydrocyclone separation using burr milled HD VCM powder
Intensity [counts]
Position [2θ]
15
20
25
30
35
40
45
50
55
60
65
70
75
80
85
90

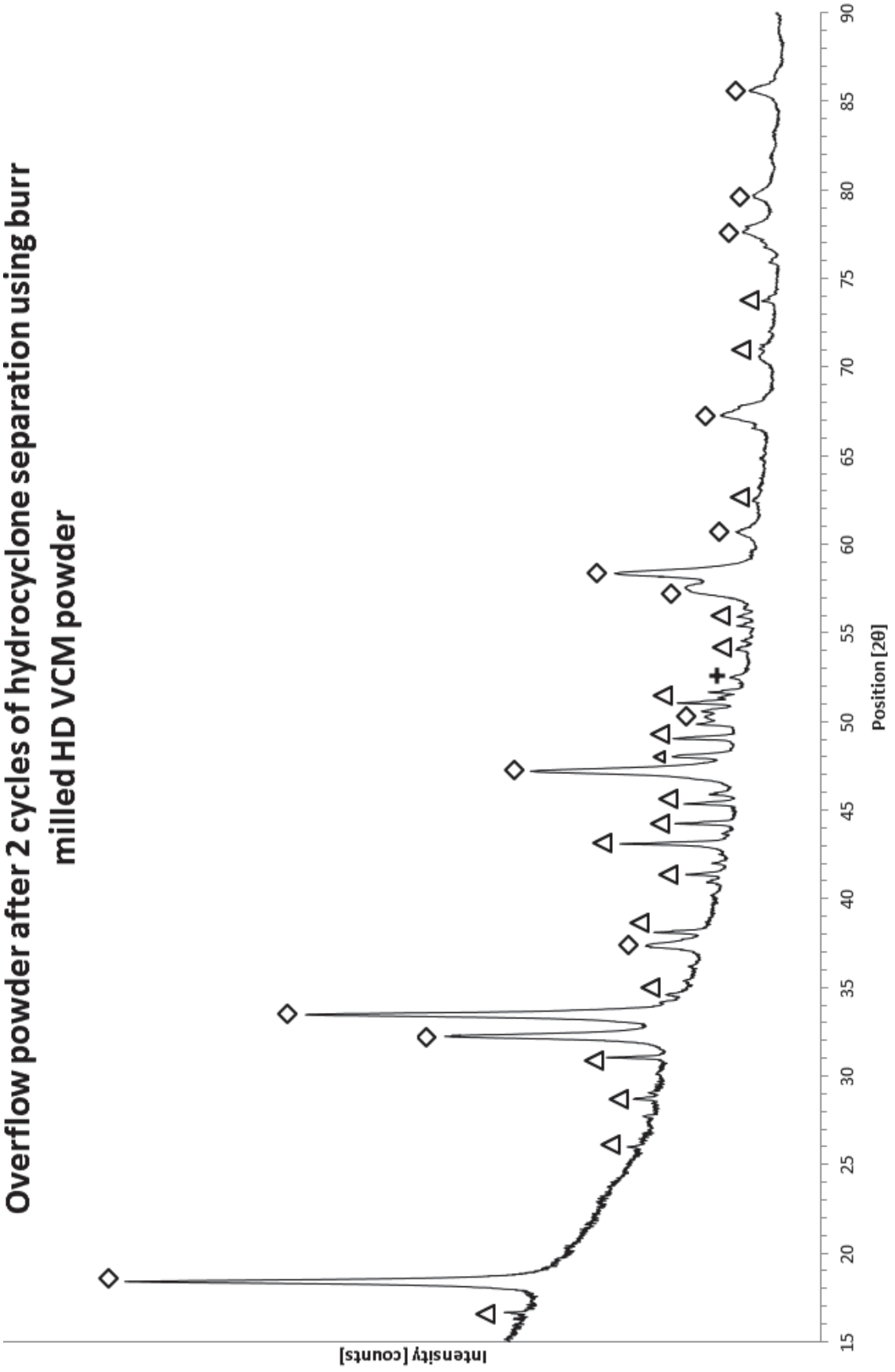
Overflow powder after 2 cycles of hydrocyclone separation using burr milled HD VCM powder
Intensity [counts]
Position [2θ]
15
20
25
30
35
40
45
50
55
60
65
70
75
80
85
90

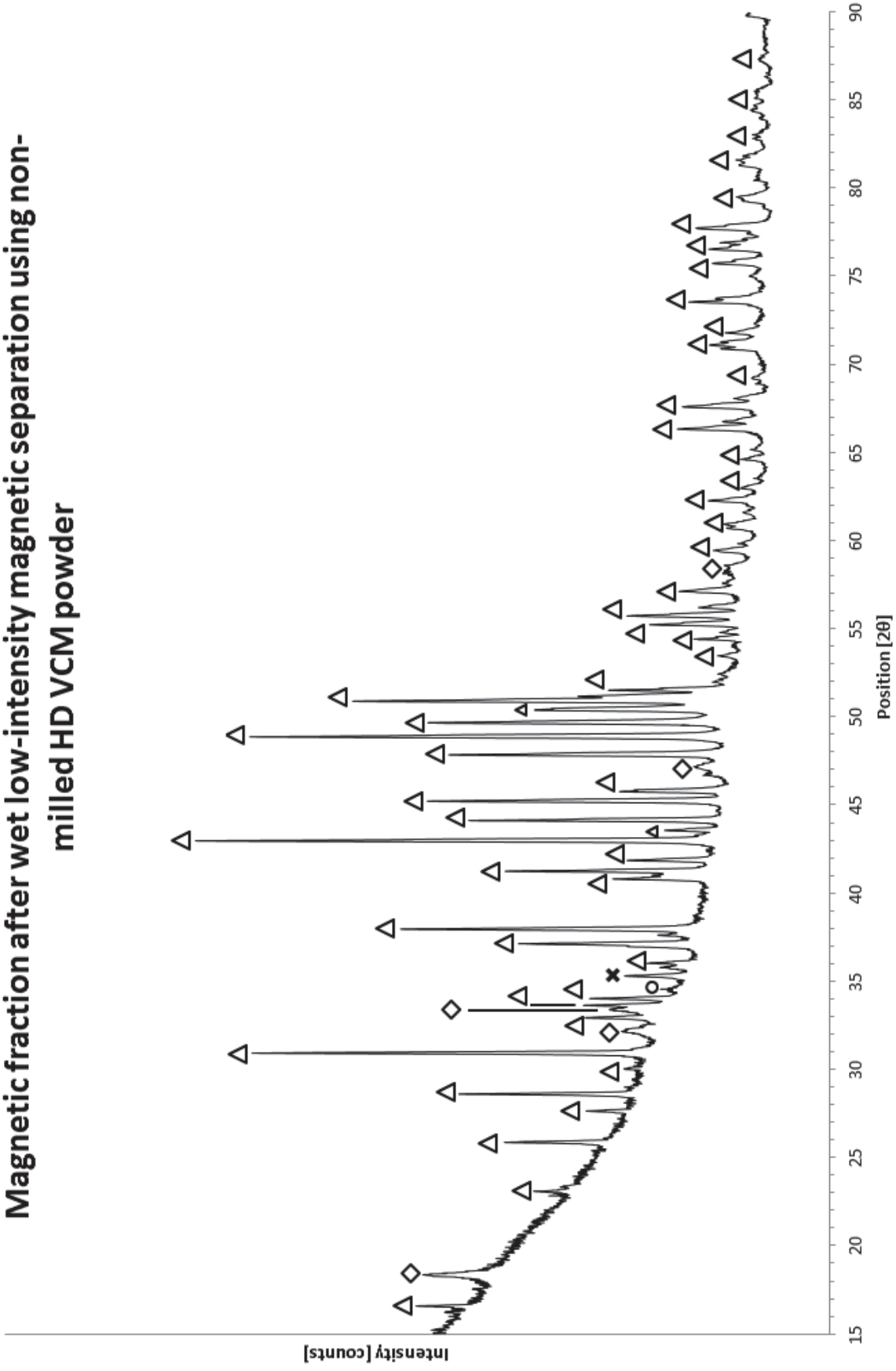
Magnetic fraction after wet low-intensity magnetic separation using non-milled HD VCM powder
Intensity [counts]
Position [2θ]
15
20
25
30
35
40
45
50
55
60
65
70
75
80
85
90

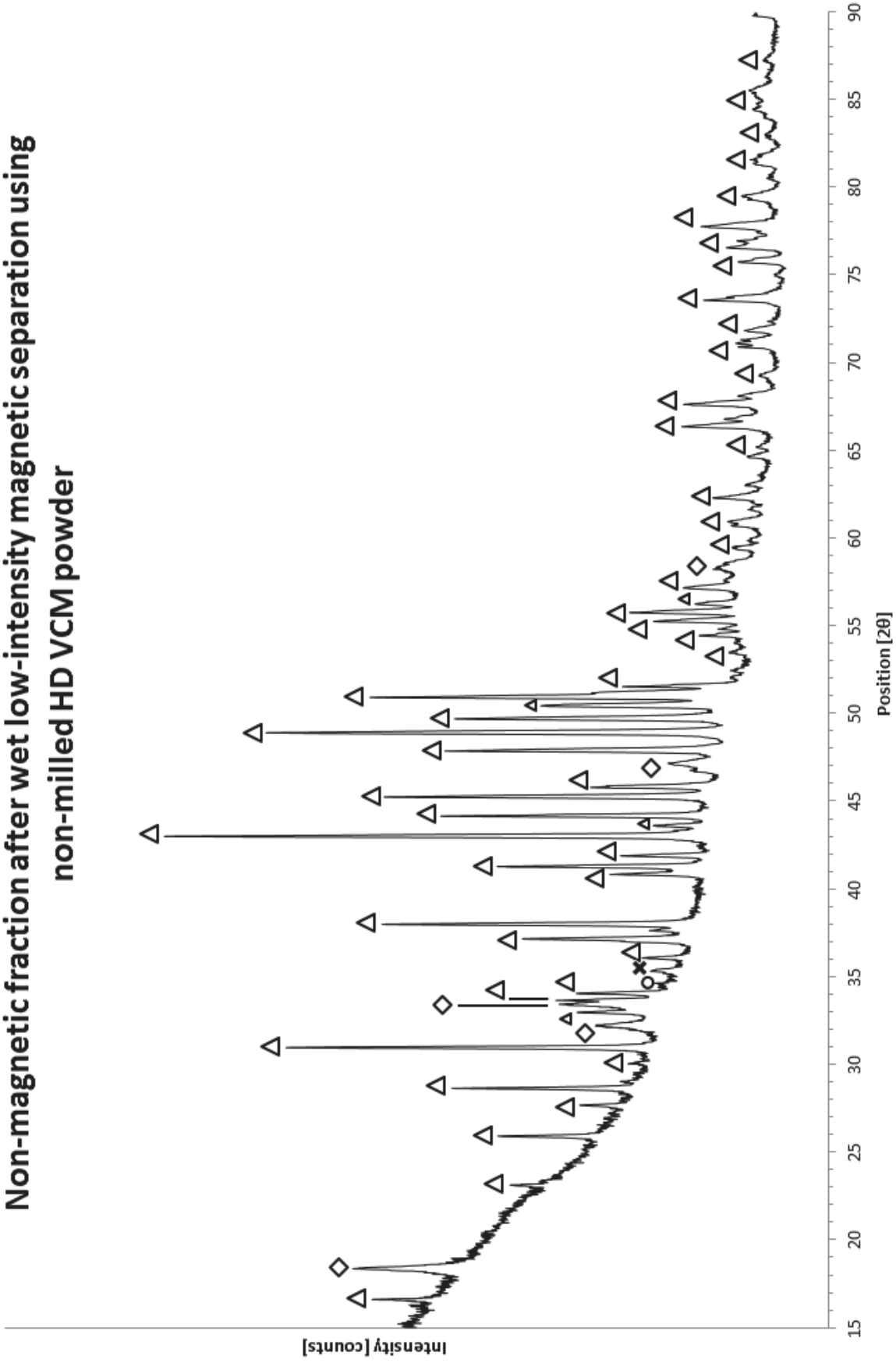
Non-magnetic fraction after wet low-intensity magnetic separation using non-milled HD VCM powder
Intensity [counts]
Position [2θ]
15
20
25
30
35
40
45
50
55
60
65
70
75
80
85
90

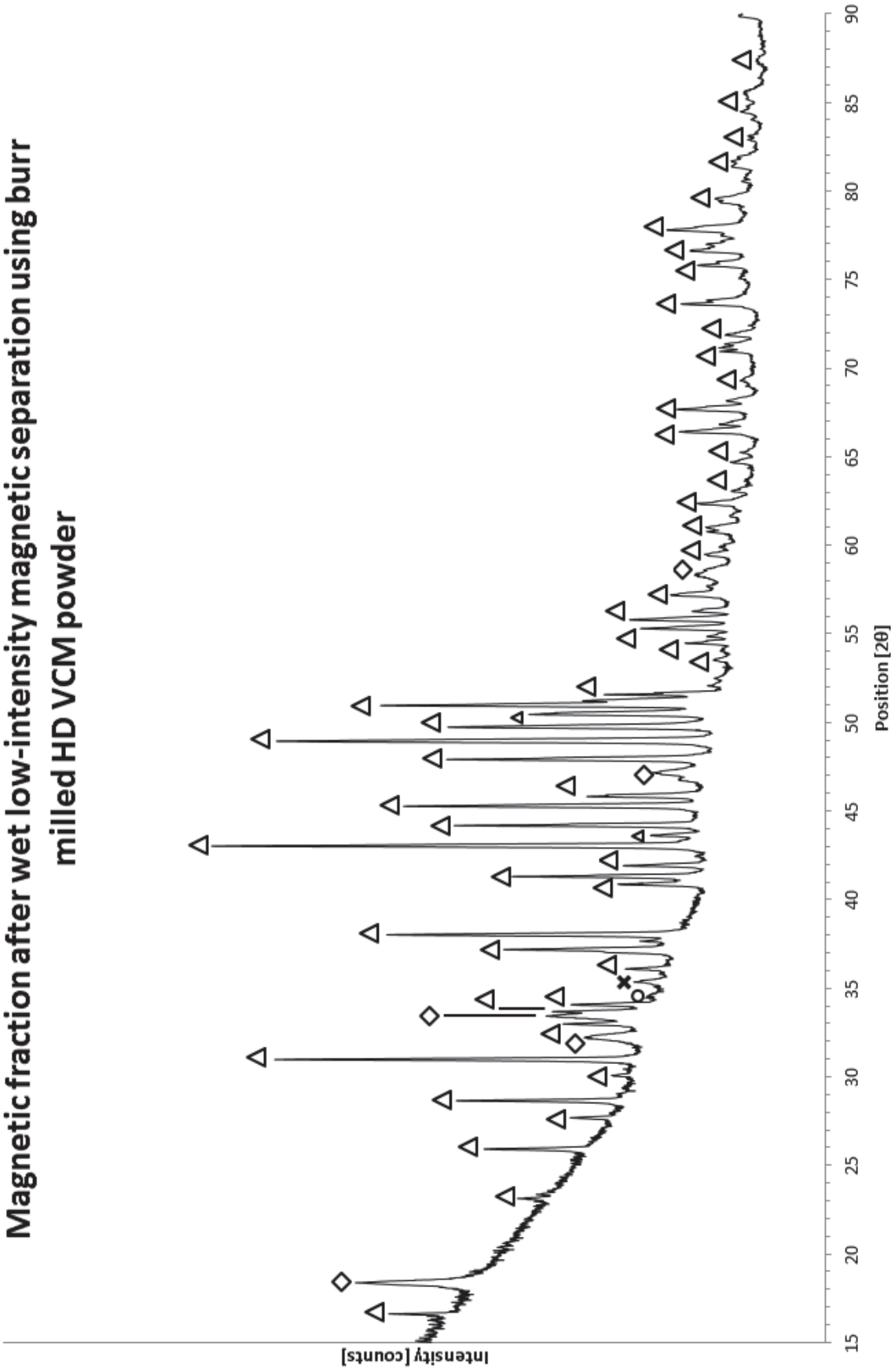
Magnetic fraction after wet low-intensity magnetic separation using burr milled HD VCM powder
Intensity [counts]
Position [2θ]
15
20
25
30
35
40
45
50
55
60
65
70
75
80
85
90

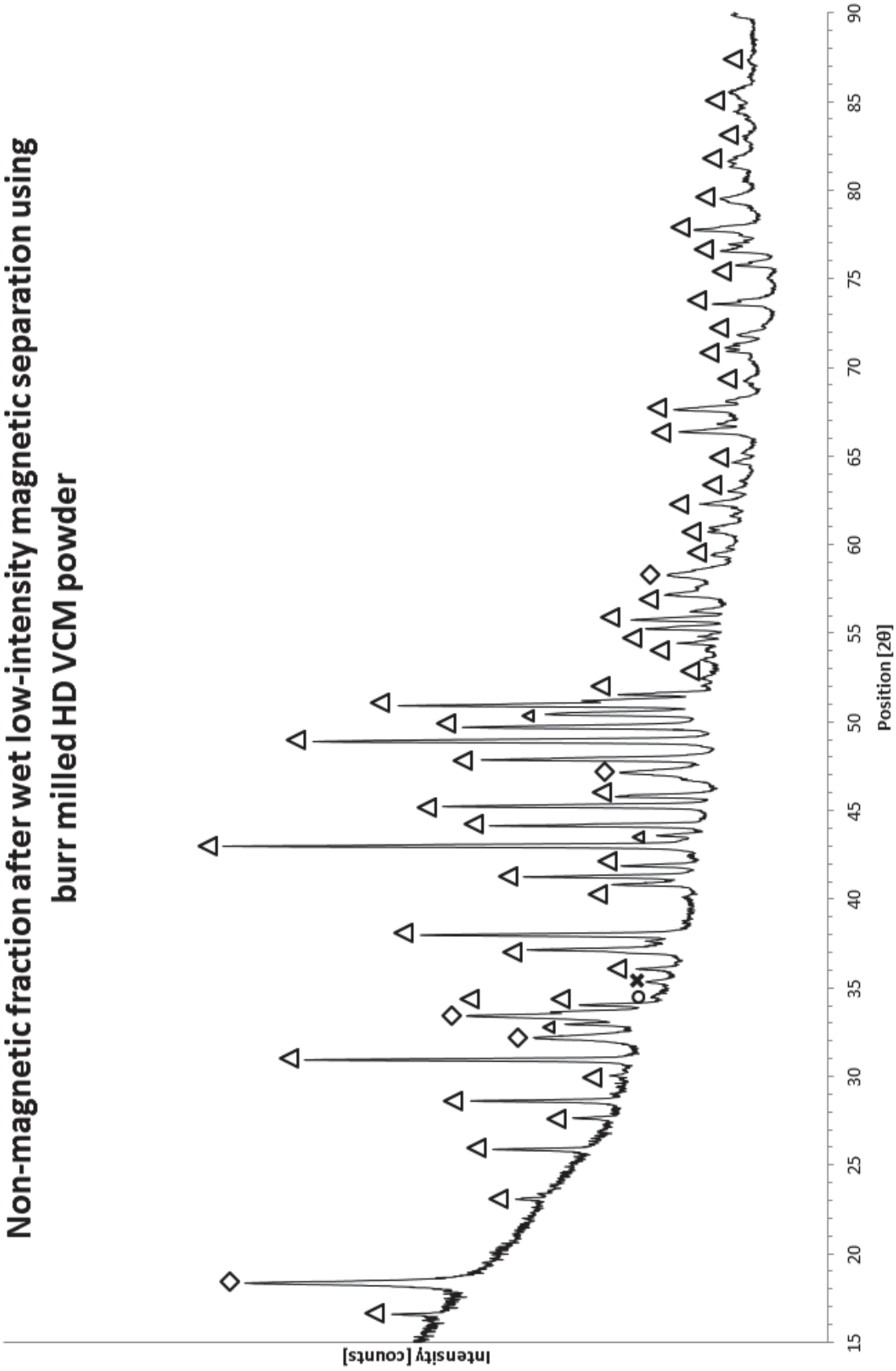
Non-magnetic fraction after wet low-intensity magnetic separation using burr milled HD VCM powder
Intensity [counts]
Position [2θ]
15
20
25
30
35
40
45
50
55
60
65
70
75
80
85
90

X-Ray Fluorescence Spectroscopy Results from Chapter 8

Results expressed in wt% from all the samples on the performance of three cycles of hydrocyclone separation. UF refers to underflow, OF to overflow and the number to the cycle of hydrocyclone.

Sample		Fe	Nd	Dy	Nb	Si	Pr	Gd	Sn	Al	ΣREEs
VCM magnet		61.54	34.87	1.38	0.64	0.39	0.22	0.21	0.17	0.11	36.68
Non-milled HD NdFeB magnet	Air	60.97	35.23	1.42	0.64	0.39	0.23	0.23	0.21	0.12	37.11
	UF - 1	61.62	34.71	1.40	0.56	0.40	0.24	0.21	0.19	0.12	36.56
	UF - 2	65.62	30.80	1.36	0.50	0.38	0.20	0.26	0.16	0.18	32.62
	UF - 3	66.45	29.94	1.38	0.52	0.39	0.17	0.25	0.18	0.19	31.74
	OF - 1	33.90	60.21	1.56	2.09	0.78	0.37	n/d	0.27	0.08	62.14
	OF - 2	17.34	77.26	1.62	1.81	0.72	0.60	n/d	0.33	0.03	79.48
	OF - 3	35.11	59.93	1.39	1.70	0.61	0.47	n/d	0.28	0.06	61.79
Burr milled HD NdFeB magnet	Air	60.42	35.84	1.39	0.65	0.40	0.19	0.23	0.23	0.11	37.65
	UF - 1	62.02	34.29	1.36	0.59	0.39	0.20	0.20	0.23	0.12	36.05
	UF - 2	65.64	30.62	1.33	0.54	0.40	0.19	0.23	0.21	0.18	32.37
	UF - 3	66.85	29.58	1.33	0.52	0.37	0.18	0.26	0.18	0.18	31.35
	OF - 1	18.82	75.13	1.65	2.30	0.72	0.62	n/d	0.35	0.03	77.40
	OF - 2	20.43	74.00	1.67	1.82	0.72	0.63	n/d	0.35	0.05	76.30
	OF - 3	Contaminated									

n/d – not detected

Inductively Coupled Plasma Emission Spectroscopy Results from Chapter 8

Results expressed in wt% from all the samples on the performance of three cycles of hydrocyclone separation. UF refers to underflow, OF to overflow and the number to the cycle of hydrocyclone.

Sample		Fe	Nd	Dy	Nb	Si	Pr	Gd	Sn	Al	ΣREEs
VCM magnet		61.92	34.21	0.95	0.06	0.60	0.24	0.05	0.06	1.91	35.45
Non-milled HD NdFeB magnet	Air	61.37	35.31	1.01	0.06	0.14	0.22	0.05	0.06	1.79	36.59
	UF - 1	63.27	33.59	0.97	0.06	0.05	0.24	0.04	0.01	1.76	34.85
	UF - 2	68.71	28.25	2.09	0.13	0.03	0.47	0.01	0.01	0.30	30.82
	UF - 3	68.89	28.06	2.09	0.12	0.02	0.46	0.03	n/d	0.32	30.63
	OF -1	36.38	59.12	0.97	0.06	1.62	0.44	0.09	0.06	1.24	60.62
	OF - 2	20.50	74.96	2.67	0.15	0.03	1.35	0.04	0.08	0.22	79.02
	OF - 3	39.40	56.95	2.12	0.14	0.02	1.02	0.03	0.03	0.29	60.12
Burr milled HD NdFeB magnet	Air	62.05	34.52	1.76	0.14	0.02	0.61	0.01	0.01	0.88	36.90
	UF - 1	64.72	31.69	2.57	0.13	0.03	0.49	0.01	0.01	0.37	34.76
	UF - 2	68.97	28.13	2.00	0.11	0.02	0.46	0.01	0.01	0.29	30.60
	UF - 3	69.33	27.70	2.03	0.14	0.02	0.45	0.03	0.01	0.30	30.21
	OF - 1	23.29	72.52	2.37	0.14	0.02	1.32	0.01	0.07	0.26	76.22
	OF - 2	22.36	73.29	2.46	0.12	0.03	1.33	0.07	0.11	0.23	77.15
	OF - 3	41.95	54.55	2.16	0.09	0.02	0.97	0.01	0.02	0.24	57.68

n/d – not detected

Publications

Journal Papers

E. Herraiz, M. Degri, A. Bradshaw, Sheridan, R.S., Mann, V.S.J., Harris, I.R., A. Lixandru, K. Guth, O. Gutfleisch, A. Walton, 2016. Recycling of rare earth magnets by hydrogen processing and re-sintering, submitted to the Journal of Alloys and Compounds.

E. Herraiz, A. Bradshaw, N. Rowson, M.A.R. Onal, A. Franczak, I. Poenaru, A. Walton, 2016. Recycling of rare earth magnets by hydrocyclone separation and re-sintering, submitted to the journal of Alloys and Compounds.

E. Herraiz, G. Ross, A. Bradshaw, R.S. Sheridan, V.S.J. Mann, I.R. Harris, A. Walton, 2016. Corrosion behavior and mechanical properties of recycled NdFeB magnets by hydrogen processing, being written at the moment.

Conference Papers

E. Herraiz, M. Degri, A. Bradshaw, R. Sheridan, V. Mann, I.R. Harris, A. Walton, 2016. Recycling of rare earth magnets by hydrogen processing and re-sintering. Joint European Magnetic Symposia (JEMS 2016), Glasgow (Scotland).

E. Herraiz, M. Degri, A. Bradshaw, R. Sheridan, V. Mann, I.R. Harris, A. Lixandru, I. Poenaru, K. Guth, R. Gauss, O. Gutfleisch, A. Walton, 2016. Recycling of rare earth magnets by hydrogen processing and re-sintering. Proceedings of the 24th International Workshop on Rare-Earth and Future Permanent Magnets and their Applications (REPM 2016), Darmstadt (Germany), 517-522.

E. Herraiz, A. Bradshaw, N. Rowson, M.A.R. Onal, A. Franczak, I. Poenaru, A. Walton, 2016. Recycling of rare earth magnets by hydrocyclone separation and re-sintering. Proceedings of the 24th International Workshop on Rare-Earth and Future Permanent Magnets and their Applications (REPM 2016), Darmstadt (Germany), 498-503.

E. Herraiz, M. Degri, A. Bradshaw, R. Sheridan, V. Mann, I.R. Harris, A. Walton, 2016. Recycling of rare earth magnets by hydrogen processing and re-sintering. Proceedings of the World Powder Metallurgy Congress (WORLDPM 2016), Hamburg (Germany).

Patents

E. Herraiz, A. Walton, 2016. British Patent 1,614,484.2

References

Ahmad, A., 1994. Effect of Homogenization on the structure of some RFeB alloys. Proceedings of 13th International Workshop on Rare-Earth Magnets and their Applications, 523-532.

Alander, T.K.R., Talvitie, M.J., Aittoniemi, K.T.J, Lindroos, V.K., 1994. Corrosion Resistance of $Nd_2Fe_{14}B$ Single Phase Based Magnets with HD Processed Sintering Additive. Proceedings of the 13th International Workshop on Rare-Earth Magnets and their Applications, 301-308.

Aldrich, C., 2015. Hydrocyclones. In: Progress in Filtration and Separation. Academic Press, 1-24.

Anderson, C.D., Anderson, C.G., Taylor, P.R., 2012. . A survey of recycled rare earths metallurgical processing. Proceedings of the 51st Annual Conference of Metallurgists of CIM, Niagara Falls, Canada, 411-422.

Angerer, G., Marscheider-Weidemann, F., Luellmann, A., Erdmann, L., Scharp, M., Handke, V., Marwede, M., 2009. Raw Materials for Emerging Technologies. The Influence of Sector-specific Feedstock Demand on Future Raw Materials Consumption in Material-Intensive Emerging Technologies. Final report – Abridged. Fraunhofer IRB Verlag.

Arai, S., Shibata, T., 1985. Highly heat-resistant Nd-Fe-Co-B system permanent magnets. IEEE Transactions on Magnetics, 21, 1952-1954.

Asabe, K., Saguchi, A., Takahashi, W., Suzuki, R., Ono, K., 2001. Recycling of rare earth magnet scraps: Part I carbon removal by high temperature oxidation. Materials Transactions, 42, 2487-2491.

ASTM B 962, 2008. Standard Test Methods for Density of Compacted or Sintered Powder Metallurgy (PM) Products Using Archimedes' Principle. American Society for Testing and Materials.

ASTM E 384, 2012. Standard Test Method for Knoop and Vickers Hardness of Materials. American Society for Testing and Materials.

ASTM E 92, 2013. Test Method for Vickers Hardness of Metallic Materials. American Society for Testing and Materials.

Bagdi, P., Bhardwaj, P., Sen, A.K., 2012. Analysis and Simulation of a Micro Hydrocyclone Device for Particle Liquid Separation. Journal of Fluids Engineering, 134, 021105-021113.

Bala, H., Szymura, S., Owczarek, E., Nowy-Wiechula, W., 1997. Corrosion behaviour of sintered Nd-(Fe,Al)-B magnets. Intermerallics, 5, 493-495.

Bartekova, E., 2014. An introduction to the economics of rare earths. Working Papers, United Nations University.

Bell Laboratories, 1983. A History of Engineering and Science in the Bell System. Bell Telephone Laboratories.

Benz, M.G., Martin, D.L., 1970. Cobalt-samarium permanent magnets prepared by liquid phase sintering. Applied Physics Letters, 17, 176-177.

Bernardi, J., Fidler, J., Sagawa, M., Hirose, Y., 1998. Microstructural analysis of strip cast Nd-Fe-B alloys for high $(BH)_{max}$ magnets. Journal of Applied Physics, 83, 6396-6398.

Bezinge, A., Braun, H.F., Muller, J., Yvon, K., 1985. Tetragonal rare earth (R) Iron borides, $R_{1+\varepsilon}Fe_4B_4$ ($\varepsilon \cong 0.1$), with incommensurate rare earth and iron substructures. Solid State Communications, 55, 131-135.

BGS, 2011. Rare earth elements. British Geological Survey Commodity Profile.

Bikbov, M.A., Karmazin, V.V., Bikbov, A.A., 2004. Low-intensity magnetic separation: principal stages of a separator development – What is the next? Physical Separation in Science and Engineering, 13, 53-67.

Binnemans, K., 2007. Lanthanides and actinides in ionic liquids. Chemical Reviews, 107, 2592-2614.

Binnemans, K., Jones, P.T., Blanpain, B., Gerven, T.V., Yang, Y., Walton, A., Buchert, M., 2013a. Recycling of rare earths: a critical review. Journal of Cleaner Production, 51, 1-22.

Binnemans, K., Pontikes, Y., Jones, P.T., van Gerven, T., Blanpain, B., 2013b. Recovery of rare earths from industrial waste residues: A concise review. Proceedings of the 3rd International Slag Valorisation Symposium, Leuven, Belgium, 191-205.

Blackford, J.R., Skouvlakis, G., Pursera, M., Koutsosa, V., 2012. Friction on ice: stick and slip. Faraday Discussions, 156, 243-254.

Boardman, R.P., 2005. Computer simulation studies of magnetic nanostructures. Ph.D. Thesis, University of Southampton.

Book, D. & Harris, I.R., 1995. Hydrogen absorption/desorption and HDDR studies on $Nd_{16}Fe_{76}B_8$ and $Nd_{11.8}Fe_{82.3}B_{5.9}$. Journal of Alloys and Compounds, 221, 187-192.

Bounds, C.O., 1994. The recycle of sintered magnet swarf. Symposium on Metals and Materials Waste Reduction, Recovery and Remediation, Rosemont, USA, 173-186.

Bradley, D., Pulling, D.J., 1959. Flow patterns in the hydraulic cyclone and their interpretation in terms of performance. Transactions of the Institution of Chemical Engineers, 37, 34–45.

Braun, H.F., Pelizzone, M., Yvon, K., 1982. Ferromagnetic borides with incommensurate rare earth (R) and iron sublattices: $R_{1+\varepsilon}Fe_4B_4$. Proceedings of the VIIth International Conference on Solid Compounds of Transition Elements, Grenoble, France, IIB11.

Brennan, M., 2006. CFD simulations of hydrocyclones with an air core comparison between large eddy simulations and a second moment closure. Chemical Engineering Research and Design, 84, 495–505.

Bretney, E., 1891. U.S. Patent 453,105.

Brown, D.N., Smith, B., Ma, B.M., Campbell, P., 2004. The Dependence of Magnetic Properties and Hot Workability of Rare Earth-Iron-Boride Magnets Upon Composition. IEEE Transactions on Magnetics, 40, 2895-2897.

Brown, W.F., 1945. Virtues and weaknesses of the domain concept. Reviews of Modern Physics, 17, 15-21.

Brown, W.F., 1959. Relaxational behaviour of fine magnetic particles. Journal of Applied Physics, 30, S130-S132.

Buschow, K.H.J., de Mooij, D.B., Van Noort, H.M., 1986. Properties of metastable ternary compounds and amorphous alloys in the Nd-Fe-B system. Journal of the Less Common Metals, 125, 135-146.

Cadogan, J.M., Coey, J.M.D., 1986. Hydrogen absorption and desorption in $Nd_2Fe_{14}B$. Applied Physics Letters, 48, 442-444.

Calle, G., Henao, E., 2009. Dureza Vickers. Universidad Tecnológica de Pereira.

Casali, A., Gonzalez, G.D., Torres, F., Vallebuona, G., Castelli, L., Gimenez, P., 1998. Particle size distribution soft-sensor for a grinding circuit. Powder Technology, 99, 15–20.

Case, E.D., Smyth, J.R., 1981. Room-temperature fracture energy of monoclinic Gd_2O_3. Journal of Materials Science, 16, 3215-3217.

Castor, S.B., Hendrick, J.B., 2006. Rare earth elements. Industrial mineral and rocks: commodities, markets, and uses. Presentation at the SME Annual Conference 2006, Phoenix, USA.

Chaban, N.F., Kuzma, Y.B., Bilanizhko, N.S., Kachmar, O.O., Petriv, N.V., 1979. Ternary (Nd,Sm,Gd)-Fe-B Systems. Dopov. Akad. Nauk USSR, Ser. A: Fiz. Mat. Tekh. Nauki., 873-876.

Chen, L., Xiong, D., 2015. Magnetic Techniques for Mineral Processing. In: Progress in Filtration and Separation, Academic Press, 287-324.

Chen, W., Zydek, N., Parma, F., 2000. Evaluation of hydrocyclone models for practical applications. Chemical Engineering Journal, 80, 295–303.

Chuenarrom, C., Benjakul, P., Daosodsai, P., 2009. Effect of indentation load and time on Knoop and Vickers microhardness test for enamel and dentin. Materials Research, 12, 4, 473-476.

Chun-lin, T., Shu-xin, B., Hong, Z., Ke, C., Jia-chun, Z., Zun, C., 2004. Effects of hydrogen on the oxidation of coarse decrepitated powder of Nd–Dy–Fe–B alloy. Journal of Alloys and Compounds, 368, 333–336.

Cilliers, J.J., 2000. Hydrocyclones for particle size separation. In: II Particle Size Separation. Academic Press, 1819-1825.

Clarke, J.C., 1997. Production and characterisation of bonded and sintered magnets based on stoichiometric $Nd_2Fe_{14}B$. Ph.D. Thesis, University of Birmingham.

Coey, J.M. Sun, H., 1990. Improved magnetic properties by treatment of iron-based rare earth intermetallic compounds in anmonia. Journal of Magnetism and Magnetic Materials, 87, 251-254.

Coey, J.M.D, 1996. Rare-earth iron permanent magnets. Oxford Science Publications.

Commission of the European Communities, 1985. Nd-Fe permanent magnets: their present and future applications. Elsevier.

Corfield, M.R., 2003. Production of sintered permanent magnets based on (Nd/Pr)Fe-B alloys. Ph.D. Thesis, University of Birmingham.

Corfield, M.R., Harris, I.R., Williams, A.J., 2008. Influence of oxygen content on grain growth in Pr–Fe–B/Nd–Fe–B sintered magnets. Journal of Alloys and Compounds, 463, 180–188.

Croat, J.J., Herbst, J.F., Lee, R.W., Pinkerton, F.E., 1984. High-energy product Nd-Fe-B permanent magnets. Journal of Applied Physics, 55, 2078-2083.

Cui, X.G., Cui, C.Y., Cheng, X.N., Xu, X.J., Mac, T.Y., Yan, M., Wang, C., 2013. Effects of alignment on the magnetic and mechanical properties of sintered Nd–Fe–B magnets. Journal of Alloys and Compounds, 563, 161–164.

Cullity, B.D., Graham, C.D., 2009. Introduction to magnetic materials. Wiley.

Curie, P., 1895. Propriétés magnétiques des corps à diverses temperatures. PhD Thesis, University of Paris.

Darnell, F.J., Cloud, W.H., 1964. Magnetization of gadolinium near its curie temperature. Journal of Applied Physics, 35, 935-939.

Davies, B.E., Mottram, R.S., Harris, I.R., 2001. Recent developments in the sintering of NdFeB. Materials Chemistry and Physics, 67, 272-281.

Degri, M.J.J., 2014. The Processing and Characterisation of Recycled NdFeB-type Sintered Magnets. Ph.D. Thesis, University of Birmingham.

Delgadillo, J.A., Rajamani, R.K., 2007. Exploration of hydrocyclone designs using computational fluid dynamics. International Journal Mineral Processing, 84, 252–261.

Dempsey, N.M., Woodcock, T.G., Sepehri-Amin, H., Zhang, Y., Kennedy, H., Givord, D., Hono, K., Gutfleisch, O., 2013. High-coercivity Nd–Fe–B thick films without heavy rare earth additions. Acta Materialia, 61, 4920-4927.

Derkach, V.G., Datsuk, I.S., 1947. Electromagnetic Processes of Beneficiation. Metallurgizdat.

Dobbins, M., Dunn, P., Sherrell, I., 2009. Recent advances in magnetic separator designs and applications. Proceedings of the 7th International Heavy Minerals Conference, Drakensberg, South Africa, 63-70.

Dobbins, M., Sherrell, I., 2010. Significant developments in dry rare-earth magnetic separation. Mining Engineering, 62, 49-54.

Driessen, M.G., 1951. Theory of Flow in a Cyclone. Revue de L'Industrie Minerale, Numero Special, Saint-Etienne, 449–461.

Drozzina, V., Janus, R., 1935. A New Magnetic Alloy with Very Large Coercitive Force. Nature, 135, 3401, 36-37.

Durst, K.D., Kronmuller, H., 1987. The coercive field of sintered and melt-spun NdFeB magnets. Journal of Magnetism and Magnetic Materials, 68, 63-75.

Dwari, R.K., Biswas, M.N., Meikap, B.C., 2004. Performance characteristics of sand FCC and fly ash in a novel hydrocyclone. Chemical Engineering Science, 59, 671–684.

Edgley, D.S., Le Breton, J.M., Steyaert, S., Ahmed, F.M., Harris, I.R., Teillet, J., 1997. Characterisation of high temperature oxidation of Nd-Fe-B magnets. Journal of Magnetism and Magnetic Materials, 173, 29-42.

Ellis, T.W., Schmidt, F.A., Jones, L.L., 1994. Methods and opportunities in the recycling of rare earth based materials. Report No. IS-M 796, Ames Laboratory.

EPA, 2012. Rare earth elements: a review of production, processing, recycling and associated environmental issues. United States Environmental Protection Agency, Region 7: Kansas.

EPMA, 2008. Introduction to Powder Metallurgy: the process and its products. European Powder Metallurgy Association.

ERECON, 2015. Strengthening the European rare earths supply chain: Challenges and policy options. Kooroshy, J., G. Tiess, A. Tukker, and A. Walton.

Ertan, H.B., Üçtug, M.Y., Colyer, R., Consoli, A., 2013. Modern electrical devices. Springer Science and Business Media.

European Commission, 2010. Critical raw materials for the EU, Report of the Ad-hoc Working Group on defining critical raw materials.

European Commission, 2014. Report on critical raw materials for the EU, Report of the Ad-hoc Working Group on defining critical raw materials.

Evans, A.G., Tappin, G., 1972. Effects of microstructure on the stress propagate inherent flaws. Proceedings of the British Ceramic Society, 23, 275-296.

Ewing, J.A., 1900. Magnetic induction in iron and other metals. The Electrician Printing and Publishing Company Limited.

Falconnet, P., 1985. The economics of rare-earths. Journal of the Less Common Metals. 111, 9-15.

Farr, M., 2013. A study on the impact of surface and bulk oxidation on the recyclability of NdFeB magnets. M.Sc. Thesis, University of Birmingham.

Fernengel, W., Schrey, P., Wall, B., 1995. Magnetic properties and microstructure of high-energy sintered (Nd,Dy)-(Fe,Co,Cu)-B magnets. Proceedings of the 3rd International Symposium on Physics of Magnetic Materials, Seoul, South Korea, 748-753.

Fidler, J., 1985. Analytical microscope studies of sintered Nd-Fe-B magnets. IEEE Transactions on Magnetics, 21, 1955-1957.

Fidler, J., 1987. On the role of the Nd-rich phases in sintered Nd-Fe-B magnets. IEEE Transactions on Magnetics, 23, 2106-2108.

Fidler, J., 1990. The Effect of Dopants (Al, Ga, Cu, Mo, V) on Microstructure and Coercivity of Sintered $Nd_2Fe_{14}B$ Based Magnets. Proceedings of the 6th International Symposium on Magnetic Anisotropy and Coercivity in Rare-Earth Transition Metal Alloys, Pittsburgh, USA, 176-180.

Fidler, J., Bernardi, J., Schrefl, T., 1995. Permanent magnets - New microstructural aspects. Scripta Metallurgica Et Materiala, 33, 1781-1791.

Fidler, J., Groiss, C., Tokunga, M., 1990. The influence of Ga-substitution on the coercivity of Nd-(Fe,Co)-B sintered permanent magnets. IEEE Transactions on Magnetics, 26, 1948-1950.

Fullerton, W., 1792. British Patent.

Gao, R., Zhang, D., Li, H., Jiang, S., Zhou, S., Li, F., Zhang, L., 1995. Coercivity and its dependence on the strength of alignment magnetic field in Nd-Fe-B sintered magnets. Journal of Applied Physics, 78, 1156-1159.

Gao, R.W., Zhang, D.H., Li, H., Zhang, J.C., 1998. Effects of the degree of grain alignment on the hard magnetic properties of sintered NdFeB magnets. Applied Physics A, 67, 353-356.

Geng, Y., 2014. Microstructure and Magnetic Behavior Studies of Processing-controlled and Composition-modified Fe-Ni and Mn-Al Alloys. Ph.D. Thesis, University of Nebraska.

German, R.M., 1996. Sintering Theory and Practice. Wiley-Interscience Publication.

German, R.M., Suri, P., Park, S.J., 2009. Review: liquid phase sintering. Journal of Materials Science, 44, 1-39.

Gilbert, W., 1600. On the Magnet and Magnetic Bodies, and on That Great Magnet the Earth, De Magnete, Magneticisque Corporibus, et de Magno Magnete Tellure.

Givord, D., Li, H.S., Moreau, J.M., 1984a. Magnetic properties and crystal structure of $Nd_2Fe_{14}B$. Solid State Communications, 50, 497-499.

Givord, D., Li, H.S., Perrier de la Bâthie, R., 1984b. Magnetic properties of $Y_2Fe_{14}B$ and $Nd_2Fe_{14}B$ single crystals. Solid State Communications, 51, 857-860.

Givord, D., Moreau, J.M., Tenaud, P., 1985. $Nd_5Fe_{18}B_{18}$ ($Nd_{1.11}Fe_4B_4$), a new nowotny-like phase. structural and magnetic properties. Solid State Communications, 55, 303-306.

Givord, D., Tenaud, P., Viadieu, T., 1988. Angular dependence of coercivity in sintered magnets. Journal of Magnetism and Magnetic Materials, 72, 247-252.

Graedel, T.E., Allwood, J., Birat, J.P., Buchert, M., Hageluken, C., Reck, B.K., Sibley, S.F., Sonnemann, G., 2011. What do we know about metal recycling rates? Journal of Industrial Ecology, 15, 355-366.

Grauch, R., Mariano, A., 2008. Ion-adsorption type lanthanide deposits. Presentation at the SME Annual Conference 2008, Denver, USA.

Grieb, B., Henig, E.-Th., Schneider, G., Knoch, G., Petzow, G., de Mooij, D., 1992. Phase diagrams of Fe-Nd-B and related systems for optimisation of hard magnetic properties. Journal of Powder Metallurgy, 35, 221-229.

Grieb, B., Pithan, C., Henig, E.-Th., Petzow, G., 1991. Replacement of Nd by an intermetallic phase in the intergranular region of Fe-Nd-B sintered magnets. Journal of Applied Physics, 70, 6354-6356.

Gschneidner, K.A., Capellen, J., 1987. 1787-1987. Two hundred years of rare earths. Rare-earth Information Center.

Gupta, C.K., Krishnamurthy, N., 2005. Extractive metallurgy of rare earths. CRC Press.

Gutfleisch, O., Willard, M.A., Bruck, E., Chen, C.H., Sankar, S.G., Liu, J.P., 2011. Magnetic materials and devices for the 21st century: stronger, lighter and more energy efficient. Advanced Materials, 23, 821-842.

Hadjipanayis, G.C., 2003. Bonded magnets. Springer.

Hadjipanayis, G.C., Hazelton, R.C., Lawless, K.P., 1984. Cobalt-free permanent magnet materials based on iron-rare-earth alloy. Journal of Applied Physics, 55, 2073-2077.

Hallemans, B., Wollants, P., Roos, J.R., 1995. Thermodynamic assessment of the Fe-Nd-B phase diagram. Journal of Phase Equilibria, 16, 137-149.

Harkins, W.D., 1917. The Evolution of the Elements and the Stability of Complex Atoms. Journal of the American Chemical Society, 39, 856.

Harris, I.R. Evans, J. & Nyholm, P.S., 1979. British Patent 1,554,384.

Harris, I.R., McGuiness, P.J., 1991. Hydrogen: its use in the processing of NdFeB-type magnets. Journal of the Less Common Metals, 172-174, 1273-1284.

Harris, I.R., McGuiness, P.J., Jones, D.G.R., Abell, J.S., 1987. Nd-Fe-B Permanent Magnets: Hydrogen Absorption/Desorption Studies (HADS) on $Nd_{16}Fe_{76}B_8$ and $Nd_2Fe_{14}B$. Physica Scripta, T19, 435-440.

Harris, I.R., Noble, C. & Bailey, T., 1985. The hydrogen decrepitation of an $Nd_{15}Fe_{77}B_8$ magnetic alloy. Journal of the Less-Common Metals, 106:L1-L4.

Harris, I.R., Williams, A., Walton, A., Speight, J., 2012. Magnet recycling. U.S. Patent 0137829.

Hatch, G., 2015. TMR Advanced Rare-Earth Projects Index. Technology Metals Research.

Heisenberg, W., 1928. Zur Theorie du Ferromagnetismus. Zeitschrift für Physik, 49, 619-636.

Heisz, S., Hilscher, G., 1987. The origin of graduated demagnetization curves of Nd-Fe-B magnets. Journal of Magnetism and Magnetic Materials, 67, 20-28.

Herbst, J.F., Croat, J.J., Pinkerton, F.E., 1984. Relationships between crystal structure and magnetic properties in $Nd_2Fe_{14}B$. Physical Review B, 29, 4176-4178.

Higgins, B.E., Oesterreicher, H., 1987. Properties and stability of $Nd_2Fe_{14}B$ particles. IEEE Transactions on Magnetics, 23, 92-93.

Hilsum, L., 2009. Chinese pay toxic price for a green world. The Sunday Times, December 6, 2010.

Hiraga, K., Hirabayashi, M., Sagawa, M., Matsuura, Y., 1985. A study of microstructures of grain boundaries in sintered $Fe_{77}Nd_{15}B_8$ permanent magnet by high-resolution electron microscopy. Japanese Journal of Applied Physics, 24, 699-703.

Hirosawa, S., Matsuura, Y., Yamamoto, H., Fujimura, S., Sagawa, M., Yamauchi, H., 1985. Single crystal measurements of anisotropy constants of Re2Fe14B (R=Y, Ce, Pr, Nd, Gd, Tb, Dy and Ho). Japanese Journal of Applied Physics, 24, L803-L805.

Hirosawa, S., Sagawa, M., 1985. Spin reorientation and magnetization anomaly in $Er_2Fe_{14}B$ and $Tm_2Fe_{14}B$. Solid State Communications, 54, 335-337.

Hirosawa, S., Tomizawa, H., Mino, S., Hamamura, A., 1990. High-coercivity Nd-Fe-B-type permanent magnets with less dysprosium. IEEE Transactions on Magnetics, 26, 1960-1962.

Hirose, Y., Hasegawa, H., Sasaki, S., Sagawa, M., 1998. Microstructure of strip case alloys for high performance NdFeB magnets. Proceedings of the 15th International Workshop on Rare-Earth Magnets and their Applications, 1, 77-86.

Hitachi, 2010. Hitachi Develops Recycling Technologies for Rare Earth Metals. Press release.

Hitachi, 2013. Rare-earth Magnet Recycling. Hitachi Review, 62, 452-455.

Holc, J., Besenicar, S., Kolar, D., 1990. A study of $Nd_2Fe_{14}B$ and a neodymium-rich phase in sintered NdFeB magnets. Journal of Materials Science, 25, 215-219.

Honda, K., Kaya, S., 1926. On the magnetisation of single crystals of iron. Scientific Reports of Tohoku University, 15, 721-753.

Hong, Y.G., Nakamura, H., Sugimoto, S., Kagotani, T., Okada, M., Homma, M., 1995. Magnetic properties of Nd-Fe-B sintered magnets prepared by powder mixing method utilizing hydrogen decrepitated powders. Proceedings of the 3rd International Symposium on Physics of Magnetic Materials, Seoul, South Korea, 665-669.

Hook, L., 2011. Rare earth prices soar as China stocks up. The Financial Times, June 19, 2011.

Horton, J.A., Wright, J.L., 1996. Fracture toughness of commercial magnets. IEEE Transactions on Magnetics, 32, 4374-4376.

Hsu, S.E., Wang, K.L., Su, L.C., 1987. Studies on heat treatment for Nd-Fe-B magnets. IEEE Transactions on Magnetics, 23, 2515-2517.

Hu, Z., Wang, H., Ma, D., Luo, C., 2013. The Influence of Co and Nb Additions on the Magnetic Properties and Thermal Stability of Ultra-high Intrinsic Coercivity Nd-Fe-B Magnets. Journal of Low Temperature Physics, 170, 313-321.

Hu, Z.H., Chu, L.H., Li, J., Liu, Y., 2012. Effect of die-upset level on the mechanical properties and microstructure of Nd-Fe-B magnets prepared by spark plasma sintering. Journal of Magnetism and Magnetic Materials, 324, 101-104.

Hu, Z.H., Qu, H.J., Zhao, J.Q., Yan, C.J., Liu, X.M., 2014. Effect of sintering process on the magnetic and mechanical properties of sintered Nd–Fe–B magnets. Journal of Magnetism and Magnetic Materials, 368, 54-58.

Huang, M.Q., Oswald, E., Boltich, E., Hirosawa, S., Wallace, W.E., Schwab, E., 1985. Magnetic characteristics of $R_2Fe_{14}B$ systems prepared with high purity rare earths (R =Y, Nd, Sm or Gd). Physica B+C, 130, 319-322.

Isotahdon, E., Huttunen-Saarivirta, E., Kuokkala, V.-T., Paju, M., 2012. Corrosion behaviour of sintered Nd–Fe–B magnets. Materials Chemistry and Physics, 135, 762–771.

Itoh, M., Masuda, M., Suzuki, S., Machida, K.I., 2004a. Recycle for sludge scrap of Nd-Fe-B sintered magnet as isotropic bonded magnet. Journal of Rare Earths, 22, 168-171.

Itoh, M., Masuda, M., Suzuki, S., Machida, K.I., 2004b. Recycling of rare earth sintered magnets as isotropic bonded magnets by melt-spinning. Journal of Alloys and Compounds, 374, 393-396.

Iwamura, E., Nagayama, K., Suzuki, T., Umeda, T., 1989. High coercivity of melt-spun $Nd_{15}Fe_{77}B_8$ ribbons with a new metastable boundary phase. Proceedings on the 10th International Workshop on Rare-Earth Magnets and their Applications, 293-301.

Jiang, J., Zeng, Z., Wu, J., Tokunaga, M., 2000. Influence of alloying elements on mechanical properties and microstructure of sintered Nd-Fe-Co-B magnet. Journal of Magnetism and Magnetic Materials, 214, 61-68.

Jiang, J., Zeng, Z., Yu, J., Wu, J., Tokunaga, M., 2001. The effect of Co addition on the fracture strength of NdFeB sintered magnets. Intermetallics, 9, 269-272.

Jin, S, Gayle, N.V., Bernardidi, J.E., 1980. Deformation-Aged Cr-Co-Cu-Fe Permanent Magnet Alloys. IEEE Transactions on Magnetics, 16, 1050-1052.

Jin, S., 1979. Deformation-Induced Anisotropic Cr-Co-Fe Permanent Magnet Alloys. IEEE Transactions on Magnetics, 15, 1748-1750.

Jones, P.T., Geysen, D., Tielemans, Y., Van Passel, S., Pontikes, Y., Blanpain, B., Quaghebeur, M., Hoekstra, N., 2012. Enhanced Landfill Mining in view of multiple resource recovery: a critical review. Journal of Cleaner Production, 55, 45-55.

Jones, P.T., Van Gerven, T., Van Acker, K., Geysen, D., Binnemans, K., Fransaer, J., Blanpain, B., Mishra, B., Apelian, D., 2011. CR3: cornerstone to the sustainable inorganic materials management (SIM2) research program at KU Leuven. The Journal of The Minerals, Metals & Materials Society, TMS, 63, 14-15.

Jönsson, C., Zaim, A., Zhou, W., Sheridan, R.S., Degri, M.J.J., Bradhsaw, A., Mann, V.S.J., Rowson, N., Walton, A., 2016a, The potential separation of neodymium from Nd-Fe-B magnets using the hydrogenation disproportionation reaction, Proceedings of the 24th International Workshop on Rare-Earth and Future Permanent Magnets and their Applications, 356-361.

Jönsson, C., Walton, A., 2016b. British Patent 1,501,370.

JRC, 2011. Critical Metals in Strategic Energy Technologies. Assessing Rare Metals as Supply-Chain Bottlenecks in Low-Carbon Energy Technologies. Joint Research Center, European Commission.

Jun, L., Yung, L., Yilong, M., 2012. Effect of niobium on microstructure and magnetic properties of bulk anisotropic NdFeB/α-Fe nanocomposites. Journal of Magnetism and Magnetic Materials, 324, 2292-2297.

Kamiyoshi, M., Miyamoto, H., Nishigaki, N., Taira, Y., Irie, T., 2012. Recycling Process of Rare Earth from Re-Fe-B Sintered Magnets at SANTOKU Corporation. Lecture at the 8th International Conference on f-Elements, Udine, Italy.

Kanazawa, Y., Kamitani, M., 2006. Rare earth minerals and resources in the world. Journal of Alloys and Compounds, 408-412, 1339-1343.

Kaneko, A., Ohrai, H., 2007. WO Patent 2007119846.

Kaneko, Y., 2000. Rare earth magnets with high energy products. Proceedings of the 16th International Workshop on Rare-Earth Magnets and Their Applications, 83-98.

Kaneko, Y., Ishigaki, N., 1994. Recent developments of high-performance NEOMAX magnets. Journal of Materials Engineering and Performance, 3, 228-233.

Kaneko, Y., Kuniyoshi, F., Ishigaki, N., 2003. Proven technologies on high-performance Nd–Fe–B sintered magnets. Joiurnal of Alloys and Compounds, 408-412, 1344-1349.

Katter, M., Zapf, L., Blank, R., Fernengel, W., Rodewald, W., 2001. Corrosion mechanism of Re-Fe-Co-Cu-Ga-Al-B magnets. Proceedings of the 8th Joint MMM-Intermag Conference, San Antonio, USA, 1-3.

Kawai, T., Ma, B.M., Sankar, S.G., Wallace, W.E., 1990. Effect of crystal alignment on the remanence of sintered NdFeB magnets. Journal of Applied Physics, 67, 4610-4612.

Kawasaki, T., Itoh, M., Machida, K., 2003. Reproduction of Nd-Fe-B sintered magnet scraps using a binary alloy blending technique. Materials Transactions, 44, 1682-1685.

Kaya, S., 1928. On the magnetisation of single crystals of cobalt. Scientific Reports of Tohoku University, 17, 1157-1177.

Kelsall, D.F., 1953. A study of the motion of solid particles in a hydraulic cyclone. Transactions of the Institution of Chemical Engineers, 30, 87-104.

Kianvash, A., Harris, I.R., 1984. Coercivity dependence of a $Sm_2(Co, Cu, Fe, Zr)_{17}$ type alloy on magnetic processing procedure. Journal of Materials Science, 19, 353-358.

Kianvash, A., Harris, I.R., 1985. Hydrogen decrepitation as a method of powder preparation of a 2:17-type, $Sm(Co, Cu, Fe, Zr)_{8.92}$ magnetic alloy. Journal of Materials Science, 20, 682-688.

Kianvash, A., Harris, I.R., 1991. Magnetic properties of the sintered magnets produced from a Nd-Fe-B-Cu-type material. Journal of Applied Physics, 70, 6453-6455.

Kim, A.S., Camp, F.E., Missell, F.P., 1996. Design of High Coercivity ReFeB Permanent Magnets. Proceedings of the 14th International Workshop on Rare-Earth Magnets and their Applications, 678-688.

Kim, J.W., Kim S.H. & Kim, Y.D., 2012b. Mechanical properties of (Nd,Dy)-Fe-B magnets sintered via cyclic sintering. Materials Science and Engineering A, 535, 325-329.

Kim, J.W., Kim S.H., Song, S.Y. & Kim, Y.D., 2013. Nd-Fe-B permanent magnets fabricated by low temperature sintering process. Journal of Alloys and Compounds, 551, 180-184.

Kim, J.W., Song, S.Y. & Kim, Y.D., 2012a. Effect of cyclic sintering process for NdFeB magnet on microstructure and magnetic properties. Journal of Alloys and Compounds, 540, 141-144.

Kingsnorth, D., 2010. Rare earths: facing new challenges in the new decade. Presentation at the SME Annual Meeting 2010.

Kingsnorth, D., 2014. The rare earths industry: sustainable or stagnant? 2014 forecast. Presentation at the ERECON Steering Committee in Brussels, Belgium, June 26.

Knoch, K.G, Reinsch, B., Petzow, G., 1994. The Nd-Fe-B phase diagram and the primary solidification of $Nd_2Fe_{14}B$. Proceedings of the 13th International Workshop on Rare Earth Magnets and their Applications, 503-510.

Knoch, K.G., Grieb, B., Henig, E.T., Kronmuller, H., Petzow, G., 1990. Upgraded Nd-Fe-B-AD (AD=Al,Ga) magnets: wettability and microstructure. IEEE Transactions on Magnetics, 26, 1951-1953.

Knoch, K.G., Harris, I.R., 1992. Preparation of a New Ternary Phase $Nd_{30}Fe_{65}Cu_5$. Zeitschrift für Metallkunde, 83, 338-340.

Knoch, K.G., Schneider, G., Fidler, J., Henig, E.T., Kronmuller, H., 1989. Al-doped Nd-Fe-B permanent magnets: wetting and microstructural investigations. IEEE Transactions on Magnetics, 25, 3426-3428.

Koon, N.C., Das, B.N., 1984. Crystallization of FeB alloys with rare earths to produce hard magnetic materials. Journal of Applied Physics, 55, 2063-2066.

Koon, N.C., Das, B.N., Rubinstein, M., Tyson, J., 1985. Magnetic properties of $R_2Fe_{1\ 4}B$ single crystals. Journal of Applied Physics, 57, 4091-4093.

Kraipech, W., Chen, W., Dyakowski, T., Nowakowski, A., 2006. The performance of the empirical models on industrial hydrocyclone design. International Journal of Mineral Processing, 80, 100–115.

Kronmuller, H., 1962. Mikromagnetisehe Bereehnung der Magnetisierung in der Umgebung unmagnetischer Einschliisse in Ferromagnetika. Zeitschrift für Physik, 168, 478-494.

Kronmuller, H., Durst, K.D., Sagawa, M., 1988. Analysis of the magnetic hardening mechanism in RE-FeB permanent magnets. Journal of Magnetism and Magnetic Materials, 74, 291-302.

Kumar, G., 2004. Structural and magnetic characterization of Nd-based Nd-Fe and Nd-Fe-Co-Al metastable alloys. RNDr. Thesis, Technical University Dresden.

Kwon, H.W., Harris, I.R., 1991. Study of $Sm(Co,Fe,Cu,Zr)_{7.1}$ magnets produced using a combination of hydrogen decrepitation and ball milling. Journal of Applied Physics, 69, 5856-5858.

Larsen, J.W., Livesay, B.R., 1980. Hydriding kinetics of $SmCo_5$. Journal of the Less Common Metals, 73, 79–88.

Legras, L., Delmare, J., Lemarchand, D., Dinh, J.V., Vigier, P., 1995. Characterization of the Nd-Fe-Al μ phase in the microstructure of an aluminium- and vanadium-substituted Nd-Fe-B magnet. Journal of Alloys and Compounds, 218, 17-21.

Leonowicz, M., and Davies, H.A., 1994. Induced magnetic anisotropy in hot deformed Fe-RE-B alloys. Proceedings of the 13th International Workshop on Rare Earth Magnets and their Applications, 623-634.

Li, C., Liu, W.Q., Yue, M., Liu, Y.Q., Zhang, D.T., Zuo, T.Y., 2014. Waste Nd-Fe-B Sintered Magnet Recycling by Doping With Rare Earth Rich Alloys. IEEE Transactions on Magnetics, 50, 12-14.

Li, W.F., Ohkubo, T., Hono, K., Sagawa, M., 2009. The origin of coercivity decrease in fine grained Nd–Fe–B sintered magnets. Journal of Magnetism and Magnetic Materials, 321, 1100 – 1105.

Li, X.T., Yue, M., Liu, W.Q., Li, X.L., Yi, X.F., Huang, X.L., Zhang, D.T., Chen, J.W., 2015. Large batch recycling of waste Nd-Fe-B magnets to manufacture sintered magnets with improved magnetic properties. Journal of Alloys and Compounds, 649, 656-660.

Li, Y., Evans, H.E., Harris, I.R., Jones, I.P., 2003. The oxidation of NdFeB magnets. Oxidation of Metals, 59, 167-182.

Lian, F.Z., Wallace, W.E., 1995. Proceedings of the 3rd International Symposium on Physics of Magnetic Materials, Seoul, South Korea, 748-753.

Linetsky, Y.L., Raigorodsky, V.M., Tsvetkov, V.Y., 1992. Phase transformations in sputtered Nd-Fe-B alloys. Journal of Alloys and Compounds, 184, 35-42.

Liu, N.C., Kim, A.S., 1990. Abnormal grain growth in sintered Nd-Fe-B magnets. Journal of Applied Physics, 67, 4629-4631.

Liu, W., Li, C., Zakotnik, M., Yue, M., Zhang, D., Huang, X., 2015. Recycling of waste Nd-Fe-B sintered magnets by doping with dysprosium hydride nanoparticles. Journal of Rare Earths, 3, 846-849.

Liu, W., Sun, C., Yue, M., Sun, H., Zhang, D., Zhang, J., Yi, X., Chen, J., 2013. Improvement of coercivity and corrosion resistance of Nd-Fe-B sintered magnets by doping aluminium nano-particles. Journal of Rare-Earths, 31, 65-68.

Liu, X.-L., He, J.-P., Dong, Q.-F., Zhou, S.-Z., 2001. A Study of Grain Growth Kinetics in Sintered NdFeB Magnets. Journal of Rare Earths, 19, 209-213.

Livingston, J.D., 1996. Driving Force: The Natural Magic of Magnets. Harvard University Press.

Lü, L., Fuh, J., Wong, Y., 2001. Laser-Induced Materials and Processes for Rapid Prototyping. Kluwer Academic Publishers.

Lukin, A.A., Kol'chugina, N.B., Burkhanov, G.S., Klyueva, N.E., Skonitseva, K., 2013. Role of Terbium Hydride Additions in the Formation of Microstructure and Magnetic Properties of Sintered Nd–Pr–Dy–Fe–B Magnets. Inorganic Materials: Applied Research, 4, 256-259.

Lyman, J.W., Palmer, G.R., 1992. US Patent 5,129,945.

Lynas, 2010. Investor Presentation 2010.

Lynas, 2015. From Mine to Market. Lynas Corporation Annual Report 2014.

Ma, B.M., Bounds, C.O., 1991. The impact of the directional solidification on the magnetic properties of NdFeB magnets. Journal of Applied Physics, 70, 6471-6473.

Madaah Hosseini, H.R., Dadoo, A., Dolati, A., Kianvash, A., 2006. A study on the corrosion behavior of the (Nd, MM)2(Fe, Co, Ni)14B-type sintered magnets. Journal of Alloys and Compounds, 419, 337–341.

Man, H.H., Man, H.C., Leung, L.K., 1996. Corrosion protection of NdFeB magnets by surface coatings - Part I: salt spray test. Journal of Magnetism and Magnetic Materials, 152, 40-46.

Marthinussen, S.-A., 2011. The Effect of Fluid Viscosity on Hydrocyclone Performance. M.Sc. Thesis, University of Bergen

Matsushita, J., Nagashima, H., Saito, H., 1991.Journal of Ceramic Society of Japan International Edition, 99, 77-80.

Matsuura, Y., Hirosawa, S., Yamamoto, H., Fujimura, S., Sagawa, M., Osamura, K., 1985a. Phase diagram of the Nd-Fe-B ternary system. Japanese Journal of Applied Physics, 24, L635-L637.

Matsuura, Y., Hirosawa, S., Yamamoto, H., Fujimura, S., Sagawa, M., 1985b. Magnetic properties of the $Nd_2(Fe_{1-x}Co_x)_{14}B$ system. Applid Physics Letters, 46, 308-310.

McCaig, M., 1977. Permanent Magnets in Theory and Practice. Pentech Press.

McCain, S., 2011. Characterisation of the Aqueous Corrosion Process in NdFeB Melt Spun Ribbon and MQI Bonded Magnets. Ph.D. Thesis, University of Birmingham.

McGuiness, Devlin, E., P.J., Harris, I.R., Rozendaal, E., Ormerod, J., 1989b. A study of Nd-Fe-B magnets produced using a combination of hydrogen decrepitation and jet milling Journal of Materials Science, 24, 2541-2548.

McGuiness, P.J., Ahmed, A., Jones, D.G.R., Harris, I.R., Burns, S., Rozendaal, E., 1990a. The hydrogen decrepitation behavior of alloys and magnets based on $Nd_{16}Fe_{76}B_8$. Journal of Applied Physics, 67, 4626-4628.

McGuiness, P.J., Fitzpatrick, L., Yartys, V.A., Harris, I.R., 1994. Anisotropic hydrogen decrepitation and corrosion behaviour in NdFeB magnets. Journal of Alloys and Compounds, 206, L7-L10.

McGuiness, P.J., Harris, I.R., 1988. The use of hydrogen in the production and characterization of NdFeB magnets. Journal of Applied Physics, 64, 5308-5310.

McGuiness, P.J., Harris, I.R., Rozendaal, E., Romerod, J., Ward, M., 1986. The production of a Nd-Fe-B permanent magnet by a hydrogen decrepitation/attritor milling route. Journal of Materials Science, 21, 4107-4110.

McGuiness, P.J., Scholz, U.D., Nagel, H., Harris, I.R., 1989a. Hydrogen absorption and desorption in NdFeB alloys. Zeitschrift für Physikalische Chemie Neue Folge, 163, 687-692.

McGuiness, P.J., Williams, A.J., Harris, I.R., 1989c. Sintering behaviour of NdFeB magnets. IEEE Transactions on Magnetics, 25, 3773-3775.

Meakin, J.P., Speight, J.D., Sheridan, R.S., Bradshaw, A., Harris, I.R., Williams, A.J., Walton, A., 2016. 3-D laser confocal microscopy study of the oxidation of NdFeB magnets in atmospheric conditions. Applied Surface Science, 378, 540–544.

Meor Yusoff, M.S., 1994. Analysis of thorium and uranium in Malaysian samples by using EDXRF. Presented at Seminar Kebangsaan sinaran Bahan Radioaktif Tabii dalam alam sekitar, October 17-18, 1994.

Meyer, L., Bras, B., 2011. Rare earth metal recycling, sustainable systems and technology. Presentation at IEEE International Symposium on Sustainable Systems and Technology, Chicago, USA, 1-6.

Mishima, T., 1931. British Patents 378,478 and 392,658.

Mizogouchi, T., Sakai, I., Niu, H., Inomata, K., 1986. Nd-Fe-B-Co-Al based permanent magnets with improved magnetic properties and temperature characteristics. IEEE Transactions on Magnetics, 22, 919-921.

Mo, W., Zhang, L., Liu, Q., Shan, A., Wu, J., Komuro, M., 2008. Dependence of the crystal structure of the Nd-rich phase on oxygen content in an Nd–Fe–B sintered magnet. Scripta Materialia, 59, 179-182.

Möller, P., 1986. Rare earth mineral deposits and their industrial importance. Lanthanides, tantalum and niobium. Proceedings of a workshop in Berlin.

Molycorp, 2015a. Form-10k. Annual Report for the Fiscal Year Ended on December 31, 2014. Molycorp.

Molycorp, 2015b. Molycorp, Inc. Signs Restructuring Support Agreement With Key Creditors; Agreement Covers More Than 70% of 10% Secured Noteholders. Molycorp.com, June 25, 2015.

Moores, S., 2014. China Admits 40% of Magnetic Rare Earths Supply Is Illegal. Mining.com. Benchmark Mineral Intelligence, October 21, 2014.

Moosa, I.S. & Nutting, J., 1988. Hydrogen decrepitation of a permanent magnet Nd-Fe-B alloy. Journal of the Less Common Metals, 144, 221-225.

Moosa, I.S., 2014. History and Development of Permanent Magnets. International Journal for Research & Development in Technology, 2, 18-26.

Moosa, I.S., Nutting, J., 1988. Hydrogen decrepitation of a permanent magnet Nd-Fe-B alloy. Journal of the Less Common Metals, 144, 221-225.

Mottram, R.S., 1998a. Properties of sintered neodymium iron boron magnets produced by a powder blending process. Ph.D. Thesis, University of Birmingham.

Mottram, R.S., Davies, B.E., Taylor, M.G., Harris, I.R., 2000a. Effect of Blending Additions on the Sintering Behaviour of NdFeB-Type Magnets. Proceedings on the 16th International Workshop on Rare-Earths and their Applications, 247-256.

Mottram, R.S., Harris, I.R., 1998b. Production of Sintered NdFeB Magnets by a Powder Blending Technique. Proceedings of the 15th International Workshop on Rare-Earth Magnets and their Applications, 473-479.

Mottram, R.S., Kianvash, A., Harris, I.R., 1999. The use of metal hydrides in powder blending for the production of NdFeB-type magnets. Journal of Alloys and Compounds, 283, 282-288.

Mottram, R.S., Williams, A.J., Harris, I.R., 2000b. Blending additions of cobalt to $Nd_{16}Fe_{76}B_8$ milled powder to produce sintered magnets. Journal of Magnetism and Magnetic Materials, 217, 27-34.

Mottram, R.S., Williams, A.J., Harris, I.R., 2000c. Blending additions of aluminium and cobalt to $Nd_{16}Fe_{76}B_8$ milled powder to produce sintered magnets. Journal of Magnetism and Magnetic Materials, 222, 305-313.

Mottram, R.S., Williams, A.J., Harris, I.R., 2001a. The effects of blending additions of copper and cobalt to $Nd_{16}Fe_{76}B_8$ milled powder to produce sintered magnets. Journal of Magnetism and Magnetic Materials, 234, 80-89.

MPIF, 1986. Standard 42, Method for Determination of Density of Compacted or Sintered Metal Powder Products. Metal Powder Industries Federation.

Murray, H.H., 1980. Major kaolin processing developments. International Journal of Mineral Processing, 7, 263–274.

Nageswararao, K., Wiseman, D.M., Napier-Munn, T.J., 2004. Two empirical hydrocyclone models revisited. Minerals Engineering, 17, 671–687.

Nakamura, H., Fukuno, A., Yoneyama, T., 1989. Corrosion resistance of Nd-Fe-B base magnet alloys. Proceedings on the 10th International Workshop on Rare-Earth Magnets and their Applications, 315-322.

Namkung, S., Kim, D.H., Jang, T.S., 2011. Effect of particle size distribution on the microstructure and magnetic properties of sintered NdFeB magnets. Reviews on Advanced Materials Science, 28, 185-189.

Nasseri-Pouryazdi, M.R., Johnson, G.W., Moulson, A.J., 1993. Microstructural development and sintering of NdFeB alloys. Journal of Materials Science, 28, 5237-5239.

Naumov, A.V., 2008. Review of the world market rare-earth metals. Russian Journal of Non Ferrous Metals, 49, 14-22.

Neesse, T., Dueck, J., Minkov, L., 2004a. Separation of finest particles in hydrocyclones. Minerals Engineering, 17, 689–696.

Nenu, R.K.T., Yoshida, H., 2009. Comparison of separation performance between single and two inlets hydrocyclones. Advanced Powder Technology, 20, 195–202.

Nesbitt, E.A., 1946. Vicalloy: A Workable Alloy for Permanent Magnets. Metals Technology, 13, 1-11.

Nesbitt, E.A., Kelsall, G.A., 1940a. Vicalloy, a New Permanent Magnet Material, Physical Review, 58, 203.

Nesbitt, E.A., Kelsall, G.A., 1940b. U.S. Patent 2,190,667.

Nesbitt, E.A., Kelsall, G.A., Dunlop, K.S., 1939. U.S. Patent 2,298,225.

Ni, J., Zhang, W., Jia, Z., Wang, C., Ma, J., 2014b. Effects of post-sinter annealing on the electrochemical corrosion resistance of Nd-Fe-B sintered magnets. Journal of Magnetism and Magnetic Materials, 367, 60–63.

Ni, J., Zhou, S., Jia, Z., Wang, C., 2014a. Improvement of corrosion resistance in Nd–Fe–B sintered magnets by intergranular additions of Sn. Journal of Alloys and Compounds, 588, 558–561.

Niarchos, D., Zouganelis, G., Kostikas, A., Simopoulos, A., 1986. Magnetic properties of the $R_{1+e}Fe_4B_4$ compounds (R = rare earth) from magnetization and Mössbauer measurements. Solid State Communications, 59, 389-391.

Nothnagel, P., Muller, K.H., Eckert, D., Handstein, A., 1991. The influence of particle size on the coercivity of sintered NdFeB magnets. Journal of Magnetism and Magnetic Materials, 101, 379-381.

Nozieres, J.P., Taylor, D.W., Bala, H., Malik, M., Szymura, S., Stoklosa, H.J., 1992. Corrosion behaviour of hot-worked Nd-Fe-B and Nd-Fe-Cu-B permanent magnets. Journal of Alloys and Compounds, 186, 201-208.

NRC, 2008. Minerals, Critical Minerals, and the U.S. Economy. National Research Council of the National Academies. The National Academies Press.

Oddo, G., 1914. Die Molekularstruktur der radioaktiven Atome. Zeitschrift für anorganische Chemie, 87, 253.

Oesterreicher, K., Oesterreicher, H., 1984. Structure and Magnetic Properties of $Nd_2Fe_{14}BH_{2.7}$. Physica Status Solidi A, 85, K61-K64.

Okabe, T.H., Takeda, O., Fukuda, K., Umetsu, Y., 2003a. Direct extraction and recovery of neodymium metal from magnet scrap. Materials Transactions, 44, 798-801.

Okabe, T.H., Takeda, O., Fukuda, K., Umetsu, Y., 2003b. Scrap Combination for Recycling of Valuable Metals: Direct Extraction and Recovery of Neodymium Metal from Magnet Scraps. In: Metallurgical and Materials Processing: Principles and Technologies, vol. 1. Materials Processing Fundamentals and New Technologies, 1079-1091.

Olson, T.J., Turner, P.A., 2002. Hydrocyclone selection for plant design. Mineral Processing Plant Design, Operating Practices and Control Proceedings, 1, 880– 893.

Ormerod, J., 1985. The physical metallurgy and processing of sintered rare earth permanent magnets. Journal of the Less Common Metals, 111, 49-69.

Ormerod, J., 1988. Permanent Magnet Materials. IEE Colloquium Permanent Magnet Machine.

Ormerod, J., 1989. Powder Metallurgy of Rare Earth Permanent Magnets. Powder Metallurgy, 32, 244-249.

Otsuki, E., Otusuka, T., Imai, T., 1990. Processing and magnetic properties of sintered Nd–Fe–B magnets. Proceedings of the 11th International Workshop on Rare-Earth Magnets and their Applications, Pittsburgh, 328-340.

Overshott, K.J., 1991. Magnetism: It is Permanent. IEE Proceedings A, 138, 22-30.

Pan, M., Zhang, P., Li, X., Ge, H., Wu, Q., Jiao, Z., Liu, T., 2010. Effect of Terbium addition on the coercivity of the sintered NdFeB magnets. Journal of Rare Earths, 28, 399-402.

Park, K.T., Hiraga, K., Sagawa, M., 2000. Effect of Metal-Coating and Consecutive Heat Treatment on Coercivity of Thin Nd-Fe-B Sintered Magnets. Proceedings of the 16th International Workshop on Rare-Earth Magnets and their Applications, 257-.

Pastushenkov, J., Durst, K.D., Kronmuller, H., 1987. Domain observations under applied fields of sintered $Fe_{77}Nd_{15}B_8$ permanent magnets. Physica Status Solidi, 140, 487-495.

Pei, W., He, C., Lian, F., Zhou, G., Yang, H., 2002. Structures and magnetic properties of sintered Nd-Fe-B magnets produced by strip casting technique. Journal of Magnetism and Magnetic Materials, 239, 475-478.

Pourarian, F., Simizu, S., Obermyer, R.T, Sankar, S.G., Wallace, W.E., 1990. High field magnetic behaviour of $Pr_{15}Fe_{63}Co_{16}GaB_5$ sintered magnet. Proceedings on the 11th International Workshop on Rare-Earth Magnets and their Applications, 401-407.

Pourarian, F., Wallace, W.E., Malik, S.K., 1982a. Magnetic characteristics of $RCo_{2-x}Fe_x$ hydrides (R ≡ Tb,Dy). Journal of the Less Common Metals, 83, 95-103.

Pourarian, F., Wallace, W.E., Malik, S.K., 1982b. Magnetic behavior of Laves phase $RCo_{2-x}Fe_x$ (R = Ho, Er) compounds and their hydrides. Journal of Magnetism and Magnetic Materials, 25, 299-306.

Puprasert, C., Hebrard, G., Lopez, L., Aurelle, Y., 2004. Potential of using hydrocyclone and hydrocyclone equipped with Grit pot as a pre-treatment in run-off water treatment. Chemical Engineering and Processing: Process Intensification, 43, 67–83.

Rabinovich, Y.M., Sergeev, V.V., Maystrenko, A.D., Kulakovsky, V., Szymura, S., Bala, H., 1996. Physical and mechanical properties of sintered Nd-Fe-B type permanent magnets. Intermetallics, 4, 641-645.

Ragg, O.M., Harris, I.R., 1997. A study of the effects of the addition of various amounts of Cu to sintered Nd-Fe-B magnets. Journal of Alloys and Compounds, 256, 252-257.

Ramesh, R., 1990. A microstructure based magnetization reversal model in sintered Fe-Nd-B magnets. II. Effect of post sintering treatments. Journal of Applied Physics, 68, 5772-5777.

Ramesh, R., Chen, J.K., Thomas, G.J., 1987. On the grain-boundary phase in iron rare-earth boron magnets. Journal of Applied Physics, 61, 2993-2998.

Ramesh, R., Thomas, G., 1988a. Effect of quench rate on the intrinsic coercivity of iron-rare earth-boron permanent magnets. Acta Metallurgica, 36, 3137-3147.

Ramesh, R., Thomas, G., Ma, B.M., 1988b. Magnetization reversal in nucleation controlled magnets. II. Effect of grain size and size distribution on intrinsic coercivity of Fe-Nd-B magnets. Journal of Applied Physics, 64, 6416-6423.

Reck, B.K., Graedel, T.E., 2012. Challenges in metal recycling, Science 337, 690-695.

Reiners, C.S., 2001. Was ist das Seltene an den Seltenen Erden? Eine chemiedidaktische Reflexion. Chemie in unserer Zeit, 35, 110–115.

Riaño, S., Binnemans, K., 2015. Extraction and separation of neodymium and dysprosium from used NdFeB magnets: an application of ionic liquids in solvent extraction towards the recycling of magnets. Green Chemistry, 17, 2931-2942.

Rice, R.W., 1996. Grain size and porosity dependence of ceramic fracture energy and toughness at 22 °C. Journal of Materials Science, 31, 1969-1983.

Rietema, K., 1961. Performance and design of hydrocyclones – parts I–IV. Chemical Engineering Science, 15, 298–325.

Rivoirard, S., Noudem, J.G., de Rango, P., Fruchart, D., Liesert, S. & Soubeyroux, J.L., 2000. Anisotropic and coercive NdFeB for bonded magnets. Proceedings of the 16th International Workshop on Rare Earth Permanent Magnets and their Applications, 347-354.

Rodewald, W., 1987. Magnetic properties of sintered Nd-Fe-Al-B alloys. Proceedings of the 9th International Workshop on Rare-Earth Magnets and their Applications, 609.

Rodewald, W., Wall, B., 1989. Structure and magnetic properties of sintered Nd-Fe-Nb-B magnets. Journal of Magnetism and Magnetic Materials, 80, 57-60.

Rodewald, W., Wall, B., Fernengel, W., 1997. Grain Growth Kinetics in Sintered Nd-Fe-B Magnets. IEEE Transactions on Magnetics, 33, 3841-3843.

Roebuck, B., 1992. Mechanical test discriminability for WC hardmetals. International Journal of Refractory Metals and Hard Materials, 11, 127-136.

Roskill, 2007. The economics of rare earths and yttrium. Roskill Information Services Limited.

Rupp, B., Resnik, A., Shaltiel, D. & Rogl, P., 1988. Phase-relations and hydrogen absorption of neodymium iron (boron) alloys. Journal of Materials Science, 23, 2133-2141.

Rushton, A., Ward, A.S., Holdich, R.G., 2000. Solid-liquid filtration and separation technology. Wiley-VCH.

Sagawa, M., Fujimora, S., Togawa, N., Yamamoto, H., Matsuura, Y., 1984a. New Material for Permanent Magnets on a Base of Nd and Fe. Journal of Applied Physics, 55, 2083-2087.

Sagawa, M., Fujimura, S., Yamamoto, H., Matsuura, Y, Hiraga, K., 1984b. Permanent magnet materials based on the rare earth-iron-boron tetragonal compounds. IEEE Transactions on Magnetics, 20, 1584-1589.

Sagawa, M., Fujimura, S., Yamamoto, H., Matsuura, Y., Hirosawa, S., 1985. Magnetic properties of rare-earth-iron-boron permanent magnet materials. Journal of Applied Physics, 57, 4094-4096.

Sagawa, M., Hirosawa, S., Yamamoto, H., Fujimura, S., Matsuura, Y., 1987. Nd-Fe-B Permanent Magnet Materials, Japanese Journal of Applied Physics, 26, 785-800.

Sagawa, M., Nagata, H., 1993. Novel processing technology for permanent magnets. IEEE Transactions on Magnetics, 29, 2747-2751.

Sagawa, M., Nagata, H., Itatani, O., Watanabe, T., 1994. Improvements of manufacturing process for Nd-FeB sintered magnets. Proceedings of the 13th International Workshop on Rare-Earth Magnets and their Applications, 13-16.

Sagawa, M., Nagata, H., Itatani, O., Watanabe, T., 1995. How are the magnetic properties of NdFeB sintered magnets improved. Proceedings of the 2nd International Workshop on Materials Science, IWOMS 95, 635–640.

Sagawa, M., Nagata, H., Watanabe, T., Itatani, O, 2000. Rubber isostatic pressing (RIP) of powders for magnets and other materials. Materials and Design, 21, 243-249.

Saguchi, A., Asabe, K., Fukuda, T., Takahashi,W., Suzuki, R.O., 2006. Recycling of rare earth magnet scraps: carbon and oxygen removal from Nd magnet scraps. Journal of Alloys Compounds, 408, 1377-1381.

Saguchi, A., Asabe, K., Takahashi, W., Suzuki, R.O., Ono, K., 2002. Recycling of rare earth magnet scraps part III carbon removal from Nd magnet grinding sludge under vacuum heating. Materials Transactions, 43, 256-260.

Saguchi, A., Uesugi, T., Takigawa, Y., Higashi,K., 2014. Development of highly efficient saving processes of rare earth in R-T-B permanent magnet. Physics Procedia, 54, 168-173.

Saito, T., Fukui, M., Takeishi, H., 2005. Sm–Fe–N bulk magnets produced by compression shearing method. Scripta Materialia, 53, 10, 1117-1121.

Saito, T., Sato, H., Motegi, T., 2006. Recovery of rare earths from sludges containing rare-earth elements. Journal of Alloys and Compounds, 425, 145-147.

Saito, T., Sato, H., Ozawa, S., Yu, J., Motegi, T., 2003. The extraction of Nd from waste Nd-Fe-B alloys by the glass slag method. Journal of Alloys and Compounds, 353, 189-193.

Sasaki, S., Fidler, J., Sagawa, M., 2000. High Performance Sintered Nd-Fe-B Magnets Made by New RIP from SC Alloys. Proceedings on the 16th International Workshop on Rare-Earth Magnets and their Applications, 109-118.

Sattler, K., Feindt, H.J., 1995. Thermal Separation Processes. Principles and design. VCH.

Savery, S., 1730. Magnetical Observations and Experiments. Philosophical Transactions of the Royal Society, 36, 295-340.

Schmidt, F.A., Peterson, D.T., Wheelock, J.T., Jones, L.L., 1992. U.S. Patent 5,174,811.

Schneider, G., Henig, E.-Th., Petzow, G., Stadelmaier, H.H., 1986. Phase relations in the system Fe-Nd-B. Zeitschrift für Metallkunde, 77, 755-761.

Schubert, W.D., Neumeister, H., Kinger, G., Lux, B., 1998. Hardness to toughness relationship of fine-grained WC-Co hardmetals. International Journal of Refractory Metals & Hard Materials, 16, 133-142.

Schüler, D., Buchert, M., Liu, R., Dittrich, S., Merz, C., 2011. Study on Rare Earths and Their Recycling. Oeko-Institut e.V, Germany.

Seljasater, K.S., Rogers, B.A., 1932. Magnetic and Mechanical Hardness of Dispersion-Hardened Iron Alloys. Transactions of the American Society for Steel Treating, 19, 553-572.

Shanghai Metals Market, 2016. http://www.metal.com/metals/rare-earth/prices. Accessed 02/11/2016.

Shatsov, A.A., Ryaposov, I.V., Larinin, D.M.,2011. Model of Fracture, Friction, and Wear Phenomena of Porous Iron. Advances in Tribology, 1-16.

Shaw, S., Constantinides, S., 2012. Permanent magnets: the demand for rare earths. 8th International Rare Earths Conference, Hong Kong, China.

Shinba, Y., Konno, T.J., Ishikawa, K., Hiraga, K., Sagawa, M., 2005. Transmission electron microscopy study on Nd-rich phase and grain boundary structure of Nd–Fe–B sintered magnets. Journal of Applied Physics, 97, 503-504.

Shoemaker, C.B., Shoemaker, D.P., Fruchart, R., 1984. The structure of a new magnetic phase related to the sigma phase: iron neodymium boride $Nd_2Fe_{14}B$. Acta Crystallographica, C40, 1665-1668.

Sinnema, S., Radwanski, R.J., Franse, J.J.M., de Mooij, D.B., Buschow, K.H.J., 1984. Magnetic properties of ternary rare-earth compounds of the type $R_2Fe_{14}B$. Journal of Magnetism and Magnetic Materials, 44, 333-341.

Skulj, I., Evans, H.E., Harris, I.R., 2008. Oxidation of NdFeB-type magnets modified with additions of Co, Dy, Zr and V. Journal of Materials Science, 43, 1324-1333.

Smithells, J.C., 1976. Metals Reference Book. Butterworth-Heinemann.

Soccol, O.J., Botrel, T.A., 2004. Hydrocyclone for pre-filtering of irrigation water. Scientia Agricola, 61, 134-140.

Sotnik, A.A., Vasilev, A.D., Firstov, S.A., Slis, I.G., Chernychov, L.I., 2013. Effect of porosity on fracture toughness of brittle powder materials. ECF8 Fracture Behaviour and Design of Materials and Structures, 439-444.

Sprecher, B., Kleijn, R., Kramer, G.J., 2014a. Recycling Potential of Neodymium: The Case of Computer Hard Disk Drives. Environmental Science and Technology, 48, 9506-9513.

Sprecher, B., Xiao, Y, Walton, A., Speight, J., Harris, R., Kleijn, R., Visser, G., Kramer, G.J., 2014b. Life cycle inventory of the production of rare earths and the subsequent production of NdFeB rare earth permanent magnets. Environmental Science & Technology, 48, 3951–3958.

Strnat, K., Hoffer, G., Olson, J., Ostertag, W., 1967. A family of new Cobalt-base permanent magnet materials. Journal of Applied Physics, 38, 1001.

Strnat, K.J., 1978. Rare-earth magnets in present production and development. Journal of Magnetism and Magnetic Materials, 7, 351-360.

Sun, W., Zhu, M., Fang, Y., Liu, Z., Chen, H., Guo, Z., Li, W., 2015. Magnetic properties and microstructures of high-performance Sm_2Co_{17} based alloy. Journal of Magnetism and Magnetic Materials, 378, 214-216.

Suzuki, R.O., Saguchi, A., Takahashi, W., Yagura, T., Ono, K., 2001. Recycling of rare earth magnet scraps: Part II Oxygen removal by calcium. Materials Transactions, 42, 2492-2498.

Svarovsky, L., 2000. Solid-liquid separation. Butterworth-Heinemann.

Svoboda, J., 2004. Magnetic Techniques for the Treatment of Materials. Springer.

Szymura, S., Bala, H., Pawlowska, G., Rabinovich, Y.M., Serheev, V.V., Pokrovskii, D.V., 1991. Modification of the magnetic properties and corrosion resistance of Nd-Fe-B permanent magnets with addition of cobalt. Journal of the Less Common Metals, 175, 185-198.

Takakuwa, O., Mano, Y., Soyama, H., 2014. Effect of indentation load on Vickers hardness of austenitic stainless steel after hydrogen charging. Pressure Vessels and Piping Conference, Garden Grove, USA, Vol. 6B, 28280-28285.

Takeda, O., Okabe, T.H., Umetsu, Y., 2004. Phase equilibrium of the system Ag-Fe-Nd, and Nd extraction from magnet scraps using molten silver. Journal of Alloys and Compounds, 379, 305-313.

Takeda, O., Okabe, T.H., Umetsu, Y., 2006. Recovery of neodymium from a mixture of magnet scrap and other scrap. Journal of Alloys and Compounds, 408, 387-390.

Tanaka, M., Oki, T., Koyama, K., Narita, H., Oishi, T., 2013. Recycling of rare earths from scrap. In: Handbook on the Physics and Chemistry of Rare Earths, Elsevier, 159-212.

Tang, W., Zhou, S., Wang, R., 1988b. On the neodymium-rich phases in Nd-Fe-B magnets. Journal of the Less Common Metals, 141, 217-223.

Tang, W., Zhou, S., Wang, R., Graham Jr., C.D., 1988a. An investigation of the Nd-rich phases in the Nd-Fe-B system. Journal of Applied Physics, 64, 5516-5519.

Tawara, Y., Senno, H., 1972. Sintered magnets of copper- and iron-modified cerium cobalt. IEEE Transactions on Magnetics, 8, 560-561.

Thoburn, W.C., Legvold, S., Spedding, F.H., 1958. Magnetic properties of terbium metal. Physics Reviews, 112, 56-61.

Thümmler, F., Oberacker, R., 1993. Introduction to Powder Metallurgy. The Institute of Materials.

Tokunaga, M., Kogure, H., Endoh, M., Harada, H., 1987. Improvement of thermal stability of Nd-Dy-Fe-Co-B sintered magnets by additions of Al, Nd and Ga. IEEE Transactions on Magnetics, 23, 2287-2289.

Uestuener, K., Katter, M., Rodewald, W., 2006. Dependence of the Mean Grain Size and Coercivity of Sintered Nd–Fe–B Magnets on the Initial Powder Particle Size. IEEE Transactions on Magnetics, 2897-2899.

UNCTAD, 2014. Commodities at a Glance. Special issue on rare earths. No. 5. United Nations Conference on Trade and Development.

USGS, 2002. Rare-earth elements – critical resources for high technology. United States Geological Survey Mineral Resources Program. Fact Sheet 087-02.

USGS, 2009. Mineral Commodity Summaries, January 2009. United States Geological Survey. Rare Earths.

USGS, 2014. The rare-earth elements – vital to modern technologies and lifestyle. United States Geological Survey Mineral Resources Program. Fact Sheet 2014-3078.

USGS, 2015a. Historical Data. DS 140, Rare Earths Statistics. XLS-spreadsheet.

USGS, 2015b. Mineral Commodity Summaries 2015. United States Geological Survey.

USITC, 1996. Certain neodymium-iron-boron magnets, magnet alloys, and articles containing same. U.S. International Trade Commission, Investigation No. 337-TA-372.

Vander Hoogerstraete, T., Blanpain, B., Van Gerven, T., Binnemans, K., 2014 From NdFeB magnets towards the rare-earth oxides: a recycling process consuming only oxalic acid. RSC Advances, 4, 64099-64111.

Velicescu, M., Schrey, P., Rodewald, W., 1995. Dy-distribution in the grains of high-energy (Nd,Dy)-Fe-B magnets. Transactions on Magnetics, 31, 3623-3625.

Verdier, M., Morros, J., Pere, D., Shell, N. & Harris I.R., 1994. Stability of Nd-Fe-B powders obtained by hydrogen decrepitation. IEEE Transactions on Magnetics, 30, 657-659.

Vial, F., Rozendaal, E., Sagawa, M., 1998. Improvement of microstructure and magnetic properties of sintered NdFeB permanent magnets. Proceedings of the 15th International Workshop on Rare-Earth Magnets and their Applications, 401-410.

Vicente, C.M.S., André, P.S., Ferreira, R.A.S., 2012. Simple measurement of surface free energy using a web cam. Revista Brasileira de Ensino de Física, 34, 3312-1-3312-5.

Vorobev, V.V., Krupotkin, M.Ya., Finkel, V.A., 1989. Anomalous behaviour of elastic moduli of terbium and dysprosium in magneto ordered state. Physica Status Solidi, 113, 2, 375-381.

Wallace, W.E., Craig, R.S., Rao, V.U.S., 1980. Hydrogen absorption by intermetallic compounds. Advances in Chemistry Series, 186, 207-240.

Walton, A., 2001. Low Pressure Pack Sublimation (LPPS): A zinc coating process for NdFeB magnets. PhD Thesis, University of Birmingham.

Walton, A, Yi, H. Rowson, N.A., Speight, J.D., Mann, V.S.J., Sheridan, R.S., Bradshaw, A., Harris, I.R., Williams, A.J., 2015. The use of hydrogen to separate and recycle neodymium-iron-boron-type magnets from electronic waste. Journal of Cleaner Production, 104, 236-241.

Walton, A., Han Yi, Mann, V.S.J., Bevan, A.I., Speight, J.D., Harris, I.R., Williams, A.J., 2012. The Use of Hydrogen to Separate and Recycle NdFeB Magnets from Electronic Waste, Proceedings of the 22nd International Workshop on Rare-Earth Magnets and their Applications, 10-13.

Walton, A., Williams, A.J., 2011. Rare earth recovery. Materials World, 19, 24-26.

Wang, S.C., Li, Y., 2005a. A new structure of $Nd_{1+\varepsilon}Fe_4B_4$ phase in NdFeB magnet. Journal of Materials Science, 40, 3853-3855.

Wang, S.C., Li, Y., 2005b. In situ TEM study of Nd-rich phase in NdFeB magnet. Journal of Magnetism and Magnetic Materials, 285, 177–182.

Wang, X.L., Zhao, L.N., Ding, K.H., Cui, S.L., Sun, Y.C., Li, M.S., 2015. Effect of optimized aging processing on properties of the sintered Dy-doped Nd–Fe–B permanent magnet. Chinese Physics B, 24, 037506-1–037506-4.

Wecker, J., Cerva, H., Kuhrt, C., Schnitzke, K., Schultz, L., 1994. Microstructure and magnetic properties of mechanically alloyed anisotropic Nd-Fe-B. Journal of Applied Physics, 76, 6238-6240.

Weiss, P., 1906. La variation du ferromagnetisme du temperature. Comptes Rendus, 143, 1136-1149.

Wellens, S., Thijs, B., Binnemans, K., 2012. An environmentally friendlier approach to hydrometallurgy: highly selective separation of cobalt from nickel by solvent extraction with undiluted phosphoniumionic liquids. Green Chemistry, 14, 1657-1665.

White, D.A., 1991. Efficiency curve model for hydrocyclones based on crowding theory. Transactions of the Institution of Mining and Metallurgy, Section C: Mineral Processing and Extractive Metallurgy, 100, 135–138.

Wiesinger, G., Hilscher, G., Grossinger, R., 1987. Effect of hydrogen absorption on the magnetic properties of $Nd_{15}Fe_{77}B_8$. Journal of the Less Common Metals, 131, 409-417.

Williams, A.J., 1994. Hydrogen absorption and desorption studies on NdFeB type alloys used for the production of permanent magnets. PhD Thesis, University of Birmingham.

Williams, A.J., McGuiness, P.J., Harris, I.R., 1990. Mass spectrometer studies of hydrogen desorption from hydrided NdFeB. IEEE Transactions on Magnetics, 26, 1945-1947.

Williams, A.J., McGuiness, P.J., Harris, I.R., 1991. Mass spectrometer hydrogen desorption studies on some hydrided NdFeB-type alloys. Journal of the Less Common Metals, 171, 149-155.

Woodcock, T. G., Hrkac, G., Schrefl, T., Gutfleisch, O., 2012. Multiscale Characterisation and Modelling of Grain Junctions in Nd-Fe-B Sintered Magnets. Proceedings of the 22nd International Workshop on Rare-Earth Magnets and their Applications, Nagasaki, Japan, 61-65.

Woodcock, T.G., Zhang, Y., Hrkac, G., Ciuta, G., Dempsey, N.M., Schrefl, T., Gutfleisch, O., Givord, D., 2012b. Understanding the microstructure and coercivity of high performance NdFeB-based magnets. Scripta Materialia, 67, 536-541.

Woolley, A.R., Kjarsgaard, B.A., 2008. Carbonatite occurrences of the world: map and database. Geological Survey of Canada, report 5796.

WTO, 2015. Dispute DS431. China — Measures Related to the Exportation of Rare Earths, Tungsten and Molybdenum. World Trade Organisation.

Xinhua, 2014. China Illegal Rare Earth Mining Hit 40,000 Tonnes Each Year, Expert.

Xiong, D.H., Liu, S.Y., Chen, J., 1998. New technology of pulsating high gradient magnetic separation. International Journal of Mineral Processing, 54, 111–127.

Xu, Y., 1999. Liquid metal extraction of Nd from Nd-Fe-B magnet scrap. M.Sc. Thesis, Iowa State University.

Xu, Y., Chumbley, L.S., Laabs, F.C., 2000. Liquid metal extraction of Nd from Nd-Fe-B magnet scrap. Journal of Materials Research, 15, 2296-2304.

Yalamanchili, M.R., Miller, J.D., 1995. Removal of insoluble slimes from potash ore by air-sparged hydrocyclone flotation. Minerals Engineering, 8, 169-177.

Yamamoto, H., Matsuura, Y., Fujimura, S., Sagawa, M., 1984. Magnetocrystalline anisotropy of $R_2Fe_{14}B$ tetragonal compounds. Applied Physics Letters, 45, 1141-1143.

Yang, I.H., Shin, C.B., Kim, T.-H., Kim, S., 2004. A three-dimensional simulation of a hydrocyclone for the sludge separation in water purifying plants and comparison with experimental data. Minerals Engineering, 17, 637–641.

Yang, J.P., Pi, S.H., Kim, Y.P., Kim, Y.G., 1993. Effect of Cyclic Heat Treatment on Coercivity and Microstructure of Sintered $Nd_{15}Fe_{77}B_8$ Magnets. Journal of Materials Science and Engineering B18, 78-82.

Yartys, V.A., Gutfleisch, O., Panasyuk, V.V., and Harris, I.R., 1997. Desorption Characteristics of Rare Earth (R) hydrides (R=Y, Ce, Pr, Nd, Sm, Gd and Tb) in Relation to The HDDR Behaviour of R–Fe-Based-Compounds. Journal of Alloys and Compounds, 253–254, 128 – 133.

Yu, L.Q., Wen, Y.H., Yan, M., 2004. Effects of Dy and Nb on the magnetic properties and corrosion resistance of sintered NdFeB. Journal of Magnetism and Magnetic Materials, 283, 353–356.

Yuan, J., 2005. Numerical simulation of hysteresis effects in ferromagnetic material with the finite integration technique. Ph.D. Thesis, Technischen Universität Darmstadt.

Zakotnik, M., Devlin, E., Harris, I.R., Williams, A.J., 2006. Hydrogen decrepitation and recycling of Nd-Fe-B-type sintered magnets. Proceedings of the 19th Workshop on Rare Earth Permanent Magnets and Their Applications, 289-295.

Zakotnik, M., Harris, I.R., Williams, A.J., 2008a. Possible methods of recycling Nd-Fe-B-type sintered magnets using the HD/degassing process. Journal of Alloys and Compounds, 450, 525-531.

Zakotnik, M., Harris, I.R., Williams, A.J., 2009. Multiple recycling of Nd-Fe-B-type sintered magnets. Journal of Alloys and Compounds, 469, 314-321.

Zakotnik, M., Tudor, C.O., 2015. Commercial-scale recycling of NdFeB-type magnets with grain boundary modification yields products with 'designer properties' that exceed those of starting materials. Waste Management, 44, 48–54.

Zakotnik, M., Williams, A.J., Harris, I.R., 2004. Possible methods of recycling NdFeB-type sintered magnets using the HD/degassing or HDDR process. Proceedings of the 18th Workshop on High Performance Magnets and their Applications, 1, 267-274.

Zakotnik, M., Williams, A.J., Martinek, G., Harris, I.R., 2008b. Hydrogen decrepitation of a 2/17 sintered magnet at room temperature. Journal of Alloys and Compounds, 450, L1-L3.

Zepf, V., 2013. Rare Earth Elements. A New Approach to the Nexus of Supply, Demand and Use. Exemplified along the Use of Neodymium in Permanent Magnets. Springer.

Zepf, V., 2015. An overview of the usefulness and strategic value of rare earth metals. Rare Earths Industry. Technological, Economic and Environmental Implications. Elsevier.

Zhang, P., Ma, T., Liang, L., Yan, M., 2014. Improvement of corrosion resistance of Cu and Nb co-added Nd-Fe-B sintered magnets. Materials Chemistry and Physics, 147, 982-986.

Zhang, X.J., Yin, X.J., McGuiness, P.J., Harris, I.R., 1995. Metallurgical processing of $Nd_2Fe_{14}B$ type permanent magnetic alloys. Journal of Materials Processing Technology, 48, 461-467.